PICOSECOND STUDIES OF MOLECULAR ENERGY TRANSFER, REORIENTATION, AND INTERNAL MOTION DYNAMICS

Thesis by

David Philip Millar

In Partial Fulfillment of the Requirements

for the Degree of

Doctor of Philosophy

California Institute of Technology

Pasadena, California

1982

(Submitted March 19,1982)

ACKNOWLEDGMENTS

I would like to thank my research advisor Professor Ahmed Zewail for his encouragement, help, and support during my years at Caltech. I am very grateful for the opportunity that Ahmed provided to continue my interest in picosecond spectroscopy. I am also grateful to Professors G. Wilse Robinson and Graham Fleming, then at the University of Melbourne, for initiating me into picosecond spectroscopy, and for their interest in my subsequent progress. I thank my collaborator Dr. Ray Robbins for his contributions and help in all aspects of the DNA project, and for graciously sharing his knowledge of photon counting and computing. It was a pleasure to work with Ray, and not simply because we are old friends and fellow Australians. I am also grateful to Dan Dawson and Dr. Rajiv Shah for their work on the passively mode-locked CW dye laser. Dr. Michael Becker and Dr. Richard Scheller are responsible for stimulating my interest in DNA, and for their help, advice, and gifts of some samples I am very grateful. The members of the Zewail group have been friendly, supportive, and helpful at all times; I especially thank fellow students Joe Perry and Bill Lambert.

I am very grateful to Bill Schuelke and the other members of the Chemistry Division Instrument Shop for their expert services, which were essential in carrying out this research. Financial support was from the National Science Foundation under grants CHE79-05683 and DMR-8105034. The Australian-American Educational Foundation is gratefully acknowledged for the award of a Fulbright Fellowship (1977-82). I am very grateful to Tina Wood for her secretarial assistance, and to Ruth Stratton for her expert

typing of this thesis.

Finally, I thank my parents for their love, trust, and support, and Sally for her love and financial support.

ABSTRACT

This thesis describes the development and characterization of mode-locked CW dye lasers and their application to time-resolved studies of molecular reorientation in liquids, electronic energy transfer in solution, and the internal motions of nucleic acids. Both passive and synchronous mode-locking are found to produce slightly structured pulses with coherence times $\Delta t_c \sim 0.8$ psec, and pulse envelope widths $\Delta t_p \sim 2$ to 3 psec.

The dynamics of reorientation of cresyl violet in alcohol solvents is directly studied on the picosecond time scale. The observed rotational correlation function decays as a single exponential, with a rotational relaxation time that is linearly dependent on solvent viscosity. Rotation times calculated from hydrodynamics are a factor of 2 smaller than observed. The discrepancy is attributed to hydrogen-bonding interactions with the solvent that cause additional friction.

Electronic energy transfer between cresyl violet donors and azulene acceptors in solution is studied. The excited donor decay is in excellent agreement with the Förster dipole-dipole model over the time range from 2 psec to 10 nsec. The critical transfer distance inferred from the decay $R_0 = 26\text{Å}$ agrees well with the value calculated from the spectral properties, $R_0 = 27\text{Å}$. The increased energy transfer rate in fluid solutions due to translational motion is accurately predicted by the approximate solution to a diffusion equation for the donor excitation. However, the energy transport due to donor-donor transfer was nondiffusive on the picosecond time scale.

The dynamics of the torsional and bending motions of nucleic acids are studied by sub-nanosecond time-dependent fluorescence depolarization of intercalated ethidium bromide. The non-exponential relaxation behavior is observed for the first time, and is in excellent agreement with the theoretical predictions of an elastic model for DNA internal motions. The intrinsic torsional rigidity of calf thymus DNA is $C = 1.43 \pm 0.11 \times 10^{-19}$ erg.cm. The torsional rigidity is shown to be sensitive to details of primary, secondary, and tertiary nucleic acid structure. The polyelectrolyte contribution to the torsional rigidity of DNA has been measured for the first time.

TABLE OF CONTENTS

Chapter 1

INTRODUCTION

Many of the elementary physical processes in chemistry and biology occur on a picosecond time scale. The advent of picosecond optical spectroscopy [1] has enabled the first direct observation of these processes. This new field of spectroscopy utilizes the ultrashort optical pulses generated by mode-locked lasers [1,2] to initiate and probe rapid processes in a wide variety of materials. Picosecond spectroscopy is thus concerned with both the nature of the transient species produced by optical excitation, and the time-evolution of such species as the system relaxes to an equilibrium. Picosecond techniques have proven to be useful in solid state physics, electronics, and optics [1], but perhaps the most significant and certainly the most widespread application of these new techniques has been in chemistry and biology. The pioneering work of Eisenthal [3] and Rentzepis [4] in the first applications of picosecond spectroscopy to chemistry demonstrated that many fundamental chemical processes occurring in the liquid state are now amenable to study. During the past decade the number of new applications in chemistry and biology has continually grown, and picosecond research is now in progress in many chemistry departments around the world. The number of publications in this field is by now very large, and several excellent reviews have appeared [1,5-7].

Despite this progress, picosecond spectroscopy remains a state-of-the-art technique. The generation of optical pulses and detection of transient events on the picosecond time scale involves a relatively high

level of technical sophistication and complexity, which has unfortunately limited an even more widespread application of picosecond techniques. The traditional problems in picosecond spectroscopy include: the low repetition rate at which picosecond pulses can be generated by mode-locked solid state lasers such as Nd^{3+}:glass [2]; the fluctuations in the energy, intensity, and duration of the pulses generated by these lasers; the complexity of experimental systems; and the high cost of picosecond resolution detectors such as the streak camera [8]. These problems must be circumvented before picosecond spectroscopic techniques can become a routine instrumental procedure.

The objective of this thesis is to investigate the potential usefulness of mode-locked CW dye lasers in chemical and biophysical measurements. These new generation picosecond lasers [9] have several attractive features compared with the solid state lasers that have been used in the past. However, these lasers have not yet been as widely used in picosecond experiments. This thesis describes the construction, characterization, and application of mode-locked CW dye lasers. The phenomena that were studied include intermolecular energy transfer in solution, molecular reorientation and solute-solvent interactions in liquids, and the internal twisting and bending motions of macromolecules in solution. All these phenomena are important for an understanding of molecular energy flow and the dynamic structural properties of molecules in liquids. The application of picosecond techniques to these problems has yielded a considerable amount of new information that has not been available from more conventional physical chemical techniques.

The thesis is organized into two parts. Part I deals with the experimental techniques, and includes a description of the construction and characterization of mode-locked CW dye lasers in Chapter 2, and the transient absorption techniques in Chapter 3, and time-resolved fluorescence techniques in Chapter 4 that were found to be ideally suited to these new lasers. Part II describes the application of these laser techniques to molecular reorientation in solution in Chapter 5, intermolecular energy transfer solution in Chapter 6, and the internal motions of nucleic acids in Chapter 7.

Two types of mode-locked CW dye lasers are described in Chapter 2. A passively mode-locked CW dye laser was constructed at Caltech, and a synchronously mode-locked CW dye laser was later obtained commercially. The zero-background second harmonic autocorrelation method for pulse analysis is described, and the type of information that can be obtained and the limitations of the method are discussed. An important consideration is the effect of substructure in the pulse enevelope, as would occur in an imperfectly mode-locked laser. The pulse duration inferred from the autocorrelation data can be seriously underestimated if the substructure is not accounted for. A procedure for including the substructure in the analysis of autocorrelation data, based on the Pike-Hercher model [10] is then described. Both the laser pulse duration and the laser coherence time appear in theoretical expressions for the pulse autocorrelation function. The application of the model to the autocorrelation data obtained from the passively mode-locked and synchronously mode-locked CW dye lasers showed that both these lasers do indeed produce slightly structured pulses.

Good estimates of the pulse duration, coherence time, and pulse envelope shape have been obtained in each case. The results show that many of the characteristics of these two lasers are very similar. The pulse properties of the synchronously mode-locked laser were, however, strongly dependent on cavity length. The dependence has been carefully measured, and interpreted in terms of a simple model for pulse generation in this type of laser. These results demonstrate several advantages of the mode-locked CW dye lasers over the traditional solid state lasers: the pulse durations from the dye lasers are 2 to 3 times shorter; the repetition rates are 7 orders of magnitude higher, enabling extensive signal averaging; the pulse properties are highly reproducible; the dye lasers are tunable; and, finally, the dye lasers are much simpler to operate than the solid state lasers.

Many of the experimental techniques in picosecond spectroscopy utilize the pump-probe method: an intense picosecond pulse excites the sample and a weaker, delayed pulse probes the transient response of the sample. Chapter 3 describes a pump-probe technique that is well suited to mode-locked CW dye lasers. This technique is known as ground state recovery, since the pump pulse depletes the ground state population and the probe pulses monitor the return of the population. The kinetics of ground state repopulation are obtained from this type of experiment, which is very useful for an understanding of intramolecular relaxation processes, and excited state quenching reactions such as energy transfer that cause ground state recovery. An important practical consideration is the influence of the relative polarization states of the pump and probe pulses. The phenomenon of anisotropic absorption saturation is

discussed and included in a simple theoretical derivation of the ground state recovery signal. It is shown how the rate of reorientation of the anisotropic angular distribution of molecules due to excitation with linearly polarized light can be obtained from these experiments. Some refinements are then included in the derivation that illustrate the limitations of time resolution in ground state recovery experiments. Another complication in these experiments is the additional signal contributions that occur around zero delay time due to a coherence effect that results when both pump and probe pulses are derived from the same laser [11]. It is shown how substructure in the pulses can have observable consequences in the form of these signal contributions.

Time-dependent fluorescence depolarization is a technique that has been widely applied on the nanosecond time scale to study the rotational motion of large macromolecules [12]. Chapter 4 describes the extension of the fluorescence depolarization method to the sub-nanosecond time scale. Fluorescence decay curves were obtained using the time-correlated single photon counting technique [13]. Many of the traditional problems encountered with this method are avoided by using mode-locked CW dye lasers rather than discharge lamps as the excitation source: the short pulse duration improves the time resolution, which is then only limited by the transit-time spread in the detector; the high laser repetition rate enables rapid data collection rates; and the excitation intensity from the laser is much higher than from a discharge lamp. The system described in Chapter 4 combines high sensitivity excellent signal-to-noise ratio, and time resolution of 250 psec. Shorter lifetimes than 250 psec

can be estimated by deconvolution of the instrumental response. In many applications this system is expected to achieve better performance than streak camera [8] detection, and at a much cheaper price.

The study of reorientation of molecules in the liquid state due to rotational Brownian motion can yield considerable information on molecular size and shape, and the nature of solute-solvent interactions. Chapter 5 presents a study of the reorientation of the dye cresyl violet in alcohol solvents using the ground state recovery technique. It is shown that the rotational correlation function measured in this system decays as a single exponential with a rotational relaxation time linearly dependent on the solvent viscosity. The exponential decay can be predicted from the rotational diffusion model, which also relates the measured relaxation time to the principal rotational diffusion coefficients of the molecule. Classical hydrodynamics is often used to relate the diffusion coefficients to the molecular size and shape. The hydrodynamic calculations for cresyl violet predict rotational relaxation times that are at least a factor of two smaller than observed. This anomalous behavior is attributed to the retarding effect of hydrogen-bonding interactions between solute and solvent molecules, which causes an additional friction that is not predicted by hydrodynamics.

The transfer of electronic excitation energy from an excited donor molecule to a ground state acceptor molecule is an important process in condensed phases. Exciton propagation in molecular solids [14] and the elementary steps in photosynthesis [15,16] both involve this process. A detailed understanding of energy transfer processes is best obtained by first studying a simple prototype system. Chapter 6 describes a study of

energy transfer between cresyl violet donors and azulene acceptors distributed at random in solution. A combination of ground state recovery and fluorescence decay techniques was used. The donor decay kinetics were measured over a range of both donor and acceptor concentrations, and in both viscous and fluid solvents. The effects of relative motion of the donor and acceptor due to translational diffusion and due to donor-donor energy transfer were also observed. A theoretical model of energy transfer due to multipole-multipole Coulombic interactions is compared with the data, and shows that the energy transfer in this system is due to a dipole-dipole interaction. Recent theoretical treatments of the diffusion effects and donor-donor transfer are also experimentally tested on the picosecond time scale.

Time-dependent fluorescence depolarization is applied in Chapter 7 to a study of the internal motions of macromolecules in solution. A study of internal motions can potentially provide information on the time-dependent structure and flexibility of macromolecules which cannot be obtained from conventional techniques. As a first step in this direction, the nucleic acids were studied as possible prototype systems because of their relatively simple structure and uniform flexibility. The torsional and bending modes of the double helix were studied by fluorescence depolarization of intercalated ethidium bromide. Although the relaxation behavior of these modes occurs on a nanosecond time scale, the application of sub-nanosecond techniques has enabled new and unambiguous information to be obtained. The non-exponential time dependence of the depolarization due to torsional and bending modes has been established for the first time, and accurate values of the torsional rigidity of DNA has been obtained. Experiments were

performed on a wide variety of nucleic acid samples to investigate the effects of primary, secondary, and tertiary nucleic acid structure on the internal motions. Significant effects were observed and suggest the possibility of using the fluorescence depolarization technique for probing structural effects in these systems. The polyelectrolyte contribution [16] to the torsional rigidity of DNA has also been measured for the first time.

Two appendices complete the thesis. Appendix I presents a system for amplifying the picosecond pulses from mode-locked CW dye lasers. Appendix II presents some details of the data analysis methods used in this work.

References - Chapter 1

1. "Ultrashort Light Pulses," S. L. Shapiro, ed., Topics in Appl. Phys. 18 Springer Verlag, Berlin, 1977.
2. A. J. De Maria, D. A. Stetser, H. Heynau, Appl. Phys. Lett. 8, 174 (1966).
3. K. B. Eisenthal, Acc. Chem. Res. 8, 118 (1975).
4. P. M. Rentzepis, Adv. Chem. Phys. 23, 189 (1973).
5. K. J. Kaufmann, CRC Critical Reviews in Solid State Sci. 8, 265 (1978).
6. K. B. Eisenthal, Ann. Rev. Phys. Chem. 28, 207 (1977); also see ref. [1].
7. G. R. Fleming, Adv. Chem. Phys. 49, 1 (1982).
8. D. J. Bradley, Opt. and Laser Tech., 11, 23 (1979).
9. G. R. Fleming, G. S. Beddard, Opt. and Laser Tech., 10, 257 (1978).
10. M. A. Pike and M. Hercher, J. Appl. Phys. 41, 4562 (1970).
11. H. E. Lessing, A. von Jena, Laser Handbook, Vol. 3, ed. M. L. Stitch, North-Holland, Amsterdam, 1979, p. 753.
12. J. Yguerabide, Methods Enzymol. 26, 498 (1972).
13. W. R. Ware, Creation and Detection of the Excited State, Vol. 1A, A. A. Lamola, ed., Marcel Dekker, New York, 1971.
14. R. C. Powell, Z. G. Soos, J. Lumin 11, 1 (1975).
15. J. Barber, Rep. Prog. Phys. 41, 1158 (1978).
16. A. J. Campillo, S. L. Shapiro, Photochem. Photobiol. 28, 975 (1978).
17. G. S. Manning, Q. Rev. Biophys. 11, 179 (1978).

PART I

EXPERIMENTAL TECHNIQUES

Chapter 2

MODE-LOCKED CW DYE LASERS

2.1 Introduction

The new field of picosecond spectroscopy has its origins in the discovery of mode-locked lasers in 1965 [1]. Mode-locking is a process in which either the gain or loss of the laser is modulated so as to constrain the laser to oscillate in a mode of operation in which a single intense pulse circulates inside the laser cavity. The output of such a laser is a train of nearly identical pulses separated by the round-trip time of the laser cavity. The duration of the individual pulses is limited by the inverse of the spectral bandwidth of the lasing transition; thus, solid-state lasers, which exhibit broad inhomogeneously broadened transitions, produce shorter pulses than gas lasers, which have much narrower spectral widths. Thus most attention has been focussed on mode-locked solid state lasers, such as Nd^{3+}:glass and ruby. Indeed, these lasers have been used in essentially all published experiments during the first decade of picosecond spectroscopy. The characteristics of these lasers are now well known and their advantages and disadvantages in application to picosecond experiments are fully realized. The attractive features of mode-locked solid state lasers are their short pulse duration, typically 3-6 psec, and the high intensity of the pulses, in the MW/cm^2 to GW/cm^2 range. Their main disadvantages in picosecond experiments are extremely low repetition rate and the variation of the individual pulses within the pulse train. Solid state lasers typically operate in a giant pulse mode, wherein a microsecond

duration flash is produced in each laser "shot," the time between shots being typically 3 minutes (this is necessary to allow the laser rod to cool). When mode-locked, a single laser shot consists of a microsecond duration pulse train comprised of a thousand or so ultrashort pulses. The intensity, energy, and duration of the individual pulses vary quite significantly within the pulse train, and also, at a given position within the train they vary from shot to shot. Because of this variability, experimenters are usually forced to select a single pulse from each pulse train. Thus, in practice these lasers produce one ultrashort pulse every 3 minutes, and there is still some shot-to-shot variation in these selected pulses. This limitation has proven to be extremely inconvenient in picosecond experiments requiring many careful measurements. Some techniques have been developed so that the experiment requires only one pulse from one laser shot, such as real-time fluorescence detection with a streak camera, but in general the limitation is a serious one.

Mode-locking of CW gas lasers would produce high repetition rate pulses, but the narrow spectral widths of these lasers do not allow pulses shorter than about 100 psec to be generated. Thus, attention has recently turned to CW dye lasers which can have very broad spectral widths due to the extremely broad gain bandwidths of the laser dyes. In principle, pulses with much shorter duration than the mode-locked solid state lasers should be possible by mode-locking of a dye laser. Also, because the dye lasers readily oscillate in continuous wave (CW) operation, mode-locking will result in a high repetition rate "quasi-CW" operation. That is, the output will consist of a <u>continuous</u> train of pulses, each pulse separated from the next by the round-trip time of

the cavity. Another important difference between the dye laser and solid-state laser has to do with the relaxation dynamics in the gain medium. Because the excited state lifetimes of laser dyes are only a few nanoseconds, considerably shorter than the typical cavity round-trip time, the gain medium is fully recovered by the time of each arrival of the circulating optical pulse, resulting in a type of equilibrium operation. As a result, each pulse in the output train is nearly identical. However, in solid state laser materials the relaxation times are in the microsecond to millisecond range and this equilibrium cannot be established. Consequently, the characteristics of the gain medium evolve in time, which results in the variations of the pulses within the train already mentioned. The nonlinear interactions which occur in the laser medium because of the high optical powers generated by these lasers give rise to additional pulse evolution effects within the pulse-train. Thus an important disadvantage of the mode-locked solid state lasers is completely avoided in mode-locked dye lasers. A further advantage is the wavelength tunability of dye lasers, which is absent in the quasi-monochromatic solid state lasers. Also, the dye laser output is in the more convenient visible spectrum rather than the near infra-red region of ruby and Nd^{3+}:glass lasers.

This discussion has suggested that all the disadvantages inherent in the solid state lasers, mainly pulse to pulse variations, low repetition rate, and lack of tunability, are expected to be absent in mode-locked CW dye lasers. This was the motivation for the development and characterization of mode-locked CW dye lasers undertaken in this work. At the time this work was begun in 1977, mode-locked CW dye lasers were

not available from commercial sources, and our first laser of this type was constructed at Caltech. The design considerations, relevant details of construction, and performance of this passively mode-locked dye laser will be described in Section 2.3 Also, some of the disadvantages which became apparent when working with this system will be described. A second type of mode-locked CW dye laser, which was commercially built, has also been investigated and used in experiments. Since some of the disadvantages of the home-built system are avoided in this laser, it will be evaluated here also and compared with the other system. The different mode-locking mechanisms operative in each laser will be discussed and used as a basis for explaining the characteristics of each laser. Finally, the usefulness of each laser in actual picosecond experiments will be evaluated, and compared with existing laser sources that are popular in picosecond spectroscopy.

2.2 Mode-Locking

The physical process underlying mode-locking is most easily understood by first considering the case of an inhomogeneously broadened laser. The output of such a laser consists of a superposition of many oscillating longitudinal cavity modes. Because the relative phases of the cavity modes tend to vary randomly, the superposition has a chaotic temporal profile due to the random interferences between modes. The purpose of mode-locking is to force the cavity mode phases to maintain their relative values. The superposition then consists of a single intense pulse of radiation circulating in the cavity, with an intensity and duration determined by the number of locked cavity modes. Mode-locking can be achieved

by modulating the gain or loss at a frequency equal to the intermode frequency spacing of the cavity, $\omega = \pi c/\ell$, where ℓ is the cavity length, and c is the speed of light. The lowest threshold of operation under these conditions will be obtained when the laser oscillates with a single pulse circulating in the cavity and synchronized with the modulation; that is, the modulation forces mode-locked operation of the laser. Actually, the modulation discriminates against any broadening of the pulse as would occur when the cavity phases begin to wander and thus in effect continually restores the phases to their fixed, optimal values.

In the normal operation of a homogeneously broadened laser (such as a dye laser) only one longitudinal cavity mode oscillates. The effect of modulation at frequency ω is to transfer power between this oscillating mode, ω_i, and the modes at frequencies $\omega_i \pm \omega$. When $\omega = \pi\ell/c$, these sidebands correspond to the adjacent cavity modes ω_{i-1} and ω_{i+1}. Thus, these modes will also oscillate and transfer power to their sidebands, and so on, resulting in the simultaneous oscillation of a large number of cavity modes with fixed phases. The process is best viewed in this case as one of "mode generation" [2] rather than mode-locking, but the net result is the same as in the inhomogeneously broadened laser: a phase-locked superposition of many oscillating longitudinal cavity modes.

In practice, there are two methods of obtaining mode-locking: "active" mode-locking and "passive" mode-locking. Both methods were used in this work to mode-lock CW dye lasers, and are briefly described below. A detailed discussion of mode-locking can be found in references [3] and [4].

Active Mode-Locking

Active mode-locking refers to any process in which the cavity losses or gain are externally modulated at a frequency equal to the intermode frequency spacing of the cavity, $\omega = \pi\ell/c$. The loss modulation is frequently achieved with an electro-optic or acousto-optic modulator installed in the laser cavity and driven by an external RF source. This method was used here to actively mode-lock an argon gas laser, and will be described further in Section 2.4.

The simplest way to modulate the gain at the required frequency is to pump the laser with a train of pulses with interpulse repetition frequency exactly equal to (or a submultiple of) the intermode frequency spacing, $\omega = \pi\ell/c$. In practice this means that the cavity length of the laser must be exactly equal to (or an exact submultiple of) the cavity length of the pump laser. This form of active mode-locking is now widely referred to as synchronous mode-locking, and was one method used to mode-lock CW dye lasers in this work.

Passive Mode-Locking

In passive mode-locking the required loss modulation (not the gain in this case) is achieved internally; that is, by a passive element in the laser cavity (not driven externally). In practice a solution of a saturable absorber is used; this solution exhibits a transmission which increases at high light intensities. The absorber thus encourages the oscillation of a single intense light pulse, which will have lower transmission losses than oscillation in which the cavity energy is spread more evenly. This method was used to mode-lock solid state lasers [1] and is

one method of mode-locking CW dye lasers.

2.3 Passively Mode-Locked CW Dye Laser

The first approach to mode-locking of a CW dye laser was passive mode-locking with a saturable absorber. The laser built at Caltech was based on the design developed by Ippen and Shank [5], and is shown in Figure 2.1. The rhodamine 6G gain medium was dissolved in ethylene glycol (2×10^{-3}M) and was flowed through a narrow nozzle to produce a high optical quality jet stream located at a beam waist between mirrors M1 and M2. The horizontally polarized 5145Å output of a CW argon ion laser (Spectra Physics model 170) was focussed into the jet by mirror M1. Typical pump power was 5 to 6 watts. Mirrors in the conventional folded geometry were used for all focussing in the laser cavity. The astigmatic distortions of the laser beam so produced were compensated by an appropriate choice of the folding angle [6]. All mirrors had broadband, high reflectivity dielectric coatings (Laser Energy Corp.) and were mounted in high precision angular orientation positioners (Lansing). The vertical jet streams were carefully positioned, using X-Y-Z micropositioners (Line Tool Co.) The saturable absorber, a mixture of the dyes DODCI and malachite green in ethylene glycol, flowed in a jet stream located at a beam waist near one end of the cavity between M6 and M7. The concentrations of each dye (about 2×10^{-4}M each) were adjusted such that their absorbances at 615 nm were about equal. The function of the malachite green was to stabilize mode-locking when the laser was operated well above threshold [5]. A Brewster angle prism located between M2 and M5 was used as a wavelength tuning and bandwidth limiting element.

Figure 2.1

Diagram of the passively mode-locked CW dye laser used in this work.

M1, M2, M4	R = 10 cm	spherical mirrors
M6, M7	R = 5 cm	spherical mirrors
M3	R = 20 cm	spherical mirror
M5		plane mirror
RF	Driver for the cavity dumper	
Pulser	Variable frequency pulse generator	

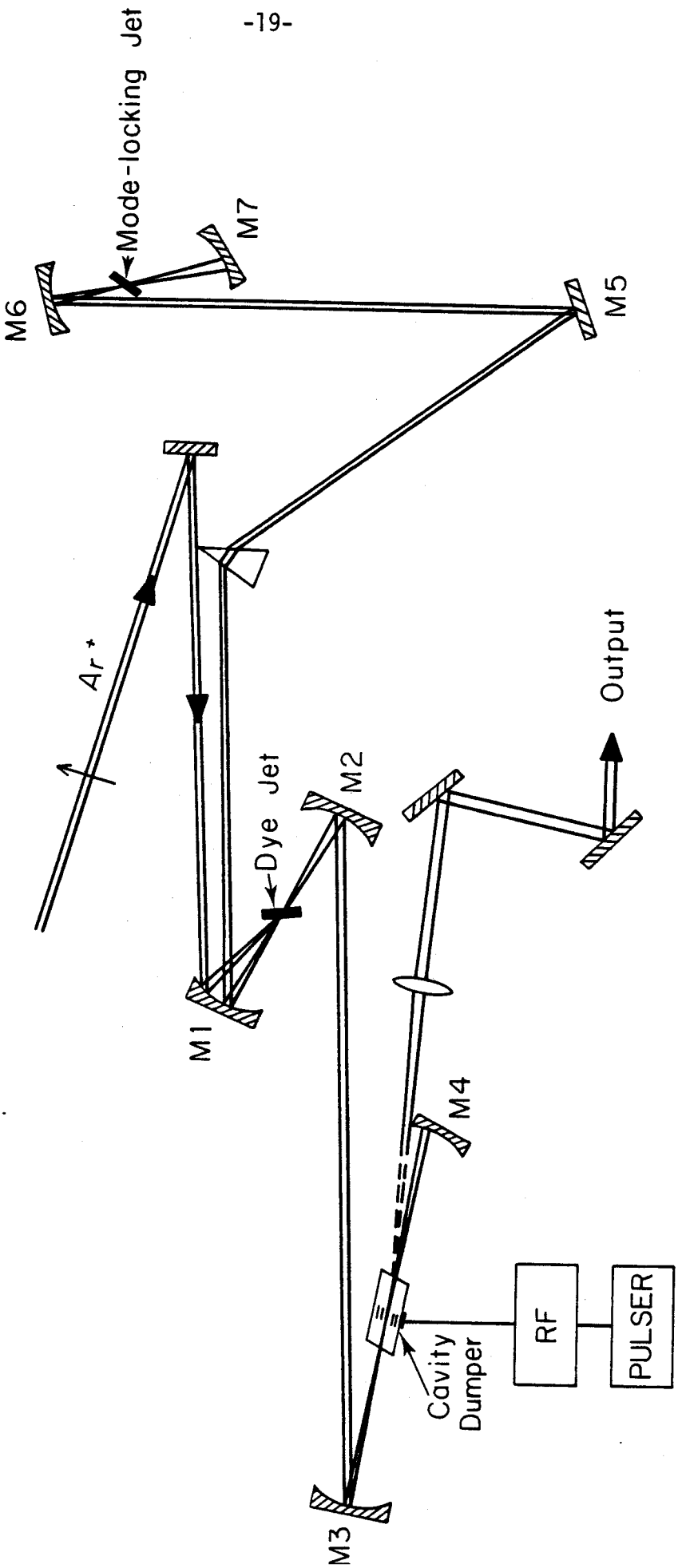
Mode-locking Jet
M7
M6
M5
Ar+
Output
Dye Jet
M2
M1
M4
M3
Cavity Dumper
RF
PULSER

An acousto-optic beam deflector [7] (Spectra Physics model 365 cavity dumper) was located at a beam waist between M3 and M4. The purpose of this device was two-fold: (1) to increase the energy of the output pulses, since diffraction efficiency approaching 50% could be obtained; and (2) to allow a variable repetition rate output, from single shot to about 1.0 MHz. The second consideration is important in relation to excitation of molecular systems with slow recovery times, where too high a repetition rate could cause cumulative, distorting effects. The cavity dumper was a fused quartz cube with a bonded ZnO transducer oriented at Brewster's angle. When RF at 470 MHz was applied to the transducer from the RF driver (Spectra Physics model 465), a travelling acoustic wave was launched into the quartz which diffracted a portion of the incident laser beam via the acousto-optic effect. The RF was gated by a 10 nsec pulse from a pulse generator connected to the RF driver. The rise time of the dumper was determined by the transit time of the acoustic wave across the beam waist. Thus strong focussing was required to ensure that a single pulse was diffracted from the cavity. The cavity dumper had to be carefully positioned between M3 and M4 to achieve the best results. In practice, a small fraction of the pulses immediately adjacent to the main diffracted pulse were also present in the output.

It is worth mentioning that a few different designs for passively mode-locked CW dye lasers have appeared in the literature in recent years. Diels et al. [8] used a composite gain medium and saturable absorber by dissolving all the dyes in one solution. O'Neill [9] has used an optically contacted thin cell of saturable absorber, rather than a jet stream. Yasa

et al. [10] have reported a novel dual-wavelength, passively mode-locked CW laser in which the saturable absorber is also a laser dye. The most significant advance in passive mode-locking of CW dye lasers was recently reported by Fork et al. [11], who have mode-locked a travelling wave ring dye laser and generated sub-picosecond pulses.

2.4 Synchronously Mode-Locked CW Dye Laser

The synchronously mode-locked dye laser (Spectra Physics model 375) is shown in Figure 2.2, and consists of a conventional 3-mirror astigmatically compensated folded cavity. The gain medium was again a solution of rhodamine 6G in ethylene glycol flowing in a horizontal jet stream oriented at Brewster's angle to the dye laser beam. A pump mirror focussed the vertically polarized output beam of an actively mode-locked argon ion laser into the jet stream. The 30% transmission output mirror was mounted on an ultra-precise translation stage (Aerotech ATS300) located at the appropriate distance from the fold mirror to achieve the correct cavity length for mode-locking. The translation stage provided very accurate adjustment of the cavity length to optimize the mode-locking. A coarse wedge etalon was used as a bandwidth limiting and wavelength tuning element. All components were mounted on a steel-top vibration isolation table to ensure mechanical stability of the laser cavity, which was important in view of the length stability requirements for good mode-locking.

Actively Mode-Locked Argon Ion Laser

The CW argon ion laser (Spectra Physics model 171) was actively mode-locked by an acousto-optic loss modulator (Spectra Physics model 342)

Figure 2.2

Diagram of the synchronously mode-locked dye laser cavity used in this work. The output mirror had 30% transmission.

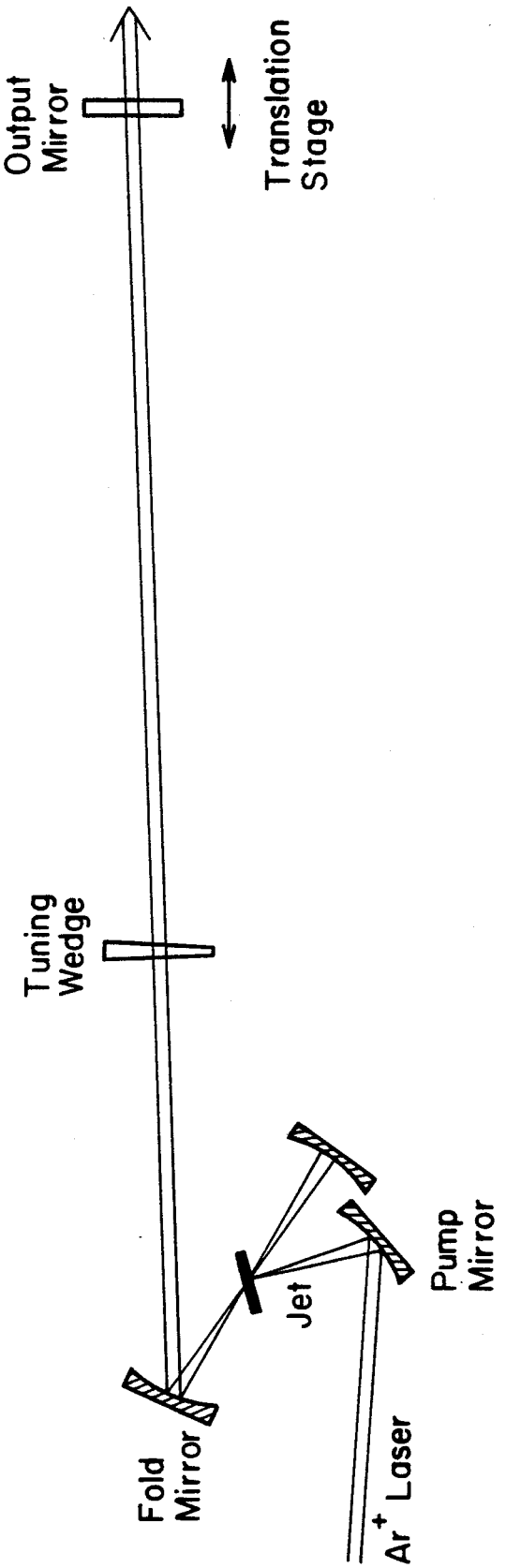
Output Mirror
Translation Stage
Tuning Wedge
Jet
Pump Mirror
Fold Mirror
Ar+ Laser

driven by an ultra-stable RF source (Spectra Physics model 452). Loss modulation occurred by Bragg diffraction from a standing wave acoustic field in a quartz prism. Stable RF was applied to the prism at a frequency very close to, but slightly lower than an acoustic resonance of the prism. Since the resonance frequencies were temperature dependent, the prism temperature was well regulated. Loss modulation occurred at twice the RF frequency, since loss occurred on both halves of the acoustic cycle. The RF frequency used was 41.0945 MHz, giving a mode-locked pulse train with repetition frequency of 82.189 MHz, corresponding to an interpulse separation of about 12·16 nsec. The cavity length of the argon laser was carefully adjusted to match this repetition frequency by monitoring the duration of the mode-locked pulses with a high speed detector (Spectra Physics model 403B) and sampling oscilloscope combination (Tektronix S6 sampling head, 7S11 sampling plug-in, 7T11 sampling sweep unit, and 7904 mainframe). This detection system had an impulse response width of 75 psec (FWHM). The apparent FWHM of the mode-locked pulses at the optimum cavity length setting was 120 psec. After deconvolution of the instrument response, the true duration of the mode-locked argon laser pulses was 95 psec. The average power was about 1.1 W, corresponding to a pulse energy of 13.5 nJ and a peak pulse power of 140 watts. Single line operation at 5145Å was used.

Reliable mode-locking of the argon ion laser requires very high frequency stability of the RF applied to the loss modulator. Frequency variations will shift the modulation away from the intermode frequency of the cavity required for perfect mode-locking. Yariv [2,12] has shown that in this case the repetition frequency of the mode-locked pulses is always

equal to the modulation frequency, rather than equal to the cavity intermode frequency spacing. That is, the frequency variations in the RF will be transferred to the mode-locked pulse train. The same situation also applies to synchronous mode-locking of the dye laser. Thus noise in the RF applied to the loss modulator will ultimately be transferred to the dye laser pulse train. It is for this reason that particular attention must be paid to the frequency stability of the RF source. The driver unit used here consisted of a phase-locked, crystal-controlled frequency synthesizer and RF power amplifier. The bandwidth of the RF applied to the modulator was about 100 Hz, corresponding to a stability of 2.5 parts per million. This stability sets the precision to which the dye laser cavity length must be adjusted.

2.5 Pulse Autocorrelation Measurements

A reliable and routine method for measuring the duration of the ultrashort pulses produced by mode-locked lasers is essential. Not only is this a useful diagnostic of laser performance and hence an aid to laser alignment, but it is often essential in interpreting data obtained in time-resolved experiments. Since mode-locked CW dye laser pulses are only a few picoseconds, or in some cases subpicoseconds, in duration, it is a challenging problem in measurement. Conventional detectors and electronics are too slow for this application. Even the commercially available streak cameras do not have the required subpicosecond time resolution for this application. Thus a nonlinear optical technique has evolved, wherein the mode-locked pulse itself is used in the measurement. The laser pulse train is divided in a Michelson interferometer and the

output sent to a frequency doubling crystal. The resulting signal, which is a function of the path delay introduced by the interferometer, is proportional to the autocorrelation function of the pulse intensity. This simple technique, first developed in 1966 [13] is now widely used for measuring the duration of mode-locked dye laser pulses.

Experimental Set-Up

The experimental arrangement is shown in Figure 2.3. The dye laser pulse train was divided at beam splitter into a strong beam (95%) and a weaker replica beam (5%). The two beams travelled different paths in the interferometer and emerged parallel but non-colinear at the lens, where they were focussed to a common spot in the 0.5 mm thick KDP crystal. The path difference between the two beams could be varied by means of the stepper motor driven translation stage. The crystal was oriented such that the phase-matched second harmonic generated by the interaction between the two beams propagated along their bisector, as shown in Figure 3.3. This arrangement is referred to as background free second harmonic autocorrelation, since the second harmonic generated by each beam alone is spatially separated, and was blocked by the aperture. The required second harmonic beam passed through bandpass filters (Corning 7-54) to a photomultiplier (EMI 6256S), whose signal was processed in a lock-in amplifier. A mechanical chopper in the path of the pump beam caused a modulation of the second harmonic intensity, which was phase sensitively detected in the lock-in using an electrical signal derived from the chopper as the reference signal. The lock-in output was digitized by a voltage to frequency converter and input to a multi-channel analyzer operating in multichannel scaling mode (Tracor Northern TN1706). The MCA was triggered by

Figure 2.3

Experimental setup for background-free second harmonic autocorrelation measurements.

SMC: stepping motor controller

MCA: multichannel analyzer

VFC: voltage to frequency convertor

PM: photomultiplier

F: Corning 7-54 bandpass filters

BS: 95/5 beam splitter

A time delay τ between the pulses in each beam is indicated in the figure.

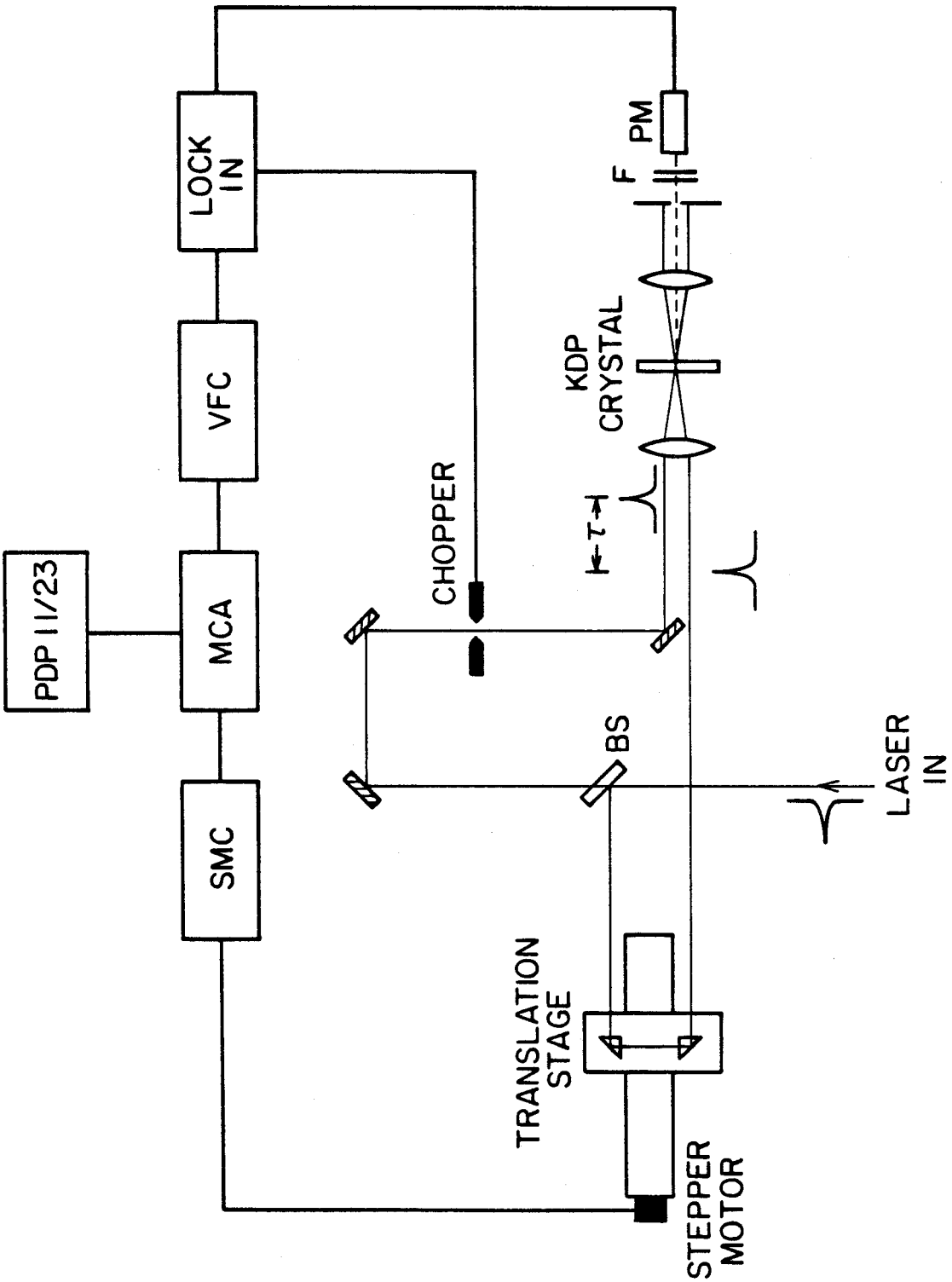
LOCK IN
VFC
MCA
PDP 11/23
SMC
CHOPPER
KDP CRYSTAL
F
PM
τ
BS
LASER IN
TRANSLATION STAGE
STEPPER MOTOR

the stepper motor controller so that data were accumulated in the memory as the time delay between the pulses was slowly varied. The controller provided variable scan speed, dwell time, scan range, and automatically repeated scans to allow for signal averaging by overlaying successive scans in the MCA memory. The contents of the MCA memory could be transferred to a PDP 11/23 mini-computer for disk storage, analysis, and plotting.

2.6 Interpretation of Autocorrelation Data

The signal measured in background free second harmonic generation for a time delay τ between the pulses is proportional to the autocorrelation function of the pulse intensity I(t), given in normalized form by

$$G(\tau) = \frac{\langle I(t+\tau)\ I(t)\rangle}{\langle I^2(t)\rangle} \qquad (2.1)$$

where the brackets denote an average over a sufficiently long period of time. $G(\tau)$ has a maximum value of 1 at zero delay, and decays to zero at longer delay if the intensity I(t) is a single isolated pulse. $G(\tau)$ is always symmetric about $\tau = 0$ and so contains no information on possible asymmetry in the pulse I(t). The relationship between I(t) and $G(\tau)$ depends on the functional form of I(t). In Table 2.1 are given some representative examples for I(t) and their corresponding autocorrelation functions $G(\tau)$. For example, a Gaussian pulse intensity also has a Gaussian autocorrelation function, with a FWHM which is larger than the intensity FWHM by a factor of $\sqrt{2}$. In general, smooth pulse profiles yield smooth autocorrelation functions, with their widths related by a numerical constant between 1 and 2. A simple procedure for estimating the pulse

TABLE 2.1

Autocorrelation Functions of Common Pulse Shapes

	I(t)	G(τ)	Δτ/Δt
Gaussian	$\exp\{-\frac{4\ln 2}{\Delta t^2}\cdot t^2\}$	$\exp\{-\frac{4\ln 2}{\Delta\tau^2}\cdot t^2\}$	$\sqrt{2}$
Squared Hyperbolic Secant	$\operatorname{sech}^2\{\frac{1.76t}{\Delta t}\}$	$3\{(\frac{2.72\tau}{\Delta\tau})\cdot\coth(\frac{2.72\tau}{\Delta\tau}) - 1\} / \sinh^2(\frac{2.72\tau}{\Delta\tau})$	1.55
Lorentzian	$1/\{1 + 4t^2/\Delta t^2\}$	$1/\{1 + 4\tau^2/\Delta\tau^2\}$	2
Single Sided Exponential	$\begin{cases}\exp\{-\frac{\ln 2}{\Delta t}\cdot t\}, & t\geq 0\\ 0, & t<0\end{cases}$	$\exp\{-\frac{2\ln 2}{\Delta\tau}\lvert\tau\rvert\}$	2

Δt is the FWHM of I(t) (Pulse duration).

$\Delta\tau$ is the FWHM of G(τ).

duration is thus to divide the width of the observed autocorrelation trace by the appropriate numerical form factor, such as those listed in the fourth column of Table 2.1. Unfortunately, this requires an assumption concerning the pulse shape which cannot be independently verified. Thus in practice this method gives only an estimate of the pulse duration with about 50% uncertainty. Even so, this method has been used almost universally for dye laser pulse-width determinations. A better approach is to analyze the entire autocorrelation trace by nonlinear least-squares fitting of the functional forms shown in the third column of Table 2.1 with $\Delta\tau$ as a variable parameter. Several different functional forms could be fit and the best representation of the pulse shape be determined by comparison of the goodness-of-fit parameter, such as the reduced chi-squared value, for each fit. This procedure is thus expected to yield some information on the pulse shape and a much more precise estimate of the pulse duration (since the uncertainty concerning the best pulse-shape has been removed). This was the approach used in this work, and its application to mode-locked dye laser pulses will be described in the following sections of this chapter.

An important consideration, which is often overlooked in autocorrelation analysis, is the effect of pulse sub-structure on the autocorrelation functions. This is important because in practice most lasers are not perfectly mode-locked but experience some fluctuations of the cavity mode phases which result in sub-structure in the pulse intensity envelope. This situation has been treated theoretically by Pike and Hercher [14] who considered the limiting case of a short burst of thermal radiation. They described the pulse intensity function as the product of

an envelope function and a Gaussian-distributed random variable describing the thermal noise. The pulse autocorrelation function was found to be

$$G(\tau) = G_p(\tau)\,[1 + G_N(\tau)] \tag{2.2}$$

where $G_p(\tau)$ is the autocorrelation function of the pulse envelope and $G_N(\tau)$ that of the Gaussian noise sub-structure. If the width $\Delta\tau_N$ of $G_N(\tau)$ is much smaller than the width $\Delta\tau_p$ of $G_p(\tau)$, then the autocorrelation described by Eq. (2.2) has the form of a narrow "coherence spike" superimposed on a broad base, with equal relative amplitudes at $\tau = 0$. An example of such an autocorrelation trace is shown in Figure 2.7c, and was obtained from the synchronously mode-locked dye laser when the cavity was too long for optimum mode-locking. Physically, the broad base results from overlap of the pulse envelope, while the "coherence spike" results from overlap of the substructure. The width of the broad base $\Delta\tau_p$ (the full width at the quarter height of the total autocorrelation trace) is related to the pulse duration Δt_p by the form factors in Table 2.1. The width of the coherence spike $\Delta\tau_N$ is related to the correlation time of the thermal radiation field. Since a Gaussian noise distribution was considered, the coherence spike also has a Gaussian shape with a FWHM $\Delta\tau_N$ equal to $\sqrt{2}\,\Delta t_c$, where Δt_c is the correlation time of the Gaussian noise distribution. This quantity is often referred to as the coherence time of the radiation field (hence the subscript "c"). Numerical simulations of autocorrelation traces were calculated using Eq. (2.2). A Gaussian pulse envelope with $\Delta t_p = 5$ psec was assumed in the calculation, and the coherence time Δt_c was varied from 0.5 psec, to 2.5 psec to 15 psec. The results are shown in Figure 2.4.

Figure 2.4

Autocorrelation functions calculated using Eq. (2.2). A Gaussian pulse envelope, with $\Delta t_p = 5.0$ psec, was assumed in all calculations. A Gaussian substructure noise distribution was also assumed with three choices for the coherence time:

(a) $\Delta t_c = 0.5$ psec "Incoherent" limit

(b) $\Delta t_c = 2.5$ psec Intermediate regime

(c) $\Delta t_c = 15.0$ psec "Coherent" limit

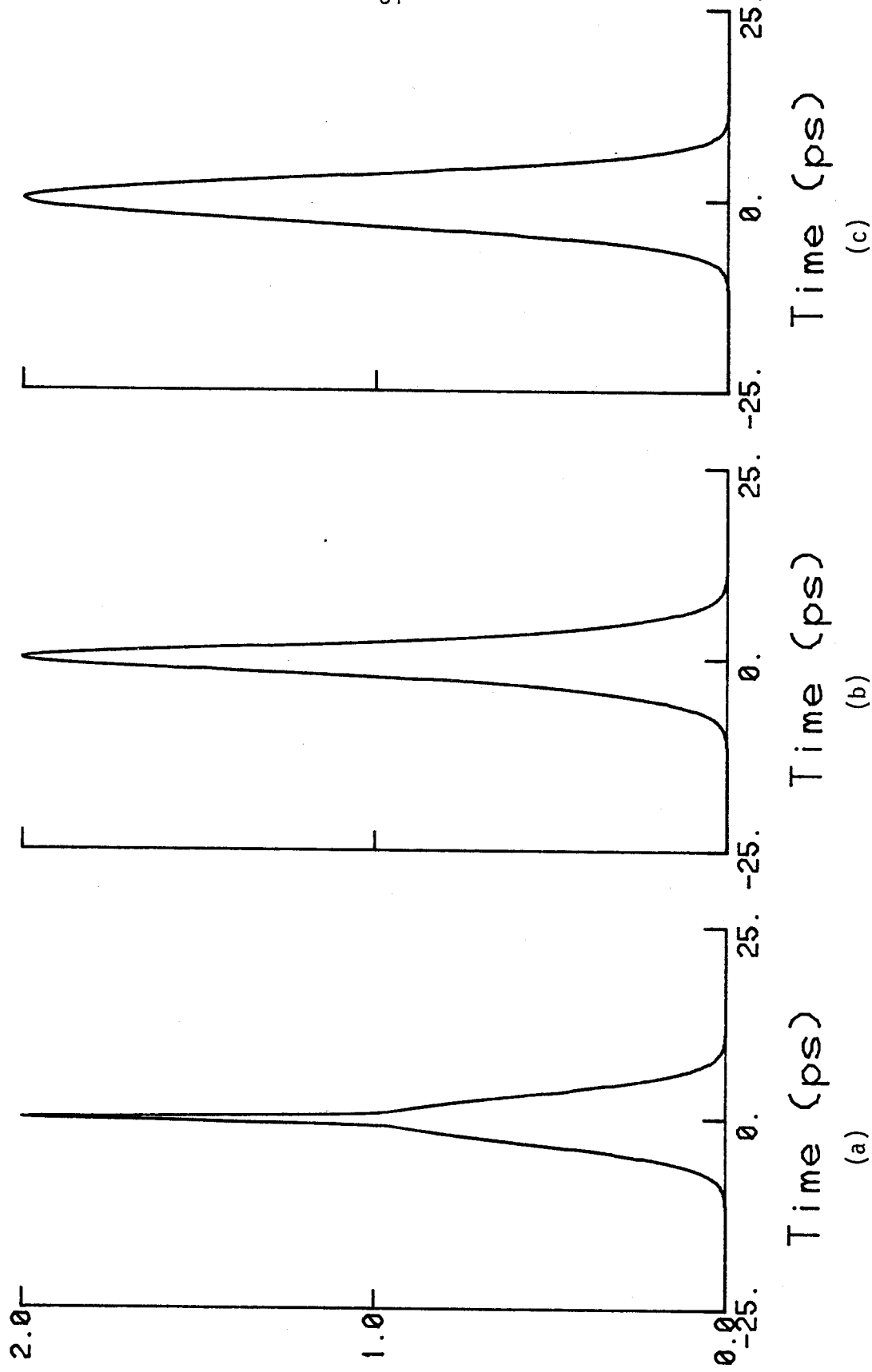
I(2ω)
2.0
1.0
0.0
-25.
0.
25.
Time (ps)
(a)
-25.
0.
25.
Time (ps)
(b)
-25.
0.
25.
Time (ps)
(c)

The numerical simulations show that if the coherence time of the laser radiation is much shorter than the pulse duration, $\Delta t_c << \Delta t_p$, a characteristic and readily identifiable autocorrelation trace is produced, shown in Figure 2.4a. This case will be referred to as the "incoherent" or highly structured limit. The coherence spike is obvious in this case. However, if $\Delta t_c \simeq \Delta t_p$, the difference between the base and the coherence spike is difficult to discern and the autocorrelation trace appears to be quite smooth, as in Figure 2.4b. The apparent FWHM of the autocorrelation trace in this case is considerably less than the true envelope autocorrelation width, which is Figure 2.4c. Obviously, special attention is required to interpret autocorrelation traces in this intermediate regime, as recently demonstrated by McDonald et al. [15]. In the limit $\Delta t_c >> \Delta t_p$, the autocorrelation of the pulse envelope $G_p(\tau)$ only is observed, as shown in Figure 2.4c. This will be referred to as the "coherent" or unstructured limit. Only in this limit is the FWHM of the autocorrelation trace related to the pulse duration via the form factors listed in Table 2.1.

A single equation can be written to represent both limits and the intermediate regime discussed above,

$$G(\tau) = AG_p(\tau)\,[1 + RG_N(\tau)] + B \qquad (2.3)$$

where A, B, and R are variable parameters. For example, the incoherent limit $\Delta t_c << \Delta t_p$ corresponds to $A = 1$, $R = 1$. The coherent limit $\Delta t_c >> \Delta t_p$ can be represented by $A = 2$, $R = 0$. In practice, A is an empirical amplitude parameter and B an empirical background parameter (very close to zero).

All the autocorrelation traces obtained in this work were analyzed using Eq. (2.3). The approach was to fit the observed traces with this

equation by nonlinear least squares using A, B, R, Δt_p, and Δt_c as parameters. The curve fitting methods are described in Appendix II. This was done for each envelope shape given in Table 2.1 (i.e., four choices for $G_p(\tau)$). The noise autocorrelation function was taken to be a Gaussian in all cases, which has been shown to be reasonable [15]. The reduced chi-squared values for each type of fit were compared and used to determine the best representation of the pulse shape. In some cases unphysical results were generated for particular functions chosen for $G_p(\tau)$; for example, the fitted parameters might be $\Delta t_c >> \Delta t_p$, but $R < 1$, which is unphysical; or solutions where $R > 1$, which is also unphysical. These solutions were rejected regardless of the goodness of fit. Thus, by a combination of statistical analysis and physical intuition, an autocorrelation function could be interpreted in detail and the pulse described as "incoherent" (highly structured), "coherent" (no sub-structure), or in the intermediate regime. Both the pulse duration Δt_p and the laser coherence time Δt_c were well determined by this method. As will be shown in Chapter 3, both these time constants are important in deconvoluting the instrumental response in pump-probe experiments. Also important is that this method provides information on the mode-locking of the laser, which can provide insight into the pulse formation mechanisms in these lasers. Certainly this degree of information cannot be obtained from measurements of the FWHM of the autocorrelation trace only.

2.7 Characteristics of Mode-Locked CW Dye Laser Pulses

a. Passive Mode-Locking

Autocorrelation traces of pulses from the passively mode-locked CW dye laser are presented in Figures 2.5 and 2.6. These data, obtained under

Figure 2.5

(a) Autocorrelation trace of the optimal output from the passively mode-locked CW dye laser. The points are experimental data and the solid line is the best-fit to Eq. (2.3) with $\Delta t_p = 2.38$ psec, $\Delta t_c = 0.77$ psec, and $R = 0.94$. The fit is excellent.

(b) The laser pulse envelope function, corresponding to the best-fit in part (a). The envelope shape is a squared hyperbolic secant, $I(t) = \text{sech}^2\ (1.76t/\Delta t_p)$. The substructure is not shown in the figure.

(a)

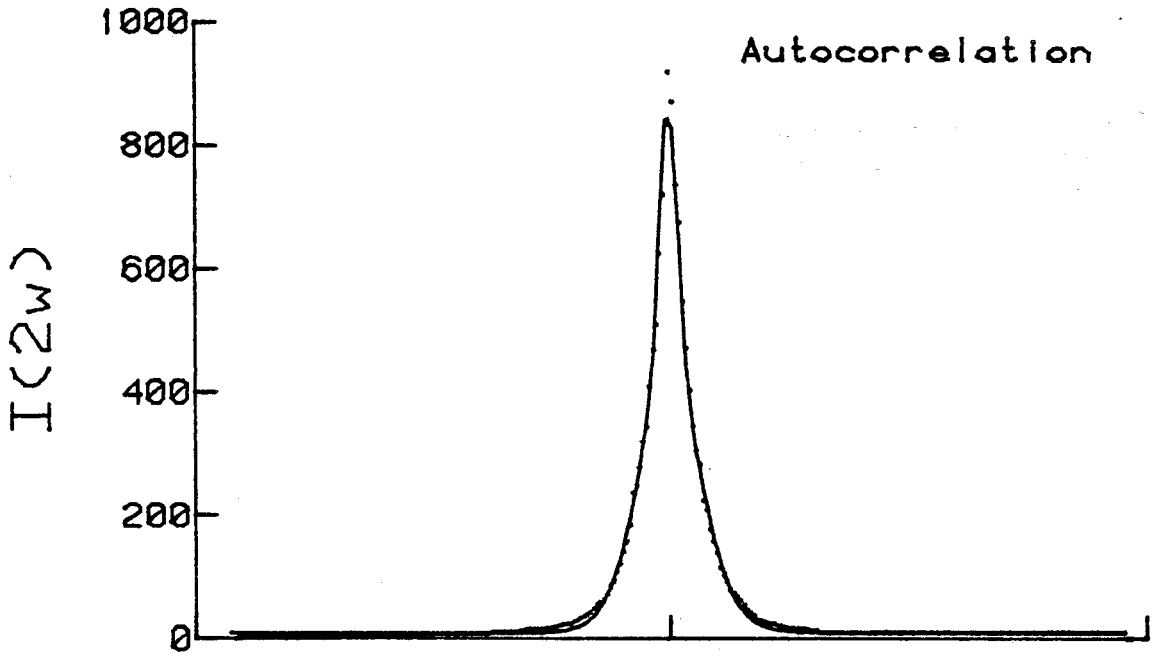
1000
800
600
400
200
0
I(2w)
Autocorrelation

(b)

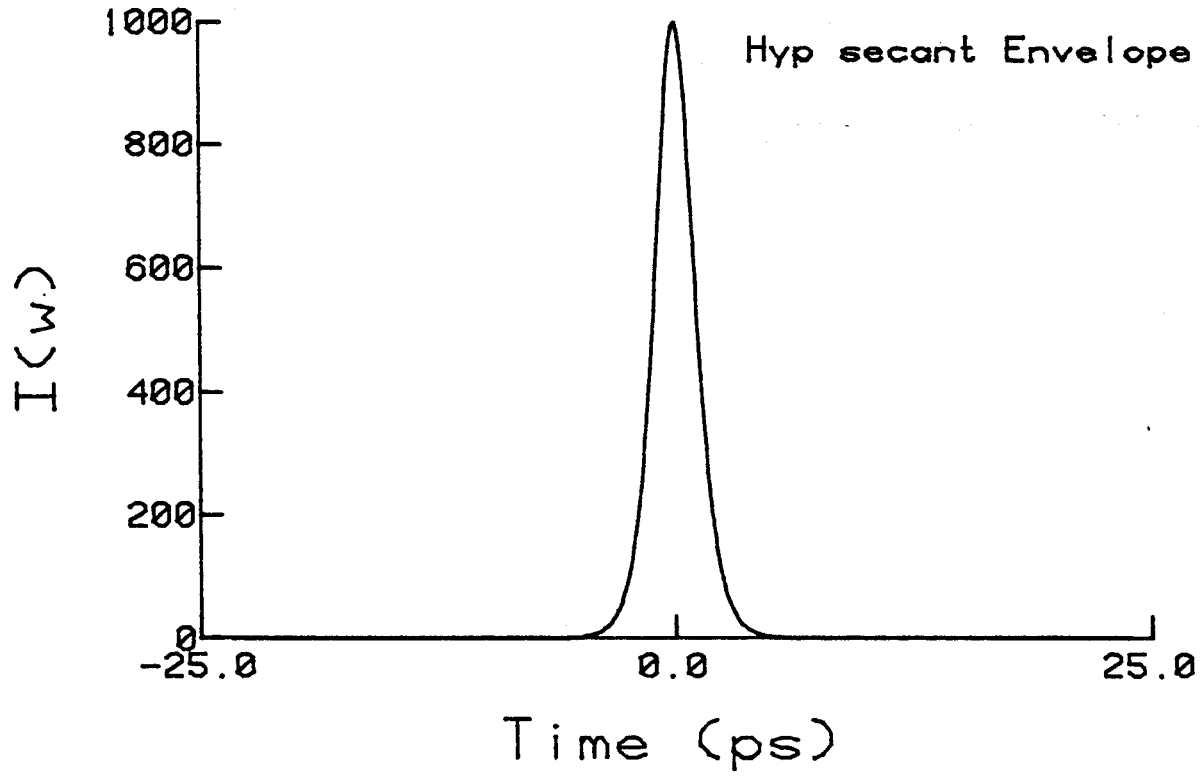
1000
800
600
400
200
0
I(w)
Hyp secant Envelope
-25.0
0.0
25.0
Time (ps)

Figure 2.6

(a) Autocorrelation trace of another common output from the passively mode-locked dye laser under different operating conditions. The points are experimental data and the solid line is the best-fit to Eq. (2.3), with $\Delta t_p = 3.19$ psec, $\Delta t_c = 1.45$ psec, and $R = 0.69$. The fit is excellent.

(b) The laser pulse envelope function corresponding to the best-fit in part (a). The envelope shape is a single-side exponential,

$$I(t) = \begin{cases} 0 & , \quad t < 0 \\ \exp(-\ell n\, 2t / \Delta t_p) & , \quad t \geq 0 \end{cases}$$

The substructure is not shown.

(a)

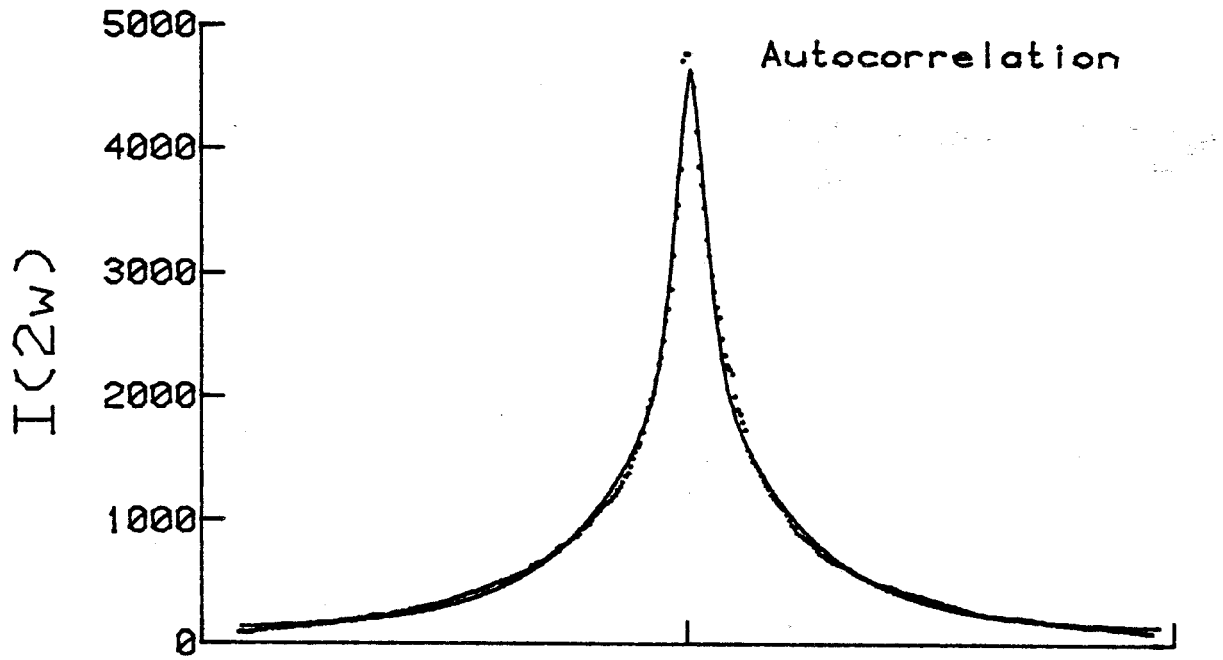
5000
4000
3000
2000
1000
0
I(2w)
Autocorrelation

(b)

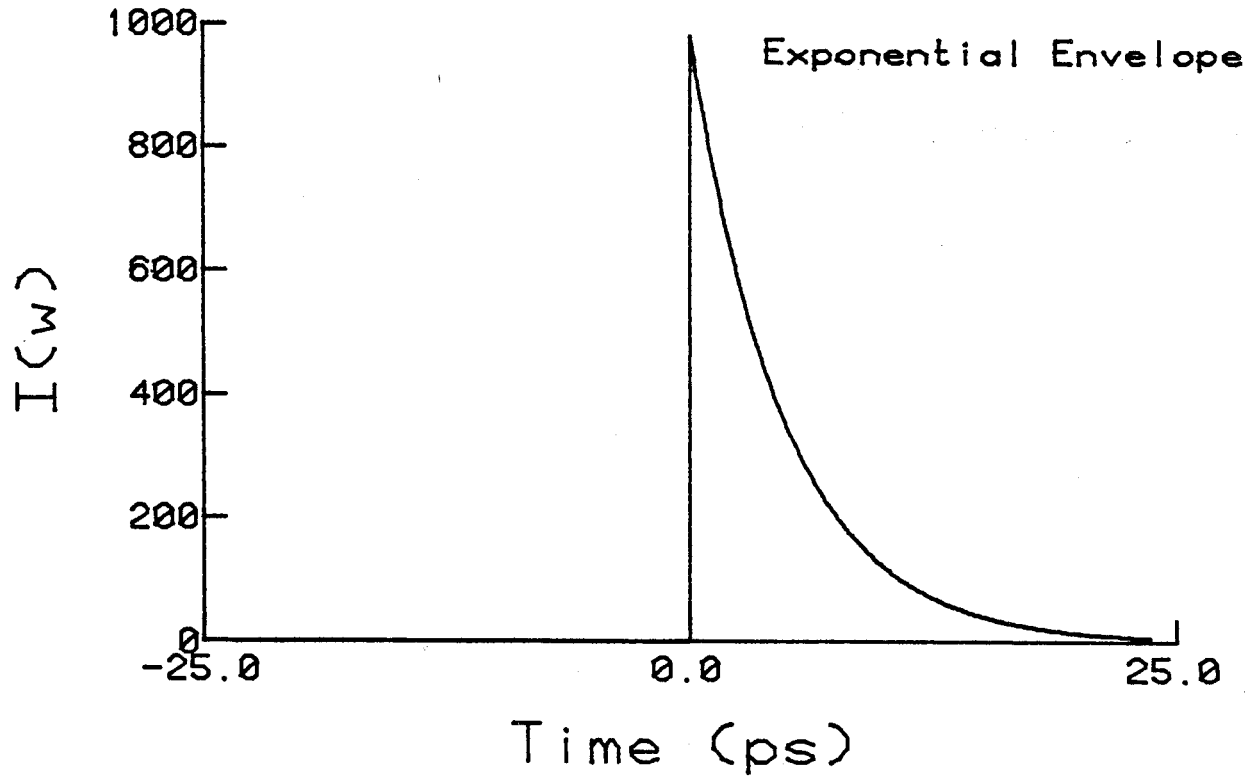
1000
800
600
400
200
0
I(w)
Exponential Envelope
-25.0
0.0
25.0
Time (ps)

different laser operating conditions, show that there is some variability in the pulse generated by this laser. The optimal output, shown in Figure 2.5, was characterized by a narrow autocorrelation trace with very steep wings. Another common output, obtained under different focussing conditions in the absorber jet and different pump power, is shown in Figure 2.6, and was characterized by a broader autocorrelation with exponentially decaying wings. Obviously the pulse energy was less concentrated in this type of output. Both autocorrelation traces are quite smooth with no obvious evidence of a coherence spike. The choice between the "coherent" limit and intermediate regime behavior discussed in the previous section must be carefully considered in relation to these autocorrelation functions.

The results of analyzing these autocorrelation traces (and many others of each type) according to Eq. (2.3) are summarized in Table 2.2. In the case of the optimal pulses, shown in Figure 2.5 and entered in the first row of the table, the autocorrelation traces were consistently better fit with a squared hyperbolic secant pulse envelope (the second entry in Table 2.1). The best-fit curve is also shown in Figure 2.5 (solid line) and can be seen to provide an excellent fit to the data. A Gaussian pulse envelope gave a somewhat worse, but still acceptable fit, with similar results to those in Table 2.2. Exponential and Lorentzian pulse envelopes gave significantly poorer fits and yielded unphysical estimates for the parameters Δt_c and R. As shown in Table 2.2, the best parameters characterizing this optimal pulse autocorrelation were $\Delta t_p = 2.4 \pm 0.3$ psec, $\Delta t_c = 0.8 \pm 0.1$ psec, and $R = 1.0 \pm 0.1$. These results strongly imply that the pulses do indeed have intermediate substructure, and that the application of the Pike-Hercher noise burst model [14] is very successful in this case.

TABLE 2.2

Autocorrelation Analysis of the

Passively Mode-Locked CW Dye Laser

	Envelope	Δt_p	Δt_c	R
1.	$Sech^2$	2.40 ± 0.3	0.80 ± 0.1	0.95 ± 0.10
2.	Single-side Exponential	2.7 ± 0.9	1.9 ± 0.5	0.70 ± 0.15

Analysis of the second type of output, shown in Figure 2.6, is presented in the second entry of Table 2.2. The best fit (solid line in Figure 2.6) was consistently obtained for a single-side exponential pulse envelope. The analysis also implied the existence of intermediate substructure, although the application of the Pike-Hercher model was not entirely satisfactory in this case, which was indicated by the R values that departed significantly from the theoretically expected value of unity. Other choices for the pulse envelope gave even less satisfactory results for the ratio R.

It is significant that Haus et al. [16] have also observed these two modes of operation in a passively mode-locked CW dye laser. Near laser threshold they observed smooth autocorrelation traces with exponential wings, while at high pump power they observed broader autocorrelation traces with a narrow coherence spike. The broad base of the autocorrelation was well fit by a sech^2 pulse envelope with $\Delta t_p = 17$ psec. These authors also noted that such an envelope shape can be predicted theoretically, with certain assumptions [16,31]. Their findings are consistent with the results of this work, except that the sech^2 pulses from our laser were much narrower.

The autocorrelation analysis presented above suggests the following description of the passively mode-locked dye laser. Under optimal conditions the laser produced symmetric sech^2-like pulses, which were characterized by a sharply rising pulse envelope with essentially no wings. This is shown in Figure 2.5b. The pulse duration was about 2.4 psec. However, the presence of substructure in the pulses ($R \simeq 1.0$) indicated that the laser was not perfectly mode-locked even under these conditions.

With changes in pump power or cavity focussing, the pulses became asymmetric with a long exponential tail, shown in Figure 2.6b. These pulses were also structured. The transition to this mode of operation was characterized by a "spilling over" of the pulse intensity into the tail of the pulse. This is readily appreciated by comparison of the pulse envelopes shown in Figure 2.5b and 2.6b. The symmetric $sech^2$ pulses were preferable for experimental purposes because the energy was concentrated in a narrower pulse.

The other laser characteristics are listed in Table 2.4, where they are compared with data for the synchronously mode-locked dye laser.

b. Synchronous Mode-Locking

The characteristics of this laser varied dramatically with cavity length over a narrow range of about 140 microns in either direction from the length of exact synchrony. The pulse shape, pulse duration, coherence time, pulse energy, and peak power all showed a different dependence on cavity length. These data are presented here and will be discussed in the following section of this chapter.

Figure 2.7 presents autocorrelation traces obtained at three cavity length settings; 4 micron short (part (a)), the optimum length (part (b)), and 16 micron long (part (c)). The optimum cavity length was defined as the setting producing the minimum pulse duration. It has recently been shown that this position also corresponds to the length required for exact synchrony [15,17]. A coherence spike and broad base is clearly evident in the data for the long cavity shown in Figure 2.7c. Even at the optimum cavity length there was evidence of a coherence spike,

Figure 2.7

Autocorrelation traces of the output of the synchronously mode-locked dye laser as a function of cavity length detuning:

(a) ΔL = -4 micron

(b) ΔL = 0 (exact synchrony)

(c) ΔL = +16 micron

The points are experimental data, and have all been normalized to the same maximum intensity (in practice, the peak intensity increases in going from (a) to (c)). The solid lines are the best-fit to Eq. (2.3), with:

(a) Lorentzian envelope: $\Delta t_p = 7.80$ psec, $\Delta t_c = 1.39$ psec, $R = 1.25$

(b) Lorentzian envelope: $\Delta t_p = 3.13$ psec, $\Delta t_c = 0.88$ psec, $R = 1.10$

(c) Gaussian envelope: $\Delta t_p = 9.07$ psec, $\Delta t_c = 0.54$ psec, $R = 1.02$.

The fits are excellent in all three cases, and are better than the best-fits using other pulse envelope functions.

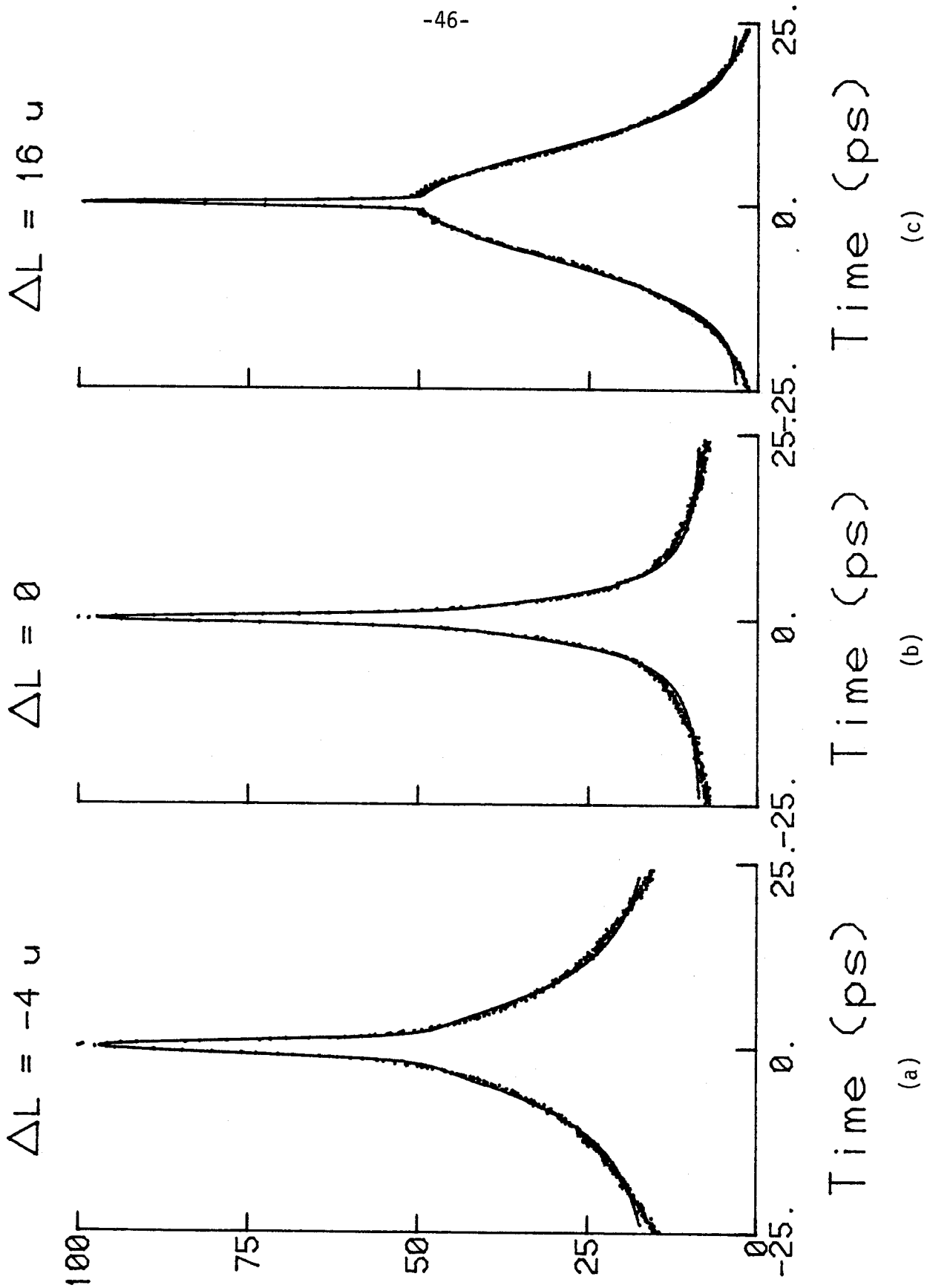
ΔL = -4 u
ΔL = 0
ΔL = 16 u
I(2w)
100
75
50
25
0
-25.
0.
25.
Time (ps)
(a)
(b)
(c)

although the base was much narrower. For the shortened cavity the autocorrelation shows a base and coherence spike superimposed on large background intensity. Longer time-delay scans often revealed subsidiary peaks displaced on either side of the central peak in the autocorrelation, indicating the presence of satellite pulses in the laser pulse train under these conditions.

The autocorrelation traces recorded at many different cavity length settings were analyzed using Eq. (2.3). The results are summarized in Table 2.3. For cavities set 15 micron or more longer than the optimum length, the autocorrelation traces were very well fit with a Gaussian pulse envelope function. The good fit is evident in Figure 2.7c (solid line). The results in this case can be summarized as $\Delta t_p >> \Delta t_c$ and $R = 1.0 \pm 0.05$. Thus the "incoherent" limit of highly structured pulses was observed for these long cavity settings. Around the optimum cavity length the best fit was obtained for a Lorentzian pulse envelope. The excellent fits with this function at the optimum cavity length and for the shortened cavity are shown in Figures 2.7a and b. In these cases $R = 0.9 \pm 0.1$, indicating that substructure was present here also. The difference between Δt_p and Δt_c was considerably smaller here than for long cavities, and the pulses generated in these cases are better described as having intermediate substructure. These findings are important, because they imply that even at exact synchrony these lasers are not perfectly mode-locked. This conclusion has not been recognized in many of the literature reports on synchronously mode-locked dye lasers. Almost all the published autocorrelation traces [18,24] of the optimal pulses show evidence of a coherence spike. Simply estimating the pulse duration from

TABLE 2.3

Autocorrelation Analysis of the

Synchronously Mode-Locked CW Dye Laser

ΔL (micron)	Δt_p (psec)	Δt_c (psec)	R	Envelope[†]
+20	12.00	0.52	1.07	G
+16	9.07	0.54	1.02	G
+12	5.78	0.50	0.80	L
+8	3.88	0.52	0.80	L
+4	3.35	0.56	0.80	L
+2	3.25	0.60	0.80	L
0	3.13	0.88	1.10	L
-2	4.03	1.03	1.25	L
-4	7.80	1.39	1.25	L

[†]Abbreviations: G = Gaussian

L = Lorentzian

the FWHM of these traces is incorrect in this case and leads to serious underestimates of the duration. For example, the FWHM of the autocorrelation trace for $\Delta L = 0$ was 2.1 psec. Assuming a single-side exponential pulse shape, as all these authors have done, one would estimate a pulse duration of 1.05 psec. However, the correct analysis, including the coherence spike, as presented in Table 2.3, has shown that the pulse duration was actually 3.13 psec. The simple procedure thus underestimates the pulse duration by a factor of 3 in this case. In view of this, the reports of sub-picosecond operation [20-24] could not be verified by this work. The present analysis also found that a symmetric Lorentzian pulse shape always gave a better fit than a single-sided exponential. For long cavities a Gaussian shape was best.

The dependence of the pulse duration and coherence time on cavity length is shown in Figure 2.8. The dependence is qualitatively similar to that reported by several groups [15,25,26] and calculated by Kim et al. [27]. The dependence is asymmetric and quite steep; short pulses are generated only over a 25 micron range of cavity length detuning. Cavity length changes as small as 4 micron, or about 2 ppm, caused noticeable changes in the pulse duration. It is significant that this tolerance is equal to the frequency stability of the RF applied to mode-lock the argon ion laser. Such a narrow detuning range was partly the result of the broad spectral bandwidth of the tuning wedge. Since more cavity modes are mode-locked when the spectral bandwidth is broad, the effect of changing the mode frequencies by changing the cavity length is more severe.

The dependence of the pulse energy and the average second harmonic power on cavity length are presented in Figure 2.9. The second harmonic

Figure 2.8

Dependence of the pulse duration Δt_p and coherence time Δt_c on cavity length detuning. The data are the best-fit parameters obtained from the autocorrelation traces at each cavity setting. Note the different vertical scales used for each graph in the figure. The cavity length detuning range covered in this figure should be compared with that in Figure 2.9.

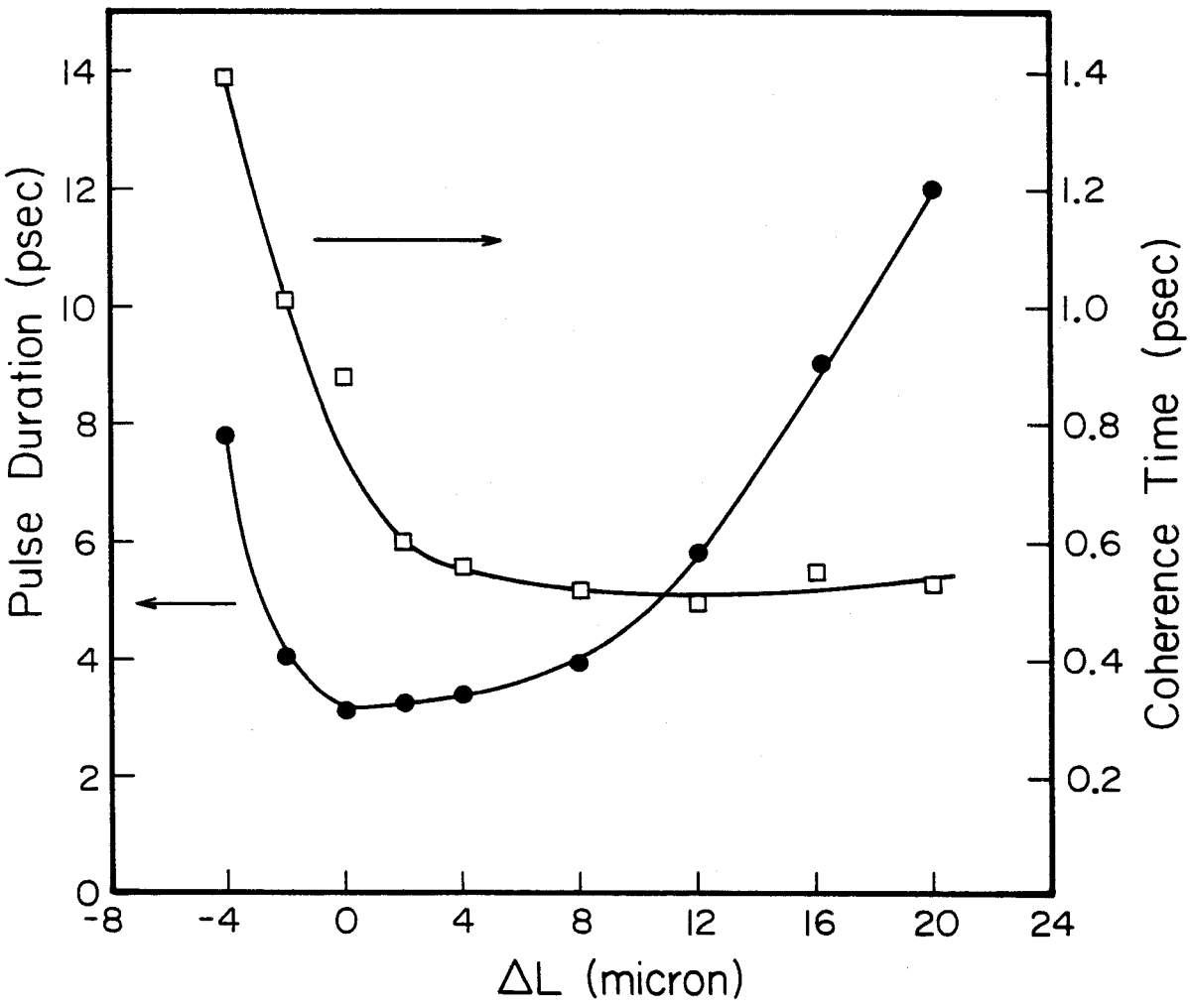
Pulse Duration (psec)
Coherence Time (psec)
ΔL (micron)
14
12
10
8
6
4
2
0
1.4
1.2
1.0
0.8
0.6
0.4
0.2
-8
-4
0
4
8
12
16
20
24

Figure 2.9

Dependence of the pulse energy and second harmonic power on cavity length. Note the much wider scale used here than in Figure 2.8.

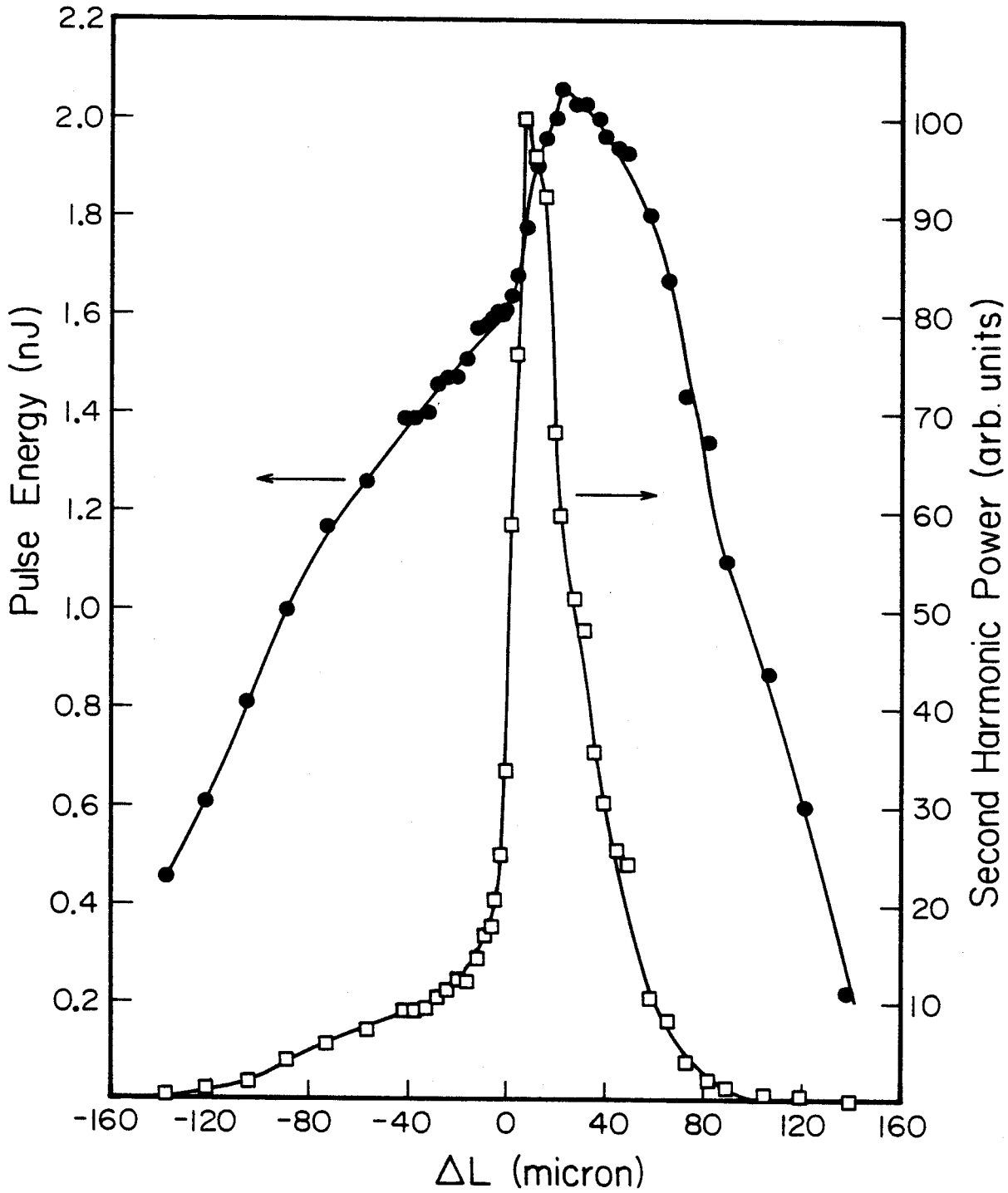
Pulse Energy (nJ)
Second Harmonic Power (arb. units)
ΔL (micron)
2.2
2.0
1.8
1.6
1.4
1.2
1.0
0.8
0.6
0.4
0.2
100
90
80
70
60
50
40
30
20
10
-160
-120
-80
-40
0
40
80
120
160

power is proportional to the square of the laser peak power and is also somewhat dependent on the pulse shape. The pulse energy was small when the cavity was too short, and increased monotonically as the cavity was lengthened. Just beyond the optimum length the energy increased more rapidly, reaching a maximum when the cavity was about 25 microns longer than optimum. The pulse energy decreased with further lenghtening of the cavity. The second harmonic power showed a similar, although much sharper dependence on cavity length. The second harmonic power was small for shortened cavities and increased very rapidly as the cavity was lengthened through the region where short pulses were produced. Surprisingly, the maximum second harmonic power was not produced at exact synchrony, but at a cavity setting 10 microns longer than the optimum length. This observation, together with the observation that the second harmonic increased much more rapidly than the pulse energy in the same region, suggests that the sudden increase in second harmonic power was due to a change in pulse shape. The autocorrelation analysis presented here has shown that a change from Lorentzian to Gaussian pulses does indeed occur in the region of maximum second harmonic power. It is quite reasonable that a Gaussian pulse, with more of its intensity in the center of the pulse, generates a higher second harmonic intensity than a Lorentzian pulse. From a practical point of view the cavity setting producing maximum second harmonic power is probably best for experimental applications, since the pulses have more energy, more peak power, less background intensity, and are only slightly broader than at exact synchrony. Recent real-time streak camera measurements [28] of the pulse train from a synchronously mode-locked dye laser

have shown that there is better discrimination against multiple pulse formation at this cavity setting than at exact synchrony. At even longer cavity settings the second harmonic power decreased due to broadening of the Gaussian pulses.

2.8 Pulse Generation in Mode-Locked CW Dye Lasers

It is an interesting question how short pulses are generated in these lasers. In passive mode-locking of solid state lasers the pulse duration is usually limited by the saturable absorber recovery time [4]. However, the DODCI absorber used in our dye laser had a 1.2 nsec recovery time, much too long to explain why 2·4 psec pulses were generated. In the synchronously mode-locked dye laser it is interesting that pulses as short as 3 psec were generated when pumping with 95 psec pulses from the argon laser. The pulse shortening mechanisms operative in each laser are briefly discussed here, and related to the experimental results presented in the previous section.

a. Passive Mode-Locking

As mentioned earlier in Section 2.1, an important difference between dye lasers and solid-state lasers is the very short (nsec) relaxation time of the gain medium in the former. As New [29] has pointed out, this means that gain saturation, or nonlinear amplification, plays a role in the dynamics of dye lasers. Gain saturation refers to the process in which an intense light pulse in an inverted gain medium reduces the inversion (or gain) by stimulated emission. The primary effect of gain saturation is to sharpen the trailing edge of a propagating pulse; i.e., the leading edge experiences more gain than the tail. The saturable absorber,

on the other hand, sharpens the leading edge of the pulse, since the leading edge experiences more absorption than the tail. By an appropriate balancing of these nonlinearities in the gain medium and the absorber, a propagating pulse can be rapidly shortened by repeated passage through these elements. This is the basic pulse shortening mechanism operative in the passively mode-locked CW dye laser. Model calculations based on these ideas have shown that stable single-pulse operation is possible with much shorter pulse duration than the absorber recovery time [29-32]. Haus [31] derived a closed form solution for the pulse shape under these conditions. With suitable approximations the pulse had a squared hyperbolic secant shape, of the form listed in Table 2.1. It is significant that this pulse shape was found to provide the best fit to the autocorrelation traces from the passively mode-locked dye laser.

b. Synchronous Mode-Locking

As mentioned above, gain saturation is very important in the dynamics of dye lasers. In Figure 2.10b is shown the hypothetical gain as a function of time. The dashed curve represents the low-level (or unsaturated) gain, and is simply the convolution of the slowly rising integral of the argon laser pump pulse and the exponential decay of the population inversion. However, when the gain first crosses threshold, the laser begins to oscillate and the gain is rapidly depleted by stimulated emission (i.e., gain saturation occurs). Thus the true gain follows the solid line in Figure 2.10b. This demonstrates how a narrow "gain shutter" can be produced by gain saturation effects. The resulting dye laser pulse is shown in the figure also; it is clear that pulses much shorter than the argon laser pulse can be generated in this way.

Figure 2.10

(a) Hypothetical laser gain as a function of time when the cavity is shorter than required for exact synchrony. The dashed line shows the small-signal or unsaturated gain. The solid line shows the actual, saturated gain. The relative timing of the argon pulse and dye pulse are also shown.

(b) Same as in (a) except that the cavity length is exactly matched.

(c) Same as in (a) except that the cavity is longer than required for exact synchrony.

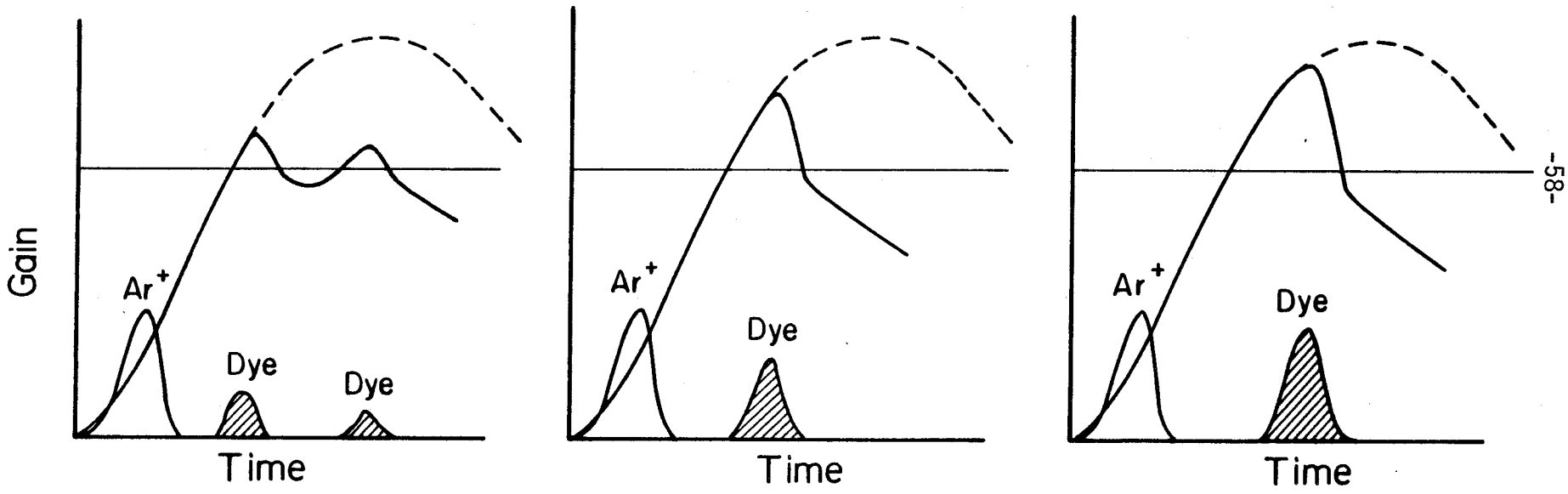
Gain
Ar+
Dye
Dye
Time
Cavity too short
(a)
Ar+
Dye
Time
Exact synchrony
(b)
Ar+
Dye
Time
Cavity too long
(c)

This simple description also explains the observed cavity length detuning characteristics presented in Section 2.6. Figure 2.10a shows the time-dependent gain and the resulting timing relationship between the argon pulse and dye pulse in the case when the cavity is shorter than the length for exact synchrony. Figure 2.10b shows the case of exact synchrony, and 2.10c the case of a cavity that is too long. These figures are for illustrative purposes, but are qualitatively identical to the experimental time-dependent gain measurements reported by Frigo et al. [33]. When the cavity is too short, the dye pulse arrives early on the rise of the gain, just after the gain crosses threshold. The gain is obviously small in this region and hence the pulses have low energy and peak power, as was observed. Because the small-signal gain (the dashed line) continues to rise in this region, it is possible for the gain to increase again after the pulse, crossing threshold a second time and thereby generating satellite pulses, as were sometimes observed. When the cavity length was exactly matched, the situation was as shown in Figure 2.10b. The gain is higher in this region, hence the pulses have more energy and peak power than for shortened cavities. With further lengthening of the cavity, the dye pulse arrives later in the gain curve where the gain has fully built up and has been above threshold for a longer time. This is the region of highest gain, and hence the pulses have maximum energy for lengthened rather than matched cavities. However, the pulses will be broader in this region, as was observed. Further lengthening of the cavity retards the dye pulse further and into the region where the gain is decaying by spontaneous emission. Hence the pulse energy decreases again.

2.9 Comparison of Passive and Synchronous Mode-Locking of CW Dye Lasers

The properties of the mode-locked pulses produced by each dye laser are summarized and compared in Table 2.4. There are obviously many similarities in the characteristics of these lasers; the pulse energies, pulse durations and peak power are very similar. The synchronously mode-locked laser has a much broader tuning range (500Å) than the mode-locked laser whose tunability was restricted by the saturable absorber, since good passive mode-locking only occurred over a narrow wavelength interval. The variable repetition output of the passively mode-locked laser was an advantage in experimental applications, and was more useful than the fixed 82 MHz repetition rate of the synchronously mode-locked dye laser. However, it would be possible to install a cavity dumper in the synchronously mode-locked system also, although broader pulses are known to be generated in this case [19]. The approach used here was to install the cavity dumper outside the laser cavity, causing no modification to the pulse properties. This approach will be described in Chapter 4.

An important conclusion of this study is that both dye lasers were only partially mode-locked and produced slightly structured pulses even under optimum conditions. This is not too surprising, since deviations from perfect mode-locking are well documented in the case of the solid-state lasers [4]. Partial mode-locking is the rule rather than the exception in real lasers. The coherence times of each laser were quite similar, $\simeq$ 0.8 psec, and in each case were about 3 to 4 times smaller than the pulse envelope width. It is worth emphasizing that this implies that the pulses were only slightly structured; that is, the deviation from perfect mode-locking was not too great. Nevertheless, the Pike-Hercher

TABLE 2.4

Comparison of Passive and Synchronous

Mode-Locking of CW Dye Lasers

	Passive	Synchronous
Average Power (mW)	0 - 2.0	180
Pulse Repetition Frequency (MHz)	0 - 1.0	82
Pulse Energy (nJ)	2.0	2.2
Photons/Pulse	6.2×10^9	6×10^9
Minimum Pulse Width (psec)	2.3	3.1
Peak Power (kW)	0.87	0.71
Tuning Range* (A)	20	500

*For R6G dye.

model worked well in this intermediate regime, as proven by the satisfying result that $R = 1.0 \pm 0.2$ in all cases. McDonald et al. [15] applied the Pike-Hercher model to analyze autocorrelation traces from synchronously mode-locked dye lasers. They found that the pulse envelope shape was neither exactly Lorentzian or Gaussian, but in between. This work found excellent agreement with a pure Lorentzian envelope. The analysis presented here leads to estimates of the pulse duration that are 2 to 3 times longer than reported in the literature. This discrepancy is due to the failure of previous investigators to include the possibility of pulse substructure.

The shape of the pulse envelope was found to be different for passive and synchronous mode-locking. The difference is illustrated in Figure 2.11, where the optimum pulse from each laser is compared. The substructure is not shown in the figure. Passive mode-locking obviously generates a better pulse shape than synchronous mode-locking; the envelope is narrower and has a smaller fraction of the pulse energy in the wings of the pulse. These pulses should be better suited for pump-probe experiments, hence the passively mode-locked dye laser was employed in all the pump-probe experiments described in Chapters 5 and 6.

Another point of comparison is the greater ease of use and simplicity of the synchronously mode-locked dye laser. The 3-mirror cavity was much easier to align and required less frequent readjustments than the 7-mirror cavity of the passive system. The only critical adjustment of the synchronous system was the cavity length, which could be very carefully controlled with a precision micrometer.

Figure 2.11

(a) Calculated pulse envelope function for the passively mode-locked dye laser, corresponding to the best-fit to the autocorrelation data. The envelope is a $sech^2$ function with $\Delta t_p = 2.4$ psec. The substructure is not shown.

(b) Calculated pulse envelope function for the synchronoulsy mode-locked dye laser. The envelope is a Lorentzian with $\Delta t_p = 3.13$ psec, which was the optimal pulse shape obtained at exact synchrony. The substructure is not shown.

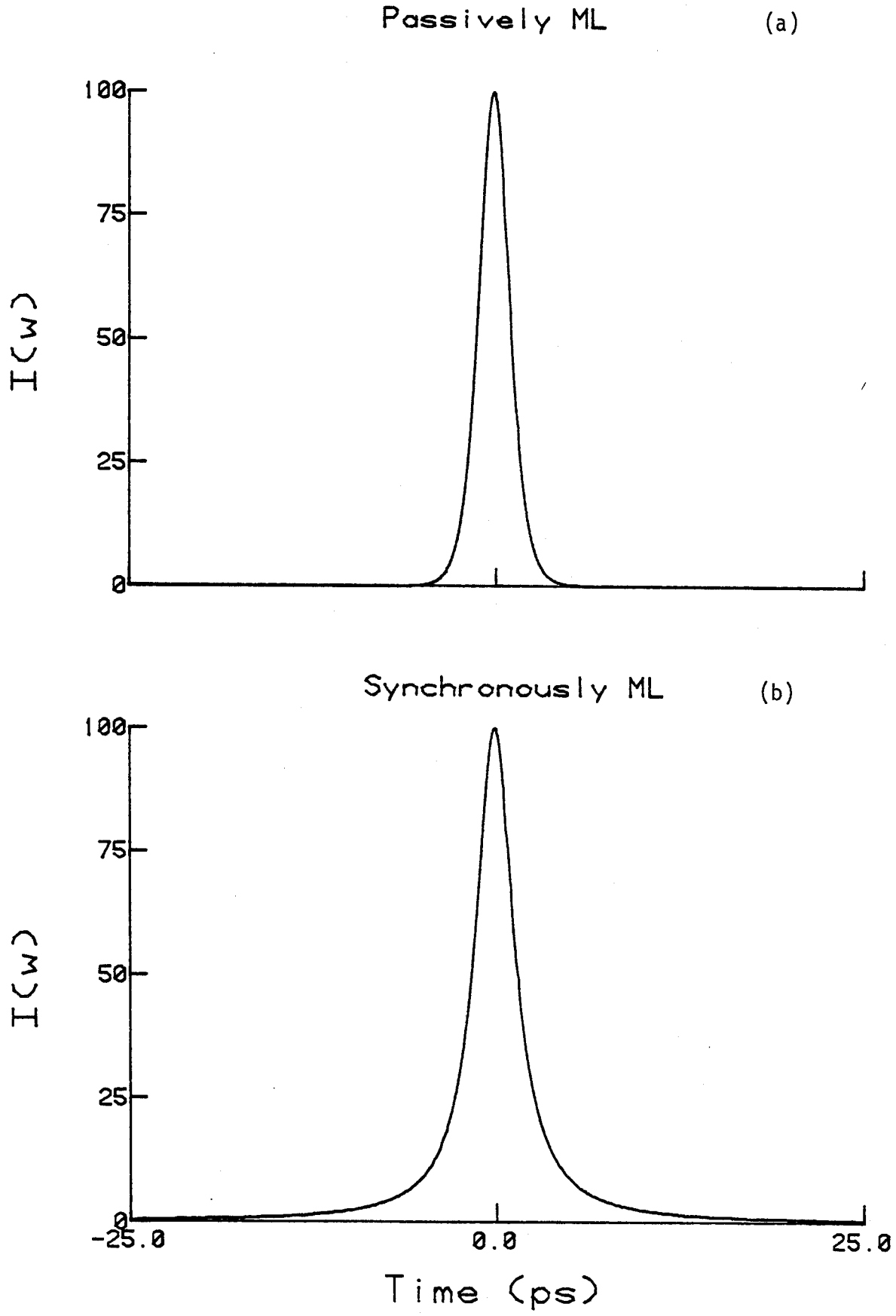
Passively ML
(a)
100
75
50
25
0
I(w)
Synchronously ML
(b)
100
75
50
25
0
I(w)
-25.0
0.0
25.0
Time (ps)

In conclusion, mode-locking of CW dye lasers has been investigated as a new source of ultrashort pulses for picosecond spectroscopy. Both passive and synchronous mode-locking yielded similar results. The important advantages of these new lasers compared with the widely used solid-state lasers are: (1) High repetition rate; (2) excellent pulse-to-pulse reproducibility; (3) shorter pulse durations; and (4) wavelength tunability. The only disadvantage is the much lower pulse energy produced by the mode-locked dye lasers. Nevertheless, this new generation of mode-locked lasers is expected to be useful in picosecond spectroscopy. Their application in several areas will be described in the remainder of this thesis.

References - Chapter 2

1. A. J. DeMaria, D. A. Stetser, H. Heynau, Appl. Phys. Lett. 8, 174 (1966).
2. A. Yariv, Quantum Electronics, 2nd ed., John Wiley & Sons, (1975).
3. P. W. Smith, Proc. IEEE 58, 1342 (1970).
4. D. J. Bradley, in Ultrashort Light Pulses (Topics in Applied Physics, Vol. 18), S. L. Shapiro, ed., Springer Verlag, Berlin (1977).
5. E. P. Ippen, C. V. Shank, Appl. Phys. Lett. 27, 488 (1975).
6. H. W. Kogelnik, E. P. Ippen, A. Dienes, C. V. Shank, IEEE J. Quantum Electr. QE-8, 373 (1972).
7. D. Maydan, J. Appl. Phys. 41, 1552 (1970).
8. J. C. Diels, E. Van Stryland, G. Benedict, Opt. Commun. 25, 93 (1978).
9. F. O'Neill,Opt. Commun. 6, 360 (1972).
10. Z. A. Yasa, A. Dienes, and J. R. Whinnery, Appl. Phys. Lett. 30, 24 (1977).
11. R. L. Fork, B. I. Greene, C. V. Shank, Appl. Phys. Lett. 38, 671 (1981).
12. A. Yariv, J. Appl. Phys. 36, 388 (1965).
13. H. Maier, W. Kaiser, J. A. Giordmaine, Phys. Rev. Lett. 17, 1275 (1966).
14. H. A. Pike, M. Hercher, J. Appl. Phys. 41, 4562 (1970).
15. D. B. McDonald, J. L. Rossel, G. R. Fleming, IEEE J. Quantum Electr. QE-17, 1134 (1981).
16. H. A. Haus, C. V. Shank, E. P. Ippen, Opt. Commun. 15, 29 (1975).
17. D. B. McDonald, D. Waldeck, G. R. Fleming, Opt. Commun. 34, 127 (1980).
18. Z. A. Yasa, N. M. Amer, Opt. Lett. 6, 67 (1981).
19. V. Sundström, T. Gillbro, Appl. Phys. 24, 233 (1981)

20. A. I. Ferguson, J. N. Eckstein, T. W. Hansch, J. Appl. Phys. 49, 5389 (1978).

21. G. W. Fehrenbach, K. J. Gruntz, R. G. Ulbrich, Appl. Phys. Lett. 33, 159 (1978).

22. R. K. Jain, C. P. Ausschnitt, Opt. Lett. 2, 117 (1978).

23. J. Kuhl, H. Klingenberg, D. von der Linde, Appl. Phys. 18, 279 (1979).

24. K. L. Sala, G. A. Kenney-Wallace, G. E. Hall, IEEE J. Quantum Electr. QE-16, 990 (1980).

25. F. Minami, K. Era, Opt. Commun. 35, 393 (1980).

26. J. Kuhl, R. Lambrich, D. von der Linde, Appl. Phys. Lett. 31, 657 (1977).

27. D. M. Kim, J. Kuhl, R. Lambrich, D. von der Linde, Opt. Commun. 27, 123 (1978).

28. S. L. Shapiro, R. R. Cavanagh, J. C. Stephenson, Opt. Lett. 6, 470 (1981).

29. G.H.C. New, Opt. Commun. 6, 188 (1972).

30. G.H.C. New, IEEE J. Quantum Electr. QE-10, 115 (1974).

31. H. A. Haus, IEEE J. Quantum Electr. QE-11, 736 (1975).

32. C. P. Ausschnitt, IEEE J. Quant. Electr. QE-13, 321 (1977).

33. N. Frigo, T. Daly, H. Mahr, IEEE J. Quantum Electr. QE-13, 101 (1977).

Chapter 3

PUMP-PROBE TECHNIQUES

3.1 Introduction

Pump-probe techniques are as old as the field of picosecond spectroscopy itself. The idea was first developed and applied to measurements of ultrafast molecular recovery times by Shelton and Armstrong in 1967 [1], soon after the discovery of passive mode-locking. The idea is a simple one: a picosecond duration pulse excites the sample of interest, usually by one-photon absorption but more generally by Raman scattering, the Kerr effect, or other nonlinear phenomena. A weaker replica pulse arrives at the sample after a time delay τ and probes the transient response of the sample, also by absorption (or fluorescence, Raman, etc.). Repeating the experiment for many τ values maps out the full time-dependent response which is related to an excited state or a ground state population of the sample. The simplest pump-probe experiment is "ground state recovery"; the first pulse depletes the ground state population due to optical absorption and the weak, delayed pulse probes the return of the excited state population by absorption at the same wavelength. Thus ground state recovery kinetics are obtained in this experiment. Frequently these data are identical to excited state decay data, such as obtained in a fluorescence decay experiment (Chapter 4). In other cases, where more than two energy levels are involved in the kinetics, the ground state recovery data are complementary to excited state decay data and both are necessary to

obtain estimates of the rate constants for all the relaxation channels involved. Such is the case when the triplet state is involved, in those molecules with an appreciable quantum yield for triplet formation by intersystem crossing [2]. However, in this work ground state recovery measurements were applied to the simple case of $S_1 \rightarrow S_0$ relaxation, where 2-level kinetics only were observed.

Pump-probe experiments require repeated measurements at various time delays τ to accumulate an entire set of data. The mode-locked solid-state lasers were consequently not very suitable for these experiments, since many laser shots were required and the precision of the data was limited by the shot-to-shot variations inherent to these lasers. The high repetition rate mode-locked CW dye lasers, however, are ideal for these experiments, and many of the original pump-probe techniques are enjoying a renaissance for this reason. The high repetition rate means that a full data set covering a long time delay interval can be accumulated rapidly, and the excellent pulse-to-pulse stability means that more precise data can be obtained. The good long-term stability of these lasers also allows powerful signal averaging techniques to be employed, which is often necessary to detect very small transmission changes in weakly absorbing samples.

This chapter presents some important details concerning the pump-probe technique employed in this work, ground state recovery (GSR). A simple derivation is presented to demonstrate how the experimental observables are related to molecular properties. The important influence of anisotropic absorption saturation is included, leading to expressions for the polarization dependence of the GSR.

Another coherence effect, related to the coherence spike in autocorrelation traces, is important when the pump and probe pulses are derived from the same laser. The relevant details are presented here. The effect of the pulse shape and possible influence of pulse substructure are then introduced into the theory to make contact with real experimental data. Some representative experimental data are included at appropriate points to illustrate the consequences and predictions of the theory. Finally, the experimental setup for ground state recovery is described. Applications of the technique are presented in Chapters 5 and 6.

3.2 Simple Theoretical Description

The general theory is first presented with a few simplifying assumptions. The ground state recovery signal is derived in the case where the pulse width is zero and propagation effects are ignored. The basic features of the result are preserved, however, and except for a few fine details the simple theory is adequate for the interpretation of experimental data. The generalizations to include propagation effects, the finite duration of the pulses, and coherence effects are more easily introduced once the basic theory has been derived.

The aim is to calculate the transmission of the probe pulse arriving at the sample a time t after excitation with the pump pulse. Assuming that the sample is very thin and that the pulses have zero width, we can simply apply Beer's law to the probe pulse at time t after excitation

$$i(t) = i_0 \, e^{-\alpha(t)\cdot\ell} \tag{3.1}$$

where i(t) is the probe pulse intensity after the sample, i_o is the intensity before the sample, $\alpha(t)$ the absorption coefficient at time t, and ℓ the sample length. Thus the quantity of interest is the instantaneous absorption coefficient at time t after excitation. Before proceeding, it is important to note that this absorption coefficient depends on the relative polarization of the pump and probe pulses. The probability for absorption of a photon depends on the angle between the electric vector of the light and the transition dipole of the molecule. Therefore, excitation of a random sample with polarized light produces an anisotropic angular distribution of excited dipoles; those dipoles that are aligned more closely with the electric vector have a higher probability of being excited. The corresponding anisotropy in the ground state population induces a dichroism; the absorption coefficient for light polarized parallel to the excitation polarization is smaller, since the effective depletion is greater in this configuration, than for light polarized perpendicular to the excitation pulse. Any theoretical description must take this important phenomenon, called anisotropic absorption saturation, into account.

The absorption coefficient for probe light with parallel polarization arriving at time t after excitation can be written,

$$\alpha_{\parallel}(t) = \sigma N \Big\langle \exp(-3\sigma I\,|\hat{\varepsilon}_i\cdot\hat{\mu}(0)|^2)\cdot 3|\hat{\varepsilon}_i\cdot\hat{\mu}(t)|^2 + \int_0^t k\,e^{-kt'}\,dt'\,[1-\exp(-3\sigma I\,|\hat{\varepsilon}_i\cdot\hat{\mu}(0)|^2)]\,3|\hat{\varepsilon}_i\cdot\hat{\mu}(t)|^2\Big\rangle \quad (3.2)$$

where $\hat{\varepsilon}_i$ is a unit vector specifying the polarization direction of the pump light, $\hat{\mu}(0)$ is a unit vector oriented along the transition dipole at time

zero, $\hat{\mu}(t)$ the same at time t, σ is the cross-section for the transition, N is the total density of molecules in the region of overlap of pump and probe beams, I is the total number of photons/unit area in the pump pulse, and k is the ground state repopulation rate. The outer brackets denote an ensemble average over the entire sample in the active region. The first term in Eq. (3.2) is the product of two probabilities; the probability that the molecule was not excited at time zero, and the probability of absorption at time t, $3|\hat{\varepsilon}_i \cdot \hat{u}(t)|^2$. The second term is the contribution from molecules which were excited at time zero but have returned to the ground state by time t. These molecules have undergone reorientation in the excited state.

The corresponding expression for probe light polarized perpendicular to the pump light is

$$\alpha_{\perp}(t) = \frac{\sigma N}{2}\Big\langle \exp(-3\sigma I\,|\hat{\varepsilon}_i \cdot \hat{\mu}(0)|^2)\; 3|\hat{\varepsilon}_i \times \hat{\mu}(t)|^2 + \int_0^t k\, e^{-kt'}\, dt' [1 - \exp(-3\sigma I\,|\hat{\varepsilon}_i \cdot \hat{\mu}(0)|^2)] \cdot 3|\hat{\varepsilon}_i \times \hat{\mu}(t)|^2 \Big\rangle \quad (3.3)$$

The expressions in Eqs. (3.2) and (3.3) must also be averaged over all possible directions for the polarization vector $\hat{\varepsilon}_i$ relative to the molecule [3]. We first expand the exponentials in (3.2) and (3.3), which is a good approximation when the pump intensity is not too high, and rearrange to get,

$$\alpha_{\parallel}(t) = \sigma N \left\langle 3|\hat{\varepsilon}_i \cdot \hat{\mu}(t)|^2 \right\rangle - 9\sigma^2 IN \left\langle |\hat{\varepsilon}_i \cdot \hat{\mu}(0)|^2 |\hat{\varepsilon}_i \cdot \hat{\mu}(t)|^2 \right\rangle e^{-kt}$$

$$\alpha_{\perp}(t) = \frac{\sigma N}{2} \left\langle 3|\hat{\varepsilon}_i \times \mu(t)|^2 \right\rangle - 9\sigma^2 \frac{IN}{2} \left\langle |\hat{\varepsilon}_i \cdot \hat{\mu}(0)|^2 |\hat{\varepsilon}_i \times \hat{\mu}(t)|^2 \right\rangle e^{-kt} \quad (3.4)$$

The averages over $\hat{\varepsilon}_i$ of each term in these equations are performed in Appendix 3.1. The results are,

$$\alpha_{\parallel}(t) = \sigma N - \frac{3}{5}\sigma^2 IN(1 + 2\left\langle|\hat{\mu}(0)\cdot\hat{\mu}(t)|^2\right\rangle)\cdot e^{-kt}$$
$$\alpha_{\perp}(t) = \sigma N - \frac{3}{5}\sigma^2 IN(2 - \left\langle|\hat{\mu}(0)\cdot\hat{\mu}(t)|^2\right\rangle)\cdot e^{-kt} \qquad (3.5)$$

As seen above, the expressions are now independent of $\hat{\varepsilon}_i$ and depend only on the ensemble average of the squared cosine of the molecular reorientation angle. The time-dependence of this ensemble average does not reflect the rotational dynamics of a single molecule, however, but rather the rotational dynamics of a macroscopic sample. Of course, the underlying phenomenon is reorientation of individual molecules due to the random torques and collisions experienced in the liquid or gas state. But ensemble averaged behavior is observed in these experiments. Rather than the ensemble averages in (3.5), it is usual to introduce the dipole autocorrelation function $\left\langle P_2[\hat{\mu}(0)\cdot\hat{\mu}(t)]\right\rangle$, where P_2 is the second Legendre polynomial. This correlation function contains all the information on rotational dynamics that is possible to be measured. We define a more useful quantity, which will be called the reduced anisotropy,

$$r(t) = \frac{2}{5}\left\langle P_2[\hat{\mu}(0)\cdot\hat{\mu}(t)]\right\rangle \qquad (3.6)$$

Introducing this definition into (3.5) gives,

$$\alpha_{\parallel}(t) = \sigma N - \sigma^2 IN(1 + 2r(t))\, e^{-kt} \qquad (3.7a)$$
$$\alpha_{\perp}(t) = \sigma N - \sigma^2 IN(1 - r(t))\, e^{-kt} \qquad (3.7b)$$

The first term in each of Eqs. (3.7) is obviously the normal absorption coefficient measured with no pump pulse excitation. The second term is the decrease in absorption due to bleaching by the pump pulse, and is obviously a time-dependent contribution. The important point is that there are two time-dependent functions involved; the ground-state recovery term, e^{-kt}, and the rotational Brownian motion term, $r(t)$. That is, not just population kinetics contribute to ground-state recovery experiments. The induced dichroism due to anisotropic absorption is also readily apparent in Eqs. (3.7), and is connected with the $r(t)$ term only. For example, when reorientation is infinitely rapid, $r(t) = 0$, the dichroism vanishes, $\alpha_{\parallel}(t) = \alpha_{\perp}(t)$, and population kinetics only contribute to the signal. More frequently, however, the time-scales of $r(t)$ and the e^{-kt} are similar, and both effects are observed. This can be exploited to learn about molecular reorientation, as discussed in Chapter 5.

Equation (3.7) shows that the absorption coefficient, for either polarization limit, can be written as,

$$\alpha(t) = \alpha_0 + \Delta\alpha(t) \tag{3.8}$$

where $\alpha_0 = \sigma N$ is the small-signal absorption coefficient, and $\Delta\alpha(t)$ is the change due to bleaching. Returning to Beer's law, the probe transmission at time t is

$$T(t) = T_0 \cdot e^{-\Delta\alpha(t)\ell} \tag{3.9}$$

where $T_0 = e^{-\alpha_0 \ell}$ is the small-signal transmission (no bleaching). When $\Delta\alpha$ is small, as is usually the case in practice, the exponential can be expanded,

$$T(t) = T_0 - T_0 \Delta\alpha(t)\ell \tag{3.10}$$

Usually the change in transmission, $\Delta T = T - T_0$, is measured. Combining (3.7) and (3.10), the final result is obtained:

$$\Delta T_{\parallel}(t) = \sigma^2 IN\, T_0 \ell (1 + 2r(t))\, e^{-kt} \tag{3.11a}$$

$$\Delta T_{\perp}(t) = \sigma^2 IN\, T_0 \ell (1 - r(t))\, e^{-kt} \tag{3.11b}$$

These equations are the main result of this section. Two points should be noted: first, since $r(0) = 2/5$, the relative values of the parallel and perpendicular GSR at zero delay are in the ratio $\Delta T_{\parallel}(0) / \Delta T_{\perp}(0) = 3$; second, at long delay times after the correlation function has decayed to zero, $r(t) = 0$, and the GSR signals become independent of polarization and contain population kinetics only, $\Delta T_{\parallel}(t) = \Delta T_{\perp}(t) = \sigma^2 IN \ell\, T_0\, e^{-kt}$.

The important approximations that have been made are low pump intensity and small transmission change. It is only under these conditions that ΔT is linearly related to the e^{-kt} term and the $r(t)$ term. Thus, it is important in practice to verify that these conditions exist.

Both molecular reorientation and population kinetics contribute to the parallel and perpendicular probe transmission change signals. It would be useful to decouple these two effects to simplify the interpretation of experimental data. An interesting property of (3.11) is revealed if we form the sum $\Delta T_{\parallel} + 2\Delta T_{\perp}$,

$$\Delta T_{\parallel}(t) + 2\Delta T_{\perp}(t) = 3\sigma^2 IN\, T_0 \ell\, e^{-kt} \tag{3.12}$$

which depends on population kinetics only. Similarly, taking the difference gives,

$$\Delta T_{\parallel}(t) - \Delta T_{\perp}(t) = 3\sigma^2 IN\, T_0 \ell\, r(t)\, e^{-kt} \tag{3.13}$$

This immediately shows how to determine r(t) independently of population kinetics, according to

$$r(t) = \frac{\Delta T_{\parallel}(t) - \Delta T_{\perp}(t)}{\Delta T_{\parallel}(t) + 2\Delta T_{\perp}(t)} \tag{3.14}$$

A linear combination like Eq. (3.12) can be measured experimentally by using a probe polarization direction intermediate between parallel and perpendicular. For a probe direction specified by an angle ψ to the parallel direction, the measured transmission change is

$$\Delta T_{\psi}(t) = \cos^2\psi\, \Delta T_{\parallel}(t) + \sin^2\psi\, \Delta T_{\perp}(t) \tag{3.15}$$

The condition to form the linear combination given in (3.12) is $\tan^2\psi = 2$. The solution is $\psi = 54.7°$, which is known as the "magic angle." The transmission change measured in this configuration is called the isotropic signal, since the anisotropic absorption saturation effects are exactly counteracted,

$$\Delta T_{iso}(t) = \Delta T_{54.7}(t) = \sigma^2 IN\, T_0 \ell\, e^{-kt} \tag{3.16}$$

The important results of this derivation are Eq. (3.11) for $\Delta T_{\parallel}$ and $\Delta T_{\perp}$, Eq. (3.14) for r(t), and Eq. (3.16) for ΔT_{iso}. These equations are quite general, and are independent of the exact details of the molecular reorientation. Identical results to Eq. (3.11) have been derived by Lessing and von Jena [4] in the special case of isotropic rotational diffusion, $r(t) = e^{-6Dt}$, where D is the rotational diffusion coefficient. The derivation presented here is more general and is independent of the model

assumed for the reorientation. An exponential ground-state recovery has been assumed, but this can be extended to the case of more complicated population kinetics. These equations can in most cases be used to analyze ground-state recovery data. The important refinements, which include the effects of pulse shape and coherence, are included next. However, as will be seen, these details do not significantly alter the results derived here.

A final important point is that no unknown parameters have been used in this derivation. The equations for the transmission change, Eqs. (3.11) and (3.16), are written in terms of known molecular constants such as the absorption cross-section, the concentration and known system parameters such as low-level transmission, pump intensity, and sample length. Thus absolute signal intensities can be calculated using these results. Consider, as an example, the following conditions which are typical of the experiments discussed in Chapter 5: $I = 8 \times 10^{15}$ photons/cm^2, $\ell = 10^{-2}$ cm, $N = 1.2 \times 10^{17}\ cm^{-3}$, $\sigma = 2 \times 10^{-17}\ cm^2$ ($\varepsilon = 5 \times 10^3$). The fractional change in transmission $\Delta T/T_o$ for the isotropic signal is $\sigma^2 N \ell I = 4 \times 10^{-3}$. That is, the initial change in transmission due to bleaching is 0.4%. The actual change may be somewhat less if the pump and probe beams do not maintain optimal spatial overlap over the entire cell length ℓ.

3.3 Effect of Pulse Shape

In practice the pulses do have a finite width and it is important to include this in the model when the recovery processes are occurring on a time scale comparable with the pulse width itself. The generaliza-

tions of the previous derivation are easily obtained.

When the pump pulse has a shape I(t) (the number of photons/unit time), Eq. (3.7) must be generalized as follows:

$$\Delta\alpha_{\parallel}(t) = \sigma^2 N \int_{-\infty}^{t} (1 + 2r(t-t')) e^{-k(t-t')} I(t')\, dt' \qquad (3.17a)$$

$$\Delta\alpha_{\perp}(t) = \sigma^2 N \int_{-\infty}^{t} (1 - r(t-t')) e^{-k(t-t')} I(t')\, dt' \qquad (3.17b)$$

The transmission of the probe pulse, which has a shape $i_0(t)$, at time delay t_0 is still given by (3.9). What is measured, however, is the time-integrated probe pulse intensity for a delay t_0. In this case the "transmission change" can be written as follows:

$$\Delta T_{\parallel}(t_0) = \sigma^2 N\ell \cdot T_0 \int_{-\infty}^{\infty} i_0(t-t_0) \int_{-\infty}^{t} (1 + 2r(t-t')e^{-k(t-t')} I(t')\, dt'\, dt \qquad (3.18a)$$

$$\Delta T_{\perp}(t_0) = \sigma^2 N\ell \cdot T_0 \int_{-\infty}^{\infty} i_0(t-t_0) \int_{-\infty}^{t} (1 - r(t-t'))e^{-k(t-t')} I(t')\, dt'\, dt \qquad (3.18b)$$

These equations are the required generalizations of Eq. (3.11). When $i_0(t)$ and I(t) are very narrow, and can be approximated by delta functions, Eqs. (3.18) reduce to the earlier result, Eq. (3.11). The results of the previous section give the delta function response, which is convoluted with both the pump pulse shape and the probe pulse shape in Eq. (3.18). The signal measured at delay t_0 contains the molecular response spread over the time region around t_0 by the pulse duration. The time resolution in a ground state recovery experiment is thus limited by the time duration of

both pump and probe pulses. The effect of the pulse duration is illustrated in Figure 3.1, which shows isotropic ground state recovery signals calculated from Eq. (3.18) for three values of the pulse duration: $\Delta t_p = 1$ psec, $\Delta t_p = 5$ psec, $\Delta t_p = 10$ psec. In all cases $k^{-1} = 10$ psec, and a Gaussian pulse shape was assumed. The GSR curve closely resembles the impulse response when $\Delta t_p = 1$ psec. A broadening and delayed rise are apparent with $\Delta t_p = 5$ psec, and the population kinetics can only be obtained from the tail of the GSR curve. When $\Delta t_p = 10$ psec, the GSR curve is dominated by the response effects, and the recovery time will only be extracted by deconvolution methods.

3.4 Propagation Effects

When the sample is not very thin, the propagation of the probe pulse in the bleached sample must be considered. The differential equation governing the propagation of the probe pulse delayed by t_o is

$$\frac{\partial i}{\partial x}(x,t-t_o) = -\alpha_o i(x,t-t_o) - \Delta\alpha(I(x,t),t) \cdot i(x,t-t_o) \tag{3.19}$$

Integrating over x gives,

$$i(\ell,t-t_o) = i_o(t-t_o)\, e^{-\alpha_o \ell}\, e^{-\overline{\Delta\alpha}(t)\ell} \tag{3.20}$$

as in Eq. (3.9), except that the sample-depth averaged absorption change appears. It is given by

$$\overline{\Delta\alpha}(t) = (1/\ell)\int_0^{\ell} \Delta\alpha(I(x,t),t)\, dx \tag{3.21}$$

Including this modification in Eq. (3.18) gives the final expressions

Figure 3.1

Isotropic ground state recovery curves calculated using Eq. (3.18) for a Gaussian pump and probe pulse shape. In all cases, $k^{-1} = 10$ psec, $\sigma = 5 \times 10^{-17} cm^2$, $I = 3 \times 10^{14} cm^{-2}$, $N = 3 \times 10^{18} cm^{-3}$, $\ell = .5$ mm. The pulse width used was: (a) $\Delta t_p = 1$ psec, (b) $\Delta t_p = 5$ psec, and (c) $\Delta t_p = 10$ psec.

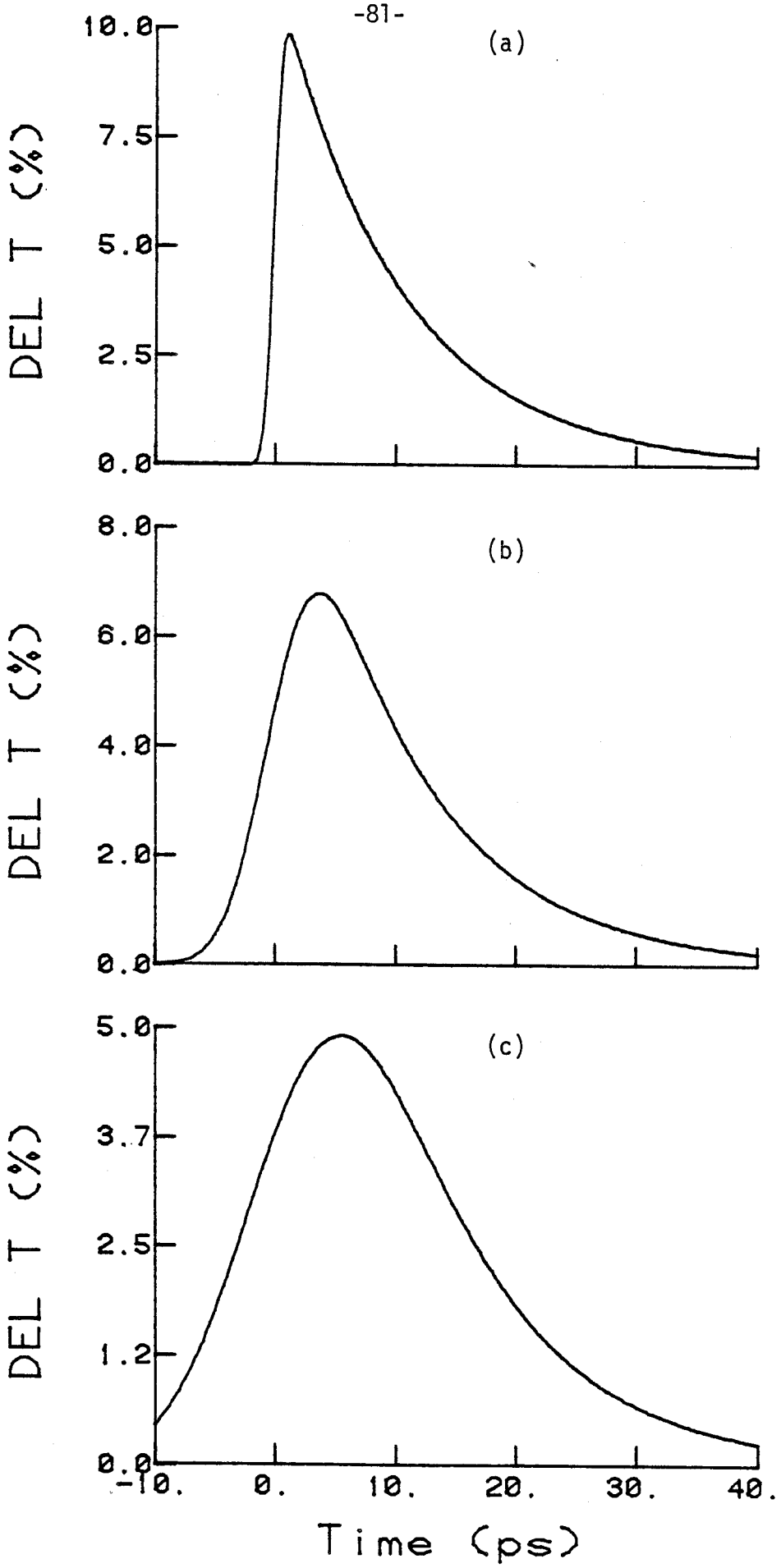
(a)
10.0
7.5
5.0
2.5
0.0
DEL T (%)
(b)
8.0
6.0
4.0
2.0
0.0
DEL T (%)
(c)
5.0
3.7
2.5
1.2
0.0
DEL T (%)
-10.
0.
10.
20.
30.
40.
Time (ps)

for the ground-state recovery signals including both pulse shape and propagation effects,

$$\Delta T_{\parallel}(t_o) = \sigma^2 N T_o \int_{-\infty}^{\infty} i_o(t-t_o) \int_{-\infty}^{t} (1 + 2r(t-t'))e^{-k(t-t')} \int_{0}^{\ell} I(x,t')\,dx\,dt'\,dt \tag{3.22a}$$

$$\Delta T_{\perp}(t_o) = \sigma^2 N T_o \int_{-\infty}^{\infty} i_o(t-t_o) \int_{-\infty}^{t} (1 - r(t-t'))e^{-k(t-t')} \int_{0}^{\ell} I(x,t')\,dx\,dt'\,dt \tag{3.22b}$$

The propagation effects do not affect the qualitative situation, but must be included when making calculations in thick samples. Note that the derivation has assumed that pump and probe pulses propagate in the same direction. This was the case in the present work, but in general a counter-propagating geometry is also often used. In this case the propagation effects in thick samples can change the signal, since the time resolution is determined by the transit time across the sample [4].

3.5 Coherent Coupling Effects

An interesting feature of pump-probe experiments is the coherence effects that produce additional signal contributions around zero delay when the pump and probe pulses are derived from a common laser. A typical experimental trace is shown in Figure 3.2. The narrow peak at zero delay is a so-called "coherence spike" and is due to the coherent interaction of pump and probe pulses. Around zero delay the pump and probe fields interfere in the sample. In this case the probe is not just responding to the population bleaching produced by the pump, but is interacting with the pump field itself. The interaction can be described as the diffraction

Figure 3.2

An experimental ground state recovery curve exhibiting a "coherence spike." Note that $\Delta T^{incoh}(0) = \Delta T^{coh}(0)$ in this figure.

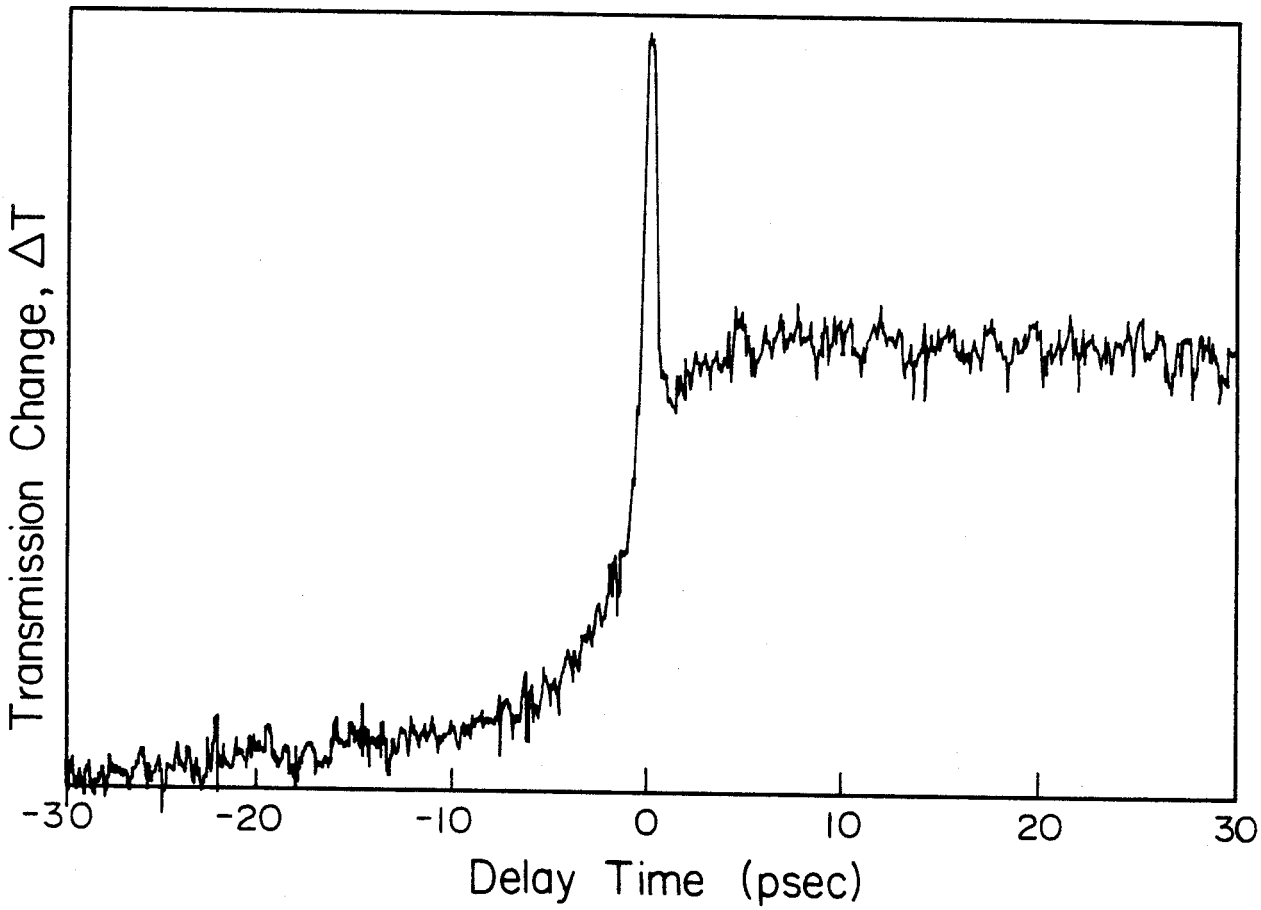
Transmission Change, ΔT
-30
-20
-10
0
10
20
30
Delay Time (psec)

of some of the pump pulse into the probe pulse direction by a transient population grating produced by interference of the two fields. The effect persists only while the interference occurs, and hence the width of the "coherence spike" is related to the coherence time of the laser.

Coherent-coupling effects were first observed in picosecond pump-probe experiments by Shank and Auston [5]. A general theoretical treatment has been given [6], which will be followed here. A very brief presentation of the important steps and the final results are given here. The coherent coupling effects are discussed in two important cases of practical interest; when $\Delta t_p > \Delta t_c$, and $\Delta t_p < \Delta t_c$. The different form of the coherent coupling artifacts in these two cases are illustrated.

Since interference phenomena are being discussed, it is necessary to consider the electric field of pump and probe pulses. Only the case of parallel polarization directions for pump and probe is considered here. The perpendicular signal is handled in a similar manner, but the derivation is somewhat more involved [6]. The electric fields are written

$$E_B(x,t) = E_B \exp(i(\omega t - kx + \phi))$$
$$E_p(x,t) = E_p \exp(i(\omega t + kx)) \tag{3.23}$$

where E_B is the amplitude of the pump pulse (bleaching), E_p the probe amplitude, k the wavevector, and ϕ the phase shift between pump and probe fields. A counterpropagating geometry in the sample has been assumed. The intensity in the sample due to the simultaneous presence of both fields is

$$I(x,t) = (\varepsilon_0/\mu_0)^{1/2} \{E_B^2 + E_p^2 + 2E_B E_p \cos(2kx - \phi)\} \tag{3.24}$$

Substituting (3.24) into (3.17), we find that the change in absorption

coefficient contains two contributions, in the parallel case given by

$$\Delta\alpha_{\parallel}(x,t) = -\frac{\sigma^2 N}{h\nu}(\varepsilon_o/\mu_o)^{1/2}\int_{-\infty}^{t} E_B^2(x,t')[1 + 2r(t-t')]\, e^{-k(t-t')}dt' \quad (3.25)$$

and

$$\Delta\alpha_{\parallel}^{mod}(x,t) = -\frac{\sigma^2 N}{h\nu}(\varepsilon_o/\mu_o)^{1/2}\int_{-\infty}^{t} E_B(x,t')\, E_p(x,t'-t_o)[1 + 2r(t-t')]e^{-k(t-t')}dt' \times 2\cos(2kx - \phi) \quad (3.26)$$

Equation (3.25) is identical to Eq. (3.17) and is the usual "incoherent" bleaching contribution to the absorption change. Equation (3.26) is a spatially modulated contribution to the absorption change. These absorption changes govern the propagation of the probe beam. The wave equation for the probe field is solved with both the spatially modulated and the constant absorption terms found above. The final result for the transmission change contains two contributions [6],

$$\Delta T_{\parallel}^{incoh}(t_o) = \sigma^2 N\, T_o \int_{-\infty}^{\infty} i_o(t-t_o)\int_{-\infty}^{t}[1 + 2r(t-t')]e^{-k(t-t')}\int_{0}^{\ell} I_B(x,t')\,dx \times dt'\,dt \quad (3.27a)$$

$$\Delta T_{\parallel}^{coh}(t_o) = \sigma^2 N\, T_o \int_{-\infty}^{\infty}[i_o(t-t_o)i_o(t)]^{1/2}\int_{-\infty}^{t}[1 + 2r(t-t')]e^{-k(t-t')}\int_{0}^{\ell}[I_B(x,t') \times I_B(x,t'-t_o)]^{1/2}dx\,dt'\,dt \quad (3.27b)$$

Equation (3.27a) is identical with (3.22a) for the transmission change including both pulse shape and propagation effects. Thus (3.27a) represents the normal GSR signal due to "incoherent" bleaching. The

additional signal contribution derived in this section is given in Eq. (3.27b). This is the signal contribution due to the coherent coupling effect.

The corresponding results for the perpendicular polarization directions are [6]

$$\Delta T_{\perp}^{incoh}(t_o) = \sigma^2 N\, T_o \int_{-\infty}^{\infty} i_o(t-t_o) \int_{-\infty}^{t} [1 - r(t-t')]\, e^{-k(t-t')} \int_{0}^{\ell} I_B(x,t')\,dx\,dt'\,dt \tag{3.28a}$$

$$\Delta T_{\perp}^{coh}(t_o) = \sigma^2 N\, T_o \int_{-\infty}^{\infty} [i_o(t-t_o)\, i_o(t)]^{1/2} \int_{-\infty}^{t} \frac{3}{2}\, r(t-t')\, e^{-k(t-t')} \times \int_{0}^{\ell} [I_B(x,t'-t_o)\, I_B(x,t')]^{1/2}\,dx\,dt'\,dt \tag{3.28b}$$

The form of the coherent signal contribution is similar for both parallel and perpendicular polarization directions. Both contain convolutions of the molecular response with first-order electric field autocorrelation functions, $\int_{-\infty}^{\infty} [i_o(t-t_o)\, i_o(t)]^{1/2}\,dt$. This correlation function is a peaked function, such as a Gaussian, with a FWHM equal to the coherence time of the laser. Hence the coherent signal only exists in a time interval equal to the coherence time about zero delay. The relative signal contributions are illustrated in Figure 3.3 in two limiting cases: (a) when the coherence time is much shorter than the pulse duration, $\Delta t_c << \Delta t_p$, and (b) when the coherence time is longer, $\Delta t_c >> \Delta t_p$. In (a) the electric field correlation has a width related to Δt_c, and ΔT^{coh} also has a width related to Δt_c. The incoherent signal ΔT^{incoh} on the other hand has

Figure 3.3

Effect of rise time and coherent coupling on ground state recovery curves. The separate contributions $\Delta T^{coh}(t)$ and $\Delta T^{incoh}(t)$ are shown in two cases:

(a) $\Delta t_c < \Delta t_p$; the width of the coherent contribution is narrower than the rise time of the incoherent bleaching.

(b) $\Delta t_c > \Delta t_p$; the width of the coherent contribution is equal to the rise time of the incoherent bleaching.

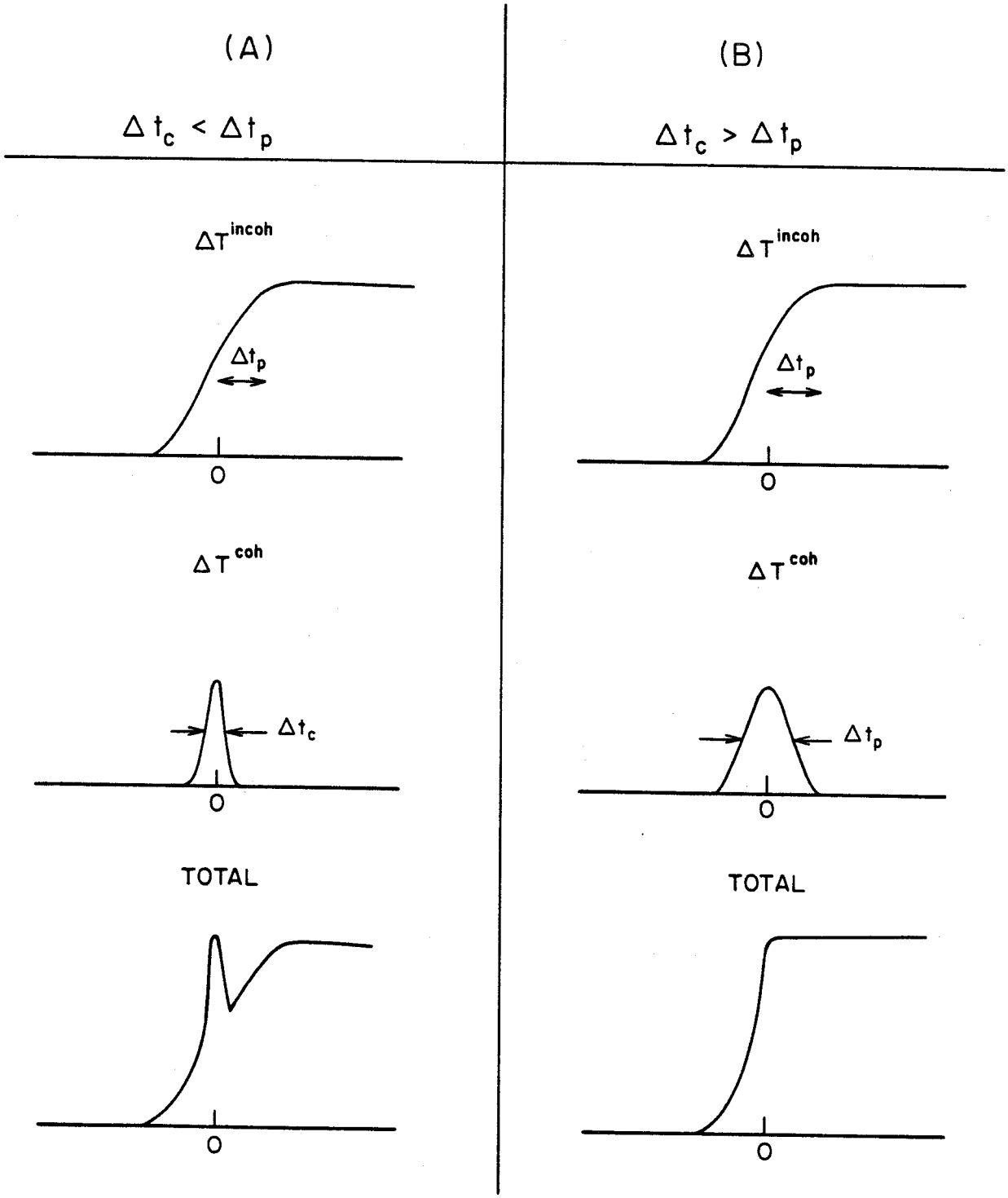
(A)
$\Delta t_c < \Delta t_p$
(B)
$\Delta t_c > \Delta t_p$
ΔT^{incoh}
Δt_p
0
ΔT^{incoh}
Δt_p
0
ΔT^{coh}
Δt_c
0
ΔT^{coh}
Δt_p
0
TOTAL
0
TOTAL
0

a "rise time" determined by the Δt_p in the region of zero delay. The total signal thus appears as in Figure 3.3a. In the other limit, $\Delta t_c \gg \Delta t_p$, the $[i(t-t_o)\ i(t)]^{1/2}$ terms have a FWHM now limited by the pulse width. Thus the shape of the coherent contribution ΔT^{coh} is also determined by Δt_p rather than by Δt_c (which is longer). The incoherent signal again has a rise determined by Δt_p. Thus the total signal appears as in Fig. 3.3b. In this case there is no "coherence spike" but a sharpening of the signal rise at zero delay due to the coherent coupling effect. Thus the appearance of the ground state recovery signals around zero delay can provide some information on the relative magnitudes of Δt_p and Δt_c.

An important property of the parallel signal is observed at zero delay. From Eq. (3.27),

$$\Delta T_{\parallel}^{coh}(0) = \sigma^2 N\ell\, T_o \int_{-\infty}^{\infty} i_o(t) \int_{-\infty}^{t} [1 + 2r(t-t')]e^{-k(t-t')}\,(1/\ell) \int_0^{\ell} I_B(x,t')dx\,dt'dt$$

$$= \Delta T_{\parallel}^{incoh}(0). \qquad (3.29)$$

Thus the parallel polarization ground state recovery signal is exactly doubled at zero delay due to coherent coupling effects. This is also illustrated in Figure 3.3.

In the case of perpendicular probe polarization $\Delta T_{\perp}^{incoh}(0) \neq \Delta T_{\perp}^{coh}(0)$ in general, because of the different terms involving $r(t-t')$ in Eqs. (3.28a) and (3.28b). However, when $r(t) = 0.4$ (its maximal value) throughout the pulse duration, then these equations show that $\Delta T_{\perp}^{incoh}(0) = \Delta T_{\perp}^{coh}(0)$ and the signal is doubled at zero delay. This is the case of infinitely slow rotation compared with the pulse duration. In the opposite limit of

fast rotation, $r(t) = 0$ throughout the pulse, and $\Delta T_{\perp}^{coh}(t) = 0$. There is no coherent coupling contribution to the perpendicular polarization GSR signal when rotation is fast compared with the pulse width. Thus, in general, the relative magnitudes of $\Delta T_{\perp}^{incoh}(0)$ and $\Delta T_{\perp}^{coh}(0)$ depend on the relative magnitudes of the rotational relaxation time and pulse duration.

3.6 Experimental Arrangement

The experimental arrangement for ground state recovery pump-probe measurements is shown in Figure 3.4. It is quite similar to the setup used for background-free second harmonic autocorrelation analysis. The pulse train entered an interferometer which produced the pump train and a weaker, delayed probe train. The probe beam passed through a polarizer and half-wave plate, which could be rotated to select the appropriate polarization direction. The pump beam was vertically polarized. The two noncolinear but parallel beams were focussed to a common spot in a 100 micron thick sample solution. The transmitted probe beam passed to a photomultiplier and the transmitted pump beam was blocked by an aperture. The pump beam was modulated before the sample by a mechanical chopper. The lock-in amplifier phase-sensitively detected the modulation of the transmitted probe intensity due to modulation of the pump beam. This signal was proportional to the transmission change caused by the pump beam. The lock-in output was digitized by a voltage-to-frequency convertor and input to a multichannel analyzer operating in the multichannel scaling mode. The MCA memory location was incremented by the stepper motor controller as the variable delay was scanned over the desired delay interval. Many repetitive scans of the same interval were overlaid in the MCA memory to enhance

Figure 3.4

Experimental setup for ground state recovery measurements:

P	Polarizers
$\lambda/2$	Half-wave plate
SMC	Stepper motor controller
VFC	Voltage-to-frequency converter
PM	Photomultiplier
MCA	Multichannel analyzer
PDP 11/23	Mini-computer

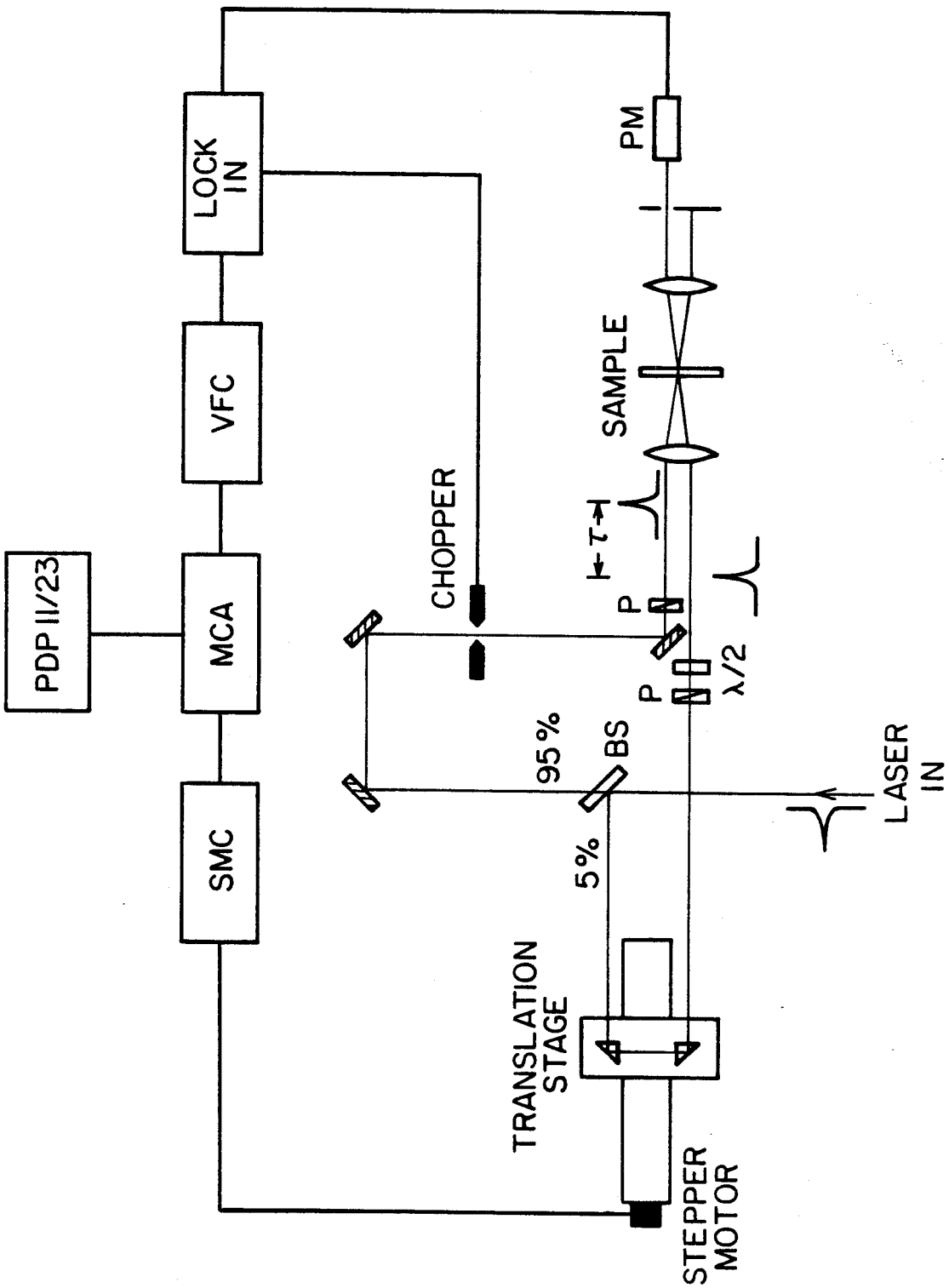
LOCK IN
VFC
MCA
SMC
PDP 11/23
PM
SAMPLE
CHOPPER
τ
P
λ/2
P
95%
BS
5%
LASER IN
TRANSLATION STAGE
STEPPER MOTOR

the signal-to-noise ratio. The memory contents could be transferred to a PDP 11/23 mini-computer for disk storage, analysis, and plotting.

References - Chapter 3

1. J. W. Shelton, J. A. Armstrong, IEEE J. Quant. Electr. QE-3, 302 (1967).
2. H. E. Lessing, A. von Jena, M. Reichert, Chem. Phys. Lett. 42, 218 (1976).
3. R. G. Gordon, J. Chem. Phys. 45, 1643 (1966).
4. H. E. Lessing, A. von Jena, in Laser Handbook, vol. 3, M. L. Stitch, ed., North-Holland, Amsterdam, 1979.
5. C. V. Shank, D. H. Auston, Phys. Rev. Lett. 34, 479 (1975).
6. A. von Jena, H. E. Lessing, Appl. Phys. 19, 131 (1979).

Appendix 3.1

Angular Averaging of Dipole Projections

As mentioned in Section (3.2), for an isotropic system it is necessary to average the dipole projections over all directions of $\hat{\varepsilon}_i$.

The terms involving single projections only are considered first. It is useful to employ a coordinate system aligned with the molecule at time t, as shown below.

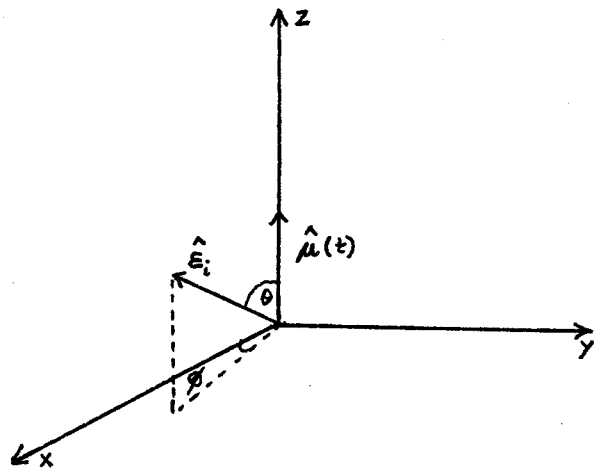

In this coordinate system,

$$\hat{\varepsilon}_i = (\sin\theta\cos\phi\ ,\ \sin\theta\sin\phi\ ,\ \cos\theta\ )$$

$$\hat{\mu}(t) = (0\ ,\ 0\ ,\ 1)$$

Thus $3|\hat{\varepsilon}_i\cdot\hat{\mu}(t)|^2 = 3\cos^2\theta$, and the average is performed as follows:

$$\frac{1}{4\pi}\int_0^{2\pi} d\phi \int_0^{\pi} \sin\theta\ d\theta\ 3\cos^2\theta \ = \ 1 \qquad (3.1.1)$$

Similarly, $\frac{3}{2}\ |\hat{\varepsilon}_i \times \hat{\mu}(t)|^2 = \frac{3}{2}\ (1 - |\hat{\varepsilon}_i\cdot\hat{\mu}(t)|^2)$ and the average is

$$\frac{1}{4\pi}\int_0^{2\pi} d\phi \int_0^{\pi} \sin\theta \, d\theta \, \frac{3}{2}(1-\cos^2\theta) = \frac{3}{2} - \frac{1}{2} = 1 \qquad (3.1.2)$$

For averaging the terms involving products of the projections at time zero and at time t, it is convenient to choose an axis system aligned with the molecule at time zero.

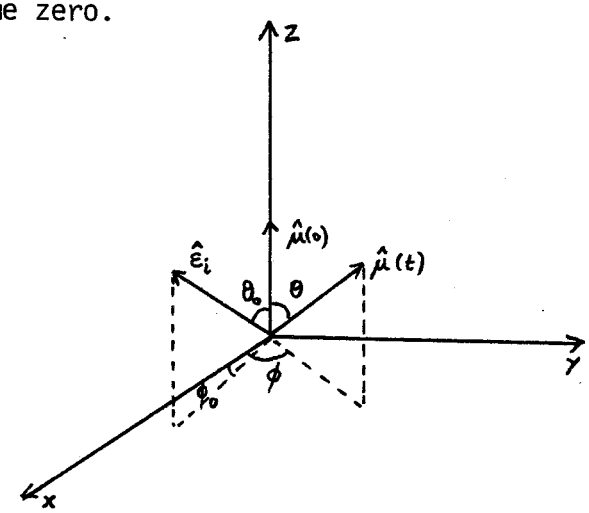

In this coordinate system,

$$\hat{\varepsilon}_i = (\sin\theta_0 \cos\phi_0, \sin\theta_0 \sin\phi_0, \cos\theta_0)$$

$$\hat{\mu}(0) = (\ 0\ ,\ 0\ ,\ 1\ )$$

$$\hat{\mu}(t) = (\sin\theta\cos\phi\ ,\ \sin\theta\sin\phi\ ,\ \cos\theta\ )$$

The projections are

$$|\hat{\varepsilon}_i \cdot \hat{\mu}(0)|^2 = \cos^2\theta_0 \quad ,$$

$$|\hat{\varepsilon}_i \cdot \hat{\mu}(t)|^2 = (\sin\theta_0 \sin\theta \cos\phi_0 \cos\phi + \sin\theta_0 \sin\theta \sin\phi_0 \sin\phi + \cos\theta_0 \cos\theta)^2$$

$$= \sin^2\theta_0 \sin^2\theta \cos^2(\phi - \phi_0) + \cos^2\theta \cos^2\theta_0$$

$$+ 2 \sin\theta_o \sin\theta \cos\theta_o \cos\theta \cos(\phi - \phi_o)$$

$$|\hat{\varepsilon}_i \times \mu(t)|^2 = 1 - |\hat{\varepsilon}_i \cdot \hat{\mu}(t)|^2 \quad .$$

The average over $\hat{\varepsilon}_i$ is equivalent to integration over θ_o and ϕ_o, as follows:

$$\frac{1}{4\pi} \int_0^{2\pi} d\phi_o \int_0^{\pi} \sin\theta_o \, d\theta_o (|\hat{\varepsilon}_i \cdot \hat{\mu}(0)|^2 \, |\hat{\varepsilon}_i \cdot \hat{\mu}(t)|^2)$$

$$= \frac{\sin^2\theta}{4\pi} \int_0^{2\pi} d\phi_o \cos^2(\phi - \phi_o) \int_0^{\pi} \sin\theta_o \, d\theta_o \cos^4\theta_o \sin^2\theta_o$$

$$+ \frac{\cos^2\theta}{4\pi} \int_0^{2\pi} d\phi_o \int_0^{\pi} \sin\theta_o \, d\theta_o \cos^4\theta_o$$

$$+ \frac{2 \sin\theta \cos\theta}{4\pi} \int_0^{2\pi} d\phi_o \cos(\phi - \phi_o) \int_0^{\pi} \sin\theta_o \, d\theta_o \cos^3\theta_o \sin\theta_o$$

$$= \frac{1}{15} (3 \cos^2\theta + \sin^2\theta)$$

$$= \frac{1}{15} (1 + 2|\hat{\mu}(0) \cdot \hat{\mu}(t)|^2) \qquad (3.1.3)$$

since $|\hat{\mu}(0) \cdot \hat{\mu}(t)|^2 = \cos^2\theta$ in the chosen coordinate system.

The cross-product term is similarly treated, with the result

$$\frac{1}{4\pi} \int_0^{2\pi} d\phi_o \int_0^{\pi} \sin\theta_o \, d\theta_o \frac{1}{2} (|\hat{\varepsilon}_i \cdot \hat{\mu}(0)|^2 \, |\hat{\varepsilon}_i \times \hat{\mu}(t)|^2)$$

$$= \frac{1}{15} (\cos^2\theta + 2 \sin^2\theta)$$

$$= \frac{1}{15} (2 - |\hat{\mu}(0) \cdot \hat{\mu}(t)|^2) \qquad (3.1.4)$$

Equations (3.1.1) to (3.1.4) are the desired results.

Chapter 4

TIME-DEPENDENT FLUORESCENCE DEPOLARIZATION

4.1 Introduction

Time-dependent fluorescence depolarization is a powerful technique for the direct measurement of molecular reorientation in the time domain. The underlying physics is very similar to anisotropic absorption saturation discussed in the previous chapter. An isotropic system is excited by a pulse of linearly polarized light producing an anisotropic angular distribution of excited molecules. The fluorescence is consequently partially polarized; for example, the fluorescence viewed through a polarizer parallel to polarization of the exciting light has a higher intensity than fluorescence viewed with a perpendicular polarizer. As the excited molecules reorient, the angular distribution becomes isotropic and the intensities of parallel and perpendicular polarization components of the fluorescence become equal. The time course of the reorientation can thus be monitored by the time-dependent fluorescence anisotropy.

The relationship between fluorescence depolarization and rotational Brownian motion was first formulated by Perrin in 1934 [1], and later extended by Weber [2]. The time-dependent depolarization was considered theoretically by Gordon [3] and in great detail by Tao [4], and by Chuang and Eisenthal [5]. A very brief summary of the theory is provided in Section 4.2 to illustrate the relationship between experimental observables and ensemble-averaged molecular properties. A simplified derivation, following Gordon [3] is given. The most general derivation can be found in

reference [5].

Numerous time-dependent fluorescence depolarization experiments have been performed on biological systems in the nanosecond and microsecond time scales [4,6]. Recent advances in instrumentation have extended the technique into the subnanosecond and picosecond time-domain [7,8]. Time-correlated single photon counting is a powerful method for measuring fluorescence decay curves with subnanosecond time resolution, excellent sensitivity and wide dynamic range. This method was employed in this work and is described in Section 4.3. The laser source, detector, timing electronics, and computer are then described in Section 4.4. The methods for data analysis and the effects of convolution are described in Section 4.4. The application of time-dependent fluorescence depolarization is presented in Chapter 7.

4.2 Theory

The derivation of the polarized components of the fluorescence at time t following excitation is very similar to the anisotropic absorption problem treated in Chapter 3. The intensity of the two orthogonal polarization components at time t after excitation can be written as

$$I_{\parallel}(t) = a \left\langle |\hat{\varepsilon}_i \cdot \hat{\mu}(0)|^2 \; |\hat{\varepsilon}_i \cdot \hat{\mu}(t)|^2 \right\rangle P(t) \tag{4.1a}$$

$$I_{\perp}(t) = \frac{a}{2} \left\langle |\hat{\varepsilon}_i \cdot \hat{\mu}(0)|^2 \; |\hat{\varepsilon}_i \times \hat{\mu}(t)|^2 \right\rangle P(t) \tag{4.1b}$$

where P(t) is the probability that a molecule excited at t = 0 is still excited at time t (the fluorescence decay law), a is a constant, and the other symbols have the same meaning as in Section 3.2. The first term

in each ensemble average is the probability that a molecule was excited at $t = 0$. The second term is the probability of observing an emitted photon at time t later through an analyzing polarizer with parallel or perpendicular orientation relative to the polarization of the exciting light. For an isotropic system these expressions have to be averaged over all equivalent directions of $\hat{\varepsilon}_i$ [3]. The averaging of the above expressions has already been performed in Appendix 3.1, since identical terms were involved in the derivation of the isotropic absorption saturation [see Eq. (3.4)].

The averaged expressions are

$$I_{\parallel}(t) = a\,[1 + 2r(t)]\,P(t) \tag{4.2a}$$

$$I_{\perp}(t) = a\,[1 - r(t)]\,P(t) \tag{4.2b}$$

where $r(t)$ is the reduced fluorescence anisotropy defined as

$$r(t) = \frac{2}{5} \left\langle P_2[\hat{\mu}(0)\cdot\hat{\mu}(t)] \right\rangle \tag{4.3}$$

The close formal similarity with anisotropic absorption saturation is obvious, since the definition for $r(t)$ is the same in each case and since the expressions for the polarized components of the fluorescence, Eq. (4.2), and for the polarization dependent transmission changes, Eq. (3.11), are identical. This theoretical equivalence underlines the physical similarity between these two phenomena; both involve photoselection with polarized light and subsequent randomization by molecular reorientation. However, it is important to note one difference. In Eq. (4.3) the ensemble averaged reorientation angle refers to the reorientation of electronically excited molecules, whereas the ground state

recovery involves a time-dependent mixture of both ground state and excited state reorientation. If the reorientation is the same in the ground and excited states, as was assumed in Section 3.2, and if the excited state decay law is the same as the ground-state recovery law (two-level approximation), then the expressions for the intensities $I_{\parallel}(t)$ and $I_{\perp}(t)$ are formally identical to those for $\Delta T_{\parallel}(t)$ and $\Delta T_{\perp}(t)$ except for a numerical factor.

The fluorescence anisotropy can be extracted from the measured intensities according to

$$r(t) = \frac{I_{\parallel}(t) - I_{\perp}(t)}{I_{\parallel}(t) + 2I_{\perp}(t)} \tag{4.4}$$

which again illustrates the close connection between ground-state recovery and fluorescence depolarization (compare Eq. (3.14)). The isotropic fluorescence decay can be measured at the magic angle 54.7° just as in the ground-state recovery,

$$I_{iso}(t) = I_{54.7}(t) = \frac{1}{3}\left(I_{\parallel}(t) + 2I_{\perp}(t)\right) = a\,P(t) \tag{4.5}$$

Thus the excited state decay kinetics can be monitored independently of molecular reorientation by observing the fluorescence through an analyzing polarizer oriented at 54.7° with respect to the polarization direction of the exciting light.

Equations (4.2), (4.4), and (4.5) are the main results of this section, and will be used in subsequent sections of this chapter and in Chapters 6 and 7.

4.3 Time-Correlated Single Photon Counting

Time-correlated single photon counting (TCSPC) is a technique for measuring the time-resolved fluorescence decay from samples repetitively excited with short pulses of light. The technique recognizes and utilizes the discrete nature of the fluorescence rather than attempting to measure a time-dependent average photon flux which is the basis of real-time measurements. In TCSPC the time intervals between excitation and the arrival of single photons at a photomultiplier are measured. This leads to a substantial improvement in time resolution compared with real-time measurements. The latter are limited by the rise and fall times of the photomultiplier, typically a few nanoseconds. However, measurement of the time interval between excitation and when the photomultiplier current pulse from a detected single photon reaches a certain amplitude is mainly limited by transit-time spread in the photomultiplier, which is typically 0.25 to 0.5 nsec, much less than the rise time or the duration of individual current pulses.

The idea of TCSPC is a simple one. A sample is excited by a short pulse of light. The excitation pulse also initiates the sweep of a time-to-amplitude converter (TAC). If a single fluorescent photon is detected during the sweep the TAC is stopped and an output voltage proportional to the time interval between the "start" signal and the "stop" signal is produced. The TAC output is processed by a pulse height analyzer (PHA) which records a count in a multichannel memory at a channel location dependent on the input voltage pulse amplitude. By repeating this sequence many times with a repetitive excitation source a histogram of the emission

probability versus time is built up in the PHA memory. This is just the fluorescence decay curve.

TCSPC was first developed in 1961 [9,10] and has been widely used since in time-resolved fluorescence measurements in the nanosecond region [11-14]. All the early work employed repetitively pulsed discharge lamps for excitation. The use of these sources led to several important experimental limitations: the flash duration was typically 2-3 nsec, so that subnanosecond lifetimes could not be measured; the excitation pulse shape was variable during the course of the experiment, leading to severe problems in deconvolution; the excitation intensity was rather low; the repetition rate was low; and, the excitation light could only be weakly focussed into the sample. Replacement of the discharge lamps with a CW mode-locked dye laser should alleviate all these traditional problems encountered in TCSPC. The picosecond pulse durations enable subnanosecond time-resolution, limited only by the transit time spread of the photomultiplier. The pulse train is extremely stable, making convolution at short times more reproducible. The repetition rate (82 MHz) is a factor of 10^4 higher than possible with discharge lamps. The high intensity and monochromatic output, which is also tunable if a synchronously mode-locked CW dye laser is used, are also important advantages. Some of these advantages have already been realized with the use of these lasers [15,16]. The system developed for use in this work is described in the following section.

4.4 Experimental Arrangement

The experimental setup for TCSPC is shown in Figure 4.1. The apparatus consists of three basic units: the excitation source, consisting of a mode-locked laser and external modulator; the optical and detection system; and, the timing electronics. Each of these units is discussed in detail below.

Excitation Source

The excitation source shown in Figure 4.1 is a mode-locked argon ion laser. However, a synchronously mode-locked CW dye laser was also used in some cases. Depending on the sample, either the 5145Å, Δt_p = 95 psec output of the argon laser, or the 5700-6200Å, Δt_p = 3 psec output of the dye laser could be used. The time resolution was approximately equal in either case, since the pulse duration made a small contribution to the overall width of the response function, which was dominated by transit-time jitter and electronic jitter in the STOP channel (see Section 4.5). The 82 MHz repetition rate of these lasers is too high for reliable operation of the TAC and also too high for many samples of interest, especially those with lifetimes comparable to the interpulse separation. Therefore an external acousto-optic modulator was used to reduce the repetition rate. The AO modulator (Spectra Physics model 365 cavity dumper) was driven by a lower repetition rate synchronized to the 82 MHz pulse train. Synchronization was achieved by focusing a small portion of the laser output onto a fast photodiode (HP 5082-4203), gating the resultant electrical pulses at the desired frequency with a fast linear gate and discriminator combination (ORTEC models LG101 and 436), and then

Figure 4.1

Experimental setup for time-correlated single photon counting. PMT = Amperex XP2020Q photomultiplier; HV = high voltage power supply; CFD = constant fraction discriminator; DISC = discriminator; TAC = time-to-amplitude converter; MCA = multichannel analyzer; GATE = fast linear gate; 250 KHz pulse generator; RF = driver for acousto-optic modulator. See text for details.

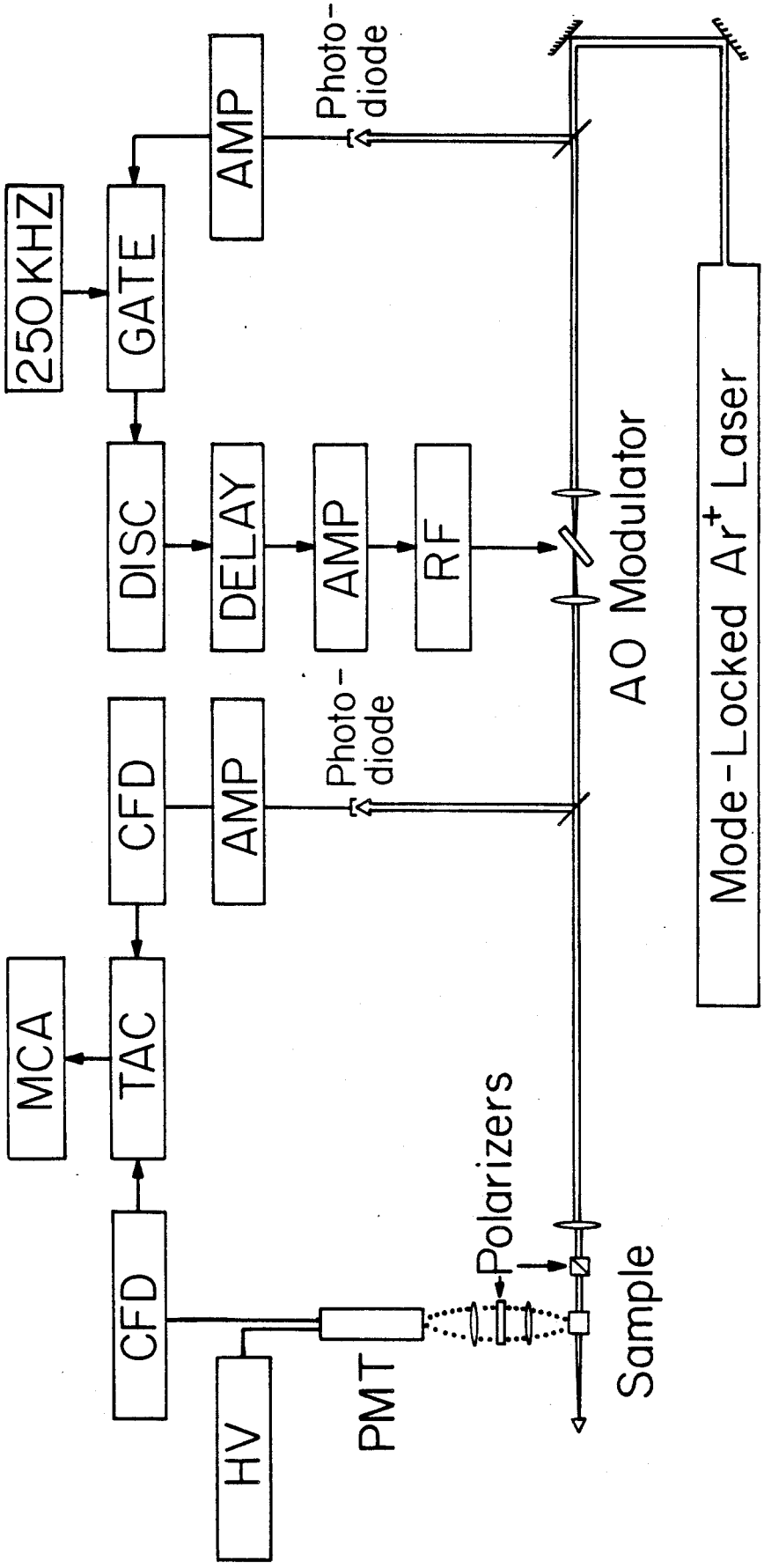
Mode-Locked Ar+ Laser
AO Modulator
Photo-diode
AMP
250 KHZ
GATE
DISC
DELAY
AMP
RF
Photo-diode
CFD
AMP
MCA
TAC
CFD
HV
PMT
Polarizers
Sample

using the gated pulses to trigger the RF driver (Spectra Physics model 465) via a variable delay (ORTEC model 425); see Figure 4.1. After careful optical alignment of the AO modulator and electrical synchronization, a contrast ratio between the main pulse and subsidiary pulses of better than 300:1 was routinely obtained. The excitation pulses were attenuated by a factor of about 1000 and passed through a vertical polarizer before being focussed into the sample with a 30 cm focal length lens. A small fraction of the excitation was focussed onto a second fast photodiode to provide the START signal for the TAC.

Optics and Detection

The sample was contained in a 1 cm quartz fluorescence cuvette. The excitation light was focussed to a line just behind the wall of one face of the cuvette. Fluorescence was collected in a 90° geometry from the same face with a large aperture quartz lens (f/1.25) and passed through a rotatable polarizer. A second quartz lens focussed the fluorescence onto the photocathode of a high-gain photomultiplier (Amperex XP2020Q). A calcite depolarizer and appropriate band pass filters to block scattered laser light were placed before the PMT. The entire optical and detection system was contained in a light-tight housing.

Timing Electronics

Photodiode pulses from the START channel were amplified by a wide bandwidth amplifier (HP 8447D) and input to a constant fraction discriminator (ORTEC model 473). The fast timing output of the CFD was connected to the START input of the TAC (ORTEC model 457). The PMT output was input to another constant fraction discriminator (ORTEC model 583) with

both adjustable upper and lower level limits. Careful adjustment of these levels prevented distortions due to multiple photon events and pulse pile-up [12]. The CFD output was connected to the STOP input of the TAC. The TAC outputs were processed and stored in a multichannel pulse-height analyzer (Tracor Northern TN1706) which was interfaced to a PDP 11/23 computer.

4.5 System Response

The time resolution of a TCSPC system is ultimately limited by the width of the system response function. Although lifetimes comparable to or shorter than this width can be estimated by deconvolution of the response function, the shortest lifetime that can accurately be measured still depends in some way on this width. The instrument response function was measured by scattering the laser pulses from a dilute suspension of milk. A typical response function of the system described in the previous section is shown in Figure 4.2. The FWHM of the peak is 250 psec. The peak is slightly asymmetric and there is evidence of a small subsidiary peak which is a common feature in response functions obtained in TCSPC [13]. The response function was dependent on the overall PMT bias voltage and the bias levels of the individual dynodes. Under some conditions the peak of the response function could be narrowed to 150 psec by adjustment of these levels. However, the response function in Figure 4.2 is more typical of that obtained in routine operation.

The main contributions to the width of the response function are the transit-time spread of the PMT, estimated to be in the range 150-190 psec [17], and time walk in the STOP CFD. Because the PMT produces a

Figure 4.2

Response function of the time-correlated single photon counting instrument obtained by scattering the excitation pulses from a dilute milk solution. The apparent FWHM of the peak is 270 psec. The true FWHM of 250 psec is obtained after deconvolution of the argon ion laser pulse duration (95 psec).

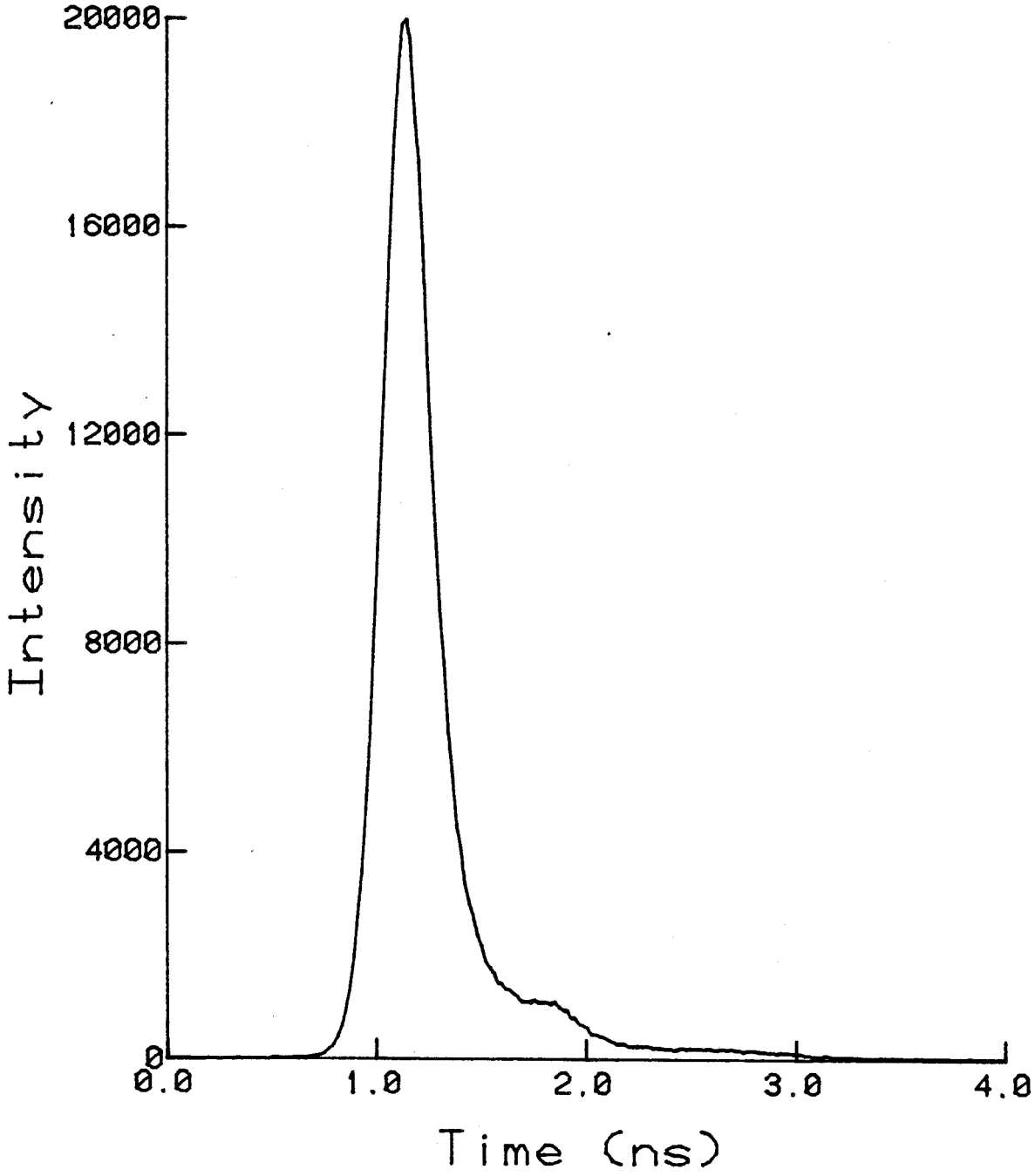
20000
16000
12000
8000
4000
0
Intensity
0.0
1.0
2.0
3.0
4.0
Time (ns)

distribution of single photon pulse amplitudes due to the statistical nature of the electron multiplication process, there will result a timing spread or "walk" in the STOP discriminator. The walk is minimized with constant fraction timing for a given input pulse distribution. The time walk in the START channel is much smaller, since a photodiode was used in a non-photon-counting mode, with a consequently much narrower pulse height distribution. Assuming that the lower estimate of the transit time jitter of the XP2020Q quoted above is correct, the observation of a system response function with FWHM as narrow as 150 psec implies that the time walk in the STOP discriminator was very small, certainly much less than 100 psec.

4.6 Data Analysis

To measure excited state decay kinetics only, as done in Chapters 6 and 7, the isotropic fluorescence decay curve measured at 54.7° is recorded and then fit to a single exponential, sum of exponentials, or more complicated decay law, depending on the sample. All three situations will be covered in later chapters.

For the analysis of fluorescence depolarization data the experimental sum and difference curves are first formed,

$$s(t) = i_{\parallel}(t) + 2i_{\perp}(t) \tag{4.6a}$$

$$d(t) = i_{\parallel}(t) - i_{\perp}(t) \tag{4.6b}$$

respectively. These functions were taken to be of the form

$$s(t) = A \exp(-t/\tau) \tag{4.7a}$$

$$d(t) = r(t) \cdot s(t) \tag{4.7b}$$

where $r(t)$ is defined by the particular model being used to interpret the

molecular reorientation (see Chapter 7 for an example), A is an amplitude parameter, and τ is the fluorescence lifetime. Usually r(t) will contain at least one variable parameter such as the rotational diffusion coefficient. The total set of parameters is adjusted so as to simultaneously obtain the best fit of the experimental s(t) and d(t) curves to the model defined by Eq. (4.7). The curve fitting was performed on a PDP 11/23 computer using a nonlinear least squares routine discussed in Appendix II. The quality of the fits was judged by the reduced chi-squared (χ_r^2) criterion and by inspection of the weighted residuals and the residual autocorrelation function (see Appendix II for details).

The above discussion has not mentioned the effects of the system response function, and the procedure outlined above is only valid when the decay data span a time scale much longer than the width of the response function. This is often true in practice. However, on shorter time scales, in this case shorter than 1 nsec, the effects of the response function must be included in the analysis. In general, the experimental intensity i(t) is related to the "ideal intensity" I(t) obtained for an impulse response by the convolution integral,

$$i(t) = \int_0^t I(t-t')\, g(t')\, dt' \tag{4.8}$$

where g(t') is the normalized system response function. Since g(t') can be independently measured, it is possible to evaluate the convolution integrals numerically. The model in this case is, instead of Eq. (4.7),

$$s(t) = A \int_0^t \exp(-(t-t')/\tau)\, g(t')\, dt' \tag{4.9a}$$

$$d(t) = \int_0^t r(t-t')\, s(t-t')\, g(t')\, dt' \qquad (4.9b)$$

With these modifications, the data analysis is performed in exactly the same manner as described above.

References - Chapter 4

1. F. Perrin, J. Phys. Radium 5, 497 (1934).
2. G. Weber, Biochem. J. 51, 145 (1952).
3. R. G. Gordon, J. Chem. Phys. 45, 1643 (1966).
4. T. Tao, Biopolymers 8, 609 (1969).
5. T. J. Chuang, K. B. Eisenthal, J. Chem. Phys. 57, 5094 (1972).
6. J. Yguerabide, Meth. Enzym. 26, 498 (1972).
7. G. R. Fleming, J. M. Morris, G. W. Robinson, Chem. Phys. 17, 91 (1976).
8. K. G. Spears, L. E. Cramer, Chem. Phys. 30, 1 (1978).
9. L. M. Bollinger, G. E. Thomas, Rev. Sci. Instrum. 32, 1044 (1961).
10. Y. Koechlin, A. Raviart, Nucl. Instrum. Meth. 29, 45 (1964).
11. A. E. W. Knight, B. K. Selinger, Aust. J. Chem. 26, 1 (1973).
12. W. R. Ware, in Creation and Detection of the Excited State, Vol. 1, Part A, A. Lamola, ed., Dekker, New York, 1971.
13. C. Lewis, W. R. Ware, L. J. Doemeny, T. L. Nemzek, Rev. Sci. Instrum. 44, 107 (1973).
14. J. B. Birks, I. H. Munro, Progress in Reaction Kinetics, Vol. 4, (1967), p. 239.
15. K. G. Spears, L. E. Cramer, L. D. Hoffland, Rev. Sci. Instrum. 49, 255 (1978).
16. V. J. Koester, R. M. Dowben, Rev. Sci. Instrum. 49, 1186 (1978).
17. R. J. Robbins, Ph.D. Thesis, University of Melbourne (1980).

PART II

APPLICATIONS

Chapter 5

ANOMALOUS ROTATIONAL DIFFUSION OF CRESYL VIOLET*

5.1 Introduction

Molecular reorientation in solution results from the random time-varying torques caused by frequency collisions with surrounding solvent molecules. Studies of this phenomenon are expected to provide information on solute-solvent interactions in the liquid state, as well as information on the size and shape of the solute molecule. Molecular reorientation in liquids has been studied by a wide variety of physical techniques including magnetic resonance [2], dielectric relaxation [3], neutron scattering [4], Raman scattering [5], and depolarized Rayleigh scattering [6]. However, all of these methods operate in the frequency domain and the reorientation dynamics are obtained indirectly by Fourier transformation to the time domain. Recently, picosecond spectroscopic techniques have provided a means for measuring the reorientation directly in the time domain. Both anisotropic absorption saturation [1,7-9] (ground state recovery) and time-dependent fluorescence depolarization [10, 11] techniques have been applied to study the reorientation of large organic molecules (usually dyes) in a variety of solvents. As shown in Chapters 3 and 4, both time-domain techniques measure the "rotational correlation function" given by $\langle P_2[\hat{\mu}(0)\cdot\hat{\mu}(t)]\rangle$.

*The work in this chapter was first reported in reference [1].

A detailed interpretation of picosecond time-domain reorientation data requires an understanding of the relationship between the rotational correlation function and the molecular properties such as size and shape, and the solute-solvent interactions. In this regard there are several important questions of current interest: (1) Can this relationship be provided by macroscopic classical hydrodynamics? (2) Under what conditions can hydrodynamics be applied? (3) What boundary condition must be imposed to solve the Navier-Stokes hydrodynamic equation? (4) How does the boundary condition relate to the nature of the solute-solvent interactions? Answers to these questions are beginning to emerge from the picosecond work. However, only a few molecules have been studied so far, and it is important to extend the study to as many different molecules as possible before general conclusions can emerge. For example, the picosecond work performed before this work was begun had implied that hydrodynamic behavior was correlated with solute charge, the rotation of monocation solutes being in agreement with hydrodynamics, whereas dianions rotate more slowly than predicted by hydrodynamics. However, the study of cresyl violet reorientation reported in this work finds anomalously slow rotation also, even though cresyl violet is a monocation. The data are presented in the following section, and then discussed in relation to the questions raised above and also compared with literature data for other solute molecules.

5.2 Results

Ground state recovery (GSR) data were obtained using the apparatus described in Chapter 3. The excitation source was the passively mode-

locked CW dye laser described in Chapter 2. A typical set of data for a methanol solution of cresyl violet is shown in Figure 5.1. The sharp peaks at zero delay are due to the coherent coupling effect discussed in Chapter 3. Comparing the coherent spikes in Figure 5.1 with the hypothetical curves shown in Figure 3.3 implies that the case $\Delta t_c < \Delta t_p$ is being observed here; that is, the laser pulses used to obtain the data in Figure 5.1 were not perfectly mode-locked. The other important features of the data in Figure 5.1 can be summarized as follows:
(i) $\Delta T_{\parallel}^{incoh}(0) = \Delta T_{\parallel}^{coh}(0)$; (ii) $\Delta T_{\perp}^{incoh}(0) = \Delta T_{\perp}^{coh}(0)$; and
(iii) $\Delta T_{\parallel}^{incoh}(0) = 3\Delta T_{\perp}^{incoh}(0)$. All these equalities are satisfied to within a few percent. Observation (i) is expected from the coherent coupling theory presented in Chapter 3, Eq. (3.29). Observation (ii) is expected from the coherent coupling theory in the case of molecular rotation, that is "slow" compared with the pulse duration, which is evidently the case here. Observation (iii) implies that r(0) attains its maximal value in this system, r(0) = 0.4. Thus the experimental data for cresyl violet confirm all the predictions of the theory developed in Chapter 3.

A log plot of the dichroism $\Delta T_{\parallel} - \Delta T_{\perp}$ is presented in Figure 5.2. From Eq. (3.13) the theoretical dichroism is

$$\Delta T_{\parallel}(t) - \Delta T_{\perp}(t) = 3\sigma^2 N\ell I T_o r(t) e^{-t/\tau} \tag{5.1}$$

where $\tau = 1/k$ is the ground state recovery time. The linearity of the log plot in Figure 5.2 implies that the anisotropy decay is exponential in this system,

$$r(t) = 0.4\, e^{-t/\tau_{rot}} \tag{5.2}$$

Figure 5.1

Ground state recovery curves of cresyl violet (1.0×10^{-3}M) in methanol for two different probe beam polarization directions; parallel to the pump beam (upper curve), and perpendicular to the pump beam (lower) curve).

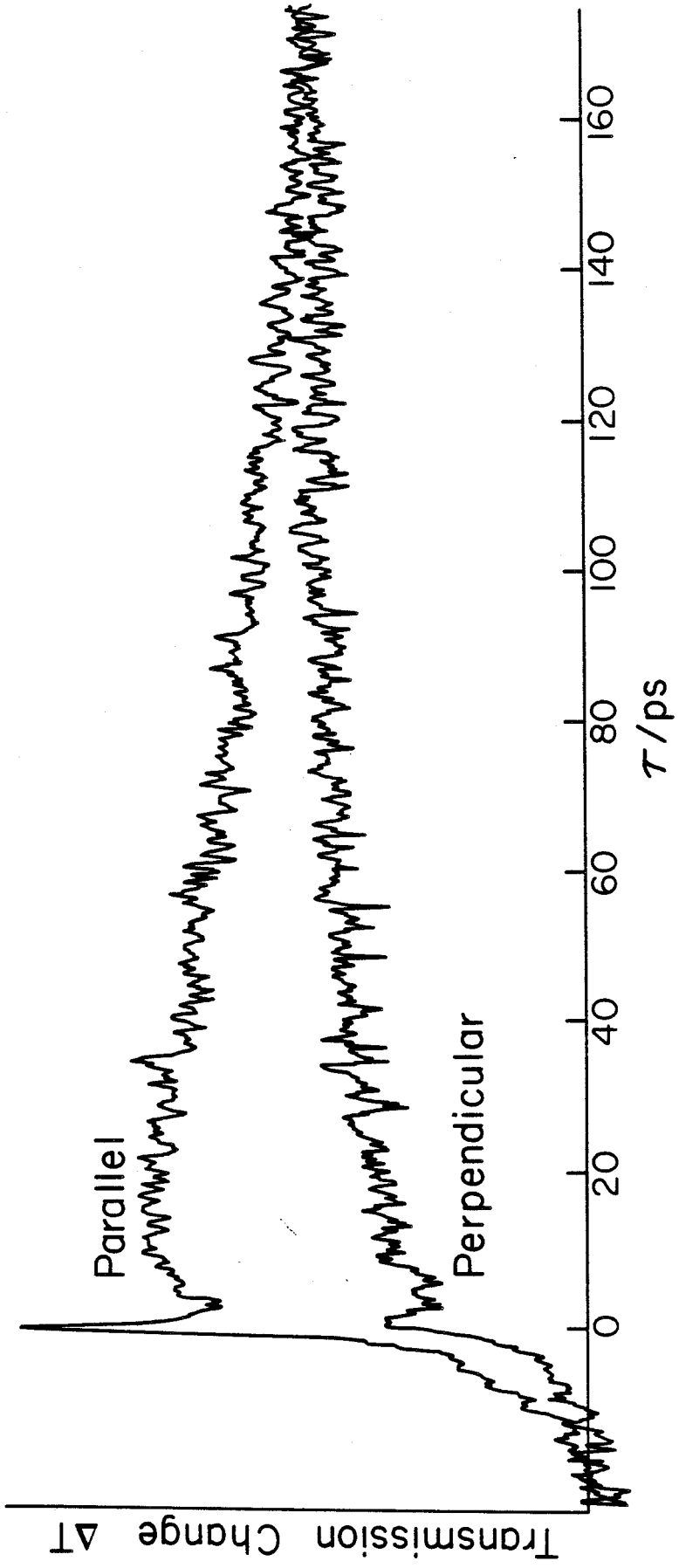
Transmission Change ΔT
Parallel
Perpendicular
0
20
40
60
80
100
120
140
160
τ / ps

Figure 5.2

Semi-log plot of the dichroism, $\log[\Delta T_{//}(t) - \Delta T_{\perp}(t)]$ against t, for the data shown in Figure 5.1. Note the linear relationship which indicates that the rotational correlation function follows a single exponential decay.

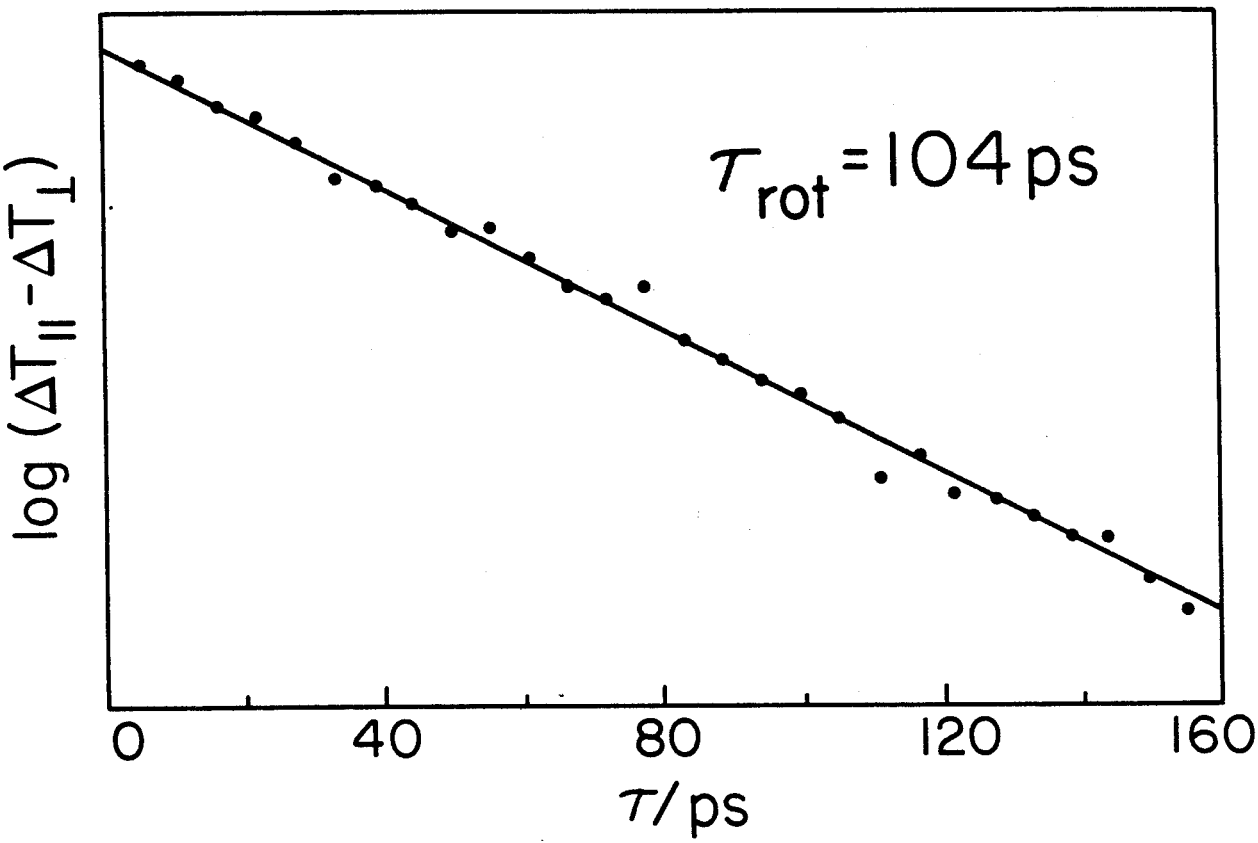
τ_{rot} = 104 ps
log ($\Delta T_{\parallel} - \Delta T_{\perp}$)
0
40
80
120
160
τ/ ps

The slope of the log plot of $\Delta T_{\parallel} - \Delta T_{\perp}$ in Figure 5.2 is thus $\tau_{rot}^{-1} + \tau^{-1}$. The excited state lifetime of cresyl violet was measured from the isotropic (54.7°) fluorescence decay curve obtained by time-correlated single photon counting (Chapter 4). The result was $\tau = 3160 \pm 15$ psec for cresyl violet in methanol. The isotropic GSR curve, measured over a long delay range, gave essentially the same result, $\tau = 3.2 \pm 0.4$ nsec, although the accuracy was much poorer. This is because GSR techniques are best suited to short time delay ranges. However, it is clear that the excited state lifetime and ground state recovery time are equal within experimental error in this system. This is an important check, since the theory in Chapter 3 is only valid in this limit. The more accurate fluorescence lifetime was used to estimate τ_{rot} from the slope of the experimental log plots.

The rotational relaxation times of cresyl violet in a number of simple alcohols are presented in Table 5.1. The dependence of τ_{rot} on bulk viscosity is shown in Figure 5.3, together with a theoretical line predicted from hydrodynamics in the "stick" limit (more will be said about this later). The data fall very close to a straight line with zero intercept and a slope of 180 ps/cpoise. The rotational relaxation time was independent of solute concentration for concentrations less than 1.0×10^{-3} M. At higher solute concentrations, the apparent value of τ_{rot} decreased with increasing concentration. Energy transfer from an excited molecule aligned by the excitation pulse to a randomly oriented unexcited molecule contributes to the dichroism decay at such high solute concentrations. The solute concentration was kept less than 10^{-3} M to avoid this artefact.

TABLE 5.1

ROTATIONAL RELAXATION TIMES OF CRESYL VIOLET

Solvent	η (cpoise)	τ_{rot} (psec)
Methanol	0.60	104 ± 7
Ethanol	1.20	220 ± 25
Iso-propanol	2.37	445 ± 25
N-butanol	2.95	560 ± 50

Figure 5.3

Viscosity dependence of the measured rotational relaxation times of cresyl violet. The broken line is an empirical linear regression fit to the data with zero intercept and a slope of 180 psec/cpoise. The solid line is the prediction of "stick" hydrodynamics, and was calculated for an oblate rotor with a volume equal to the molecular volume of cresyl violet. The calculation is discussed in the text.

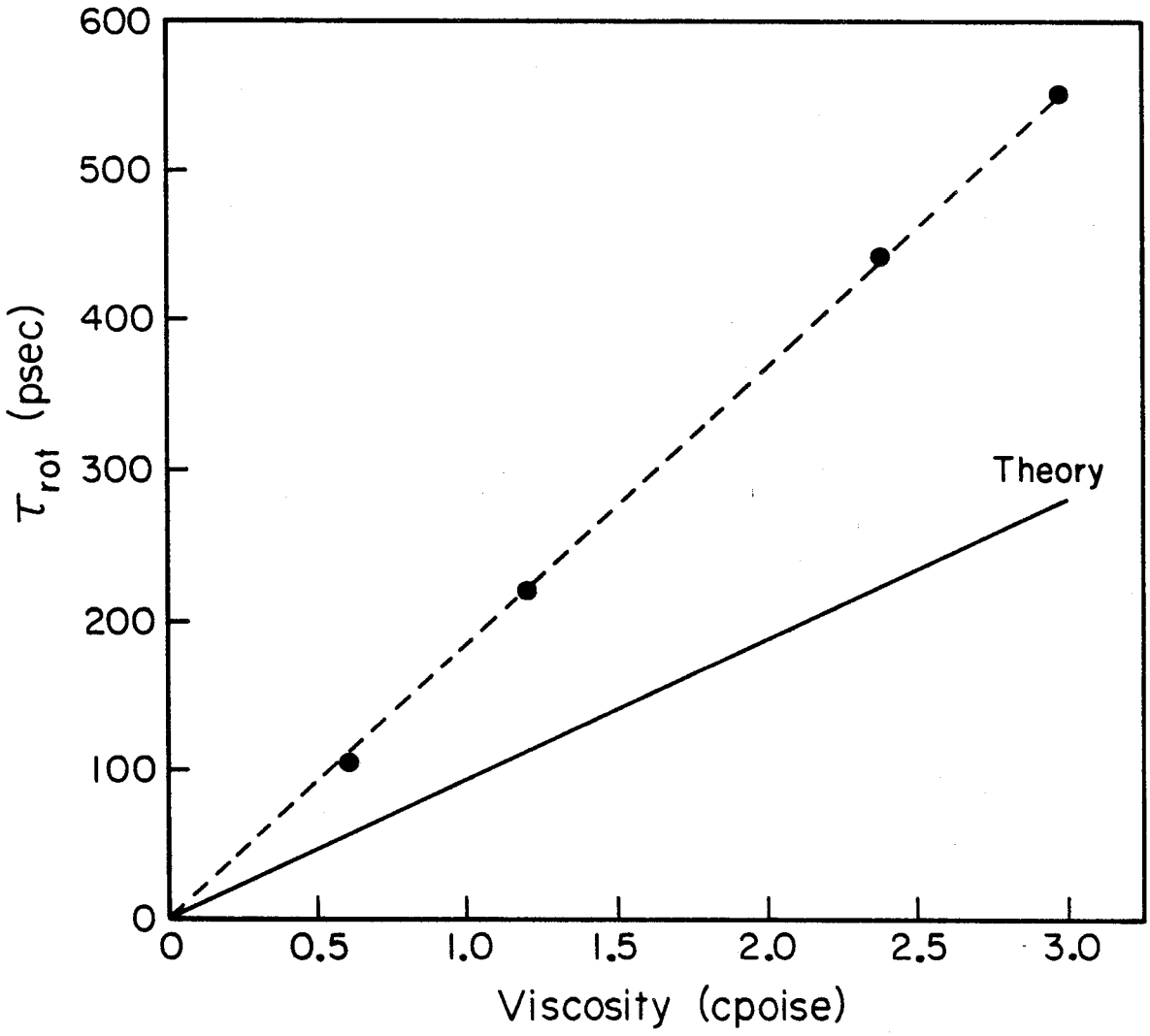
600
500
400
300
200
100
0
τ_{rot} (psec)
Theory
0
0.5
1.0
1.5
2.0
2.5
3.0
Viscosity (cpoise)

5.3 Hydrodynamic Calculations

The important experimental result is that the rotational correlation function exhibited a single exponential decay, $\langle P_2[\hat{\mu}(0)\cdot\hat{\mu}(t)]\rangle = e^{-t/\tau_{rot}}$, with a relaxation time which was linearly dependent on the solvent viscosity. It is interesting to consider to what extent theoretical models can account for these findings. First, the rotational correlation function must be related to molecular properties, usually through the choice of a model. The most appropriate model for the reorientation of large molecules in low viscosity organic solvents is the rotational diffusion model. This model describes the reorientation as a random succession of infinitesimally small angular displacements; that is, the rotational motion is diffusional. An expression for the rotational correlation function in terms of the principal diffusion coefficients of the molecule can be derived from the solution of the rotational diffusion equation. The general result is that the rotational correlation function of a totally asymmetric molecule contains five exponential decay components, with the decay constants involving various combinations of the principal diffusion coefficients [13]. When the molecule possesses some symmetry and when the transition dipole is parallel or perpendicular to a symmetry axis, fewer exponentials are observed. The next step in the analysis is to relate the principal diffusion coefficients to the size and shape of the molecule and to the solute-solvent interactions. It is at this point that the question of hydrodynamics enters. Ideally one would like to calculate the diffusion coefficients from a microscopic model of the solute-solvent interactions. This is an extremely difficult theoretical problem that has yet to be completely solved, although important progress has been made [14,15]. Thus

one resorts to models, the most developed of which is classical hydrodynamics. This is a macroscopic approach, wherein the solute is considered as a smooth rigid body immersed in a continuous fluid. The Navier-Stokes equation for steady flow is solved to find the friction exerted by the fluid on the body. A boundary condition must be imposed at the interface between the body and the fluid to solve this equation. The question of the appropriate boundary condition is another point of current interest. Two limiting cases have been identified: the so-called "stick" and "slip" limits. The "stick" boundary condition requires that the tangential component of the fluid velocity relative to the body must be zero everywhere on the surface of the body [16,17]. In effect this means that the fluid layer adjacent to the body rotates with the body.

The "slip" boundary condition requires that the tangential component of the stress imposed by the fluid must be zero everywhere on the body [17]. The principal rotational diffusion coefficients can be calculated analytically in the "stick" limit [16] and numerically in the "slip" limit [17]. From this qualitative discussion it seems reasonable that the diffusion coefficients calculated in the "slip" limit will be larger than the corresponding values in the "stick" limit. That is, the "slip" limit leads to less friction on the body than the "stick" limit. Diffusion coefficients calculated from molecular dynamics simulations of hard sphere fluids are in good agreement with "slip" hydrodynamics [18]. The rotational relaxation data for relatively small molecules in nonpolar solvents are also in good agreement with "slip" hydrodynamics [19]. The dyes BBOT [12], acridine orange [20], and pyronine G [20] also appear to exhibit "slip" limit behavior. However, several other dyes exhibit "stick"

limit behavior, or rotation that is even slower than predicted by "stick" hydrodynamics [10-12]. Thus the question of the most appropriate boundary condition is still open, and both limits should be considered when analyzing data for a new molecule.

The conditions under which the rotational diffusion model predicts a single exponential decay for the rotational correlation function are now considered. There are three cases to be considered:

(i) Spherical rotor

If the molecule rotates as a spherical rotor, the rotational diffusion model predicts [13],

$$\left\langle P_2[\hat{\mu}(0)\cdot\hat{\mu}(t)]\right\rangle = \begin{cases} e^{-6D_{SE}t} & \text{"stick limit"} \quad (5.3a) \\ \delta(t) & \text{"slip" limit} \quad (5.3b) \end{cases}$$

where D_{SE} is the rotational diffusion coefficient calculated from the Stokes-Einstein equation [21] of classical "stick" hydrodynamics:

$$D_{SE} = kT / 6V\eta \qquad (5.4)$$

V is the molecular volume, η is the solvent viscosity, T is the absolute temperature, and k is Boltzmann's constant. The rotational relaxation time is $\tau_{rot} = (6D_{SE})^{-1}$, or, using Eq. (5.4),

$$\tau_{rot} = \begin{cases} V\eta/kT & \text{"stick" limit} \quad (5.5a) \\ 0 & \text{"slip" limit} \quad (5.5b) \end{cases}$$

A linear dependence of τ_{rot} on viscosity is predicted in the "stick" limit. Rotation is infinitely fast for a sphere in the "slip" limit.

(ii) Prolate symmetric rotor

Only in the case where the transition dipole lies parallel to the long axis does a single exponential decay result [13]

$$\left\langle P_2[\hat{\mu}(0)\cdot\hat{\mu}(t)]\right\rangle = e^{-6D_\perp t} \qquad \text{"stick and "slip" limits} \qquad (5.6)$$

where $D_\perp$ is the diffusion coefficient for rotation about the axes transverse to the long axis. This diffusion coefficient is related to the Stokes-Einstein result by

$$D_\perp = D_{SE} / f_\perp^p \qquad (5.7)$$

where $f_\perp^p$ is a geometrical shape factor [22] for a prolate symmetric rotor. The rotational relaxation time in this case can be written as

$$\tau_{rot} = f_\perp^p \cdot \frac{V\eta}{kT} \qquad \text{"stick" and "slip" limits} \qquad (5.8)$$

which is also proportional to viscosity. f^p has a smaller value in the "slip" limit than in the "stick" limit.

(iii) Oblate symmetric rotor

In this case the transition dipole is most often perpendicular to the principal symmetry axis (i.e., the dipole is in the molecular plane). The rotational correlation function in this case is [13],

$$\left\langle P_2[\hat{\mu}(0)\cdot\hat{\mu}(t)]\right\rangle = \begin{cases} \frac{1}{4} e^{-6D_\perp t} + \frac{3}{4} e^{-(2D_\perp + 4D_\parallel)t} \simeq e^{-(3D_\parallel + 3D_\perp)t} & \text{"stick"} \\ e^{-6D_\perp t} & \text{"slip"} \end{cases} \qquad (5.9a,b)$$

where $D_\parallel$ is the diffusion coefficient for rotation about the principal axis

and $D_\perp$ about the transverse axes. The approximation in Eq. (5.9a) is accurate to within a few percent for most oblate rotors because $D_\parallel$ and $D_\perp$ are very similar in magnitude. Thus an <u>effective</u> single exponential decay occurs in the "stick" limit.

The rotational relaxation times are given by

$$\tau_{rot} = \begin{cases} (3D_\parallel + 3D_\perp)^{-1} = \left(\frac{1}{2f_\parallel^o} + \frac{1}{2f_\perp^o}\right)^{-1} \cdot \frac{Vn}{kT} & \text{"stick"} \quad (5.10a) \\ (6D_\perp)^{-1} = f_\perp^o \cdot Vn/kT & \text{"slip"} \quad (5.10b) \end{cases}$$

where $f_\parallel^o$ and $f_\perp^o$ are shape factors for the oblate rotor [23] calculated with the appropriate choice of boundary conditions. A linear viscosity dependence is also predicted in this case.

In applying these models to cresyl violet some approximations concerning the shape are necessary. A space-filling scale model of cresyl violet reveals that the molecule does not correspond exactly to any of the three choices above. The best approximation is an ellipsoid with semi-axes $a = 7.0\text{Å}$, $b = 4.4\text{Å}$, and $c = 1.7\text{Å}$. The volume of this ellipsoid is 218Å^3, in excellent agreement with the molecular volume $V = 217\text{Å}^3$ calculated from the atomic increments [22]. However, the calculation of the shape factors must be done numerically in this case, so in order to simplify the calculations, the shape is approximated by the simple shapes considered above. The sphere is probably the worst approximation, nevertheless this possibility is included for comparison. The radius $a = 3.74\text{Å}$ was assumed in the calculation, since it is important that the volume of the sphere equal the true molecular volume ($4/3\pi a^3 = 217\text{Å}^3$). The prolate and oblate rotors provide reasonable approximations, with the oblate geometry probably being more

meaningful for cresyl violet. For a prolate rotor the approximate dimensions are a = 7Å, b = c = 2.7Å ($V = 217Å^3$), while for an oblate rotor, a = b = 5.5Å, c = 1.7Å ($V = 217Å^3$). The shape factors were calculated from standard equations in the "stick" limit [23], and from numerical tabulations in the "slip" limit [17]. The results presented in Table 5.2 are the calculated values of the rotational relaxation time in the "stick" limit τ^{stick} and in the "slip" limit τ^{slip}. The "stick" limit result for the oblate rotor is also shown in Figure 5.3. Also included in Table 5.2 are calculated values of the "stickiness factor," a quantity defined by [24]

$$S \equiv \frac{\tau_{rot} - \tau^{slip}}{\tau^{stick} - \tau^{slip}} \tag{5.11}$$

where τ_{rot} is the experimental rotational relaxation time, and τ^{stick} and τ^{slip} are relaxation times calculated in the "stick" and "slip" limits of classical hydrodynamics. From this definition it is clear that S = 0 in the "slip" limit, and S = 1 in the "stick" limit. These are the two extreme values that are consistent with hydrodynamics. Intermediate values imply hydrodynamic behavior with friction intermediate between the "slip" and "stick" values. This is a most useful parameter which neatly summarizes the important information concerning the boundary condition.

5.4 Discussion

The results in Table 5.2 show that the hydrodynamic calculations are fairly insensitive to the choice of geometry. The calculated "stick" rotational relaxation times are very similar, around 95 ps/cpoise, almost a factor of two smaller than the apparent slope of the data in Figure 5.3

TABLE 5.2

Geometry†	τ^{stick} (ps/cpoise)	τ^{slip} (ps/cpoise)	τ_{rot} (ps/cpoise)	S*
Sphere $a = 3.74\text{Å}$	99.4	0	180	1.81
Prolate rotor $7\text{Å} \times 2.7\text{Å} \times 2.7\text{Å}$	99.4	36.2	180	2.27
Oblate rotor $5.5\text{Å} \times 5.5\text{Å} \times 1.7\text{Å}$	92.4	47	180	1.95

†Molecular volume = 217Å^3 in all cases

*$S = (\tau_{rot} - \tau^{slip}) / (\tau^{stick} - \tau^{slip})$

(compare the data and theory line in Figure 5.3). The spherical rotor has zero rotational relaxation time in the "slip" limit, but as argued above, this geometry is not to be taken too seriously. The prolate rotor has a slightly faster relaxation in the "slip" limit than does the oblate rotor. The most striking results in the table are the anomalous values of the "stickiness factor." The results are very similar in each case, $S = 2.0 \pm 0.2$. The conclusion is independent of how the calculation was done: nonhydrodynamic behavior is exhibited by cresyl violet in alcohol solvents. The rotation is a factor of two slower than predicted by "stick" hydrodynamics.

Previous studies attempted to correlate the "stickiness factor" with the sign and magnitude of the solute charge [12,25]. This correlation was based on studies of several dye molecules which appeared to indicate that $S \simeq 2$ for dianion solutes [10,26], $S \simeq 1$ for monocation solutes [12,25,27], and $S \simeq 0$ for neutral solutes [12,20]. The present results clearly demonstrate that $S = 2$ is possible for a monocation. This is an important result of the present work, and indicates that the correlation mentioned above is not true in general. Clearly, other factors beside electrical charge are important. In relation to the anomalously slow rotation of xanthene dye dianions, it was suggested that specific, strong solute-solvent interactions (such as hydrogen bonding) lead to solvent attachment [10]. The molecular volume is effectively increased due to bound solvent molecules according to this hypothesis. Spears and Cramer [26] proposed a slightly different interpretation of their rotational relaxation data on the xanthene dianion Rose Bengal. According to their "solvent torque model" the anomalously slow rotation of Rose Bengal was a deviation from the "slip" limit caused

by drag introduced by specific solvent interactions at special sites in the molecule, in this case H-bonding sites. This model differs in that H-bonding causes a perturbation on the normal friction coefficients established by slip boundary conditions rather than an actual attachment of solvent. "Slip" hydrodynamics is considered to be the fundamental behavior characteristic of non-interacting solute molecules according to the solvent torque model. This assertion is based on the success of "slip" hydrodynamics in the case of hard sphere fluids [18], nonpolar systems [19], and neutral dyes [12,20] mentioned previously. The observation of $S \simeq 1$ is not given special significance in the solvent torque model, since "slip" rather than "stick" is considered to be the fundamental behavior.

The structure of cresyl violet shown in Figure 5.4 reveals that there are several sites for hydrogen bonding interactions. The terminal amino groups provide both hydrogen donor and acceptor sites, while the central N and O atoms provide hydrogen acceptor sites. Solvent attachment or solvent torque at the amino groups would be particularly effective in slowing reorientation, since these sites are located at the extrema of the molecule. This is the most plausible explanation for the anomalously slow reorientation of cresyl violet in alcohol solvents. Either solvent attachment [10] or solvent torque [26] could be responsible for this behavior. Hydrogen bonding will also occur at the N and O atoms in the central ring, but will be less effective in retarding rotation because the attached solvent is closer to the center-of-mass of the molecule.

One consequence of the solvent attachment hypothesis is that the deviation will depend on the size of the solvent. Perhaps when the solvent

Figure 5.4

Chemical structure of cresyl violet. The circled amino groups are likely sites for hydrogen bonding interactions with the solvent. Interactions at these sites would cause the most retardation of molecular reorientation.

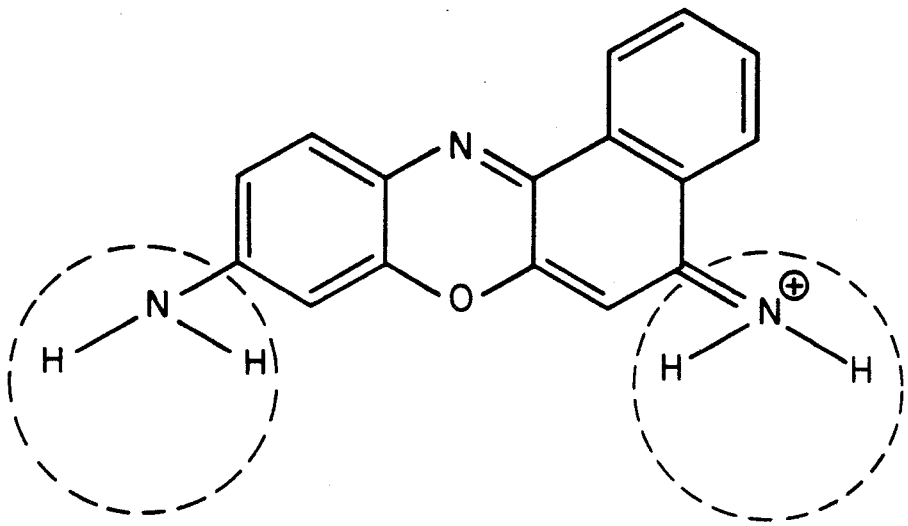
N
O
N
H
H
N⊕
H
H

molecule is much smaller than the solute, solvent attachment does not lead to much retardation. A recent report of τ_{rot} for cresyl violet in water is interesting in this respect [20]; the reported value was τ_{rot} = 75 psec, which together with the τ^{stick} and τ^{slip} values calculated here imply that S = 0.97 in water. The results for a few alcohols given in the same report [20] showed S ≃ 2, consistent (but not in perfect agreement) with our results. More will be said later about comparisons with recent work on cresyl violet. The fact that S ≃ 1 for water, while S ≃ 2 for alcohols is consistent with the smaller size of the water molecule. However, the results obtained in this work showed that S = 2.0 in <u>all</u> the alcohol solvents methanol through butanol in which the solvent size is clearly increasing. This observation is inconsistent with the solvent attachment hypothesis, but is expected in the solvent torque model, since it is the strength of the H-bonding interaction that is important here rather than solvent size, and the interaction strength is of course not expected to change in this series of simple alcohols. The observation of S ≃ 1 for cresyl violet in water [20] can also be explained within the context of the solvent torque model, since Spears and Cramer [26] point out that in those solvents where appreciable coordination, or structuring, occurs around the solute, the solvent drag is reduced by the shielding effect of the coordination layer. Thus water, which is a more highly structured solvent than the alcohols, allows a faster rotation of cresyl violet. The coordination is not envisaged as a rigid coordination layer, which is essentially equivalent to solvent attachment, but some average coordination. The dynamic coordination complex discussed by Chuang and Eisenthal

[7] in which the hydrogen bonds are rapidly breaking and reforming, and which allow considerable orientational freedom of the solute, is an appropriate description in this case. The solvent torque model appears to give the best explanation for the rotation of cresyl violet in both alcohols and in water.

An important conclusion of this work is that when H-bonding sites exist, particularly near the ends of a molecule, hydrodynamics cannot be applied and $S \simeq 2$ will be observed. But how is it that $S \simeq 1$ [12,26,28] and $S \simeq 0$ [12,20] have been reported for many other dyes that also appear to contain H-bonding sites? Examination of the structures of these dyes show that they all contain hydrogen acceptor sites only, and that these sites are always sterically hindered by methyl and ethyl groups. Solvent interaction is less likely in these molecules, although some solute-solvent interactions may still be present. Perhaps hydrogen-bonding interactions are the single most important factor in determining molecular rotation in H-bonding solvents. The bulk of the picosecond data can be interpreted in this way, although more data on differently substituted dyes would be useful to test the generality of this concept. A critical experiment designed to provide such a test is discussed in Proposition 3.

Since the publication of the present results in 1979 [1], a few other groups have reported rotational relaxation times for cresyl violet. The data are summarized in Table 5.3. The only solvent common to all studies was ethanol, and hence only the results for this solvent are given in Table 5.3. The value of τ_{rot} reported by Waldeck et al. [27] is in excellent agreement with the value obtained in this work, while the value reported by von Jena and Lessing [20] lies just outside the (combined)

TABLE 5.3

Comparison of Experimental Determinations of the Rotational Relaxation Time of Cresyl Violet in Ethanol

Report	τ_{rot} (psec)	Ref.
Millar et al., 1979	220 ± 25	[1]
Waldeck et al., 1981	223 ± 10	[27]
von Jena and Lessing, 1981	300 ± 25	[20]
Beddard et al., 1981	350 ± 14	[28]

error range. The value reported by Beddard et al. [28] is, however, much larger than the present value. It is significant that the first three values in Table 5.3 were obtained by anisotropic absorption saturation, whereas Beddard et al. [28] used fluorescence depolarization. Because the ground state recovery time of cresyl violet $\tau = 3160$ psec is much longer than the rotational relaxation time in Table 5.3, the absorption experiments are probing ground state rotational dynamics almost exclusively. Fluorescence depolarization only probes excited state rotational dynamics. It is possible, therefore, that the discrepancy between the value of the rotational relaxation time measured in this work and that reported by Beddard et al. [28] is actually due to a slower rotation in the excited state, which could be caused by stronger H-bonding interactions in the excited state. Nevertheless, despite this difference, the qualitative conclusion inferred from the values in Table 5.3 is the same; that rotational diffusion of cresyl violet in ethanol is anomalously slow.

5.5 Conclusions

This study has revealed that the rotational relaxation of cresyl violet in alcohol solvents is anomalously slow, being characterized by a "stickiness factor " $S = 2.0$. Classical hydrodynamic behavior is not observed in this system. The anomalous behavior is most likely due to solvent drag at the terminal amino groups due to specific hydrogen bonding interactions. An important conclusion is that $S \simeq 2$ can be observed for cation solutes, in contrast with earlier work, and it is suggested that the presence or absence of specific H-bonding interactions in a particular

molecule is a more important factor in determining the "stickiness" than the magnitude or sign of the molecular charge. Comparisons of this work and other results in the literature suggest that hydrodynamic behavior will only be observed when the H-bonding sites are sterically hindered or absent.

References - Chapter 5

1. D. P. Millar, R. Shah, A. H. Zewail, Chem. Phys. Lett. 66, 435 (1979).
2. J. Jonas, Ann. Rev. Phys. Chem. 26, 167 (1975).
3. N. E. Hill, W. Vaughan, A. H. Price, M. Davies, Dielectric Properties and Molecular Behavior, Van Nostrand, New York, 1969.
4. K. Carneiro, J. P. McTague, Phys. Rev. A 11, 1749 (1975).
5. F. J. Bartoli, T. A. Litovitz, J. Chem. Phys. 56, 413 (1972).
6. D. R. Bauer, J. I. Brauman, R. Pecora, Ann. Rev. Phys. Chem. 27, 443 (1976).
7. K. B. Eisenthal, K. H. Drexhage, J. Chem. Phys. 51, 5720 (1969); T. J. Chuang, K. B. Eisenthal, Chem. Phys. Lett. 11, 368 (1971).
8. H. E. Lessing, A. von Jena, M. Reichert, Chem. Phys. Lett. 36, 517 (1975).
9. C. V. Shank, E. P. Ippen, Appl. Phys. Lett. 26, 62 (1975).
10. G. R. Fleming, J. M. Morris, G. W. Robinson, Chem. Phys. 17, 91 (1976).
11. G. Porter, P. J. Sadkowski, C. J. Tredwell, Chem. Phys. Lett. 49, 416 (1977).
12. G. R. Fleming, A.E.W. Knight, M. J. Morris, R. J. Robbins, G. W. Robinson, Chem. Phys. Lett. 51, 399 (1977).
13. T. J. Chuang, K. B. Eisenthal, J. Chem. Phys. 57, 5094 (1972).
14. R. I. Cukier, R. Kapral, J. R. Lebenhaft, J. R. Mehaffey, J. Chem. Phys. 73, 5244 (1980).
15. R. Peralta-Fabi, R. Zwanzig, J. Chem. Phys. 70, 504 (1979).
16. S. Richardson, J. Fluid Mech. 59, 707 (1973).
17. C. M. Hu, R. Zwanzig, J. Chem. Phys. 60, 4354 (1974).

18. B. J. Alder, D. M. Gass, T. E. Wainwright, J. Chem. Phys. 53, 3813 (1970).

19. D. R. Bauer, J. I. Brauman, R. Pecora, J. Amer. Chem. Soc. 96, 6840 (1974).

20. A. von Jena, H. E. Lessing, Chem. Phys. Lett. 78, 187 (1981).

21. P. Debye, Polar Molecules, Reinhold, New York, 1929.

22. J. T. Edward, J. Chem. Ed. 47, 261 (1970).

23. F. Perrin, J. Phys. Radium 5, 497 (1934); 7, 1 (1936).

24. D. Kivelson in New Aspects of Molecular Relaxation Processes, Farad. Symp. 11, Chem. Soc., London, 1977.

25. R. J. Robbins, Ph.D. Thesis, University of Melbourne, 1980.

26. K. G. Spears, L. E. Cramer, Chem. Phys. 30, 1 (1978).

27. Waldeck, A. J. Cross, Jr., D. B. McDonald, G. R. Fleming, J. Chem. Phys. 74, 3381 (1981).

28. G. S. Beddard, T. Doust, G. Porter, Chem. Phys. 61, 17 (1981).

Chapter 6

PICOSECOND DYNAMICS OF ELECTRONIC ENERGY TRANSFER IN SOLUTION*

6.1 Introduction

The transfer of electronic excitation energy in condensed phases has been the subject of interest since the pioneering work of Förster [2]. Most experimental work in this field has focussed on the role of multipolar [2,4] and exchange [3,4] interactions in electronic excitation transfer. Time-resolved studies are particularly useful in this respect, since the time dependence of the excited donor (or acceptor) population depends, in part, on the spatial dependence of the interaction between a single donor and acceptor. The first time-resolved experiments of singlet-singlet energy transfer [5], which were restricted to times longer than several nonoseconds, found general agreement with the dipole-dipole resonance transfer model, originally developed by Förster [1], and later by Dexter [3] and Galanin [6]. The extension to the picosecond time domain was first achieved by Rehm and Eisenthal [7]. By monitoring the anisotropy of the transient ground-state absorption of rhodamine 6G (donor) following excitation with a picosecond pulse, the time decay of the excited donor population in the presence of malachite green (acceptor) was measured. These authors found that the decay agreed with the Förster dipole-dipole model from the earliest times they could measure, 20 psec. Furthermore, the critical transfer distance inferred from the

*The results of this work have been previously reported in reference [1].

decay, 53Å, was in approximate agreement with that calculated from the spectral overlap, 48Å [7]. More recently, Porter and Tredwell [8] have examined the rhodamine 6G (Rh6G):malachite green (MG) system using a picosecond streak camera to time resolve the donor fluorescence. They found good agreement with the Förster model and obtained $R_o = 52.5$Å in a series of mixtures containing between 1.0×10^{-3}M and 1.0×10^{-2}M of MG. These authors found that the Förster model was valid from as early as 10 psec after excitation, the limit of their time resolution [8].

Adams et al. [9] subsequently studied donor-acceptor electronic energy transfer in the DODCI (donor):MG (acceptor) and DODCI:DQOCI systems, using a synchroscan streak camera to time resolve the donor fluorescence. While these authors found that the decay curves were of the form expected from the Förster model, they also found that the apparent critical transfer distance increased rapidly with decreasing acceptor concentration, which these authors took to imply a breakdown of the Förster model at low acceptor concentrations. At the higher acceptor concentrations the R_o values attained constant values, comparable in magnitude with the values measured by Rehm and Eisenthal [7], and Porter and Tredwell [8] for Rh6G:MG under similar conditions. The apparent breakdown of the Förster model at low acceptor concentrations is puzzling, since it is in this regime that the model is expected to be valid [6].

On the theoretical side, attention has been recently directed toward the effect of diffusion on donor-acceptor energy transfer [10-15]. Because of the strong distance dependence of multipolar transfer rates, the mobility of the donor and acceptor due to translational diffusion causes a faster decay of the excited donors than expected from the simple

Förster model. The generalization of the Förster model to include diffusion was first considered by Yokota and Tanimoto [16], and more recently in a simpler approach by Gösele et al. [13-15]. These authors found approximate analytical solutions to the diffusion equation describing the donor excitation with a sink term for the donor-acceptor energy transfer. More recently, Butler and Pilling [10] solved this equation numerically; the calculations showed the expected deviations from simple Förster kinetics and were in excellent agreement with the approximate analytic solution derived by Gösele et al. [13-15]. However, these equations have not yet been experimentally tested on the picosecond time scale.

Donor-donor excitation energy transfer also results in mobility of the excited donors and causes a faster quenching by the acceptors. Recent theoretical interest in the problem of electronic excitation transfer between identical molecules in disordered systems [11,17] has focussed on whether or not the migration can be described by a diffusion equation. Förster first showed that electronic excitation transfer on an ordered cubic array, by the dipole-dipole mechanism, is diffusive at all times [18]. Recently Haan and Zwanzig [19] considered the effect of disorder; they found that the transfer is nondiffusive at early times in dilute solutions and conjectured that diffusive behavior is approached only at long times or at high concentrations. Gochanour et al. [20] subsequently expanded on this treatment by including high order terms in the diagrammatic expansion of the Green function. The time-dependent diffusion coefficients calculated by Gochanour et al. [20] clearly showed the

nondiffusive behavior at low concentrations and the diffusive behavior at long times (see Fig. 10 or Ref. [20]). The quenching of excited donors by acceptors can serve as a probe for this excitation transfer among the donors, and so test whether it is diffusive or not on the time scale of the donor-acceptor energy transfer.

It was the purpose of this work to experimentally investigate these questions by time-resolved spectroscopy on the picosecond and nanosecond time scales. One objective was to carefully test the Förster model [2] in the cresyl violet (donor):azulene (acceptor) over a very wide range of acceptor concentrations. The effects of translational diffusion in fluid solvents, and donor-donor energy transfer on the donor decay kinetics were experimentally observed and compared with theoretical models based on a diffusion equation. A combination of ground-state recovery (GSR) techniques and time-resolved fluorescence techniques were employed in this work; GSR probed the early time kinetics with ≃ 2 psec time resolution, while time-correlated single photon counting allowed the donor fluorescence decay to be accurately measured over a wide range of acceptor concentrations.

A brief summary of the relevant theoretical models is presented in the next section. The experimental results are then presented and discussed in subsequent sections of this chapter.

6.2 Theory

In this section the Förster model [2] is briefly outlined and an equation for the excited state donor population is derived. Then the additional effects of translational diffusion of the solutes and excitation

transfer among the donors are considered.

a. Förster model

Förster [2] considered the weak coupling of the electronic and vibronic states of the donor (D) and acceptor (A) by a dipole-dipole interaction, and showed that the rate constant for energy transfer between a single donor and acceptor separated by a distance R could be written as

$$K_{DA} = \frac{3}{2} \kappa^2 (1/\tau_D) \, (R_o/R)^6 \tag{6.1}$$

where κ contains the angular dependence of the dipole-dipole interaction,

$$\kappa^2 = (\sin \theta_D \sin \theta_A \cos \phi - 2 \cos \theta_D \cos \theta_A)^2 \tag{6.2}$$

where θ_D and θ_A are the angles specifying the direction of the transition moments ($S_1 \leftarrow S_o$) of D and A with respect to the vector joining them; ϕ is the azimuthal angle between D and A; τ_D is the excited donor lifetime in the absence of acceptors; and R_o is the critical transfer distance, which is related to the spectral overlap of D and A by the equation

$$R_o^6 = \frac{9000 \ln 10 \, \Phi_D (\frac{2}{3})}{128 \pi^3 n^4 N} \int_0^\infty \frac{F_D(\bar{\nu}) \, \varepsilon_A(\bar{\nu})}{\bar{\nu}^4} \, d\bar{\nu} \tag{6.3}$$

where N is Avogadro's number, Φ_D is the quantum yield of donor emission, n is the solvent refractive index, $\varepsilon_A(\bar{\nu})$ is the acceptor molar decadic extinction coefficient at wavenumber $\bar{\nu}$, and $F_D(\bar{\nu})$ is the donor fluorescence intensity at $\bar{\nu}$ (normalized to unit area on a wavenumber scale). R_o can thus be calculated from the known spectral properties of the donor and acceptor.

Consider the differential equation governing the decay of an individual donor molecule i in an ensemble of N_A acceptors

$$\frac{dP_i}{dt} = -P_i/\tau_D - 1/\tau_D \sum_{j=1}^{N_A} \frac{3}{2} \kappa_{ij}^2 (R_o/R_{ij})^6 P_i \qquad (6.4)$$

where $P_i(t)$ is the probability that the donor molecule i is excited at time t. The sum extends over all acceptors j, and depends only on the relative separations R_{ij} and orientations κ_{ij}. Back transfer from the excited acceptors to the donors is ignored in Eq. (6.4), which is valid when the donor and acceptor are different species. It follows that the individual donor decay is exponential. However, it is not the decay of a single donor that is observed in a time-resolved experiment, but rather the decay of an ensemble of donors, each with different distributions of R_{ij} and κ_{ij}. Several authors have considered the procedure for evaluating the ensemble averaged decay law [2,6,7,21-24]. Gösele et al. [21] showed that Förster's statistical averaging method [2], which has been criticized by some authors [22,23], is a correct procedure, and that it is in agreement with other methods based on averaging of the differential equation [6], or on pair probabilities [21,25]. Förster [2] averaged each of the N_A exponential decay terms in the solution of Eq. (6.4). For a random distribution of R_{ij} and κ_{ij}, the average is independent of which acceptor is considered and the ensemble averaged donor decay probability is a product of N_A identical terms,

$$P(t) = e^{-t/\tau_D}\left[\iiiint \exp\left(-\frac{3}{2}\kappa^2(R_o/R)^6\, t/\tau_D\right)\frac{R^2 \sin\theta_D \sin\theta_A}{2V}\, d\theta_D\, d\theta_A d\phi dR\right]^{N_A} \tag{6.5}$$

where V is the volume of the ensemble. The final result is [2,6,21]

$$P(t) = \exp[-t/\tau_D - g\,\frac{4}{3}\pi^{3/2}\, n_A R_o^3 (t/\tau_D)^{1/2}] \tag{6.6}$$

where R_o is the critical transfer distance defined in Eq. (6.3), and n_A is the acceptor number density. g is a numerical factor given by

$$g = (\frac{3}{2}\langle\kappa^2\rangle)^{1/2} \tag{6.7}$$

where $\langle\kappa^2\rangle$ is an averaged orientation factor, and depends on how the orientations are averaged. In the "dynamic averaging limit" [26] molecular reorientation is infinitely rapid, all possible orientations are sampled during the energy transfer, and the orientation factors Eq. (6.2) can be pre-averaged; the result is $\kappa^2_{ij} = 2/3$ for all i,j (g = 1), which is then used in Eq. (6.1) and the subsequent ensemble average. In the "static averaging limit" [26] the orientations are fixed throughout the energy transfer and the orientation terms must be ensemble averaged over a random (but static) angular distribution, as done in Eq. (6.5); then g = 0.845 [27,28]. In the intermediate regime, g will be a function of the rotational diffusion coefficients of the donor and acceptor, and the acceptor concentration. Bojarski and Dudkiewicz [29] recently derived an approximate equation for $\langle\kappa^2\rangle$ based on an interpolation between the two limits described above. Note that the effect of rotational mobility is quite minor, resulting in at most a 15% reduction of the quenching term in Eq. (6.6).

The derivation just given for the dipole-dipole interaction can be extended to the case of multipolar interactions in general [4]. Instead of Eq. (6.1), the general expression for the rate constant for energy transfer between a single donor and acceptor is

$$K_{DA} = (1/\tau_D)\ (R_o/R)^N \tag{6.8}$$

where the "dynamic averaging limit" has been assumed to remove the (uninteresting) orientational dependence. The donor decay law in this case is [4]

$$P(t) = \exp[-t/\tau_D - \frac{4\pi}{3}\,\Gamma(1-\frac{3}{N})\ n_A\ R_o^3(t/\tau_D)^{3/N}] \tag{6.9}$$

which is the generalization of Eq. (6.6). $\Gamma(x)$ is the gamma function. Equation (6.9) reduces to Eq. (6.6) when $N = 6$; this is the case of a dipole-dipole interaction. A dipole-quadrupole interaction corresponds to $N = 8$, and a quadrupole-quadrupole interaction to $N = 10$.

b. Effect of translational diffusion

The derivation of the donor decay law, Eq. (6.6), assumed that the distribution of R_{ij} was time-independent. This will not be true in fluid solutions, and deviations from the decay law are expected [10]. Several authors have considered this problem theoretically by adding a diffusion term to the differential equation for the donor excitation probability, Eq. (6.4) [10-16]. The resulting equation was first solved by Yokota and Tanimoto [16], using a method of Pade approximants. Their result for P(t) is complex, and not the most suitable form for curve-fitting. More recently, Gösele et al. [13-15] obtained an approximate

solution, based on an interpolation between the known solutions at early and long times. They showed that when long range energy transfer dominates, the donor decay law is [13,14]

$$P(t) = \exp[-t/\tau_D - 4\pi\ Dr_F n_A t - g\ \frac{4}{3}\pi^{3/2}\ n_A R_o^3 (t/\tau_D)^{1/2}] \qquad (6.10)$$

where $r_F \simeq 0.676\ (g^2 R_o^6/\tau_D D)^{1/4}$ is an "effective trapping radius," and D is the relative diffusion coefficient ($D = D_A + D_D$). This result is valid whenever $z_o = (1/2r_{AD}^2).\ (g^2 R_o^6/\tau_D D)^{1/2} >> 1$, where r_{AD} is the hard-sphere encounter distance. Later it will be shown that this condition is satisfied in these experiments. Gösele et al. [13] claim that this relatively simple equation is as accurate as the more complex solution obtained by Yokota and Tanimoto [16].

The only additional parameter appearing in Eq. (6.10) is the diffusion coefficient. For translational diffusion, D may be estimated from classical hydrodynamics, using the Stokes-Einstein equation [30]

$$D_T = \frac{k\ Tf_A}{6\pi\eta\ r_A} + \frac{k\ Tf_D}{6\pi\eta\ r_D} \qquad (6.11)$$

where r_A and r_D are the radii of the equivalent spheres of the donor and acceptor, respectively, and f_A and f_D are shape factors. The subscript T denotes a translational diffusion coefficient.

Equation (6.10) can also be generalized to describe multipolar interactions [15]. Again, starting from the general rate constant, Eq. (6.8), the donor decay law including diffusion is found to be [15]

$$P(t) = \exp[-t/\tau_D - 4\pi\ D\ r_F n_A\ t - \frac{4}{3}\pi\Gamma(1 - \frac{3}{N})n_A\ R_o^3 (t/\tau_o)^{3/N}] \qquad (6.12)$$

where the effective trapping radius is now given by

$$r_F = (R_o^N/\tau_D D)^{\frac{1}{N-2}} \cdot (N-2)^{\frac{N-4}{N-2}} \cdot \Gamma(\tfrac{N-3}{N-2}) / \Gamma(\tfrac{1}{N-2}) \qquad (6.13)$$

c. Effect of donor-donor excitation transfer

When the absorption and fluorescence of the donor overlap, long-range resonance transfer between excited and unexcited donor molecules will occur. In most cases the D-D rate will be of the same form as the D-A rate, Eq. (6.1) or (6.8), with a critical transfer distance $\underset{\sim}{R}_o$ dependent on the self-overlap. When the donor concentration is sufficiently dilute that the average donor separation is much larger than $\underset{\sim}{R}_o$, then the treatment of D-A energy transfer given above is correct. However, when the D-D and D-A rates are comparable, the situation is more complicated. The problem of simultaneous D-D and D-A energy transfer has been of interest in exciton trapping in solids [31]. Here two limits are considered, depending on the relative rates of D-D and D-A transfer. When D-A transfer dominates, the D-D transfer is included by adding diffusion terms to the donor rate equations, as done in the case of translational diffusion. In the opposite limit, where the D-D transfer is more rapid than the D-A transfer, all acceptor environments surrounding the excited donors are sampled, and a time-independent average D-A energy transfer rate is established. The donor decay is exponential in this limit [31].

In the first limit, which is of interest here, Eq. (6.10) would be appropriate with a diffusion coefficient determined by exciton diffusion. This is a sensible procedure in an ordered solid, for which the

D-D transfer (by a dipole-dipole mechanism) is diffusive at all times [18] (that is, the mean square displacement of the excitation during the excited state lifetime is linear in time, and the diffusion coefficient is time-independent). However, in a dilute solution, the effect of the disorder is to make the donor excitation transfer nondiffusive over most times of experimental interest [19,20]. In this case the diffusion coefficient is time-dependent and Eq. (6.10) would not apply since it assumes a constant diffusion coefficient.

The results of Gochanour et al. [20] imply that diffusive behavior is attained at long times, with a limiting diffusion coefficient given by

$$D_E = 0.428\ C^{4/3}\ \underset{\sim}{R}_o^2\ \tau_D^{-1} \tag{6.14}$$

where C is a reduced concentration defined by

$$C = 4\pi\ n_D\ \underset{\sim}{R}_o^3/3 \tag{6.15}$$

and n_D is the number density of donors. The subscript E denotes an excitation diffusion coefficient. Haan and Zwanzig [19] found a similar equation for the limiting diffusion coefficient, but with a numerical factor 0.324. Equation (6.14) is considered to be more accurate, since Gochanour et al. included higher order terms in the expansion of the Green function [20].

If diffusive donor excitation transfer <u>is</u> achieved on the time scale of the D-A transfer, then Eq. (6.10) will apply with D given by Eq. (6.14). Nondiffusive transport should result in deviations from this decay law.

d. Experimental observables

In the discussion of ground-state recovery (GSR) in Chapter 3, an exponential recovery law was assumed. Within the two-level approximation, the generalization of Eq. (3.16) to the case of an excited state decay law specified by P(t) is

$$\Delta T_{iso}(t) = \sigma^2 N \ell I T_o P(t) \tag{6.16}$$

Only the isotropic signal is required, since the interest here is in population kinetics only. The conclusion is that the excited donor decay function, in this case given by Eqs. (6.10) and (6.12), can be measured in GSR measurements with magic angle probe polarization.

In the fluorescence decay experiment, the instantaneous fluorescence intensity is measured at time t after excitation through an analyzing polarizer. The derivation in Chapter 4 was for a general excited state decay law and hence is valid here. The isotropic fluorescence decay curve, measured with the analyzing polarizer set at the magic angle, is proportional to the excited state decay law,

$$I_{iso}(t) = a\, P(t) \tag{6.17}$$

Both GSR and fluorescence decay experiments contain the same information in the two-level approximation, and either technique can be applied. In practice one technique may be more suitable, or both techniques may be used together to exploit the useful characteristics of each, as was done in this work.

6.3 Experimental

Cresyl violet perchlorate (laser grade) and azulene (99%) were obtained from Eastman and Aldrich, respectively, and used as supplied. Solutions were made up in methanol or ethylene glycol solvents at room temperature (23°C). The solvent viscosities at this temperature were 0.57 cP (methanol) and 19.5 cP (ethylene glycol). Donor and acceptor concentrations were carefully controlled, and checked by spectrophotometry.

Absorption spectra of cresyl violet and azulene were recorded on a Cary 14 spectrophotometer. The emission spectrum of cresyl violet was recorded on a Perkin Elmer MPF-3 spectrofluorimeter. Spectra were digitized and input to a computer for numerical integration.

Ground-state recovery measurements were performed using the apparatus described in Chapter 3. The time scale of even the fastest recovery curves was ≃100 psec (refer to the "1/e" recovery times in Table 6.2). Therefore it was not necessary to extract decay information in the region of zero delay, where the convolution effects discussed in Section 3 of Chapter 3 were dominant. The approach used was to fit the GSR curve, starting at least one pulse width from zero delay, using the impulse response function given by Eq. (6.16). In practice, this meant that a time range from ≃2 psec to several hundred picoseconds was probed by GSR in these experiments.

Fluorescence decay curves were measured using the time-correlated single photon counting apparatus described in Chapter 4. The synchronously mode-locked CW dye laser was used for excitation ($\lambda = 6000\text{Å}$). The

excitation repetition rate at the sample was 1 MHz. The pulse duration was typically 3-4 psec. Cutoff filters before the photomultiplier blocked scattered laser light. Fluorescence from the azulene acceptors had very low quantum efficiency [32] and did not interfere with the donor fluorescence. The decay curves measured for all but the sample with highest acceptor concentration did not require deconvolution. When deconvolution was required, the approach described in Section 4 of Chapter 4 was used.

6.4 Results

a. Steady state spectra

The donor fluorescence spectrum and acceptor absorption spectrum are presented in Figure 6.1, together with their chemical structures. A considerable overlap of the spectra is evident. The spectral overlap integral in Eq. (6.3) was evaluated by numerical integration of the spectra in Figure 6.1. The result was $4.5 \times 10^{-15} cm^5 mol^{-1}$ in methanol and $4.3 \times 10^{-15} cm^6 mol^{-1}$ in ethylene glycol. Using the known fluorescence quantum yield for cresyl violet in methanol [33], $\Phi_D = 0.545$, and other known constants, gave $R_o = 27.8 \pm 0.9 \text{Å}$ in methanol and $R_o = 26.3 \pm 0.9 \text{Å}$ in ethylene glycol. The cresyl violet absorption (not shown) at the excitation wavelength (6000Å) was 200 times stronger than the azulene absorption. From the overlap of the cresyl violet absorption and fluorescence spectra, the critical transfer distance for donor-donor excitation transfer was calculated to be $\underset{\sim}{R}_o = 44.5 \pm 1.5 \text{Å}$.

b. Fluorescence decay data

The isotropic (54.7°) fluorescence decays of cresyl violet were

Figure 6.1

Steady-state spectra and chemical structures of cresyl violet (donor) and azulene (acceptor). The donor fluorescence spectrum and acceptor absorption spectrum are shown in the region of overlap.

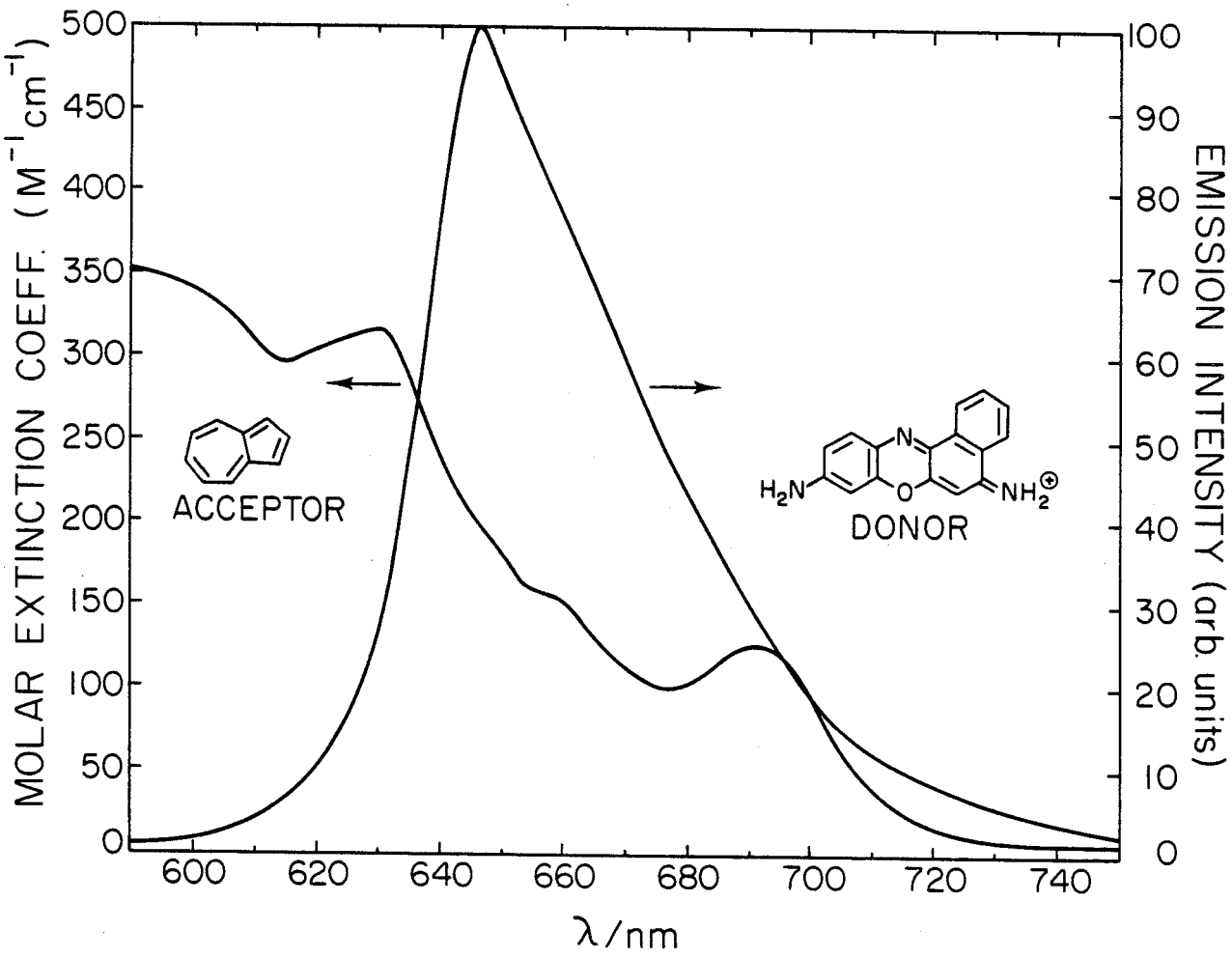
MOLAR EXTINCTION COEFF. ($M^{-1}cm^{-1}$)
EMISSION INTENSITY (arb. units)
λ/nm
ACCEPTOR
DONOR
H_2N
$NH_2^{\oplus}$
N
O
500
450
400
350
300
250
200
150
100
50
0
100
90
80
70
60
50
40
30
20
10
0
600
620
640
660
680
700
720
740

exponential in both solvents with lifetimes of 3160 ± 15 psec (methanol) and 2870 ± 15 psec (ethylene glycol). The error ranges quoted here are 95% confidence intervals. The reduced chi-squared values of the single-exponential fits were 1.0 or less. The cresyl violet concentration was 2.5×10^{-7}M in all fluorescence experiments; this was necessary to prevent distortion of the decay curves due to self-absorption, which caused observable lifetime-lengthening at concentrations above 10^{-6}M. This donor concentration was almost 3 orders of magnitude lower than used in previous picosecond experiments [7-9], and reflects the high sensitivity of the single photon counting technique. Even at such a low donor concentration, data with very high signal-to-noise ratio were obtained. Donor-donor excitation transfer was absent at this low donor concentration, as was verified using Eq. (6.14); $D_E \sim 10^{-6} D_T$.

The fluorescence decays of cresyl violet in ethylene glycol solutions containing different concentrations of azulene are presented in Figure 6.2. The fluorescence decays of cresyl violet solutions containing 1×10^{-2}M of azulene in both methanol and ethylene glycol solvents are presented in Figure 6.3. The decay curves were analyzed in two ways. First, the general multipolar decay law, including diffusion, Eq. (6.12), was fit by a nonlinear least squares method (Appendix II) to the decay curves for both methanol and ethylene glycol solutions. This yielded values for both R_0 and N, given in Table 6.1. The fit was excellent, which was indicated by $1.0 \lesssim \chi_r^2 \lesssim 1.2$. Successful optimization of the power law exponent N was dependent on the acceptor concentration; at low concentrations it was difficult to determine N with good accuracy. Thus,

Figure 6.2

Fluorescence decays of cresyl violet (2.5×10^{-7}M) in ethylene glycol containing 5.0×10^{-5}M (upper curve), 5.0×10^{-3}M (middle curve), and 4.0×10^{-2}M (lower curve) of azulene. The fluorescence was collected through an analyzer set at 54.7° from the polarization direction of the exciting light.

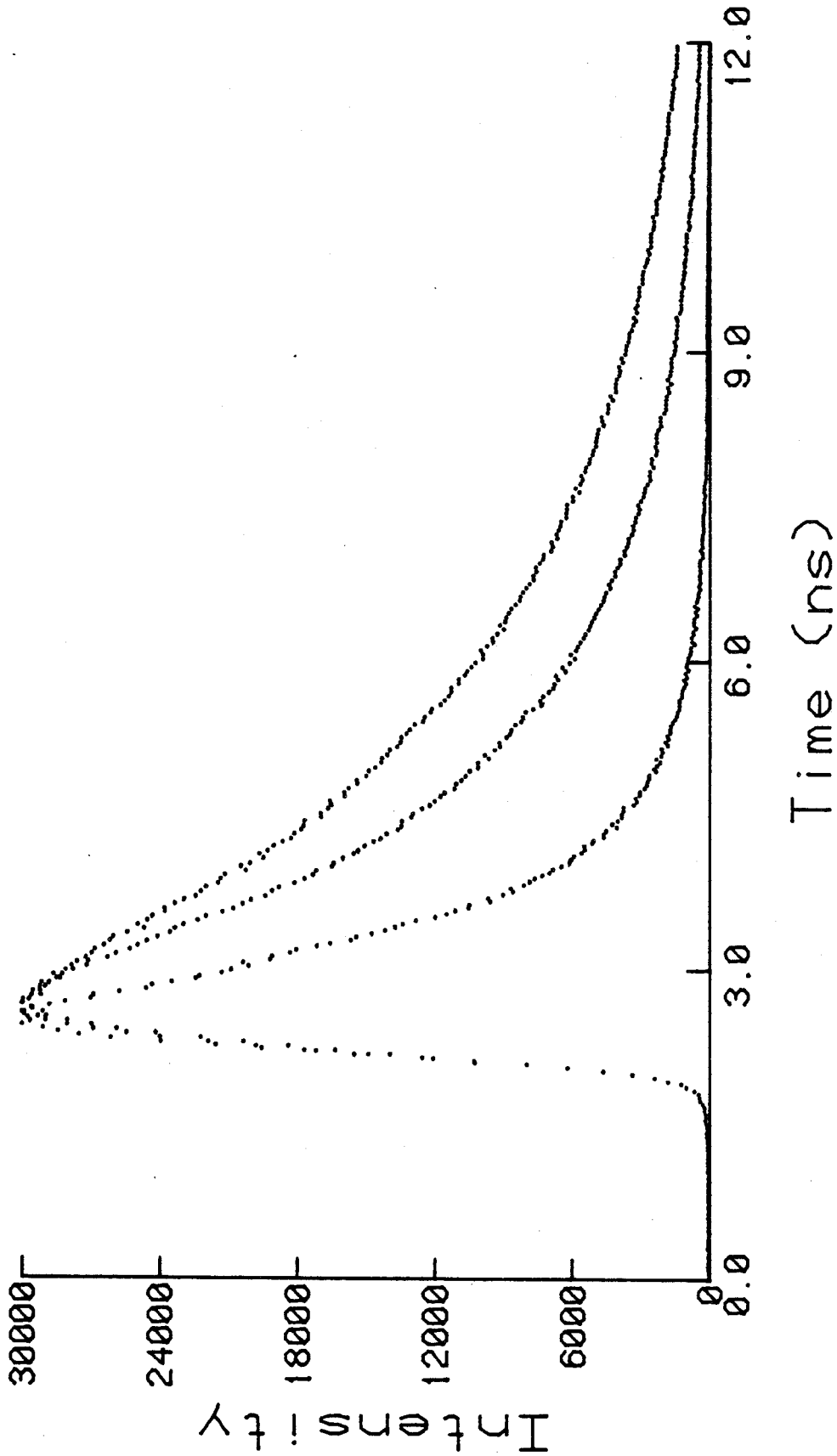
Intensity
30000
24000
18000
12000
6000
0
0.0
3.0
6.0
9.0
12.0
Time (ns)

Figure 6.3

Fluorescence decays (54.7°) of cresyl violet (2.5×10^{-7}M) containing 1.0×10^{-2}M of azulene in ethylene glycol (upper curve) and in methanol (lower curve). The points are experimental data and the smooth lines are the best-fit of Eq. (6.10), with $R_o = 25.7\text{Å}$ in ethylene glycol and $R_o = 26.4\text{Å}$ in methanol.

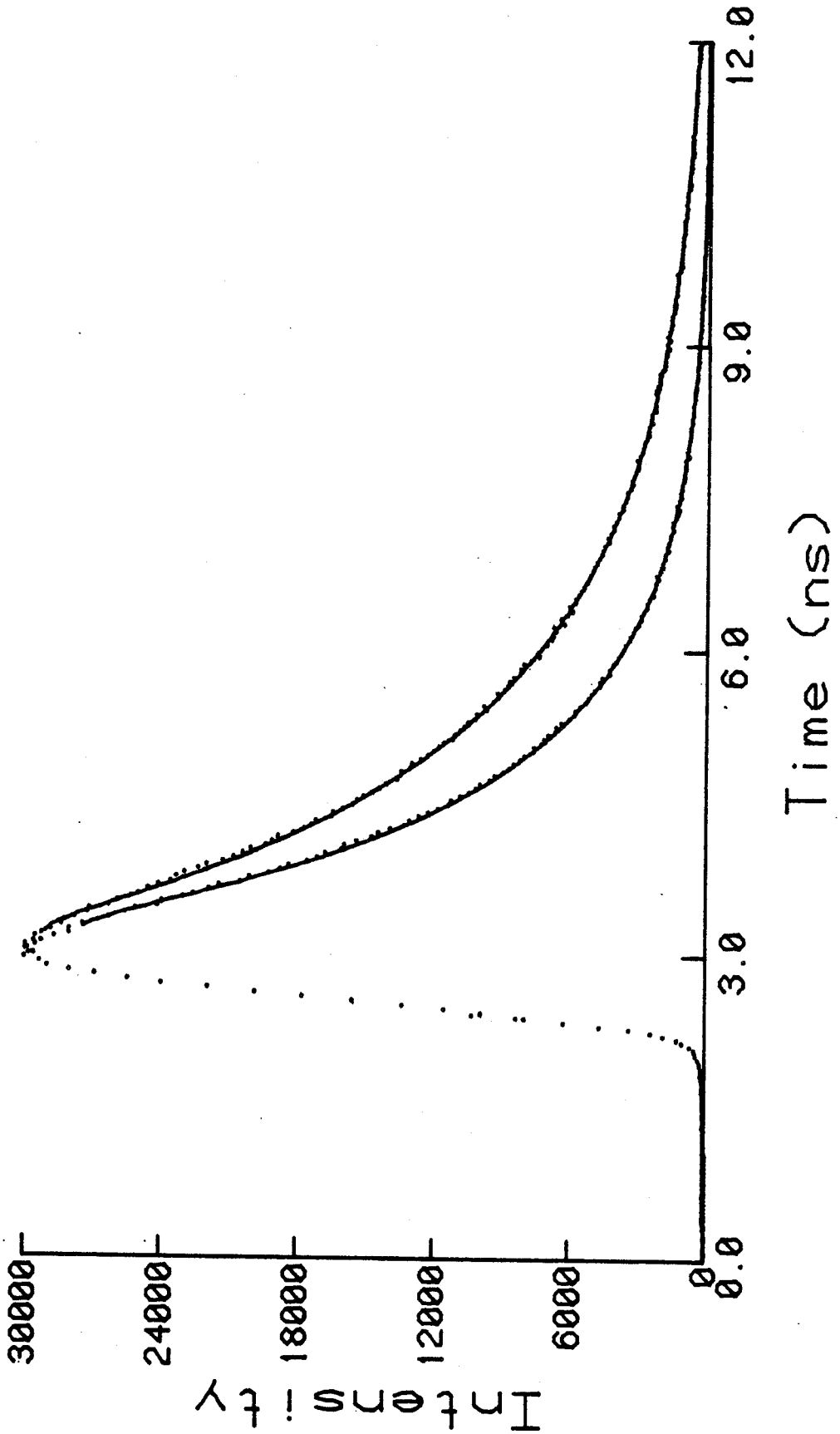
Intensity
30000
24000
18000
12000
6000
0
0.0
3.0
6.0
9.0
12.0
Time (ns)

TABLE 6.1

General Multipolar Analysis of Fluorescence Decay

Solvent	$R_o/\mathring{A}$	N
Methanol	27.3 ± 0.5	5.80 ± 0.3
Ethylene glycol	26.2 ± 0.5	6.15 ± 0.2

the results in Table 6.1 were obtained from solutions containing between 1.0×10^{-3}M and 4.0×10^{-2}M of azulene. The values of N were equal to 6.0 within experimental error for both solvents, Table 6.1. This proved that the donor-acceptor energy transfer was due to a dipole-dipole (N = 6) mechanism. Having established this, the dipole-dipole decay law, including diffusion, Eq. (6.10), was then used for all subsequent analysis. The fluorescence decay curves covering the entire range of acceptor concentration from 5.0×10^{-5} to 4.0×10^{-2}M were fit using Eq. (6.10). The fits were excellent, $1.0 \lesssim \chi_r^2 \lesssim 1.2$, and showed no systematic trends over the entire acceptor concentration range. The results are summarized in Table 6.2.

The constants appearing in Eqs. (6.10) and (6.12) were evaluated as follows: Translational diffusion coefficients were calculated from Eq. (6.11) using $r_A = 3.12\text{Å}$ and $r_D = 3.72\text{Å}$, and correcting for nonspherical shape; rotational mobility factors were calculated [29] for each solution using the measured rotational relaxation times for cresyl violet reported in Chapter 5, and estimated rotation times for azulene. The values of these constants are also included in Table 6.2. The rotational mobility factors for methanol indicate that the energy transfer occurred in the dynamic averaging limit at all acceptor concentrations in methanol. In ethylene glycol, the transfer occurred in the intermediate concentration-dependent regime, with g decreasing as the acceptor concentration increased. However, the static averaging limit was never attained in this solvent. The use of Eq. (6.10) and (6.12) was justified, since $z_o = 14$ for methanol and $z_o = 85$ for ethylene glycol, calculated for $r_{AD} = 5\text{Å}$ and the D_T values given above. Also included in Table 6.2 are values of the "1/e times,"

TABLE 6.2

Analysis of Fluorescence Decay Curves

$C_A/10^{-3}$ M	Methanol[a]			Ethylene Glycol[b]		
	t_e/ps	g	R_o/Å	t_e/ps	g	R_o/Å
0	3160	0.998		2870	0.973	-
0.050	3119	0.998	32 ± 10	2857	0.973	27 ± 22
0.100	3103	0.998	27.3 ± 7.0	2842	0.973	27.7 ± 11.6
0.500	2894	0.998	27.1 ± 2.5	2756	0.972	25.9 ± 2.5
1.00	2678	0.998	26.6 ± 0.6	2610	0.972	27.4 ± 1.2
2.50	-	-	-	2312	0.971	26.07 ± 0.50
5.00	1569	0.998	26.36 ± 0.20	1873	0.969	25.67 ± 0.30
10.00	925	0.998	26.43 ± 0.13	1353	0.965	25.72 ± 0.19
40.00	157	0.994	26.92 ± 0.10	276	0.937	25.73 ± 0.10

[a] $D_T = 2.0 \times 10^{-5}$ $cm^2 s^{-1}$

[b] $D_T = 0.06 \times 10^{-5}$ $cm^2 s^{-1}$

Error ranges are 95% confidence intervals ($\simeq 2.8\sigma$)

which are the times required for the fluorescence intensity to decay to 1/e of its initial amplitude.

c. Ground state recovery

The induced transmission change versus probe pulse delay is shown in Figure 6.4 for a 1×10^{-3}M solution of cresyl violet in methanol containing 5.0×10^{-2}M of azulene. The probe polarization was 54.7° from the pump direction, as discussed in Section 6.2d. The build-up seen to the left of the peak in Figure 6.4 was due to the finite duration of the pump and probe pulses. The sharp peak on the curves, which marks the point of coincidence of pump and probe pulses, was due to the coherent coupling effect discussed in Chapter 3. The shape of the coherent spikes suggests that $\Delta t_c \lesssim \Delta t_p$ (compare Figure 3.3).

The GSR signal observed with no azulene present (not shown) was almost constant over the time range shown in Figure 6.4. Longer scans revealed an exponential recovery, with $\tau_D = 3.2 \pm 0.4$ nsec in methanol, in good agreement with the fluorescence lifetime, $\tau = 3160$ psec. The two-level approximation mentioned in Section 6.2d was thus verified. The rate of decay of the induced transmission increased monotonically as increasing concentrations of azulene were added. The GSR curves were fit with the dipole-dipole decay law including diffusion, Eq. (6.10). The excitation diffusion coefficient calculated from Eq. (6.14), and the translational diffusion coefficients used in the previous section, were used in Eq. (6.10). The fits were excellent at all acceptor concentrations when the donor concentration was less than about 2×10^{-3}M. A typical fit under these conditions is shown in Figure 6.4; the fit is excellent, as demonstrated by the small and randomly distributed residuals

Figure 6.4

Induced transmission ΔT versus probe pulse delay for cresyl violet (1.0×10^{-3}M) in methanol containing 5.0×10^{-2}M of azulene. The direction of polarization of the probe beam was 54.7° from that of the pump beam. The vertical scale is in arbitrary units; the peak transmission change was $\simeq 3\%$. The points are experimental data and the smooth line is the best fit of the data to Eq. (6.10). Shown above are the weighted residuals between the data and the best-fit curve.

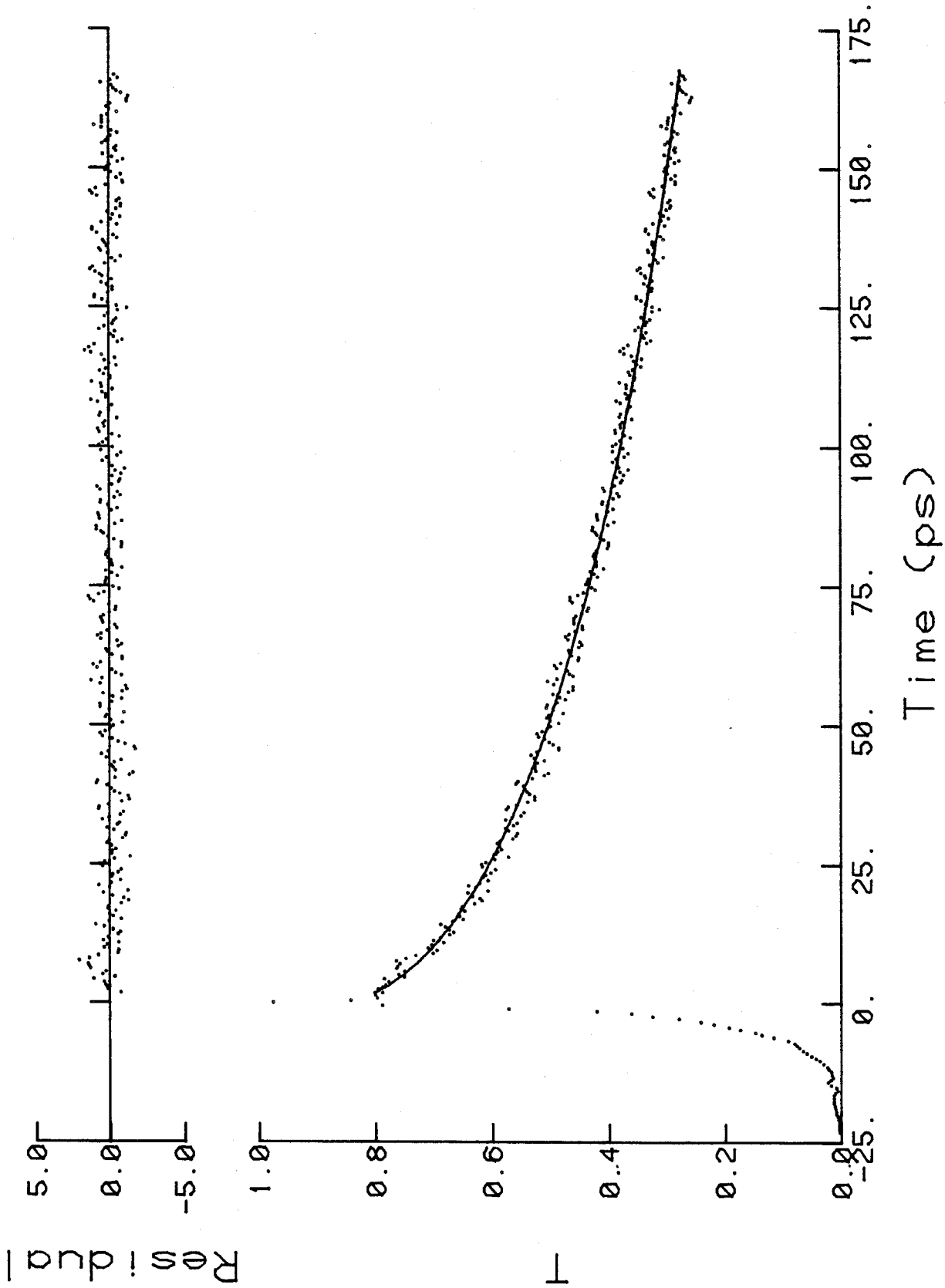
Residual
5.0
0.0
-5.0
T
1.0
0.8
0.6
0.4
0.2
0.0
-25.
0.
25.
50.
75.
100.
125.
150.
175.
Time (ps)

shown in the upper part of the figure. However, at higher donor concentrations there were apparent deviations between the GSR curves and the best-fit curves calculated from Eq. (6.10). An example is shown in Figure 6.5, which presents the GSR curve for a 5.0×10^{-3}M cresyl violet solution in ethylene glycol containing 4.0×10^{-2}M azulene. The deviations are apparent in the residuals graph.

The results of analyzing the GSR curves are summarized in Table 6.3. The values of D_T for each solvent, and of D_E at each donor concentration are also included in the table. As the D_E values indicate, donor-donor excitation transfer was important in some samples. This was because a much higher donor concentration ($\sim 10^{-3}$M) was needed to detect a reasonable GSR signal as compared with the fluorescence experiments. The last column in Table 6.3 shows the effect of ignoring the donor-donor excitation transfer. For donor concentrations $[D] \lesssim 10^{-3}$M, the apparent R_0 values obtained with $D_E = 0$ agreed well with the values obtained with all correction terms included. This was the regime where Eq. (6.10) gave good fits to the GSR curves, such as shown in Figure 6.4. Donor-donor excitation transfer was negligible in this regime.

When $[D] \gtrsim 2 \times 10^{-3}$M, the apparent R_0 values obtained with $D_E = 0$ were considerably larger than the true values. This effect was relatively greater in ethylene glycol than in methanol. The apparently larger R_0 values indicated that donor-donor excitation transfer caused an enhancement of the donor-acceptor energy transfer. When D_E was included, relatively constant R_0 values, independent of the donor concentration were obtained (compare the last two columns of Table 6.3). However, some deviations were

Figure 6.5

Induced transmission ΔT versus probe pulse delay for cresyl violet (5.0×10^{-3}M) in ethylene glycol containing 4.0×10^{-2}M of azulene. The probe polarization direction was 54.7° from that of the pump. The smooth line is the best fit of the data to Eq. (6.10). The weighted residuals are shown above. Note the deviation, which is discussed in the text.

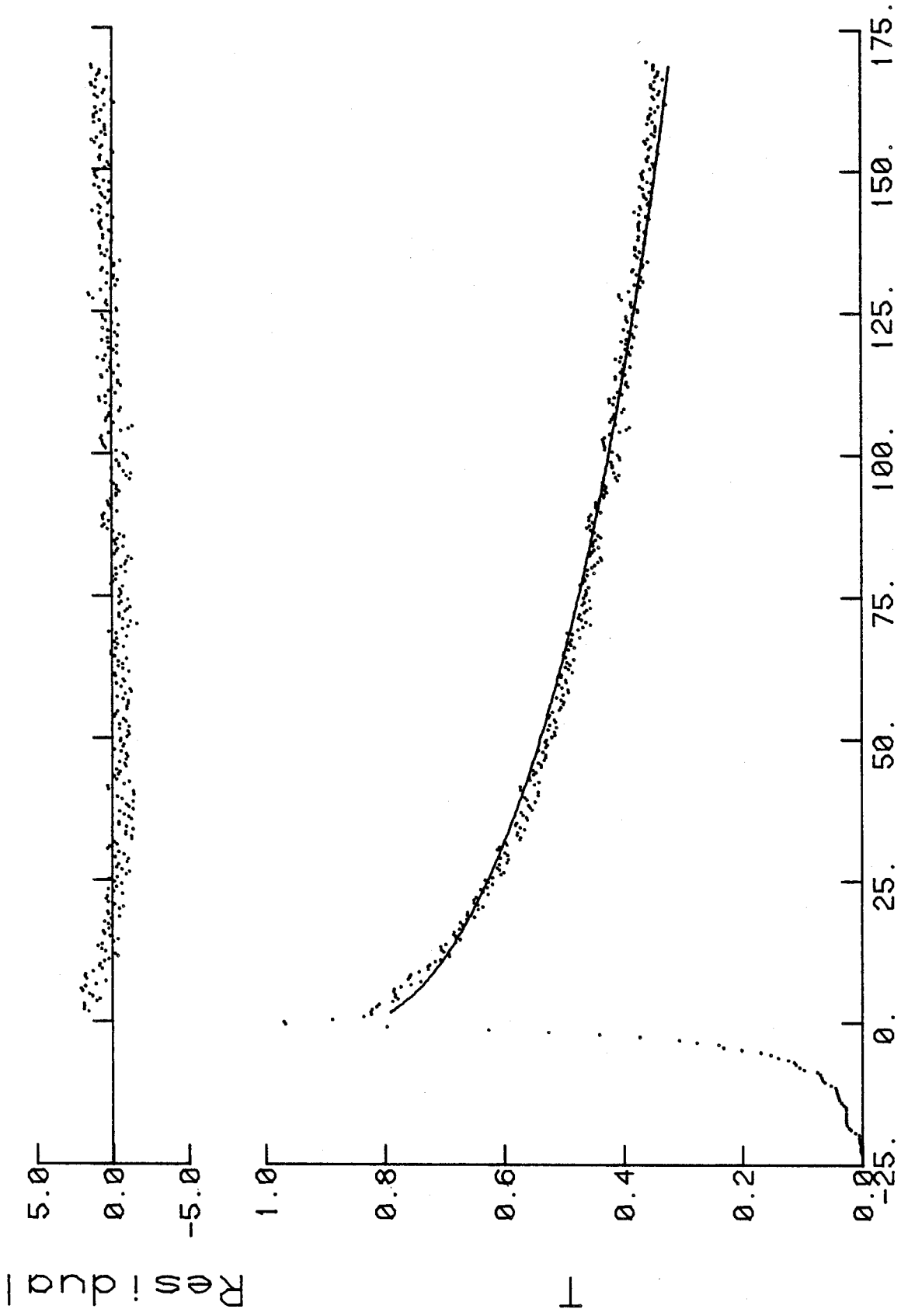
Residual
5.0
0.0
-5.0
T
1.0
0.8
0.6
0.4
0.2
0.0
-25.
0.
25.
50.
75.
100.
125.
150.
175.
Time (ps)

TABLE 6.3

Analysis of GSR Curves

Solvent	$C_D/10^{-3}$ M	$C_A/10^{-2}$ M	$D_T/10^{-5}$ $cm^2\ s^{-1}$	$D_E/10^{-5}$ [a] $cm^2\ s^{-1}$	$R_o/\mathring{A}$	$R_o/\mathring{A}$ [b] ($D_E = 0$)
MeCH	1.00	4.00	2.00	0.35	25.3 ± 0.9	25.6 ± 0.9
	2.00	3.00	2.00	0.91	26.0 ± 0.7	26.9 ± 0.7
	2.00	5.00	2.00	0.91	26.5 ± 0.5	27.3 ± 0.5
EG	0.50	4.00	0.06	0.16	26.7 ± 0.8	27.0 ± 0.8
	2.00	4.00	0.06	1.00	26.9 ± 0.5	28.2 ± 0.5
	5.00	4.00	0.06	3.40	25.8 ± 0.5	29.0 ± 0.5

[a] Calculated from Eq. (6.14) with $\underset{\sim}{R}_o = 44.5\mathring{A}$

[b] No correction was included for donor-donor excitation transfer.

apparent in the theoretical fits, as already mentioned, when $[D] \gtrsim 2 \times 10^{-3}$M. An example is shown in Figure 6.5.

6.5 Discussion

The fluorescence decay curves of the excited donors, shown as a function of acceptor concentration in Figure 6.2, displayed the qualitative features expected for donor-acceptor energy transfer: the curves decayed faster and became more nonexponential as the acceptor concentration increased. Also, the energy transfer rate in methanol was more rapid than in ethylene glycol, which is clearly evident in Figure 6.3. The difference between the two decay curves, which have the same acceptor concentration, is almost entirely due to translational diffusion (the slightly different R_0 values in the two solvents, calculated in Section 6.4a, will also cause a faster decay in methanol than in ethylene glycol). Consider the diffusion length given by the Einstein equation $\ell = (6D_T\tau_D)^{1/2}$. From the values given in Section 6.4 we calculate $\ell = 10.2\text{Å}$ in ethylene glycol and $\ell = 61.6\text{Å}$ in methanol. Thus $\ell \ll R_0$ in ethylene glycol and translational diffusion had a minor effect on the donor decay. This was confirmed by the finding that the fluorescence decay curves for ethylene glycol solutions could be equally well fit by the "no-diffusion" decay law (Eq. (6.6)) as by the full decay law including diffusion (Eq. (6.10)). The apparent R_0 values obtained using Eq. (6.6) were larger than the true values given in Table 6.2 by about 1Å. This small difference indicated that translational diffusion made a small contribution to the energy transfer observed in ethylene glycol. However, $\ell \gg R_0$ in methanol, and

considerable diffusion occurred during the energy transfer. The methanol data should thus provide a good opportunity for testing Eq. (6.10). This equation did indeed fit the methanol decay curves very well over the whole range of C_A in Table 6.2, whereas the "no-diffusion" Eq. (6.6) gave somewhat worse fits at low acceptor concentrations, but failed completely to fit the decays at higher acceptor concentrations. The smooth lines in Figure 6.2 are the best fit to Eq. (6.10) with $R_0 = 26.4\text{Å}$ in methanol and $R_0 = 25.7\text{Å}$ in ethylene glycol. These values agree within experimental error with the R_0 values calculated from the spectral data (Section 6.4a). Thus the difference between the decay curves in Figure 6.3 is accounted for theoretically by Eq. (6.10) using the calculated translational diffusion coefficients for each solvent. The results in Table 6.2 demonstrate that this was also true over the entire range of acceptor concentrations: the relatively faster energy transfer in methanol could be accounted for by Eq. (6.10) with the same R_0 values at each acceptor concentration. This was the best evidence that Eq. (6.10) could account for the enhancement of the donor-acceptor energy transfer due to translational diffusion.

The fluorescence decay curves for each solvent were also well fit by the general multipolar decay law, Eq. (6.12). Except at the lowest acceptor concentrations, the power law exponent N could actually be determined from the fluorescence decay curves by least-squares adjustment. Table 6.1 shows that $N = 6.0 \pm 0.2$ was obtained in each solvent; this was unequivocal proof that the donor-acceptor energy transfer in this system was due to a dipole-dipole mechanism, and also further proof that the diffusion correction [13-15] was accurate.

The fluorescence results discussed above have established the validity of the Förster model [2], and the translational diffusion correction term [13-15] on the nanosecond time scale. The GSR data provided the same test on the picosecond timescale. As the results in Table 6.3 show, the interpretation of the GSR data was complicated by donor-donor excitation transfer. However, for donor concentrations $[D] \lesssim 10^{-3}M$ this process had a negligible effect. Under these conditions Eq. (6.10) fit the GSR curves very well, and gave R_o values in excellent agreement with the results from the fluorescence decay curves (Table 6.4). The GSR data for a methanol solution shown in Figure 6.4 should provide a good test for Eq. (6.10), since considerable diffusion-enhanced quenching was occurring in this sample. The excellent fit demonstrates that the Förster model including translational diffusion was valid from as early as 2 psec after excitation. Combined with the results of the fluorescence decay data, it can be concluded that the approximate solution to the combined long-range energy transfer and diffusion model derived by Gösele et al. [13-15] was accurate in this system over the time range 2 psec to 10 nsec. Our results are in accord with the findings of Klein et al. [14] who also tested Eq. (6.10) in the case $\ell > R_o$, but on a much longer time scale.

The R_o values obtained from the ethylene glycol data are plotted in Figure 6.6 against the reduced acceptor concentration defined by C_A/C_o (C_A is the molar acceptor concentration, and C_o is the critical concentration, $C_o = 3000/2\pi^{3/2} N R_o^3$.) The results are plotted in the form $R_o / \overline{R}_o$, where $\overline{R}_o$ is the average of the R_o values obtained at the highest

Figure 6.6

Critical transfer distances R_o as a function of acceptor concentration C_A are shown for three donor-acceptor systems: ● Cresyl violet: azulene, this work; Δ DODCI:malachite green, Adams et al. [9]; □ rhodamine 6G:malachite green, Porter and Tredwell [8]. The data are plotted in the form $R_o / \overline{R}_o$ versus reduced acceptor concentrations and C_o is the critical concentration (see text for details).

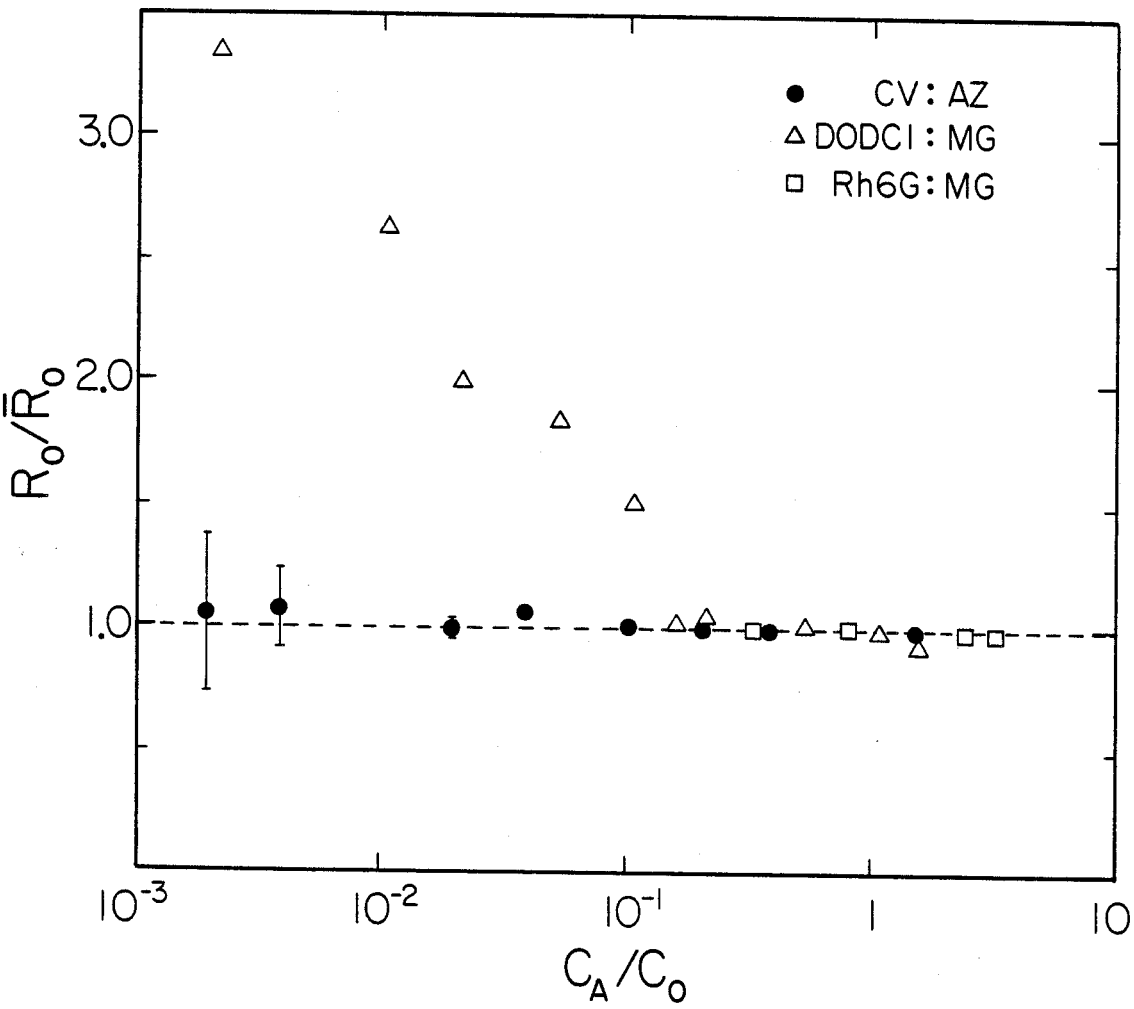
CV : AZ
DODCI : MG
Rh6G : MG
3.0
2.0
1.0
$R_o/\bar{R}_o$
10^{-3}
10^{-2}
10^{-1}
1
10
C_A/C_o

acceptor concentrations. Also plotted in Figure 6.6 are the results of Porter and Tredwell [8] for the Rh6G:MG system ($\bar{R}_o = 52.5$Å) and of Adams et al. [9] for DODCI:MG ($\bar{R}_o = 45.6$Å). Because these results are plotted in reduced units, all three sets may be directly compared. Note that our results span exactly the same range of reduced concentration as Adams et al. [9]; the Rh6G:MG results of Porter and Tredwell [8] only cover a limited portion of this range. All three sets fall close to 1.0 on the graph at the high end of the range, indicating that R_o was independent of C_A in this range. However, the R_o values of Adams et al. [9] increase rapidly as C_A/C_o decreases below 0.1, until R_o is some 200% larger at $C_A/C_o = 2 \times 10^{-3}$. On the basis of this behavior, these authors concluded that the Förster dipole-dipole rate expression (Eq. (6.1)) was not valid at low C_A. However, our results for the cresyl violet:azulene system showed no deviation: R_o was constant to within 10% over the same range. Referring to the 1/e-times in Table 6.2, it can be seen that the extent of quenching by the acceptors was very small at the lowest acceptor concentrations. Consequently, the fluorescence decay contained little information on the donor-acceptor transfer in this regime, and it was difficult to determine R_o accurately. This is indicated by the magnitude of the error bars for R_o shown in Figure 6.6. The lifetime and acceptor concentration must be very precisely known to accurately determine R_o at low C_A/C_o. The use of a <u>longer</u> lifetime in Eq. (6.10) can give rise to the same trend evident in data of Adams et al. [9]. For example, if $\tau_D = 2.98$ nsec was used in Eq. (6.10) (instead of 2.87 nsec), to fit the present data in ethylene glycol, R_o decreased from 71Å at $C_A/C_o = 2 \times 10^{-3}$ to a limiting value of 26.6Å when C_A/C_o exceeded 0.1. Thus an

error in τ_D of only 4% could yield an apparent deviation in the present data also of the same magnitude as reported by Adams et al. [9]. A small increase in the apparent lifetime could be caused by self-absorption effects, as was indeed observed here for cresyl violet at concentrations above 10^{-6}M. The donor concentration used by Adams et al. [9] was 10^{-4}M, suggesting that the inadvertent use of a longer donor lifetime was probably the cause of the concentration dependent deviation they observed.

Now that the validity of the diffusion model [13-15] has been demonstrated in treating translational diffusion, it is interesting to find whether the model can also be applied to donor-donor excitation transfer. This was best studied when translational diffusion was suppressed, such as in the GSR results for ethylene glycol, shown in Table 6.3. Obviously at the highest donor concentration, $C_D = 5 \times 10^{-3}$M, the donor quenching was considerably enhanced, as evident from comparison of the last two columns in Table 6.3. In all cases $D_E >> D_T$ in ethylene glycol. As described in Section 6.4c, R_o values that were reasonably independent of the donor concentration, and in good agreement with the fluorescence decay results, could only be obtained by the inclusion of D_E in Eq. (6.10). That is, $D = D_T + D_E$ was assumed. This procedure was valid if donor-donor excitation transfer was also diffusive. However, significant deviations between the GSR curve and the best-fit to Eq. (6.10) were observed in these cases. That is, although Eq. (6.10) in conjunction with Eq. (6.14) could provide an approximate correction for donor-donor transfer, insofar as giving the approximately correct R_o values, it could not reproduce the detailed time dependence of the donor

decay on the picosecond time scale.

In their theoretical study, Haan and Zwanzig [19] showed that donor-donor excitation transfer is nondiffusive in dilute solutions at short times. Expanding on this treatment, Gochanour et al. [20] subsequently calculated the mean-square displacement of the donor excitation for all times and concentrations. Their results clearly demonstrated that the generalized diffusion coefficient, the time derivative of the mean-square displacement, was time dependent for $t \lesssim 2.5\tau_D$ for reduced donor concentrations $C \lesssim 1.0$. At higher concentrations, D_E approached its long time limit more rapidly, and diffusive behavior was established over times of experimental interest. For the data shown in Figure 6.5, $C = 1.1$ and nondiffusive behavior is expected. The deviation in Figure 6.5 is qualitatively consistent with a time-dependent diffusion coefficient--the donor decay was faster at early times, implying that D_E was larger than the long time limit given by (6.14). The observed deviations suggest that donor-donor excitation transfer in this system was nondiffusive over the 175 psec timescale shown in Figure 6.5 in accord with the results of Haan and Zwanzig [19], and Gochanour et al. [20].

In Table 6.4 a summary of the average R_0 value obtained by each transient experiment and from the steady state spectra is presented. Recall that different correction terms have been included in the theoretical fits of the transient data. Even so, the R_0 values obtained by each method agree very well. This is good evidence that the assumptions underlying the formal equivalence of the GSR and fluorescence experiment were valid in this system. Of the three results listed in Table 6.4, the most

TABLE 6.4

Summary of Critical Transfer Distances

Method	Methanol	Ethylene Glycol
Fluorescence decay[a]	26.6 ± 0.3	25.7 ± 0.3
GSR[a]	26.2 ± 0.6	26.4 ± 0.6
Spectral integration	27.8 ± 1.0	26.3 ± 1.0

[a]Results given here are weighted averages of the results in Tables 6.2 and 6.3.

accurate was obtained from measurements of fluorescence decays. More important, this method allowed R_0 to be obtained over a wide range of acceptor concentrations. The good agreement between R_0 from the transient experiments and from the steady-state spectra is further evidence that the Förster dipole-dipole model was valid in this system.

6.6 Conclusions

The important findings of this study may be summarized as follows:

(i) Energy transfer between cresyl violet and azulene was due to a dipole-dipole mechanism.

(ii) The Förster dipole-dipole model must be extended to include the additional donor quenching due to translational diffusion in the methanol and ethylene glycol solutions investigated here. Equations (6.10) and (6.12), which are approximate solutions [13-15] to a diffusion equation for the donor excitation including both energy transfer and translational diffusion, accurately fit both the GSR and fluorescence decay curves, spanning a time interval from 2 psec to more than 10 nsec. This was the first test of this model [13-15] on these time scales.

(iii) The values of the critical transfer distance obtained from GSR, fluorescence decay, and steady-state experiments were in agreement, which was further proof of the theory.

(iv) The critical transfer distance was constant over a 1000-fold range of acceptor concentrations, proving that the Förster model was valid over this range. There was no evidence of the apparent deviations reported by Adams et al. [9] at low concentrations for the

DODCI:MG system.

(v) Donor-donor excitation transfer increased the rate of D-A energy transfer, as did mass-diffusion. However, the deviations observed between the GSR data and the diffusion model suggested time-dependent donor excitation diffusion coefficients on the picosecond time scale, in accord with theory [12,13].

References - Chapter 6

1. D. P. Millar, R. J. Robbins, A. H. Zewail, J. Chem. Phys. 75, 3649 (1981).
2. T. Förster, Z. Naturforsch 4a, 321 (1949); Discuss. Faraday Soc. 27, 7 (1959).
3. D. L. Dexter, J. Chem. Phys. 21, 836 (1953).
4. M. Inokuti and F. Hirayama, J. Chem. Phys. 43, 1978 (1965).
5. R. G. Bennett, J. Chem. Phys. 41, 3037 (1964).
6. M. D. Galanin, Sov. Phys. JETP 1, 317 (1955).
7. D. Rehm and K. B. Eisenthal, Chem. Phys. Lett. 9, 387 (1971).
8. G. Porter and C. J. Tredwell, Chem. Phys. Lett. 56, 278 (1978).
9. M. C. Adams, D. J. Bradley, W. Sibbett, and J. R. Taylor, Chem. Phys. Lett. 66, 428 (1979).
10. P. R. Butler and M. J. Pilling, Chem. Phys. 41, 239 (1979).
11. R. A. Auerbach, G. W. Robinson, and R. Zwanzig, J. Chem. Phys. 72, 3528 (1980).
12. K. Allinger and A. Blumen, J. Chem. Phys. 72, 4608 (1980).
13. U. Gösele, M. Hauser, U.K.A. Klein, and R. Frey, Chem. Phys. Lett. 34, 519 (1975).
14. U.K.A. Klein, R. Frey, M. Hauser, and U. Gösele, Chem. Phys. Lett. 41, 139 (1976).
15. U. Gösele, Spec. Lett. 11, 445 (1978).
16. M. Yokota and O. Tanimoto, J. Phys. Soc. Japan 22, 779 (1967).
17. A. Blumen, J. Klafter, and R. Silbey, J. Chem. Phys. 72, 5320 (1980).
18. T. Förster, Ann. Phys. (Leipzig) 2, 55 (1948).

19. S. W. Haan and R. Zwanzig, J. Chem. Phys. 68, 1879 (1978).

20. C. R. Gochanour, H. C. Andersen, and M. D. Fayer, J. Chem. Phys. 70, 4254 (1979).

21. U. Gösele, M. Hauser, and U.K.A. Klein, Z. Phys. Chem. 99, 81 (1976).

22. M. Leibowitz, J. Phys. Chem. 69, 1061 (1965).

23. B. Ia. Sveshnikov, Sov. Phys. Dokl. 1, 633 (1956).

24. I. M. Rozman, Opt. Spektrosk. 4, 536 (1958).

25. T. R. Waite, Phys. Rev. 107, 463 (1957).

26. R. E. Dale and J. Eisinger, Biopolymers 13, 1573 (1974).

27. K. B. Eisenthal and S. Siegel, J. Chem. Phys. 41, 652 (1964); erratum 42, 814 (1965).

28. I. Z. Steinberg, J. Chem. Phys. 48, 2411 (1968).

29. C. Bojarski and J. Dudkiewicz, Chem. Phys. Lett. 67, 450 (1979).

30. A. Einstein, Investigations on the Theory of Brownian Movement, Dover, New York, 1956.

31. D. L. Huber, Phys. Rev. B 20, 2307 (1979), and refs. therein.

32. D. Huppert, J. Jortner, and P. Rentzepis, J. Chem. Phys. 56, 4826 (1972).

33. D. Magde, J. H. Brannon, T. L. Cremers, and J. Olmsted III, J. Phys. Chem. 83, 696 (1979).

Chapter 7

TORSION AND BENDING DYNAMICS OF NUCLEIC ACIDS*

7.1 Introduction

Time-dependent fluorescence depolarization is a powerful technique for the study of molecular reorientation, and has been widely applied on both the nanosecond and picosecond time scales. For rigid molecules, such experiments have provided considerable information about molecular size, conformation, and the strength of solute-solvent interactions. Although fluorescence depolarization can also be used to study internal motions of flexible molecules, which are relevant, for example, to photoisomerization and the function of many biological macromolecules, few time-resolved experiments have been reported to date [1-8].

Although a great deal is known about the equilibrium structures of macromolecules in solution, the dynamic properties of these structures remain relatively unexplored. Studies of internal motions of macromolecules are important as a probe of their flexibility and conformational mobility. As a first step in this direction, it is useful to begin with a relatively simple system. A typical macromolecule with a complex three-dimensional structure and regions of differing flexibility will exhibit a complex time dependence. A good choice for a prototype system are the nucleic acids labelled with a fluorescent chromophore, since they have relatively simple structures and, probably, also uniform flexibility. From the point of view

---

*The results presented in this chapter were first reported in references [1-5].

of the internal motions, the nucleic acid structure is essentially an array of identical subunits. The internal motions of this simple structure are more well defined and many of the low frequency modes have been elucidated. For example, the end-over-end persistence length rotations and coil deformation modes have been well characterized by dynamic light scattering and electric dichroism techniques. The high frequency internal modes, which dominate the short-time behavior of a fluorescence depolarization experiment, are the torsion (twisting) and bending modes of the double helix. Very little is known about these high frequency internal motions. Time-dependent fluorescence depolarization of intercalated dyes is an ideal technique for probing these motions. Theoretical models can be meaningfully applied in this case, since analytical expressions for the fluorescence anisotropy can be obtained and compared with experimental data. Thus a study of the twisting and bending modes of nucleic acids is first and foremost a problem in chemical physics, since it is a relatively simple example of the dynamic behavior of macromolecules in general, and more important, this is a system in which a quantitative rather than a qualitative approach can be employed.

The internal motions of nucleic acids are also important from a biophysical and biological perspective. Many of the large-scale structural features of duplex DNA, such as supercoiling and packaging in chromosomes and bacteriophage heads, can be accounted for by elastic models wherein DNA is completely characterized by its bending and torsional rigidities [9-12]. It is of interest whether or not the torsion and bending dynamics can be accounted for by the same elastic model. If so, quantitative estimates of the torsional and bending rigidities could be obtained, which would be useful.

Torsional modes are also relevant to biological phenomena such as transient local unwinding of the helix [13], the ability of hydrogen-bonded ring protons of the bases in DNA to exchange at temperatures well below the denaturation point [14], and, perhaps right-to-left handed (B→Z) transitions [15].

Rapid internal motions in DNA are suggested by two types of experiments. In nanosecond fluorescence depolarization experiments Wahl, Paoletti, and Le Pecq [6] detected a rapid ($\sim$28 ns) decay of the fluorescence polarization anisotropy of ethidium bromide intercalated in DNA. Presumably the dye is rigidly bound to the double-stranded DNA and thus reports local torsional and bending motions of the helix. Recent NMR experiments [16-18] suggest that fast conformational fluctuations of the sugar-phosphate backbone occur in both DNA and RNA and have time constants of the order of 0.3 ns to 1 ns. Taken together, these studies indicate that considerable flexibility of the DNA helix may be expected on nanosecond and subnanosecond time scales. Unfortunately the NMR experiments provide only an indirect probe of the internal motion, while the limited time resolution ($\sim$5 ns) of the nanosecond fluorescence depolarization experiment [6] makes it unlikely that any subnanosecond motions could have been detected.

On the theoretical side, the torsional and bending dynamics of DNA have also aroused considerable interest. In a recent paper Barkley and Zimm [11] presented an elastic continuum model of DNA. They predict that the decay of the fluorescence polarization anisotropy of an intercalated dye should be complex, containing exponentials in $t^{1/2}$ due to twisting (torsion) and in $t^{1/4}$ due to bending motions, and that the observed

depolarization arose primarily from torsional motions. However, the limited time resolution (≃ 5 nsec) of the experimental data then available [6] made a rigorous test of the model impossible, and a precise value for the torsional rigidity could not be obtained.

The elastic model is formally equivalent to the more familiar bead-spring model (except at very early times), which has been analyzed in detail by Allison and Schurr [19]. They also obtain an exponential-$t^{1/2}$ torsional relaxation at intermediate times, but predict an initial exponential decay characteristic of uncoupled motions of the individual beads at sufficiently short times. They also consider the possibility that the DNA helix is not uniformly elastic but contains isolated torsion joints (i.e., separated by more than one base pair). In fact, Allison and Schurr find that two sets of parameters--one corresponding to a bead length of 86 base pairs with the observed relaxation falling in the initial exponential decay zone, and another corresponding to a bead length 1 base pair with relaxation in the intermediate exponential-$t^{1/2}$ zone--can fit the existing fluorescence depolarization data of Wahl et al. [6] equally well. Le Bret [9] has also discussed the torsional dynamics of DNA within the context of a bead-spring model. These two models are briefly reviewed in Section 7.2.

Clearly, fluorescence depolarization data with subnanosecond time resolution and extremely high signal-to-noise ratio are needed to test and distinguish between the theoretical models outlined above. The approach used in this study has been to use picosecond pulses from a mode-locked argon laser and the subnanosecond single photon counting apparatus described in Chapter 4 to monitor the fluorescence depolarization of ethidium bromide

intercalated in DNA and RNA. The apparatus combines excellent time resolution (250 ps), good signal-to-noise ratio (> 100:1), high sensitivity, and freedom from systematic distortions of the data. This has enabled the direct observation of the nonexponential torsional and bending relaxation of both DNA and RNA in solution, and has allowed the first direct measurement of the torsional rigidity of DNA. The effect of primary, secondary, and tertiary nucleic acid structure on the torsional and bending dynamics was investigated by a series of experiments on different DNA samples. These included the dependence of the torsional rigidity on the base sequence in a series of model polynucleotides, the rigidity of intact and denatured DNA, the relative torsional rigidity of the double and triple helix, the effect of tertiary structure in supercoiled plasmid DNA, and the magnitude of the polyelectrolyte contribution to the torsional rigidity of DNA. These results are presented and discussed in subsequent sections of this chapter.

7.2 Theoretical Considerations

In fluorescence depolarization experiments, a linearly polarized light pulse preferentially excites those molecules whose transition dipoles are nearly parallel to the electric field of the exciting light. This results in an initial polarization of the fluorescence, which decays in time due to rotational Brownian motion. As shown in Chapter 4, the depolarization is conveniently represented by the time-dependent fluorescence polarization anisotropy r(t), defined by

$$r(t) = [i_{\parallel}(t) - i_{\perp}(t)] / [i_{\parallel}(t) + 2i_{\perp}(t)] \qquad (7.1)$$

where $i_{\parallel}(t)$ and $i_{\perp}(t)$ are the observed fluorescence intensities polarized parallel and perpendicular, respectively, to the polarization of the exciting light. For an asymmetric rigid molecule, r(t) consists of a sum of five exponentials whose decay times depend solely on the principal diffusion coefficients. However, for a nonrigid molecule, the anisotropy will have additional contributions from internal motions whose decay times depend on the flexibility.

In the present experiments, the internal motions of nucleic acids are monitored by the time-dependent fluorescence depolarization of intercalated dyes. The particular dye that was chosen, ethidium bromide, binds strongly to double-stranded nucleic acids [20,21] by intercalation between adjacent base pairs such that the plane of the phenanthridinium ring (which contains the transition dipole) makes an angle of about 70° with the helix axis [22]. Presumably the dye is rigidly bound and thus reports local motions of the helix. The double-stranded nucleic acids used in this work are very long ($\sim 10^3 - 10^4$ base-pairs) while the duplex structure confers stiffness on the helix, as measured by its persistence length of about 525Å [see Section 7.4b]. Rotation of the entire molecule and long-range segmental motions are therefore slow, at least of the order of microseconds, and cannot contribute to the depolarization observed on the nanosecond time-scale. What is expected to be seen in the fluorescence depolarization experiments are rapid torsional motions of the helix, with a smaller contribution from bending and, perhaps, a limited wobbling of the dye within its intercalation site.

The connection between the fluorescence depolarization experiments and the torsion and bending dynamics of DNA has been analyzed in detail by

Barkley and Zimm [11] using an elastic model, and by Allison and Schurr [19] using a bead-spring model. Both approaches are now briefly outlined and the important results presented in each case.

a. Elastic model

According to this model [11], the DNA molecule is treated as a thin, uniformly flexible rod of length 2L and circular cross-section of radius b, immersed in a viscous fluid at thermal equilibrium. The rod is characterized by a torsional rigidity C and a friction coefficient per unit length ρ, given by

$$\rho = 4\pi\eta b^2 \tag{7.2}$$

where η is the viscosity of the fluid. Dynamical equations for torsion and bending of the rod are generated using results from classical elasticity and hydrodynamic equations. An outline of the derivation for the torsional motions is now given. The rotational diffusion equation of the rod in normal coordinates is [11]

$$\frac{\partial\psi}{\partial t} = \sum_{k=0}^{\infty} \left[D_1 \frac{\partial^2\psi}{\partial\xi_k^2} + \nu\lambda_k^2 \left(\xi_k \frac{\partial\psi}{\partial\xi_k} + \psi\right)\right] \tag{7.3}$$

where $\psi(\{\xi_k\},t)$ is the multivariate time distribution of the set of normal coordinates $\{\xi_k\}$, $D_1 = k_B T/\rho$ is the diffusion equation for rotation of the rod about its long axis, $\nu = C/\rho$, k_B is the Boltzmann constant, and T is the absolute temperature. The sum extends over all the torsional modes, which are wave-like disturbances with wavenumber $\lambda_k = k\pi/L$. It is assumed that ψ can be separated into a product of distribution functions, one for each mode,

$$\psi(\{\xi_k\},t) = \prod_{k=0}^{\infty} \phi_k(\xi_k,t) \tag{7.4}$$

Substitution of this expression in Eq. (7.3) yields a set of differential equations, one for each normal mode,

$$\frac{\partial \phi_k}{\partial t} = D_1 \frac{\partial^2 \phi_k}{\partial \xi_k^2} + \nu \lambda_k^2 (\xi_k \frac{\partial \phi_k}{\partial \xi_k} + \phi_k) \text{ , for all } k \tag{7.5}$$

These equations have the form of the Fokker-Planck equation for which the general solutions are well known [11]. However, the solutions have to be adapted to some initial condition, which in this case is that the initial distribution function (at $t = 0$) is the equilibrium distribution, obtained by solving Eq. (7.3) in the case that $\partial\psi/\partial t = 0$. Since it is only the orientation of the dye that can be observed, one solves Eq. (7.5) given the initial condition described above and for an initial dye orientation γ_o. The distribution function for the dye orientation γ at time t due to torsion is then found by averaging over all the normal mode coordinates. The result is [11]

$$\psi_d(\gamma,t;\gamma_o,\{\phi'\}^o) = (\pi\Gamma)^{-1/2} \cdot \exp[-(\gamma-\gamma_o)^2 / \Gamma] \tag{7.6}$$

where $\{\phi'\}^o$ is the initial distribution of the normal mode distribution functions. The dye distribution is a Gaussian function with a time dependent width $\Gamma(t)$, which is known as the torsion decay function and is given by

$$\Gamma(t) = 4D_1 t + (4k_B T/CL) \sum_{k=1}^{\infty} (1 - e^{-t/\tau_k}) / \lambda_k^2 \tag{7.7}$$

which describes a superposition of relaxations due to all torsional normal

modes of the rod, with wavenumber λ_k, wavelength $\ell_k = 2\pi/\lambda_k$, and with relaxation times τ_k. The first term corresponds to rotation of the entire rod about its long axis. The torsional relaxation times are given by

$$\tau_k = \rho/C\lambda_k^2 \tag{7.8a}$$

$$= \ell_k^2(\eta b^2/\pi C) \tag{7.8b}$$

A similar analysis for bending gives for the distribution of dye orientations due to bending [11],

$$\psi_d(\alpha,t;\alpha_o,\{\phi'^o\}) = (\pi\Delta)^{-1/2} \cdot \exp[-(\alpha-\alpha_o)^2/\Delta] \tag{7.9}$$

which is also a Gaussian function with a width Δ . $\Delta(t)$ is the bending decay function

$$\Delta(t) = 4D_2t + (4k_BT/EIL) \sum_{k\ \text{even}}^{\infty} (1 - e^{-t/\tau'_k})/\kappa_k^2 \tag{7.10}$$

which describes a superposition of relaxations due to bending normal modes of the rod, with relaxation times τ'_k and wavenumbers $\kappa_k \simeq (2k+1)\pi/4L$, plus a term corresponding to rotation of the entire rod about a transverse axis, with diffusion coefficient D_2; EI is the bending rigidity of the rod. The bending relaxation times are

$$\tau'_k = \rho_k/EI\ \kappa_k^2 \tag{7.11}$$

where the friction coefficients for bending ρ_k depend on k,

$$\rho_k = 4\pi\eta / \kappa_k^2\ f(\kappa_k b) \tag{7.12}$$

with f(z) a sum of modified Bessel functions,

$$f(z) = K_0(z) + (z/2)\, K_1(z) \tag{7.13}$$

For certain times in the decay process, the cumbersome expressions for Γ and Δ, Eqs. (7.7) and (7.10) can be approximated by simple expressions. At sufficiently short times, the discrete sums can be replaced by integrals via the Euler-Maclaurin summation formula plus its leading correction term and integrated by parts; at very long times, the exponentials vanish and the infinite series can be summed directly. The resulting approximate expressions for Γ are

$$\Gamma(t) \simeq \begin{cases} At^{1/2} & t \lesssim \rho L^2/C \qquad (7.14a) \\ 4D_1 t + 2k_B TL/3C & t \gg \rho L^2/C \qquad (7.14b) \end{cases}$$

with

$$A = 2k_B T/\pi b\eta^{1/2} C^{1/2} \tag{7.15}$$

In Eq. (7.10) for the bending decay function, the Bessel function term appearing in the exponent is treated as a constant for purposes of integration, and the value of the argument that maximizes the integrand, z_{max}, is used to compute this constant. The resulting expressions for Δ are

$$\Delta(t) \simeq \begin{cases} B(t)\, t^{1/4} & t \lesssim \tau_1' \qquad (7.16a) \\ 4D_2 t + 0.4853\, k_B TL/EI & t \gg \tau_1' \qquad (7.16b) \end{cases}$$

where B(t) is a slowly-varying function of time,

$$B(t) = [3.466\, k_B T/\pi^{5/4}\, \eta^{1/4}\, EI^{3/4}]\, f(z_{max})^{1/4} \tag{7.17}$$

and z_{max} is determined by iteration from the equation

$$z_{max}(t) \simeq b[5.024\pi\eta/\ EIt\ f(z_{max})]^{1/4} \tag{7.18}$$

The short time behavior of $\Gamma(t)$ and $\Delta(t)$ given by Eqs. (7.14a) and (7.16a) do not depend explicitly on chain length, although the length enters through the time domain for which these expressions are valid. Thus any DNA of sufficient length to satisfy the inequalities in (7.14a) and (7.16a) for all times of experimental interest will exhibit length independent relaxation dynamics.

b. Bead-spring model

The bead-spring model has been analyzed by Allison and Schurr [19] and also by Barkley and Zimm [11], who presented a somewhat simpler derivation which will be given here. According to this model, the DNA molecule is considered as an array of (N+1) beads strung out along an axis and indexed from 0 to N. The (N+1) beads are linked by N identical torsional springs, each having an equilibrium rotation such that a helix is formed at equilibrium. The rotation angle of each bead is measured relative to this equilibrium position. The springs are assumed to obey Hooke's law with a spring constant c. The chain is immersed in a viscous fluid at equilibrium.

The rotational diffusion equation in normal coordinates for rotations of beads about the chain axis is [11]

$$\frac{\partial\psi}{\partial t} = \sum_{k=0}^{N} [D_b \frac{\partial^2\psi}{\partial\xi_k^2} + \nu_b\ \mu_k(\xi_k \frac{\partial\psi}{\partial\xi_k} + \psi)] \tag{7.19}$$

where $\nu_b = c/\rho_b$, $D_b = kT/\rho_b$ is the diffusion coefficient of a single bead, ρ_b is the friction coefficient of a single bead, and

$$\mu_k = 4 \sin^2[k\pi/2(N+1)] \tag{7.20}$$

Equation (7.19) is very similar to the rotational diffusion equation in the elastic model, Eq. (7.2). The differences, which are in the upper limits of the summations and the different definitions of λ_k^2 and μ_k, and other coefficients, reflect differences in the details of the two models. Another difference to note is that ρ_b and c are defined per bead whereas ρ and C of the elastic model are defined per unit length. Thus $\rho_b = (2L/N+1)\rho$ and $c = (N+1/2L)C$.

The time-dependent distribution function specifying the dye orientation due to torsion is found to be of the same form as Eq. (7.4), except that the torsion decay function is given by [11]

$$\Gamma_b(t) = 4D_1 + 8D_b(N+1)^{-1} \sum_{k=1}^{N/2} (1 - e^{-t/\tau_{2k}}) \cdot \tau_{2k} \tag{7.21}$$

The relaxation time of the j^{th} mode with wavelength $\ell_j = 2L/j$ is

$$\tau_j = 1/\sigma_b \mu_j \tag{7.22a}$$

$$\simeq \ell_j^2(4\eta b^2/\pi C) \tag{7.22b}$$

where the approximation in the second equation was obtained by expanding the sine function in the expression for μ_j, Eq. (7.20). This result illustrates another difference between the two models; the relaxation times of the torsional modes have different definitions in each model, as seen by comparison of Eqs. (7.8b) and (7.22b). The relaxation times in the bead-spring model are four times longer than those in the elastic model.

For certain times in the decay process Eq. (7.21) can be approximated by simple functions. At very short times the exponentials can be expanded

to first order and the series summed directly. At intermediate times the sine term in Eq. (7.20) is expanded to first order, and the summation is replaced by an integral via the Euler-Maclaurin formula. At long times the exponentials vanish and the series are summed directly. The resulting approximate equations for $\Gamma_b(t)$ are

$$\Gamma_b(t) = \begin{cases} 4D_b(t) & , \quad t \ll \rho_b/4c & (7.23a) \\ At^{1/2} & , \quad 1 \ll \pi^2 ct/\rho_b < (N+1)^2/4 & (7.23b) \\ 4D_1 t + 2k_B TL/3C & , \quad t \gg \rho_b/4c & (7.23c) \end{cases}$$

where A is the same as in the elastic model, Eq. (7.15). Comparing these expressions with the analogous approximate expressions in the elastic model, Eq. (7.14), reveals the important similarities and differences between the two models. The bead-spring model predicts an identical time-dependence to Eq. (7.14) except at very early times. The bead-spring model introduces an additional time-dependence due to the uncoupled motions of the beads at early times. Of course this limit is never attained in the case of a continuous rod. For intermediate times both models predict $\Gamma(t) = At^{1/2}$ which is a characteristic behavior due to the superposition of all the torsional modes. The relaxation dynamics in this regime are determined by the macroscopic torsional rigidity and are insensitive to whether the structure is continuous or discrete. One can verify that the upper time limit in (7.23b) is equivalent to that in (7.14a). At long times the two models are also equivalent, except that the time limits in (7.14b) and (7.23c) are slightly different.

The bending dynamics have not yet been solved for the bead-spring model.

c. Fluorescence polarization anisotropy

Barkley and Zimm [11] adapted Eqs. (7.6) and (7.9) to the initial conditions appropriate in a fluorescence depolarization experiment. Their final expression for the anisotropy can be written in the form

$$r(t) = r_0[A_4(\varepsilon) + A_5(\varepsilon)\, e^{-\Delta}]^{-1} \{A_1(\varepsilon)\, e^{-\Delta} + A_2(\varepsilon)[5/8 + 3/8\, e^{-\Delta}]\, e^{-\Gamma} + A_3(\varepsilon)\, e^{-\Delta}\, e^{-\Gamma/4} \qquad (7.24)$$

where r_0 is the limiting anisotropy (which has a theoretical maximum value of 0.4), Γ and Δ are the torsion and bending decay functions, respectively, and the $A_j(\varepsilon)$ are simple trigonometric functions of the angle ε between the transition dipole of the intercalated dye and the helix axis,

$$\begin{aligned} A_1(\varepsilon) &= \tfrac{1}{4}(1 - 3\cos^2\varepsilon)^2 \\ A_2(\varepsilon) &= \tfrac{3}{4}\sin^4\varepsilon \\ A_3(\varepsilon) &= 3\sin^2\varepsilon\cos^2\varepsilon \\ A_4(\varepsilon) &= \tfrac{3}{4}(1 + \cos^2\varepsilon) \\ A_5(\varepsilon) &= \tfrac{1}{4}(1 - 3\cos^2\varepsilon) \end{aligned} \qquad (7.25)$$

This equation is valid for both the elastic and bead-spring models (although the bending decay function has not been evaluated in the bead-spring model).

It is also useful to consider some special cases of Eq. (7.24). When bending is absent, $\Delta = 0$, the anisotropy is given by

$$r(t) = r_0\{A_1(\varepsilon) + A_2(\varepsilon)\, e^{-\Gamma} + A_3(\varepsilon)\, e^{-\Gamma/4}\} \qquad (7.26)$$

When the dye is perpendicular to the helix axis, a very simple form results,

$$r(t) = r_o\{\frac{1}{4} + \frac{3}{4} e^{-\Gamma}\} \tag{7.27}$$

Barkley and Zimm [11] have also considered the problem of an initial, very rapid, but limited disorientation of the transition dipole caused, for example, by wobbling of the dye within its intercalation site. They show that this initial disorientation can be accounted for by replacing $\Gamma(t)$ in the expression for the anisotropy, Eq. (7.24), by $\Gamma(t) + \Xi$, where Ξ is the wobble parameter. The square root of Ξ measures the width of the (Gaussian) distribution of dye orientations after wobbling.

Equation (7.24) for the fluorescence polarization anisotropy and the short-time approximations for Γ and Δ, Eqs. (7.14), (7.16), and (7.23) constitute the most useful results of this section. They will be applied to the analysis of the experimental data in Section 7.4.

7.3 Experimental

a. Samples

Ethidium bromide (2,7-diamino-10-ethyl-9-phenyl phenanthridinium bromide), calf thymus DNA and total soluble yeast RNA were obtained from Sigma and used without further purification. The chemical structure of ethidium bromide is shown in Figure 7.1. Calf thymus DNA is approximately 10,000 base pairs long and has the familiar Watson-Crick double-helical (duplex) structure. Total yeast RNA is heterogeneous: the dominant component is ribosomal RNA ($\sim$80%) which itself consists of three

Figure 7.1

Chemical structure of ethidium bromide

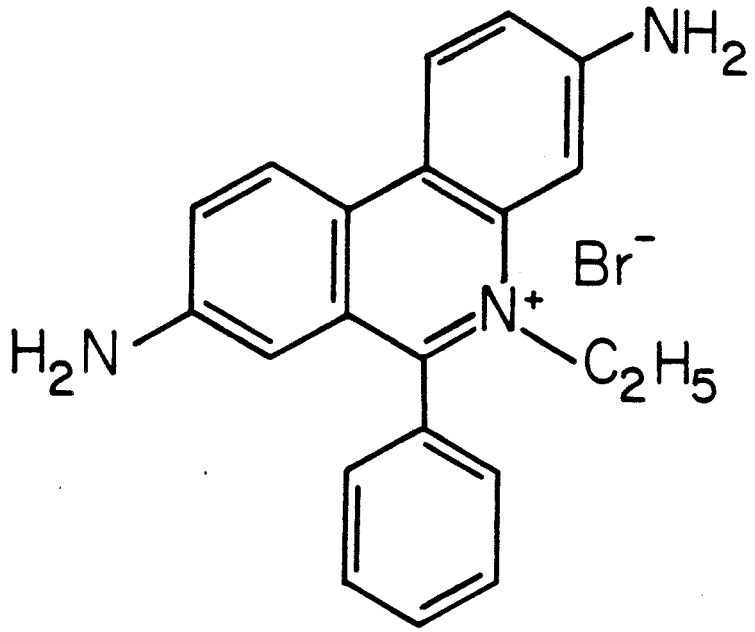
NH2
Br-
N+
H2N
C2H5

fragments with molecular weights of about 1×10^6, 5×10^5, and 4×10^4. Although RNA does not have a duplex structure, the single chain can fold back on itself to form short, irregularly distributed base-paired regions constituting ~50% of the total.

Supercoiled pBR 322 plasmid DNA was prepared according to standard procedures [23] and was purified by two cycles of density gradient ultracentrifugation. This plasmid DNA is about 4000 base pairs long and is in the form of a closed circle.

The synthetic polynucleotides (Table 7.1) were obtained from PL Biochemicals and dialyzed against appropriate buffers for 24 hours before use. Because of their very simple base sequences, the polynucleotides can form a variety of structures in solution [24]. These structures comprise individual double helical rods, end-to-end aggregates, and hairpin loops (formed when a single strand folds on itself to form a double helix. Only possible with an alternating self-complementary sequence, especially poly d(A-T) · poly d(A-T)). A typical polynucleotide solution will therefore contain a distribution of duplex lengths. The distributions for most of the polynucleotides used in this work have been reported by Becker [24]. The double-strand length in the rods is between 500 and 1000 base-pairs, in the hairpins is about 500 base-pairs, and in the aggregates is several thousand base-pairs [24]. Thus the minimum double-strand length in any of the synthetic polynucleotides is about 500 base-pairs, while the average length is considerably more. These estimates are consistent with the average molecular weights, which are between 3×10^5 and 1×10^6 dalton, inferred [25] from the sedimentation coefficients of the polynucleotide samples (between 7 and 10 S).

All the DNA samples were sufficiently long that they were expected to exhibit length-independent relaxation behavior described by Eqs. (7.14), (7.16), and (7.23). It can be verified that these equations are valid over the entire fluorescence decay for DNA chains longer than about 200 base-pairs. Samples were prepared using triply distilled water (adjusted to pH 7.7 with dilute NaOH) or Tris·HCl pH 7.7 buffer, and the desired ionic strength obtained by adding NaCl. Nucleotide-to-dye ratios (P/D) were in the range 90:1 to 900:1. All fluorescence measurements were performed at room temperature (23°C). Denaturation of DNA-ethidium samples was achieved by heating to 100°C for five minutes and then cooling rapidly to room temperature.

b. Time-resolved fluorescence measurements

Time-resolved fluorescence measurements were performed using the apparatus described in Section 4.4. The excitation wavelength was 5145Å and the pulse width 95 psec (mode-locked argon ion laser). The fluorescence components polarized parallel $i_\parallel(t)$ and perpendicular $i_\perp(t)$ to the direction of polarization of the excitation pulse were acquired alternately in the multichannel analyzer for equal total analyzer live-times (4,000 to 10,000 sec each). Cut-off filters (Schott OG 570 and OG 590) were used to isolate emission at wavelengths longer than 590 nm and remove scattered laser light.

c. Data analysis

In the experiments reported here, the instrument response function was sufficiently narrow (250 psec) that the observed fluorescence decays were not distorted by convolution. The fluorescence decay law s(t),

obtained by setting the emission polarizer at 54.7° to the direction of parallel polarization, was fit to a sum of exponentials

$$s(t) = A[f\, e^{-t/\tau_n} + (1 - f)\, e^{-t/\tau_i}] \tag{7.28}$$

where A was the amplitude, τ_n and τ_i were the lifetimes of the non-intercalated and intercalated dye species, respectively, and f was the fraction of non-intercalated dye. As discussed in Chapter 4, for the analysis of fluorescence depolarization data the experimental sum and difference curves defined by Eq. (4.6) were first formed. These functions were taken to be of the form

$$s(t) = A\, e^{-t/\tau_i} \tag{7.29a}$$

$$d(t) = r(t) \cdot s(t) \tag{7.29b}$$

with the fluorescence polarization anisotropy r(t) given by Eqs. (7.24) and (7.14) and (7.16). Of the quantities appearing in the expression for the anisotropy, the helix radius b, the flexural rigidity El, the dye-tilt ε, and the limiting anisotropy r_o were estimated from available data (Section 7.4), while the torsional rigidity C and the wobble parameter Ξ were treated as adjustable parameters and optimized by nonlinear least squares adjustment (Appendix II). The values of the four parameters A, τ_i, C and Ξ were then adjusted so as to simultaneously obtain the best fit of the experimental s(t) and d(t) curves to the model defined by Eq. (7.29). In samples where there was a significant fraction of free ethidium ($\tau_i \simeq 1.8$ nsec) it was necessary to ignore the first 5 nsec of the decays in the fitting procedure performed on a PDP 11/23 computer

using a nonlinear least-squares algorithm. The quality of the fits was judged by the reduced chi-squared (χ^2_r) criterion and by inspection of the weighted residuals and the residual autocorrelation function (Appendix II).

7.4 Results

a. Fluorescence lifetimes

The fluorescence decays of ethidium bromide in aqueous solution (1 μg/ml in 0.1 M Tris·HCl, pH 7.7/0.15M NaCl) and bound to the nucleic acids (100 μg/ml nucleic acid, P/D ≃ 120) were measured by setting the emission polarizer at 54.7° to the direction of polarization of the exciting light (Table 7.1). A typical fluorescence decay curve, for the ethidium-calf thymus DNA system is shown in Figure 7.2.

For free ethidium bromide, the fluorescence decay was exponential with a lifetime of 1.8 nsec. Upon binding to the nucleic acids there was a striking increase in the fluorescence lifetime of ethidium bromide (Table 7.1), which provided a sensitive test for intercalation. However, for none of the samples was a purely single exponential decay observed: in each case the data could be fit to a sum of two exponentials [Eq. (7.28)] with lifetimes of approximately 2-3 nsec and 20-27 nsec. The lifetime of the shorter component ($\sim$2-3 nsec) was similar to that measured for free ethidium bromide (1.8 nsec). However, due to the small fraction of this component and the resulting uncertainty in its lifetime, the possibility of a contribution from an electrostatically bound complex [21] with a lifetime intermediate between those of the free and intercalated dye could not be excluded. The two components were therefore

Figure 7.2

Isotropic fluorescence decay (54.7°) of the ethidium: calf thymus DNA complex in aqueous tris buffer, pH 7.7/0.15 M NaCl. Points are experimental data. The smooth line is the best fit to Eq. (7.28) with $\tau_n = 2.00 \pm 1.2$ nsec, $\tau_i = 22.38 \pm 0.20$ nsec, $f = 0.062 \pm 0.027$, and $\chi_r^2 = 1.078$. The weighted residuals and their autocorrelation function $A(\tau)$ are also shown (the time scale along the τ axis is 0 to 50 nsec).

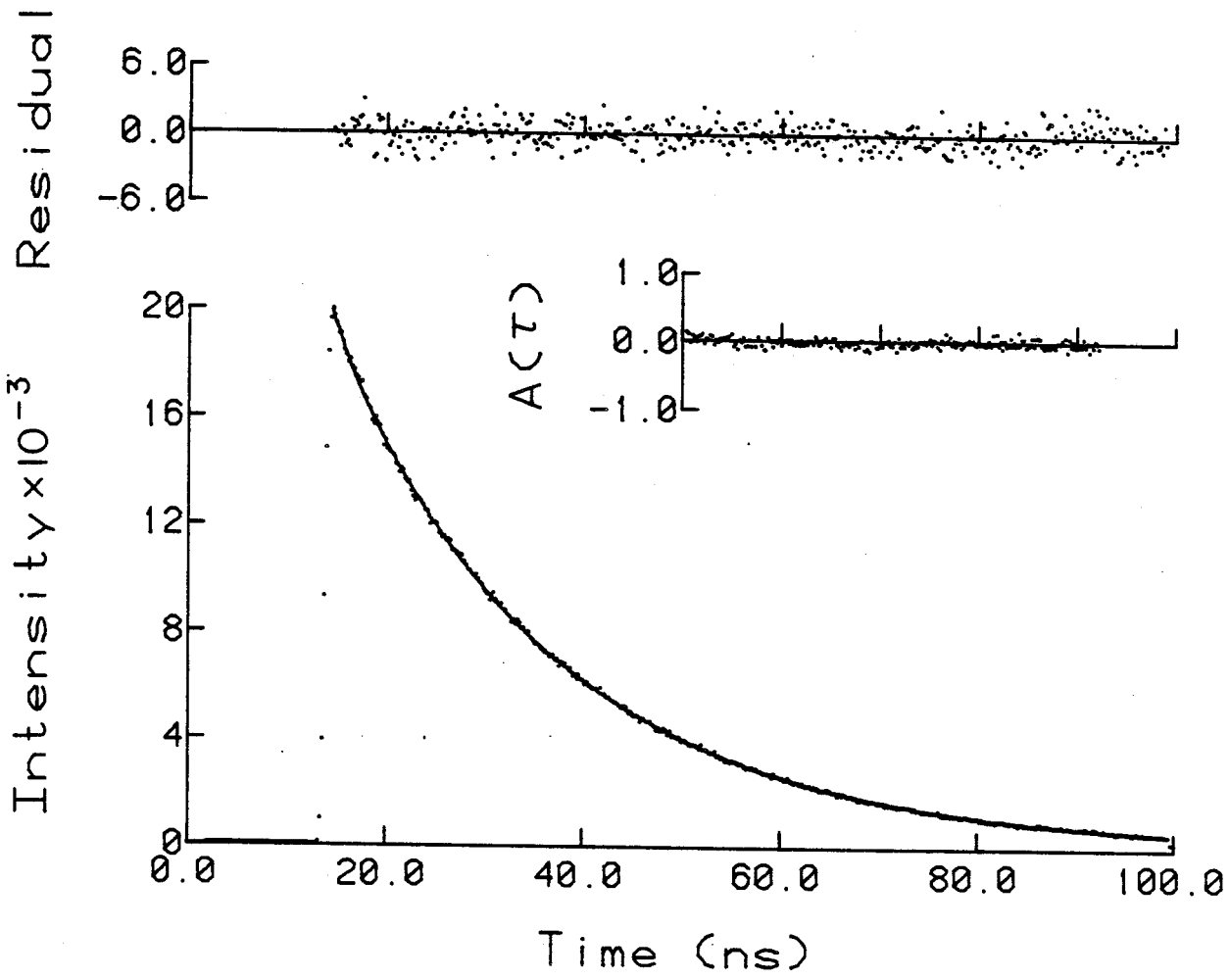
Residual
6.0
0.0
-6.0
A(τ)
1.0
0.0
-1.0
Intensity x10^{-3}
20
16
12
8
4
0
0.0
20.0
40.0
60.0
80.0
100.0
Time (ns)

TABLE 7.1

Fluorescence Lifetimes of Ethidium Bromide

Sample[a]	τ_n(ns)[c]	τ_i(ns)	f
Free	1.8(0.1)[b]		
CT	2.0(1.2)	23.0(1.2)	0.05(0.02)
RNA	2.0(1.0)	23.3(0.5)	0.06(0.02)
d(G-C) · d(G-C)	2.1(0.2)	23.5(0.2)	0.18(0.04)
d(A-T) · d(A-T)	2.5(0.8	25.4(0.4)	0.07(0.02)
dG · dC	2.4(0.2)	22.2(0.4)	0.18(0.04)
dA · dT	2.3(0.2)	19.9(0.2)	0.31(0.02)
dA · dU	2.6(0.4)	22.4(0.9)	0.31(0.06)
rA · rU	3.0(0.4)	27.6(0.7)	0.22(0.02)
dA · rU · rU	2.7(0.3)	23.9(0.5)	0.14(0.06)
pBR 322	2.8(1.1)	23.2(0.2)	0.06(0.02)

[a]Abbreviations: CT is calf thymus DNA; RNA is total soluble yeast RNA; pBR 322 is supercoiled plasmid DNA; d(G-C)·d(G-C) is poly d(G-C)·poly d(G-C), similarly for the remainder.

[b]Values in parentheses are 95% confidence intervals.

[c]The quantities τ_n, τ_i, and f are defined in Eq. (7.28).

assigned to non-intercalated and intercalated dye species, respectively. The fraction f of the shorter component thus provided a measure of the extent of ethidium intercalation, which was important for the analysis of the fluorescence depolarization data since the model for r(t) [Eq. (7.24)] applies only to the intercalated dye.

For the ethidium-calf thymus DNA sample, the lifetime of the intercalated dye was 23.0 nsec, with 5% of non-intercalated dye at an ionic strength of 0.2 M. Similar results were obtained for ethidium bromide bound to the supercoiled pBR 322 plasmid DNA, whereas there was considerable variation among the synthetic polynucleotides (Table 7.1). The lifetime of the intercalated ethidium ranged from 19.9 nsec, when bound to poly(dA) · poly(dT), to 27.6 nsec, when bound to poly(rA) · poly(rU), while the fraction of non-intercalated dye ranged from 7% for poly d(A-T)· poly d(A-T) to 31% for poly(dA)·poly(dU). Despite these variations, several trends emerged: (1) Of the polydeoxyribonucleotides, the homopolymers, poly(dA)·poly(dT) and poly(dG)·poly(dC) had shorter lifetimes and more non-intercalated dye than their alternating copolymer counterparts, poly d(A-T) · poly d(A-T) and poly d(G-C) · poly d(G-C); this effect was much larger for A-T than for G-C containing polynucleotides. (2) Ethidium bromide had a significantly longer lifetime, and there was less non-intercalated dye, when bound to the polyribonucleotide poly(rA)·poly(rU) (τ_i = 27.6 nsec, f = 0.22) than when bound to its <u>deoxy</u>-counterpart poly(dA)·poly(dU) (τ_i = 22.4 nsec, f = 0.31). (3) In series of related polynucleotides, there was a strong correlation between the fluorescence lifetime of the intercalated dye and the extent of binding,

long lifetimes being associated with small fractions of non-intercalated dye.

Changes in the nucleotide-to-dye ratio within the range P/D ≃ 90-900 at constant nucleic acid concentration had no measurable effect on the fluorescence decays. However, the fraction of non-intercalated dye was found to depend on the nucleic acid concentration and ionic strength in a fairly simple manner. In a series of experiments on the ethidium-calf thymus DNA system (0.05M Tris·HCl, pH 7.7/0.15M NaCl; P/D ≃ 300), the fraction of non-intercalated dye increased from 4% at a DNA concentration of 250 μg/ml to over 35% at 8 μg/ml. The observed concentration dependence was in accord with the neighbor exclusion model of ethidium binding [26] with an intrinsic binding constant of about $6 \times 10^4 M^{-1}$. In another series of experiments on the ethidium-calf thymus DNA system (250 μg/ml in water, pH 7.7; P/D ≃ 300), the fraction of non-intercalated dye decreased from 12% at 1M NaCl to 3% at a salt concentration of 10^{-3}M. The observation of a decrease in binding at higher salt concentrations was consistent with both competitive binding of ethidium and sodium cations to DNA [21] and the counterion condensation theory [27,28], wherein binding of an ethidium displaces a certain number of Na^+ counterions.

b. Analysis of fluorescence depolarization data

Time-resolved fluorescence depolarization studies of ethidium bromide intercalated in the nucleic acids were performed by measuring the polarized emission components $i_{\parallel}(t)$ and $i_{\perp}(t)$ separately for each sample, and then combining them in the computer. Figure 7.3 shows a typical set of

Figure 7.3

Experimental $i_{\parallel}(t)$ and $i_{\perp}(t)$ curves (center graph) and anisotropy $r(t)$ (lower graph) for the ethidium:calf thymus DNA complex in aqeous tris buffer, pH 7.7/0.01 M NaCl. The points are experimental data and the smooth lines are the best fit of Eq. (7.24) with $\tau_i = 23.3 \pm 0.05$ nsec, $C = 1.59 \pm 0.11 \times 10^{-19}$ erg cm, $\Xi^{1/2} = 16.3 \pm 1.2°$, and $\chi_r^2 = 1.4$. Also shown (upper graph) are the weighted residuals for the difference curve $i_{\parallel}(t) - i_{\perp}(t)$.

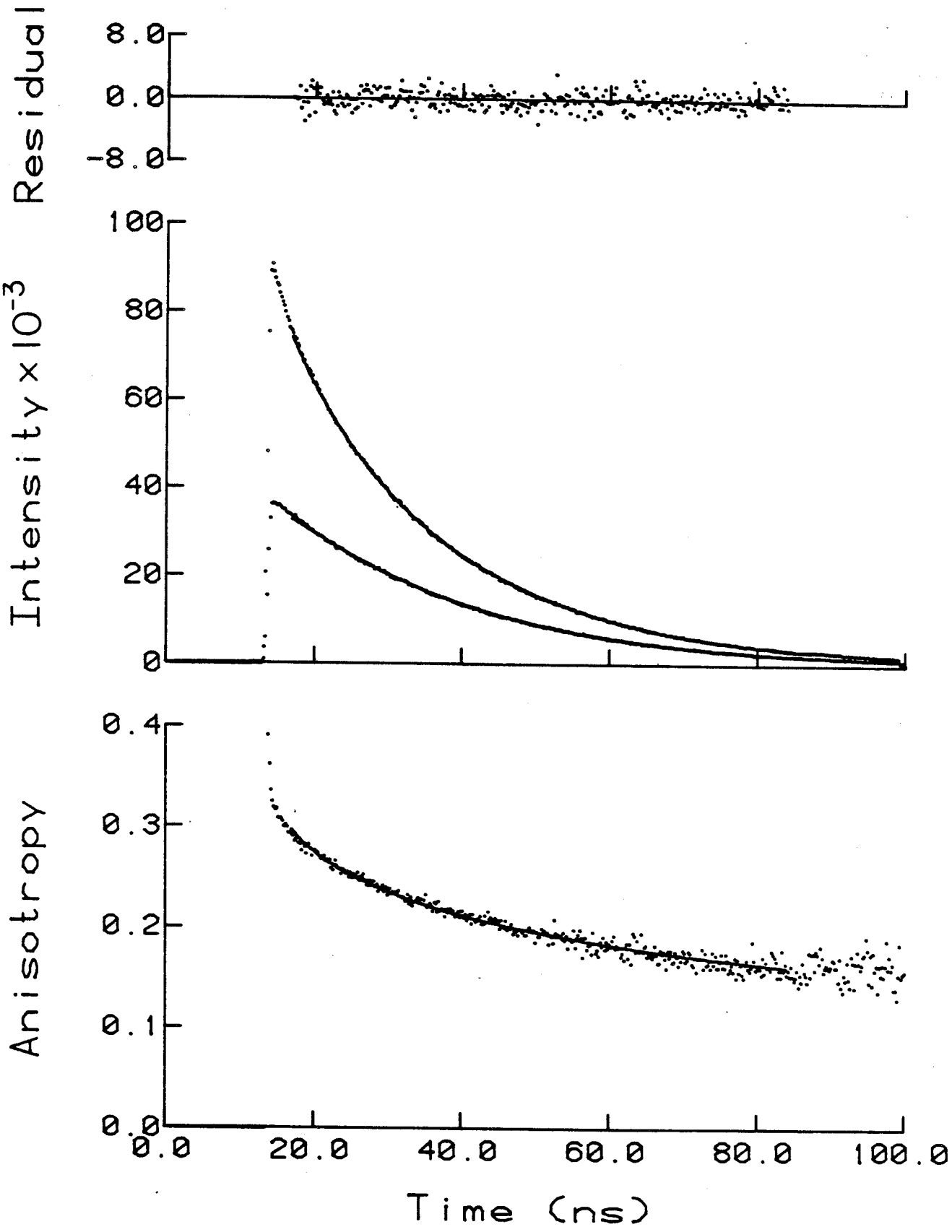
Residual
8.0
0.0
-8.0
Intensity x 10^{-3}
100
80
60
40
20
0
Anisotropy
0.4
0.3
0.2
0.1
0.0
0.0
20.0
40.0
60.0
80.0
100.0
Time (ns)

experimental data, for the ethidium-calf thymus DNA system (250 μg/ml DNA in 0.01M NaCl, pH 7.7; P/D ≃ 300), and the fluorescence polarization anisotropy r(t) constructed from these data according to Eq. (4.4). The r(t) curve in Figure 7.3 is of the general form expected on the basis of either the elastic model or the intermediate zone of the bead-spring model [Eqs. (7.24) and (7.14a), (7.16a) or (7.23b)], showing an initial rapid decay and tending to level off at longer times. This can be verified more directly by a graphical method. Assuming that the torsional dynamics dominate the observed anisotropy decay, which will be shown to be true later, Eq. (7.27) provides a good approximation and is useful for the graphical analysis. Equation (7.27) suggests that the fluorescence anisotropy be plotted as $\log[r(t) - 0.1]$ against $t^{1/2}$ in the case of the elastic or intermediate zone bead-spring model; a straight line should result. The plot is shown in Figure 7.4 and is indeed quite linear within the experimental uncertainty, confirming the exponential-$t^{1/2}$ torsional relaxation.

The validity of the elastic model, or equivalently, the intermediate zone bead-spring model, was quantitatively assessed by a curve-fitting procedure based on Eq. (7.24) and described in Section 7.3c. The bending motions were also included in the curve-fitting and hence the torsion and bending decay functions from the elastic model were used, Eqs. (7.14a) and (7.16a). However, many parameters appear in these general expressions and some additional information must therefore be introduced to reduce the number of adjustable parameters. The procedure adopted here was to estimate the helix radius b, the torsional rigidity El, the dye-tilt ε, and the limiting anisotropy r_0 from available data, and then to treat the

Figure 7.4

Plot of the experimental data in Figure 7.3 in the form $\log[r(t) - 0.1]$ against $t^{1/2}$. Note the linear relationship, which confirms the exponential-$t^{1/2}$ torsional relaxation of the double helix.

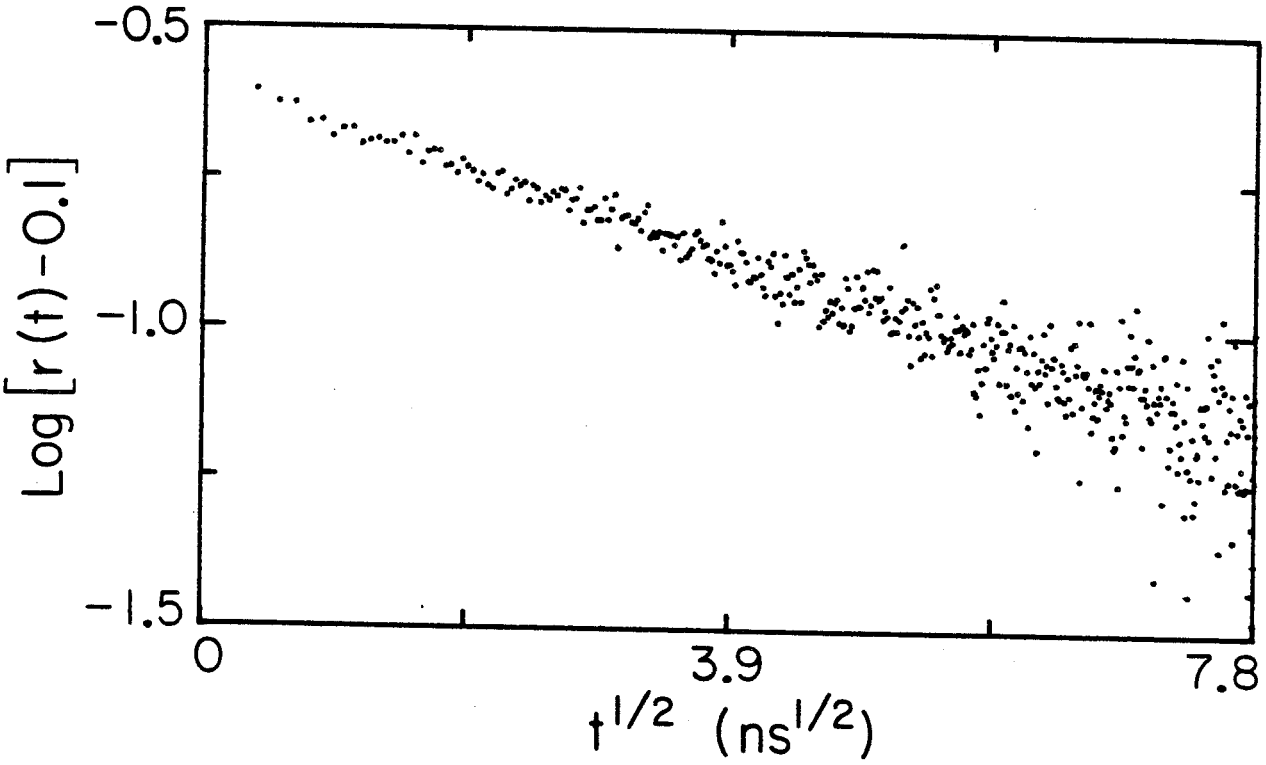
-0.5
-1.0
-1.5
Log [r (t) - 0.1]
0
3.9
7.8
t^1/2 (ns^1/2)

torsional rigidity C and the dye wobble Ξ as adjustable parameters.

The hydrodynamic radius of the native, B-form of DNA was estimated by fitting the sedimentation velocities of low molecular weight, homogeneous DNA fragments as a function of length to the theory of Yamakawa and Fujii [29]. Kovacic and van Holde [30] have made very accurate measurements of the sedimentation velocities of sixteen double-stranded PM2 DNA restriction fragments with sizes covering the range from 50 to 1735 base pairs. From a nonlinear least-squares analysis (Appendix II) of their data, a hydrodynamic radius of 13.4 ± 0.3Å and a persistence length of 522 ± 16Å were obtained; the fit was excellent ($\chi_r^2 = 0.96$). The value of 13.4Å seemed reasonable for the radius of the hydrated double helix when compared with the bare radius of about 11Å determined from X-ray diffraction studies of oriented fibers of both B-DNA and A-RNA [31]. The hydrodynamic radius of A-RNA was assumed to be the same as that of B-DNA. All of the nucleic acids investigated were double helical, except for poly(dA)·poly(rU)·poly(rU), which had an unusual triple helical structure [32]. The hydrodynamic radius of the triple helix was estimated to be 14.8Å by taking the bare radius from the X-ray diffraction studies [31], 12.4Å, and adding on the thickness of the hydration layer, 2.4Å, inferred from the data for B-DNA.

The bending rigidity EI is directly related to the persistence length P by the formula [11]

$$EI = k_B T P \tag{7.30}$$

A persistence length of 522 ± 16Å for (native) DNA under standard conditions (neutral aqueous solution, 0.2M NaCl, 20°C) was estimated

from a nonlinear least-squares analysis of the sedimentation data of Kovacic and van Holde (see above). Inclusion of the data of Reinert et al. [33], Prunell and Bernardi [34], Record et al. [35], and Godfrey [36] which together cover the size range 50-40,000 base pairs (3×10^4 - 3×10^7 daltons) in the analysis gave essentially identical results, $b = 13.3 \pm 0.3$Å and $P = 532 \pm 16$Å. This corresponds to a bending rigidity of $2.15 \pm 0.06 \times 10^{-19}$ erg cm. This estimate of the persistence length agreed with those determined by light scattering [37-40] (490-660Å), intrinsic viscosity [39,41] (500-550Å), with $b \simeq 12$Å), and electron microscopy [42] (530 ± 50Å). While native DNAs have been well characterized under standard conditions, very little is known about the persistence lengths of the synthetic polynucleotides. There has also been some controversy over the magnitude of the change in the persistence length of DNA with ionic strength. These difficulties were circumvented in the following way. First, the fluorescence depolarization data for calf thymus DNA under standard conditions were analyzed according to Eqs. (7.24), (7.14a), and (7.16a), holding the bending rigidity fixed at 2.15×10^{-19} erg cm. The fit (the solid lines in Figure 7.3) was excellent ($1.1 \leq \chi_r^2 \lesssim 1.4$) and gave a torsional rigidity C of 1.43×10^{-19} erg cm. According to classical elasticity theory, the torsional and bending rigidities are related through the formula [43]

$$C = EI/(1+\sigma) \tag{7.31}$$

where σ is Poisson's ratio. From the rigidities of calf thymus DNA under standard conditions we deduced $\sigma = 0.50$. It was then assumed that this same Poisson ratio applied to all of the nucleic acids, under all conditions, and the bending rigidity of each sample was calculated from Eq.

(7.30) at each iteration of the curve-fitting procedure.

The dye-tilt angle ε for the ethidium-calf thymus DNA system was taken directly from the transient electric dichroism studies of Hogan et al. [22]. From the limiting dicroism at high fields, they calculated that the intercalated dye was not perpendicular to the helix axis, but was tilted by about 20° along its long axis ($\varepsilon = 70 \pm 2°$). From similar dichroism experiments on the DNA bases [44], they also estimated that the bases themselves were inclined at an angle of $73 \pm 3°$ to the helix axis, in agreement with the revised model for B-form DNA proposed by Levitt [45] on the basis of energy-minimization calculations. The polynucleotides poly(rA)·poly(rU) and poly(dA)·poly(rU)·poly(rU) do not adopt the native B-DNA structure. However, there do not appear to be electric dichroism data for either native or synthetic RNA's in the literature, and therefore the value $\varepsilon = 70°$ was used, which was the base-tile obtained from X-ray fiber diffraction studies of RNA [31].

In a rigid medium, where Brownian motion is suppressed, the fluorescence polarization anisotropy should approach its theoretical maximal value of 0.4. The observation of a limiting anisotropy lower than 0.4 can be due to electronic effects within the molecule that lead to an angle between the absorption and emission dipoles, or to some experimental defect, such as imperfect polarization of the exciting light. For the ethidium-calf thymus DNA complex in saturated sucrose ($\eta \simeq 480$ cP) $r_0 = 0.39 \pm 0.01$ was in fact obtained, but the anisotropy decayed within a few nanoseconds to a constant (plateau) value of 0.36. A limiting anisotropy $r_0 = 0.39 \pm 0.01$ was also obtained for free ethidium bromide in

saturated sucrose and in glycerol ($\eta \simeq 1000$ cP). This value was used throughout the analysis.

c. Calf thymus DNA under standard conditions

Table 7.2 summarizes the results of some control experiments on the ethidium-calf thymus DNA system under standard conditions (neutral aqueous solution, $\sim$0.2M NaCl, 20°C). The theoretical fits of the elastic model for torsion and bending were excellent in all cases ($1.1 \leq \chi^2_r \leq 1.4$). Several points were noted from these results: (1) The torsional rigidity was independent of DNA concentration over the range 32-250 μg/ml, and therefore the experiments were monitoring a purely intramolecular property of the double helix. At DNA concentrations of less than 32 μg/ml, the fraction of non-intercalated dye was too high for reliable analysis of the data. (2) The torsional rigidity was also independent of the nucleotide-to-dye ratio over the range 90-900; from this observation it was inferred that electronic energy transfer between intercalated dyes was not contributing to the depolarization. (3) There appeared to be some slight dependence of the dye-wobble angle on the nucleotide-to-dye ratio, ranging from about 17° at P/D = 90 to about 13° at P/D = 900, but this difference may not be significant. (4) There was no dependence of the wobble angle on the fraction of nonintercalated dye; this fraction was varied from 2% to 35% by changing the concentrations of salt and DNA, and by binding to different nucleic acids. From the results in Table 7.2, an average torsional rigidity of $1.43 \pm 0.09 \times 10^{-19}$ erg cm was calculated for calf thymus DNA under standard conditions.

TABLE 7.2

Torsional Rigidity of DNA under Standard Conditions

[DNA](μg/ml)	P/D	$C(10^{-19}$erg cm)	$\Xi^{1/2}$ (deg)
250	300	1.48(0.14)[a]	-
125	300	1.38(0.25)	-
64	300	1.46(0.17)	-
32	300	1.56(0.29)	-
250	90	1.37(0.14)	17(3)
250	300	1.48(0.14)	17(2)
250	900	1.51(0.15)	13(3)

[a]Values in parentheses are 95% confidence intervals.

These data were also analyzed using different values for the dye-tilt angle ε and the Poisson ratio σ to determine the effect of the fixed parameters and to enable a comparison with other work. The apparent torsional rigidities are given in Table 7.3. Two dye-tilt angles were tried in these calculations, $\varepsilon = 70°$ and $90°$, which were the values deduced from transient electric dichroism [22] and X-ray fiber diffraction [31] studies, respectively. Three different Poisson ratios were also tried, $\sigma = 0$, 0.5, and ∞ . The first two were the extreme values expected for a homogeneous elastic rod [43], whereas the final value $\sigma = \infty$ corresponded to the (unphysical) situation where bending motions were suppressed. The torsional rigidity of calf thymus DNA obtained from the present analysis was $C = 1.43 \times 10^{-19}$ erg cm with $\sigma = 0.50$ and $\varepsilon = 70°$, and should be compared with the value of 1.17×10^{-19} erg cm obtained with $\sigma = \infty$ and $\varepsilon = 90°$ which corresponds to Eq. (7.27). The relatively small difference between these two values was due to a partial cancellation of the errors produced by ignoring the bending motions and by assuming that the ethidium transition dipole was perpendicular to the helix axis. Thus the much simpler Eq. (7.27) can be used to obtain a reasonable estimate of the torsional rigidity. Including the dye-tilt, but ignoring the bending motions, as was done by Thomas et al. [8], produced an error of almost 50% in the torsional rigidity (Table 7.3). These calculations demonstrate the importance of having accurate values for the helix parameters ε and σ (or EI) if accurate, absolute torsional rigidities are to be obtained from fluorescence depolarization experiments.

TABLE 7.3

Apparent Torsional Rigidity[a] of DNA as a Function of the Dye-Tilt Angle and Poisson Ratio

ε \ σ:	∞	0.5	0
70	0.93(.06)[b]	1.43(.09)	1.59(.10)
90	1.17(.07)	1.60(.10)	1.73(.11)

[a]Torsional rigidities are expressed in units of 10^{-19} erg cm.

[b]Values in parentheses are 95% confidence intervals.

d. Denatured DNA and native RNA

Fluorescent depolarization data were also recorded for ethidium bromide bound to thermally denatured calf thymus DNA and intact native RNA (total soluble yeast RNA). The fluorescence polarization anisotropy obtained for the denatured ethidium-DNA complex was of the same form as that obtained for intact DNA, Eq. (7.24), although the anisotropy decay was significantly more rapid; the apparent torsional rigidity was $C = 0.90 \pm 0.10 \times 10^{-19}$ erg cm. However, with native RNA the situation was quite different. Here the fluorescence polarization anisotropy, shown in Figure 7.5, decayed completely within ≃50 nsec, rather than tending to a constant (plateau) value at long times as observed for the ethidium-DNA complex.

e. Synthetic polynucleotides

The results of the fluorescence depolarization experiments on the synthetic polynucleotides (100 μg/ml in 0.1M Tris-HCl, pH 7.7/0.15M NaCl; P/D ≃ 120) are summarized in Table 7.4. The results for native and denatured calf thymus DNA and the supercoiled plasmid DNA are also included in Table 7.4 for comparison.

These results revealed a number of differences among the polynucleotides, which can be summarized as follows: (1) The alternating copolymers, poly d(G-C) · poly d(G-C) and poly d(A-T) · poly d(A-T), had quite different torsional rigidities from the homopolymers with the same base composition, poly(dG)·poly(dC) and poly(dA)·poly(dT). (2) The torsional rigidities of A-T and G-C containing polynucleotides were very different in the alternating copolymers, but quite similar in the homopolymers. (3) The polyribonucleotide poly(rA)·poly(rU) had a

Figure 7.5

Fluorescence polarization anisotropy constructed from the fluorescence depolarization data for the ethidium: native RNA complex in aqueous tris buffer, pH 7.7/0.15 M NaCl.

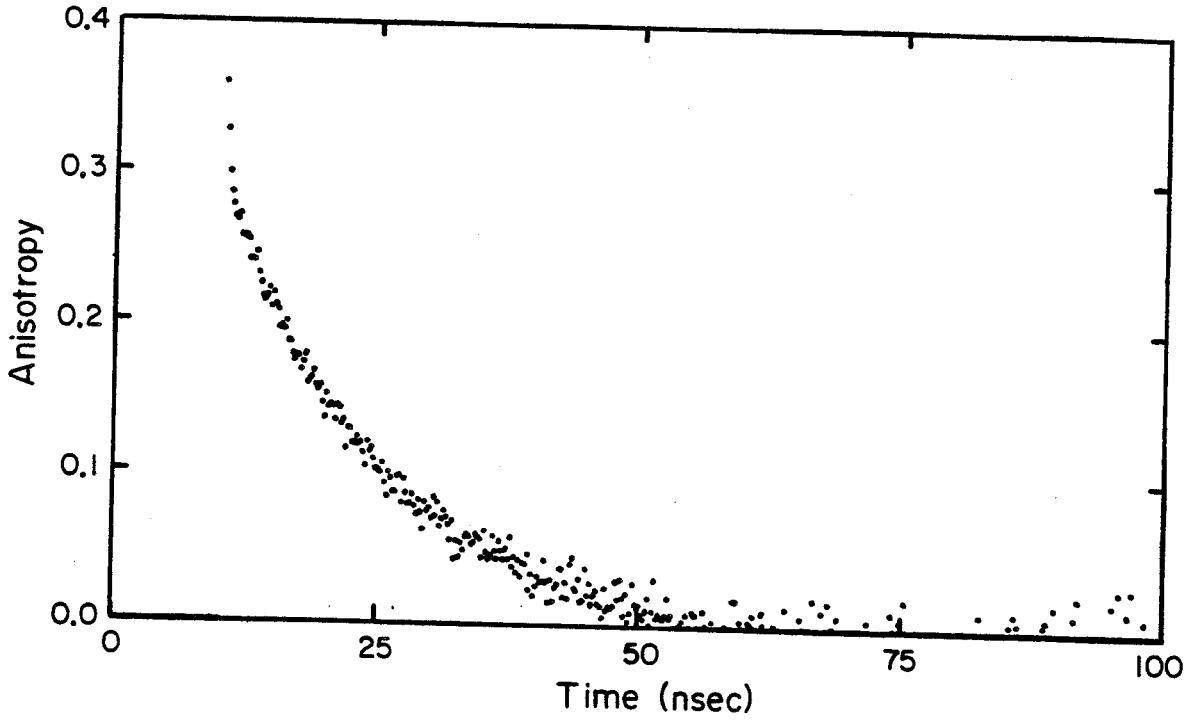
0.4
0.3
0.2
0.1
0.0
Anisotropy
0
25
50
75
100
Time (nsec)

TABLE 7.4

Torsional Rigidities of the Polynucleotides

Sample	$C(10^{-19}$ erg cm)	$\Xi^{1/2}$ (deg)
CT	1.43(0.11)[a]	17(2)
d(G-C)·d(G-C)	1.50(0.15)	19(2)
d(A-T)·d(A-T)	0.90(0.22)	12(2)
dG·dC	1.19(0.10)	10(2)
dA·dT	1.27(0.17)	12(7)
dA·dU	0.83(0.12)	15(2)
rA·rU	1.53(0.13)	6(4)
dA·rU·rU	2.65(0.33)	15(5)
pBR 322	1.95(0.18)	20(2)
Denat. CT	0.90(0.10)	0(2)

[a]Values in parentheses are 95% confidence intervals.

significantly larger torsional rigidity ($C = 1.53 \times 10^{-19}$ erg cm) than its deoxy-counterpart, poly(dA)·poly(dU) ($C = 0.83 \times 10^{-19}$ erg cm). Furthermore, the torsional rigidity of poly(dA)·poly(dU) increased to 1.1×10^{-19} erg cm upon raising the salt concentration to 1M, whereas the torsional rigidity of poly(rA)·poly(rU) showed no change. (4) The torsional rigidity of the triple helical poly(dA)·poly(rU)·poly(rU) was considerably greater than that of any of the double helical polynucleotides. (5) The dye-wobble angle was relatively large for all polydeoxyribonucleotides, 10-19°, but very small for the polyribonucleotide poly(rA)·poly(rU), about 6°. There was no apparent correlation between the dye-wobble angle and either the torsional rigidity of the helix, the fluorescence lifetime of the intercalated dye, or the fraction of non-intercalated dye.

f. Polyelectrolyte effects

Figure 7.6 shows a plot of the measured torsional rigidity of calf thymus DNA as a function of ionic strength, μ, covering the range 3×10^{-5}M - 2.0M. Most of the samples contained at least a ten-fold excess of added 1:1 electrolyte, NaCl. For those few samples in which there was no added electrolyte, the ionic strength was taken to be equal to the nucleotide concentration. From this plot several regions were distinguishable. In region I, which covered the ionic strength range $0.2 \lesssim \mu \lesssim 2.0$M, the torsional rigidity was independent of ionic strength with a mean value of about 1.4×10^{-19} erg cm. In region II, $5 \times 10^{-4} \lesssim \mu \lesssim 0.1$M, the torsional rigidity increased monotonically with decreasing ionic strength, reaching a maximal value of about 1.8×10^{-19}

Figure 7.6

Dependence of the torsional rigidity of calf thymus DNA on ionic strength μ. Error bars are one standard deviation. Results are shown for solutions containing no added NaCl (crosses) and containing excess NaCl (dots). The smooth line is shown to connect the points. The broken line was calculated from Eqs. (7.30) and (7.31), together with the equations for the persistence length discussed in Section 7.5g of the text.

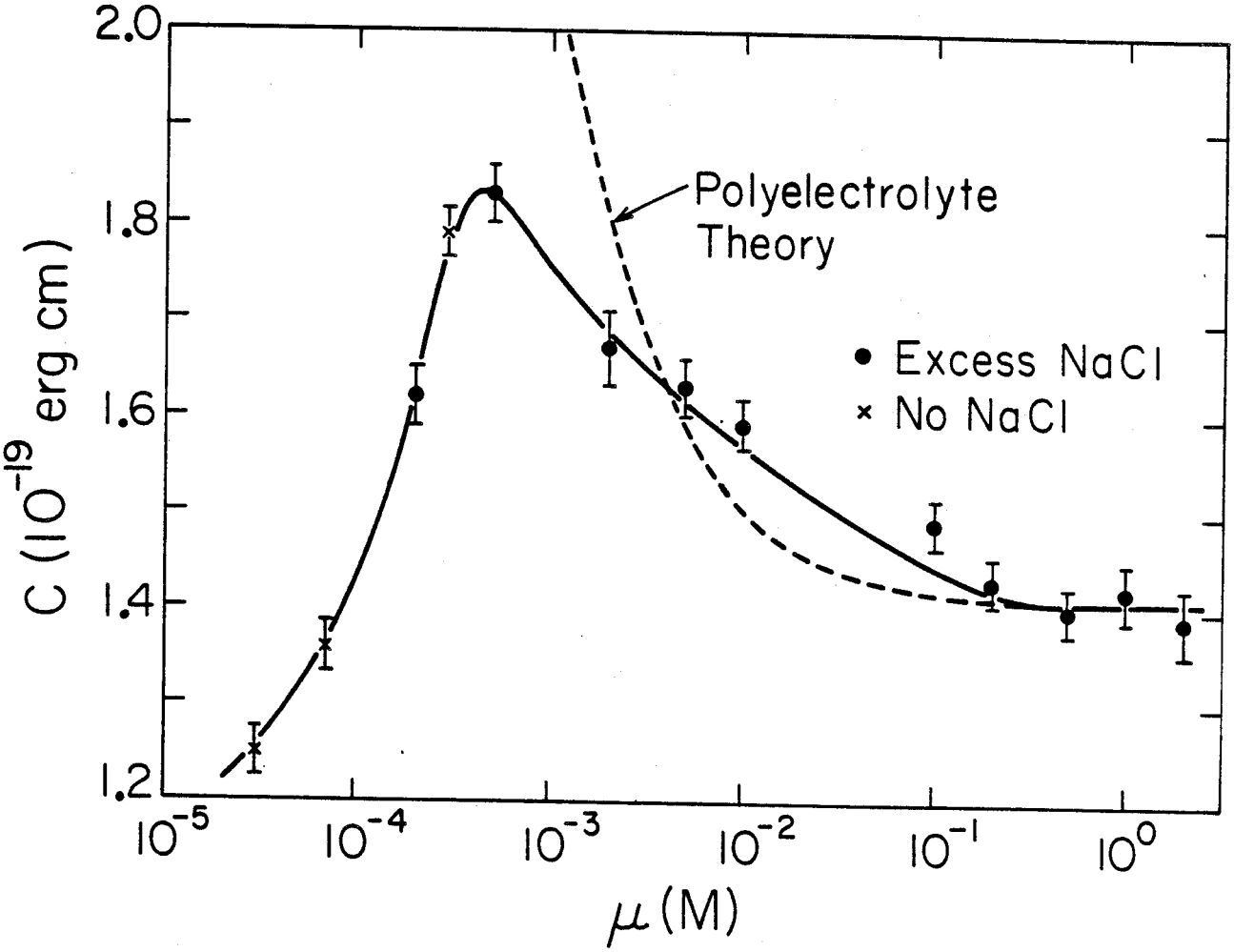
2.0
1.8
1.6
1.4
1.2
C (10^{-19} erg cm)
10^{-5}
10^{-4}
10^{-3}
10^{-2}
10^{-1}
10^{0}
μ (M)
Polyelectrolyte Theory
• Excess NaCl
× No NaCl

erg cm. And finally, at ionic strengths less than 5×10^{-4}M (region III), the torsional rigidity fell rapidly.

7.5 Discussion

a. The bound species

The isotropic (54.7°) fluorescence decays of all the nucleic acids exhibited a fast and slow component, which have been attributed to non-intercalated and intercalated dye species, respectively. Olmsted and Kearns [46] have shown that the much longer lifetime of the intercalated dye compared with free ethidium bromide is due to a reduction of the rate of an excited state proton transfer reaction with polar solvents. Variations in the lifetime τ_i of the intercalated dye are presumably due to different degrees of exposure of the dye to solvent, due to differences in double-helical structure. This mechanism was probably responsible for the consistently shorter lifetime τ_i of ethidium intercalated in homopolymers compared with alternating copolymers, and for the lifetime differences between ethidium intercalated in polydeoxyribonucleotides and in polyribonucleotides (Table 7.1). The empirical correlation between long lifetimes of the intercalated dye and the low fractions of nonintercalated dye is also consistent with this mechanism; the more strongly intercalated dye is the least exposed to solvent.

Equilibrium and kinetic studies [26] of the interaction between ethidium bromide and DNA have revealed the presence of three bound dye species, an electrostatically-bound outside form, ED_0, which accounts for $\sim$8% of the total bound dye at 1 M NaCl, and two intercalated species, ED_1 ($\sim$12%) and ED_2 ($\sim$80%). Recent studies [47] with a range of

intercalators have shown that ED_1 and ED_2 correspond to intercalation at sites in the major and minor grooves of the DNA double helix, respectively. ED_1 and ED_2 are thus expected to have very similar lifetimes, much longer than for unbound dye, whereas ED_0 is expected to have a lifetime intermediate between the intercalated species and the unbound dye. Therefore it is postulated that the long-lived component of the fluorescence decay was a combination of ED_1 and ED_2 emission, while the short-lived component was ED_0 emission. The lifetime τ_n and fraction f of the short component are in very good agreement with this hypothesis; f = 12% at 1 M NaCl compared with 8% ED_0 observed in the earlier studies [26]. There may also be a contribution to the short component from unbound dye. The excellent agreement between the experimental fluorescence anisotropy decay and the elastic model (Section 7.5c) implies that ED_1 and ED_2 have very similar tilt angles ε relative to the helix axis, which is reasonable for intercalation at sites in the major and minor grooves of the helix.

b. Elastic versus bead-spring model

The important difference between the elastic and bead-spring models is in the early time behavior of the torsion decay function, Eqs. (7.14a) and (7.23a). The elastic model predicts $\Gamma(t) \sim t^{1/2}$ at all times, whereas the bead-spring model predicts an initial $\Gamma(t) \sim t$ decay, characteristic of the free rotation of the individual beads, followed by $\Gamma(t) \sim t^{1/2}$ at later times. The good linearity of the $\log[r(t) - 0.1]$ versus $t^{1/2}$ plot shown in Figure 7.4 is strong evidence that $\Gamma(t) \sim t^{1/2}$ for all times of experimental interest. This was confirmed by the

excellent fits of Eq. (7.14a), in combination with Eqs. (7.24) and (7.16a), to the fluorescence depolarization data. The decay time $1/4D_b$ and upper time limit τ_{N+1} for the initial exponential decay zone are estimated to be about 470 ps and 2 ps, respectively, for the values of b and C given above. Apparently the exponential decay persists for only a very short time compared with its decay time, and therefore the relaxation amplitude was too small ($< 1\%$) to be detected in these experiments. It is also pertinent to note that the exponential decay time $1/4D_b \simeq 470$ ps, for rotation of an isolated base-pair about the helix axis, defines the fastest torsional motion that can appear within the context of the bead-spring model. Therefore, experiments with higher time resolution than the present one (~ 250 ps) are not expected to provide any additional information concerning the torsional dynamics.

The hypothesis advanced by Allison and Schurr [19] that calf thymus DNA contains isolated torsion joints, or other inhomogeneities in the torsional rigidity, can now be ruled out, since it was predicated on a fit of the nanosecond fluorescence depolarization data of Wahl et al. [6] to a bead-spring model for a bead length of 86 base-pair with relaxation in the initial exponential decay zone.

The torsional relaxation observed in these experiments was in excellent agreement with the predictions of the elastic model or the intermediate decay zone of the bead-spring model. However, the bead-spring model cannot be used for analyzing bending dynamics. The elastic model, however, was found to give a good fit to the data when both torsion and bending were included. The solid lines in Figure 7.3 are theoretical

fits including both torsion and bending. The elastic model developed by Barkley and Zimm [11] was valid in all the nucleic acid samples studied except native RNA (for reasons that will be discussed later). The model may be used with confidence to extract the torsional rigidity from fluorescence depolarization data.

c. Torsional rigidity of calf thymus DNA

The results in Table 7.3 show that the value of the torsional rigidity obtained from the analysis of fluorescence depolarization according to the elastic depends to some extent on the values of other helix parameters, and whether or not bending was included. Actually, the data could be well fit by the elastic model for torsion only, since it was the torsional motions which dominated the anisotropy decay of the ethidium-DNA complex. This was a consequence of the nearly perpendicular orientation of the ethidium transition dipole moment relative to the helix axis. In this configuration the bending motions have the smallest effect on the anisotropy decay [11]. This is demonstrated in Figure 7.7a, which shows the theoretical curve calculated according to Eq. (7.24) for torsion only (upper curve) and for both torsion and bending (lower curve). The values of the parameters described in Section 7.4b were used in the calculation. For purposes of comparison, the calculated r(t) curve for a parallel dipole orientation, with all other parameters the same, is shown in Figure 7.7b. In this configuration the bending motions produce all the anisotropy decay, since torsional motions cause no depolarization. The ethidium-DNA complex, which has $\varepsilon = 73°$ [22], does not provide such a good test of the bending dynamics

Figure 7.7

(a) Fluorescence polarization anisotropy curve r(t) calculated from Eq. (7.24), with $C = 1.4 \times 10^{-19}$ erg cm, $b = 13.4\text{Å}$, $\sigma = 0.5$, and $\varepsilon = 73°$. The upper curve includes torsion only, while the lower curve includes both torsion and bending.

(b) Same as for (a), except that $\varepsilon = 0$.

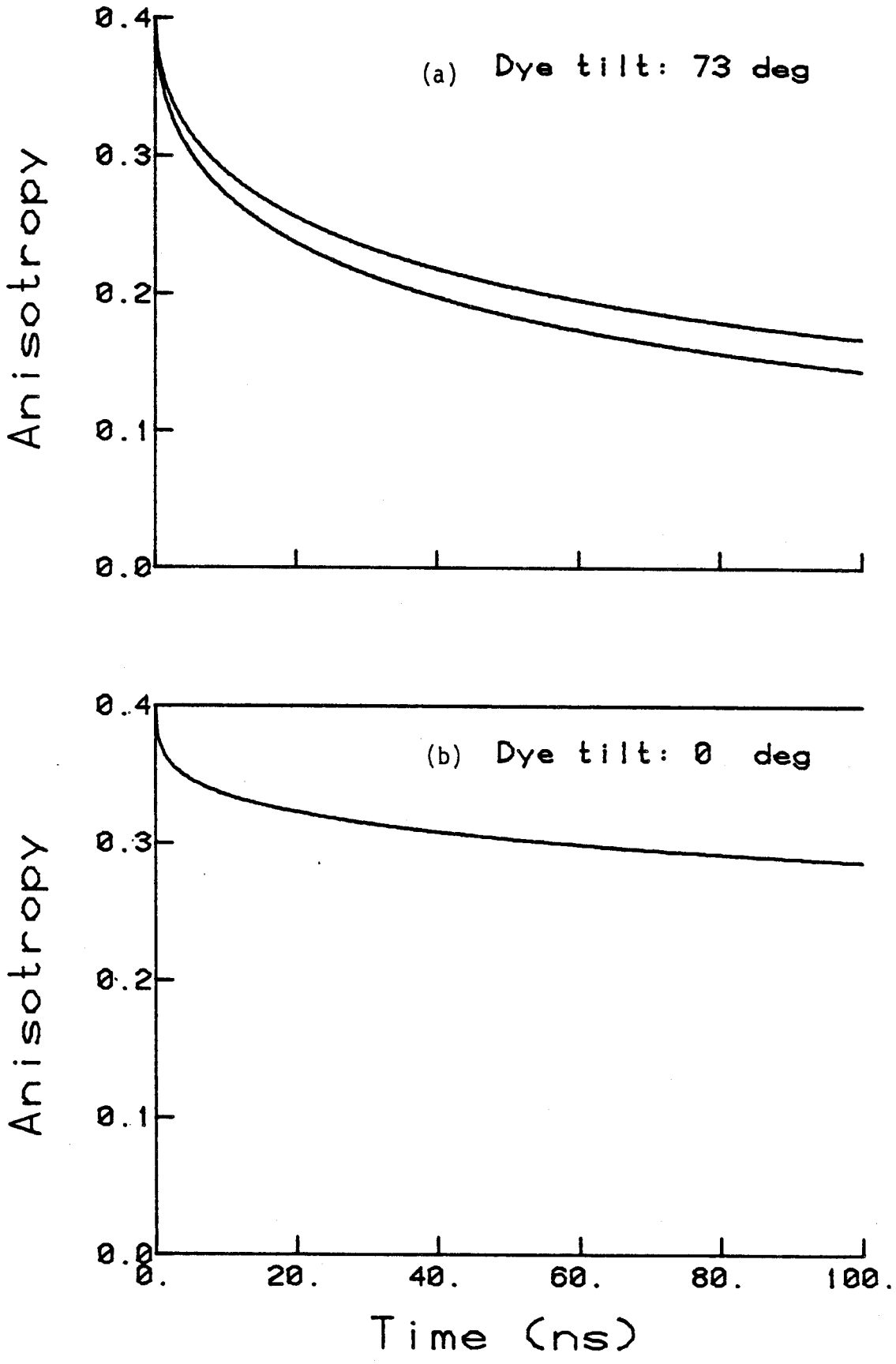
(a) Dye tilt: 73 deg
Anisotropy
0.4
0.3
0.2
0.1
0.0
(b) Dye tilt: 0 deg
Anisotropy
0.4
0.3
0.2
0.1
0.0
0.
20.
40.
60.
80.
100.
Time (ns)

as the torsional dynamics. Nevertheless, the fits to experimental data were always slightly improved by inclusion of the bending dynamics. More important, however, the value of the torsional rigidity was underestimated by almost 40% if the bending was ignored (Table 7.3). Thus it is important to include the bending contribution in order to determine accurately the torsional rigidity. A similar situation is encountered when attempting to determine the torsional rigidity from supercoil linking number distributions (Section 7.5d).

As for the other parameters involved in the elastic model, it has been shown here how the helix radius and Poisson ratio may be independently determined from published hydrodynamic data, leaving the dye tilt angle as the only unknown parameter. Fortunately, this was recently measured for native DNAs by electric dichroism. Thus, at least for calf thymus DNA, the torsional rigidity has been extracted with considerable certainty. The value for calf thymus DNA under standard conditions, $C = 1.43 \pm 0.11 \times 10^{-19}$ erg cm, should be the most accurate value attainable from fluorescence depolarization data.

Another quantity of interest is the RMS average fluctuation in the torsion angle between adjacent base pairs [11], $\langle \Delta\gamma \rangle_{rms} = (hk_BT/C)^{1/2}$, where $h = 3.4\text{Å}$ is the distance between base pairs. For the value of C above, $\langle \Delta\gamma \rangle_{rms} = 5.7°$. The corresponding quantity for bending, $\langle \Delta\alpha \rangle_{rms}$, is obtained by replacing C with the bending rigidity EI; the result is $\langle \Delta\alpha \rangle_{rms} = 4.6°$. It is clear that the structure of DNA in solution undergoes considerable fluctuations; our results show that the structure of B-DNA in solution fluctuates between a nine-fold and a twelve-fold helix due to thermal motion.

d. Other work

Thomas et al. [8] have recently reported time-dependent fluorescence depolarization measurements on ethidium intercalated in viral ϕ29 DNA at 0.01 M NaCl. They concluded that the intermediate decay zone of the bead-spring model, which is equivalent to the elastic model without the bending dynamics, provided the best fit to their data, with a torsional rigidity $C = 1.29 \times 10^{-19}$ erg cm. The data at 0.01 M NaCl obtained in this work yield the same value of the torsional rigidity as reported by Thomas et al. [8], if analyzed in the same way ($\varepsilon = 70°$, $b = 12\text{Å}$, $\sigma = \infty$). There is thus no difference in the torsional rigidities of calf thymus DNA and viral ϕ29 DNA. It should be noted that the value reported by Thomas et al. [8] is not the intrinsic torsional rigidity, since there is a $\sim$15% polyelectrolyte contribution to the torsional rigidity at 0.01 M NaCl (Section 7.4f). The intrinsic torsional rigidity can only be measured at higher salt concentrations, [NaCl] $\gtrsim$ 0.1 M, as done in this work. Also, the refined analysis of the fluorescence depolarization data presented in this work is more complete than that of Thomas et al. [8] in that the bending dynamics have been included, and a helix radius and Poisson ratio determined from independent hydrodynamic data were used.

Recently, Robinson et al. [13,48] have used EPR spectroscopy of intercalated spin probes to study the torsional dynamics of DNA. On the basis of the observed dependence of the rotational correlation time on the length of the DNA, it was concluded that the dynamics were consistent with a bead-spring model. Using this model the RMS average amplitude of the torsional fluctuations of a single base-pair could be related to the

rotational correlation time. The torsional rigidity was then calculated from the RMS amplitude. This method for measuring the torsional rigidity is thus indirect, depending on a single rotational correlation time inferred from the EPR spectrum, in contrast to the present method in which the time-dependence of the entire rotational correlation function is fit to the elastic model by least-squares adjustment of the torsional rigidity. Nevertheless, the rigidity obtained by Robinson et al. [12,38] for DNA intercalated by an ethidium spin probe, $C = 1.2 \times 10^{-19}$ erg cm, is in fair agreement with the present value, $C = 1.43 \times 10^{-19}$ erg cm. The difference is probably due to the neglect of the bending motions in the analysis of the EPR data.

Estimates of the torsional rigidity of DNA have in the past been derived from the equilibrium linking number distributions of closed circular supercoiled DNA after enzymatic conversion from the nicked to the closed form [49,50]. For example, Depew and Wang [49] estimate that C is in the range $0.64 - 1.1 \times 10^{-19}$ erg cm, which is a lower limit, since the bending energy was ignored in their calculation. More recently, Vologodskii et al. [12] have made an exact calculation of the bending contribution to the linking number distribution using statistical methods. They found that the width of the linking number distribution had approximately equal contributions from twisting and bending. The torsional rigidity calculated from the width of the twisting distribution was $C = 1.65 \pm 0.33 \times 10^{-19}$ erg cm. This result depends on the value they chose for the bending rigidity (corresponding to a persistence length of 575Å [12] but is in good agreement with the value from this work, $C = 1.43 \times 10^{-19}$ erg cm (obtained for a persistence length of 532Å), and is

a better estimate than was originally inferred from the supercoiling data.

Theoretical simulations of DNA structure [45,51], wherein the total helix energy can be calculated as a function of the local twist angle, also provide estimates of the torsional rigidity. From Levitt's calculations [45] for a 20 base-pair segment of straight DNA, a torsional rigidity $C = 20 \times 10^{-19}$ erg cm was calculated, while Miller's calculation [51] for a d(G-C)·d(C-G) dinucleotide gave $C = 36 \times 10^{-19}$ eeg cm [13]. Both theoretical calculations overestimate the torsional rigidity by more than an order of magnitude, presumably due to the excessive constraints imposed on the model structures [45,51], or due to the omission of helix-solvent interactions in the calculation.

Recent NMR studies of small fragments of double helical DNA have indicated the presence of large amplitude ($\pm 20° - 35°$) conformational fluctuations of the phosphodiester backbone, the deoxyribose sugar, and the base-planes with time constants near 1 nsec [16-18]. A corresponding large amplitude relaxation with a 1 nsec time constant was not observed in the fluorescence depolarization of calf thymus DNA or any of the synthetic polynucleotides. However, a more recent NMR study of native high molecular weight DNA [52] found no evidence for a 1 nsec internal motion, the observed microsecond correlation times being consistent with the long-range bending flexibility of DNA. In view of the discrepancy in the NMR work, it is not clear whether a 1 nsec internal motion should be observable in the fluorescence depolarization of our DNA samples. These internal motions may in fact be unique to short rod-like DNA molecules only.

e. Structural effects

The largest torsional rigidity was observed for the triple helix poly(dA)·poly(rU)·poly(rU). Since the torsional rigidity depends on the helix radius, according to $C = \frac{1}{2}\mu\pi b^4$ (for a uniform cylinder of radius b and torsional modulus μ) [53], a larger rigidity is expected for the triple helix. Using b = 14.8Å for the triple helix and b = 13.4Å for the double helix, we calculate C(triple)/C(double) = 1.3, compared with the observed value of 1.9. Thus the torsional modulus of the triple helix is larger than the double helix, μ(triple)/μ(double) = 1.5, indicating that the triple helix is inherently less flexible. Since the triple helix can be considered as a poly(dA)·poly(rU) double helix with an extra poly(rU) strand accommodated in the major groove [32], the implication is that binding large molecules to the DNA double helix reduces its conformational mobility.

The alternating self-complementary copolymer poly d(A-T) · poly d(A-T) is considerably more flexible than native B-DNA, as indicated by its smaller torsional rigidity ($C = 0.90 \times 10^{-19}$ erg cm). Several physical experiments have shown that poly d(A-T) · poly d(A-T) forms hairpin helix branches without undergoing melting [54]. Hairpin branches are formed when a single strand in an open region of the DNA (not base-paired) closes on itself into a double helix, which is possible because of the self-complementary base sequence. The ability of the DNA to open without melting confers an enhanced conformational mobility that has been observed, even at room temperature, in viscosity measurements and in the unusual activity of poly d(A-T) · poly d(A-T) in various enzymatic reactions [55]. The present results demonstrate that this enhanced conformational mobility is also manifested in the torsional rigidity.

Thermally denatured native DNA also has a much smaller torsional rigidity than intact native B-DNA (Table 7.4). This suggests that the random coil form of DNA is more flexible than the double helix, and therefore that the torsional rigidity of DNA is determined by the relative fractions of double-helical and random coil regions. It is interesting that poly(dA)·poly(dU) had a small torsional rigidity at 0.15 M NaCl, which actually increased toward the rigidity of poly(dA)·poly(dT) and poly(dG)·poly(dC) upon increasing ionic strength to 1 M. This unusual behavior is consistent with a signficant fraction of unpaired bases at 0.15 M NaCl. Thus, our results imply that poly(dA)·poly(dU) is a particularly unstable homopolymer. By contrast, poly(rA)·poly(rU) was considerably more rigid and did not show this salt effect (the torsional rigidity of poly(rA)·poly(rU) in the high salt limit was the same as shown in Figure 7.6).

The anisotropy decay observed for ethidium bound to native RNA showed a rapid and complete decay (Figure 7.5). Native RNA does not have a uniform duplex structure, but rather the single chain folds back on itself to form short, irregularly distributed duplex regions. The ethidium is presumably intercalated in these regions, since ethidium is known to bind more strongly to double strands than to single strands [20,21]. However, the macroscopic torsional and bending rigidities sample very long regions of the chain (see following paragraph) and the presence of the single strand regions results in considerably more flexibility in native RNA than in native DNA. The decay of the anisotropy to zero in native RNA clearly demonstrates the much enhanced bending flexibility.

The presence of hairpin helix branches and single-stranded regions in the DNA means that the structure is not uniform and that the elastic continuum model is therefore not strictly valid. However, a structure will be effectively uniform if the wavelengths of the torsional modes are much longer than the average size of the inhomogeneities. The average wavelength is about 100 base-pair separations (calculated from Eq. (7.8b) for a 25 nsec average relaxation time.) Inhomogeneities shorter than this will have no observable effect. The depolarization data for both poly d(A-T) · poly d(A-T) and partially denatured calf thymus DNA fit the model very well ($1.1 \lesssim \chi_r^2 \lesssim 1.3$), indicating that the nonduplex regions in these samples are sufficiently short; that is, much shorter than 100 base-pairs. However, poly(dA)·poly(dU) did show some deviation from the model ($\chi_r^2 \sim 4$), consistent with the idea that this sample was more denatured. In native RNA the structure is much more heterogeneous and, in fact, the application of the elastic model to the anisotropy decay shown in Figure 7.5 was unsuccessful. The assumption of small bending motions in the elastic theory of Barkley and Zimm [11], which is valid in the case of the relatively rigid duplex DNA, is simply not valid in native RNA where the bending motions are clearly not small (Figure 7.5).

All the DNA samples discussed so far have simple tertiary structures; they are linear double helices. The plasmid DNA sample (pBR 322), however, is a closed circular DNA with superhelical tertiary turns. The anisotropy decay of ethidium intercalated in this DNA agreed well with Eq. (7.24), but decayed more slowly than for native B-DNA: the torsional rigidity was $C = 1.95 \times 10^{-19}$ erg cm, assuming that $b = 13.4\text{Å}$. Supercoiled DNA is thus

more rigid than linear DNA, which may result from the torsional stress imposed on the double helix due to supercoiling [56]. A dependence of the torsional rigidity on the imposed torsional stress implies the existence of nonlinear terms in the torsional restoring force. Although the result for one supercoiled DNA hardly constitutes a proof of this nonlinearity, it would be possible to test this hypothesis by anisotropy measurements on a series of closed circular DNAs with varying numbers of superhelical turns. It should also be possible to test the prediction [56] that sufficiently supercoiled DNA will locally denature to relax the imposed stresses, since we have found that the torsional rigidity is sensitive to local denaturation. These possibilities are discussed further in Proposition 1.

It is possible that the slower anisotropy decay of pBR 322 DNA was due to an effectively larger helix radius, that may have resulted from a tertiary conformation in which the DNA was densely interwound. It is known that supercoiled DNA adopts several tertiary conformations in solution, depending on the ionic strength [57] and number of superhelical turns [58]. Since the tertiary conformation of the sample used in the work was unknown, this possibility could not be eliminated. However, whether the effect is due to the imposed torsional stresses or the tertiary conformation, it is clear that the anisotropy decay is sensitive to the tertiary structure of DNA.

This study of the synthetic polynucleotide complexes and supercoiled plasmid DNA has revealed that the torsional rigidity is sensitive to differences in nucleic acid structure. The major effect is due to helical

structure; the results demonstrate that the magnitude of the torsional rigidity of double stranded complexes reflects the extent of helical structure, since the intrinsic rigidities of the double helix and the random coil are quite different. The intrinsic rigidity of a triple helix is a factor of two larger than that of the double helix. The second important structural effect is due to tertiary structure, since it was found that the torsional rigidity is increased by supercoiling.

In view of these findings, the possibility of employing the torsional rigidity as a probe of these structural features should be considered. The possibility of using torsional rigidity measurements to monitor local denaturation in over-stressed supercoiled DNA has already been mentioned. Other applications should also be possible, for example, the observation of a right- to left-handed helix transition (B → Z).

f. Sequence effects

We now consider the differences in torsional rigidity among the intact double helical polydeoxyribo nucleotides in Table 7.5 . The most striking difference is between the homopolymers and the alternating copolymers; for example, poly d(G-C) · poly d(G-C) is considerably more rigid than poly(dG)·poly(dC). These results suggest the possibility of a sequence dependent contribution to the torsional rigidity, which could arise from base-base interactions. It is obvious that this contribution cannot be due to base pairing interactions alone.

In Table 7.5 we attempt to correlate the torsional rigidity with two sequence dependent properties of the polynucleotides that are sensitive to base-base interactions: the melting temperature, T_m [59], which measures

TABLE 7.5

Sequence Dependent Properties

Sequence	$C(10^{-19}$ erg cm)	T_m(°C)[a]	E_s(kcal·mol^{-1})[b]
d(G-C)·d(G-C)	1.50	115	-11.3
dA·dT	1.27	68.5	- 6.3
dG·dC	1.19	101	- 5.2
d(A-T)·d(A-T)	0.90	61	- 5.0

[a]Reference [59]

[b]Calculated values reported in Ref. [60]. Very similar values are obtained by averaging the results of the five theoretical calculations reviewed in Ref. [61].

the overall thermodynamic stability of the double stranded polynucleotide complex, and the calculated base-stacking interaction energies [60] which measure the electronic interactions between adjacent bases. The melting temperature has contributions from both base-pairing and base-stacking. These values were taken from the literature [59,60]. Although there is some variation in calculated stacking energies reported in the literature, the order and magnitude of the stacking energies shown in Table 7.5 is consistent with the majority of the theoretical calculations [61].

It is significant that the thermodynamically most stable poly d(G-C) · poly d(G-C), and the least stable, poly d(A-T) · poly d(A-T), are also the most rigid and the least rigid, respectively. However, the correlation of C with T_m breaks down for poly(dA)·poly(dT), which has a smaller T_m than poly(dG)·poly(dC) but is more rigid. The torsional rigidities of all the polynucleotides do, however, correlate with the calculated stacking energies; the order is preserved and the magnitude of the rigidity differences is reflected in the differences in stacking energy, except for poly d(A-T) · poly d(A-T) which has an unexpectedly small torsional rigidity.

Why should the torsional rigidity be partly determined by base-stacking interactions? Recall that the torsional rigidities we have measured imply considerable relative motion between adjacent base pairs, as indicated by $<\Delta\gamma>_{rms} = 5.7°$. It is reasonable that strong attractive interactions between adjacent base pairs will influence their relative motion. It is also reasonable that these interactions will depend on the torsion angle and so produce a restoring force; a large overwinding or

underwinding of the double helix will disrupt the stacking interactions and so raise the helix energy.

The observed sequence effects strongly imply that base-base interactions contribute to the torsional rigidity. It is clear that base-pairing interactions cannot account for these effects. While the correlation with the stacking energies is only suggestive, and of course depends on the calculated values [60,61], it is reasonable that the sequence effects could arise from base-stacking interactions.

g. Polyelectrolyte effects

Currently there is considerable interest in the polyelectrolyte contribution to the stiffness of DNA. Previous experimental [42,62,63, 65] and theoretical [27,64,67] work has dealt solely with the bending rigidity or the persistence length of native DNA. The results of this study presented in Figure 7.6 constitute the first measurements of the polyelectrolyte contribution to the torsional rigidity. Although a quantitative understanding of these results is not yet possible due to the lack of a theory for the change in torsional rigidity with ionic strangth, the results are consistent with the following qualitative arguments.

At ionic strengths greater than about 0.2M (region I), the Debye-Hückel screening length κ^{-1} is less than the effective contour distance between charges on the DNA phosphate backbone after counter ion condensation ($\sim$7.14Å, the Bjerrum Length, in water at 25°C). Therefore, the charges are effectively screened from one another and there should be no significant polyelectrolyte contribution to the torsional rigidity (or

the bending rigidity). The torsional rigidity is thus expected to be independent of ionic strength in this region, as was observed experimentally (Fig. 7.6). Since the measurements extend only to 2 M NaCl solutions, we cannot rule out the possibility that some structural change occurs in DNA at higher salt concentrations.

At ionic strengths less than about 0.1 M (regions II and III), the Debye-Hückel screening length is greater than the effective contour distance between charges. Therefore, the charges begin to interact with each other and an expansion and stiffening of the chain is expected; this is the so-called polyelectrolyte contribution to the chain stiffness. Experimentally, a modest increase in the torsional rigidity over the range $5 \times 10^{-4} \lesssim \mu \lesssim 0.1$ M (region II) was in fact observed. However, at ionic strengths less than 5×10^{-4} M the torsional rigidity fell rapidly. This is most likely due to denaturation or "melting" of the double helix caused by the electrostatic repulsions which cannot be accommodated by further expansion and elastic deformations of the chain.

A theory for the change in torsional rigidity with ionic strength is lacking at present. However, several authors have developed expressions describing the polyelectrolyte contribution to the persistence length of DNA [27,68,65,67]. This work has been reviewed by Schurr and Allison [66], who have also corrected a subtle geometric error in the theory of Manning [27]. According to these theories, the total persistence length is given by $P_o + P_e$, where P_o is the intrinsic persistence length of the (uncharged) double helix, and P_e is the polyelectrolyte contribution, which can be written in the form [67]

$$P_e = \frac{1}{4Q\kappa^2}$$

where Q is the Bjerrum length and κ^{-1} is the Debye-Hückel screening length, $\kappa^2 = 8\pi Q \mu$.

In principle, these expressions for the persistence length can be combined with Eqs. (7.30) and (7.31) to give an expression for the change in torsional rigidity with ionic strength. The broken line in Figure 7.6 was calculated in this manner, assuming that the Poisson ratio $\sigma = 0.5$ applies to both the intrinsic and polyelectrolyte contributions to the rigidity. The predicted change in the torsional rigidity is of the same order of magnitude as that observed experimentally for ionic strengths greater than about 10^{-3} M, but the quantitative agreement is poor. Nevertheless, both these results and the theoretical calculations [66] suggest only a modest (6-12%) increase in torsional rigidity at a salt concentration of 0.01 M compared with the 260% increase in persistence length reported by Harrington [62] from flow-birefringence measurements.

The rapid drop in the torsional rigidity at ionic strengths less than 5×10^{-4} M is not predicted by the polyelectrolyte theories, which take no account of the possibility of melting of the double helix. The melting temperature T_m as a function of ionic strength can be represented, at least approximately, by the empirical equation [68]

$$T_m = 16.6 \log_{10}\mu + 41\, \chi_{gc} + 81.5$$

where χ_{gc} is the fractional G-C content of the DNA. For calf thymus DNA ($\chi_{gc} = 0.42$) we calculate that the melting will occur at room temperature (23°C) at an ionic strength of 3×10^{-5} M. The reasonable agreement

between this calculated ionic strength and the experimental data (Fig. 7.6) further supports the idea that the drop in rigidity in region III is due to partial denaturation of the helix.

h. Initial anisotropy loss

All the nucleic acid samples studied exhibited a nonzero wobble angle $\Xi^{1/2}$, indicating that there was an initial loss of fluorescence anisotropy. In the analysis this anisotropy loss was considered to result from an infinitely rapid reorientation of the ethidium transition moment in the plane of the phenanthridinium ring. This approach is justified in the case of aqueous solvent, where the reorientation was very rapid and unresolved by the photon-counting instrument. However, in high viscosity solvents, such as saturated sucrose, the reorientation was much slower, on the order of a few nanoseconds, and was time-resolved. Thus the initial reorientation was coupled to solvent bulk viscosity. In fact, in a series of sucrose solutions of different viscosity, Genest and Wahl [69] found that the initial anisotropy decay was approximately exponential with a decay time proportional to viscosity. They also found that the reorientation amplitude increased with increasing temperature [69], from which they inferred that the motion was hindered by potential barriers resulting from the deformation of the DNA-dye complex. The present results show that the amplitude was about 15° in all the DNA samples, was smaller in RNA, about 6°, and was zero in thermally denatured DNA.

There are three possible explanations for the initial anisotropy loss: 1) reorientation of the nonintercalated dye (outside bound and possibly also unbound dye); 2) independent motion of the dye in its

intercalation site; and 3) an extremely rapid internal motion of the DNA-dye complex. Each of these possibilities is considered below.

Equation (7.24) for the anisotropy decay applies only to the intercalated dye. A more complete expression, including the short-lived component of the fluorescence is

$$r(t) = \frac{f\, e^{-t/\tau_n}\, r_n(t) + (1-f)\, e^{-t/\tau_i}\, r_i(t)}{f\, e^{-t/\tau_n} + (1-f)\, e^{-t/\tau_i}}$$

where $r_n(t)$ is the anisotropy decay of the non-intercalated dye, $r_i(t)$ is the anisotropy decay of the intercalated dye given by Eq. (7.24), and the other symbols have the same meaning as in Section 7.3c. Two points are apparent from this equation: that the anisotropy loss due to the "free" component is proportional to the fraction f, and that at times longer than about $3\tau_n$ the anisotropy decay simplifies to that of the intercalated dye only, $r_i(t)$. The results show no correlation between the wobble angle $\Xi^{1/2}$ and the fraction f of non-intercalated dye, even though the fraction was varied over a wide range (2% to 35%) by changes in ionic strength, DNA concentration, and the particular polynucleotide to which the dye was bound. Also, the theoretical fits usually began 5 nsec after the peak of the decay curves ($\simeq 3\tau_n$). Therefore, it was fairly certain that the initial anisotropy loss measured by $\Xi^{1/2}$ was not due to reorientation of the non-intercalated dye but that $\Xi^{1/2}$ was actually a property of the intercalated dye.

Independent motion of the dye within its intercalation site could be coupled to solvent viscosity via the frictional forces exerted by solvent on the bulky phenyl group projecting into the grooves of the DNA helix

[70], as suggested by Genest and Wahl [69]. Independent dye motion is consistent with a temperature dependent amplitude, and a smaller amplitude in RNA--the differences in lifetime and fraction of non-intercalated dye between poly(rA)·poly(rU) and its deoxy-counterpart poly(dA)·poly(dU) imply that dye was more strongly bound to (duplex) RNA than to DNA.

A rapid internal motion of the DNA-dye complex is also consistent with all the data; a local helix motion would be coupled to solvent viscosity and could also exhibit a temperature dependent amplitude. The absence of any correlation between the wobble angle and the torsional rigidity (Table 7.4) implies that the internal motion cannot be a torsional or bending mode. This motion was considerably faster than the $\simeq$ 1 nsec internal motions inferred from the NMR work on short fragments of DNA [16-18]. The initial reorientation observed in this work was faster than the 250 psec instrumental response. The smaller wobble angle for RNA may indicate that this motion is more restricted in (duplex) RNA than in DNA.

A detailed understanding of the different wobble angles measured in RNA and in denatured DNA must await the assignment of the initial anisotropy loss. Although it was not possible to decide between independent dye motion and a rapid internal motion of the DNA-dye complex on the basis of the present data, an experiment to resolve this question is presented in Proposition 2.

7.6 Conclusions

The ethidium-DNA systems have proven to be an extremely worthwhile starting point for an investigation of the dynamics of the internal motions

of macromolecules. The regular, well defined structure of the double helix results in a fluorescence polarization anisotropy decay that agrees very closely with an elastic model of ideal classical rods. The validity of the theoretical models, and some conditions under which deviations will occur, were established. This has allowed a thorough study of the torsion and bending modes of nucleic acids. The important conclusions of this study are summarized below.

1. The elastic model of Barkley and Zimm [11] for both torsion and bending reproduces the experimental fluorescence anisotropy of duplex DNA very accurately.
2. The intermediate zone of the bead-spring model can reproduce the torsional dynamics equivalently to the elastic model. However, the initial decay zone of the bead-spring model cannot be observed in fluorescence depolarization experiments.
3. There is no evidence of the torsional inhomogeneities postulated by Allison and Schurr [19]. Duplex DNA appears to be uniformly elastic, at least on a distance scale of a hundred base-pairs or so.
4. The torsional rigidity of calf thymus DNA under standard conditions is $C = 1.43 \pm 0.11 \times 10^{-19}$ erg cm. This refined value includes both bending and dye-tilt.
5. There is a polyelectrolyte contribution to the torsional rigidity of DNA at low ionic strengths. The magnitude of this contribution was measured over a wide range of ionic strength, and it was found that current theories for the change in persistence length with ionic strength cannot quantitatively predict this contribution. An analysis of these data must await a theory for the polyelectrolyte

contribution to the torsional rigidity.

6. Helical structure is the major structural feature affecting the torsional rigidity of nucleic acids. The order of torsional rigidities is triple strand > double strand > single strand.
7. Supercoiled DNA is more rigid than linear DNA.
8. Small sequence effects contribute to the torsional rigidity and are probably due to base-base interactions.
9. There is an initial loss of anisotropy that is either due to a rapid internal motion of the double helix or independent dye motion. This motion has a smaller amplitude in RNA than in DNA, and is absent in denatured DNA.

The fluorescence depolarization technique is now fully established as a direct and accurate probe of the internal motions of nucleic acids. We are now beginning to understand the structural and environmental effects that govern these motions and so determine the conformational flexibility of DNA. It should now be possible to extend this technique to more complex systems which are of biological interest, such as chromatin.

References - Chapter 7

1. D. P. Millar, R. J. Robbins, A. H. Zewail, Proc. Natl. Acad. Sci. USA 77, 5593 (1980).

2. D. P. Millar, R. J. Robbins, A. H. Zewail, J. Chem. Phys. 74, 4200 (1981).

3. R. J. Robbins, D. P. Millar, A. H. Zewail, in Picosecond Phenomena II, R. M. Hochstrasser, W. Kaiser, C. V. Shank, eds., Springer-Verlag, Berlin, 1980.

4. D. P. Millar R. J. Robbins, A. H. Zewail, Proc. of Conference on Laser Induced Processes in Biological Molecules, Stanford University, 1981.

5. D. P. Millar, R. J. Robbins, A. H. Zewail, J. Chem. Phys. 76, 2080 (1982).

6. Ph. Wahl, J. Paoletti, and J.-B. Le Pecq, Proc. Natl. Acad. Sci. USA 65, 417 (1970).

7. I. Munro, I. Pecht, and L. Stryer, Proc. Natl. Acad. Sci. USA 76, 56 (1979).

8. J. C. Thomas, S. A. Allison, C. J. Appellof, and J. M. Schurr, Biophys. Chem. 12, 177 (1980).

9. M. Le Bret, Biopolymers 17, 1939 (1978).

10. C. J. Benham, Biopolymers 18, 609 (1979).

11. M. D. Barkley and B. H. Zimm, J. Chem. Phys. 70, 2991 (1979).

12. A. V. Vologodskii, V. V. Anshelevich, A. V. Lukashin, and M. D. Frank-Kamenetskii, Nature 280, 294 (1979).

13. I. Hurley, B. H. Robinson, C. P. Scholes, and L. S. Lerman, in Nucleic Acid Geometry and Dynamics, R. H. Sarma, ed., Pergamon, New York, 1980.

14. S. W. Englander and J. J. Englander, Meth. Enzymology 49, 24 (1978).

15. C. J. Benham, J. Mol. Biol. 150, 43 (1981).

16. M. E. Hogan and O. Jardetzky, Biochem. 19, 3460 (1980).

17. P. H. Bolton and T. L. James, J. Amer. Chem. Soc. 102, 25 (1980).

18. P. H. Bolton and T. L. James, Biochem. 19, 1388 (1980).

19. S. A. Allison, J. M. Schurr, Chem. Phys. 41, 35 (1979).

20. M. J. Waring, J. Mol. Biol. 13, 269 (1965).

21. J.-B. Le Pecq and C. Paoletti, J. Mol. Biol. 27, 87 (1967).

22. M. Hogan, N. Dattagupta, and D. M. Crothers, Biochem. 18, 280 (1979).

23. R. H. Scheller, T. L. Thomas, A. S. Lee, W. H. Klein, W. D. Niles, R. J. Britten, and E. H. Davidson, Science 196, 197 (1977).

24. M. Becker, Ph. D. Thesis, California Institute of Technology, 1981.

25. D. M. Crothers and B. H. Zimm, J. Mol. Biol. 12, 525 (1965).

26. J. L. Bresloff and D. M. Crothers, J. Mol. Biol. 95, 103 (1975).

27. G. S. Manning, Q. Rev. Biophys. 11, 179 (1978).

28. D. W. Wilson and I. G. Lopp, Biopolymers 18, 3025 (1979).

29. H. Yamakawa and M. Fujii, Macromolecules 6, 407 (1973).

30. R. T. Kovacic and K. E. van Holde, Biochem. 16, 1490 (1977).

31. S. Arnott, Prog. Biophys. Mol. Biol. 21, 267 (1970).

32. S. Arnott and P. J. Bond, Nature 244, 99 (1973).

33. K. E. Reinert, J. Strassburger and H. Triebel, Biopolymers 10, 285 (1971).

34. A. Prunell and G. Bernardi, J. Biol. Chem. 218, 3433 (1973).

35. M. T. Record, C. P. Woodbury, and R. B. Inman, Biopolymers 14, 393 (1975).

36. J. E. Godfrey, Biophys. Chem. 5, 285 (1976).

37. H. Yamakawa and M. Fujii, Macromolecules 7, 649 (1974).

38. D. Jolly and H. Eisenberg, Biopolymers 15, 61 (1976).

39. J. E. Godfrey and H. Eisenberg, Biophys. Chem. 5, 301 (1976).

40. G. Voordouw, Z. Kam, N. Borochov, and H. Eisenberg, Biophys. Chem. 8, 171 (1978).

41. H. Yamakawa and M. Fujii, Macromolecules 7, 128 (1974).

42. C. Frontali, E. Dore, A. Ferrauto, E. Gratton, A. Bettini, M. R. Pozzan, and E. Valdevit, Biopolymers 18, 1353 (1979).

43. L. D. Landau and E. M. Lifshitz, Theory of Elasticity, 2d Ed., Pergamon, New York, 1970, pp. 13-14.

44. M. Hogan, N. Dattagupta, and D. M. Crothers, Proc. Natl. Acad. Sci. USA 75, 195 (1978).

45. M. Levitt, Proc. Natl. Acad. Sci. USA 75, 640 (1978).

46. J. Olmsted III and D. R. Kearns, Biochemistry 16, 3647 (1977).

47. L.P.G. Wakelin and M. J. Waring, J. Mol. Biol. 144, 183 (1980).

48. B. H. Robinson, L. S. Lerman, A. H. Beth, H. L. Frisch, L. R. Dalton, and C, Auer, J. Mol. Biol. 139, 19 (1980).

49. R. E. Depew and J. C. Wang, Proc. Natl. Acad. Sci. USA 72, 4275 (1975).

50. D. E. Pulleybank, M. Shure, D. Tang, J. Vinograd, and H. P. Vosberg, Proc. Natl. Acad. Sci. USA 72, 4280 (1975).

51. K. J. Miller, Biopolymers 18, 959 (1979).

52. S. J. Opella, W. B. Wise, and J. A. De Verdi, Biochem. 20, 284 (1981).

53. L. D. Landau and E. M. Lifshitz, Theory of Elasticity, 2d Ed., Pergamon, Oxford, 1970, p. 74.

54. R. L. Baldwin, Molecular Associations in Biology, B. Pullman, ed., Academic Press, New York, 1968, p. 145.

55. R. L. Baldwin, Acc. Chem. Res. 4, 265 (1971).

56. C. J. Benham, Proc. Natl. Acad. Sci. USA 76, 3870 (1979).

57. A. M. Campbell, Biochem. J. 171, 281 (1978).

58. A. M. Campbell and D. J. Jolly, Biochem. J. 133, 209 (1973).

59. R. D. Wells, J. E. Larson, R. C. Grant, B. E. Shortle, and C. R. Cantor, J. Mol. Biol. 54, 465 (1970).

60. R. Rein, N. S. Goel, N. Fukuda, M. Pollack, and P. Claverie, Annals NY Acad. Sci. 153, 805 (1969).

61. R. Rein, Intermolecular Interactions, B. Pullman, ed., Wiley, New York, 1978, Vol. 1, p. 307.

62. R. E. Harrington, Biopolymers 17, 919 (1978).

63. N. Borochov, H. Eisenberg, and Z. Kam, Biopolymers 20, 231 (1981).

64. T. Odijk, J. Polym. Sci., Polym. Phys. Ed. 15, 477 (1977).

65. J. Skolnick and M. Fixman, Macromolecules 10, 944 (1977).

66. J. M. Schurr and S. A. Allison, Biopolymers 20, 251 (1981).

67. T. Odijk, Biopolymers 18, 311 (1979).

68. C. R. Cantor and P. R. Schimmel, Biophysical Chemistry, W. H. Freeman, San Francisco, 1980, p. 1155.

69. D. Genest and P. Wahl, Biochimica et Biophysica Acta 521, 502 (1978).

70. C. Tsai, C. S. Jain, and H. M. Sobell, Proc. Natl. Acad. Sci. USA 72 628 (1975).

APPENDIX I

Design for a Dye Laser Amplifier

One possible disadvantage of the mode-locked CW dye lasers described in Chapter 2 of this thesis is their low pulse energy ($\sim$2 nJ) and peak power ($\sim$1 kW). This would be especially true in applications where high peak powers are necessary, such as in nonlinear optical experiments. For example, to generate a "$\pi/2$ pulse" in a typical photon echo [1] experiment on a large molecule such as a pentacene would require a peak power of50 kWfor a 1 psec pulse. High peak powers also enable a picosecond duration continuum emission to be generated by focussing in certain liquids [2], which is extremely useful as a spectroscopic probe pulse. Thus a means for amplifying the pulses from the mode-locked CW dye lasers was investigated. The idea was to amplify the pulses in an extermal dye amplifer. Because the gain medium in the amplifier is not contained in an optical resonator, it is prevented from "lasing" and hence much higher single-pass gain can be achieved than in the dye laser. To fully utilize this advantage, a much higher power pulse than can be obtained from a mode-locked argon ion laser should be used to pump the amplifier. The second harmonic output of a Q-switched Nd:YAG laser is a good choice, since a pump energy approaching 1 J can be readily attained. The idea is to transfer as much of this energy to the dye laser pulses as possible. Very high gains are thus anticipated. However, there are several practical considerations which limit the gain that can be achieved and which must be carefully considered in the design of a dye laser amplifier. Some

of these factors are discussed below, and a design for a three-stage dye amplifier and associated synchronization electronics is presented.

One of the most important design considerations for a dye amplifier is the effect of gain saturation. As the input pulse grows in intensity it depletes the excited state population by stimulated emission and so reduces the gain. In a long, uniformly excited gain medium, the input pulse at first increases exponentially with distance, but then continues to increase only linearly as gain saturation sets in. Thus the first design criterion is not to use a long gain medium, but several smaller stages in which the conditions are optimized as to minimize the gain saturation effects of each stage. This means that the beam diameter should increase from one stage to the next to accommodate the increasing intensity, while keeping the photon density (which is most important) nearly constant. It also means that progressively more pump energy must be deposited in the later stages to overcome the increasingly greater depletion of the gain caused by the growing intensity of the input pulses. A three-stage dye amplifier was designed with these considerations in mind. The optical arrangement is shown in Figure I.1. The first two stages are each 2.5 cm long and are pumped in a transverse geometry. The pump beam is expanded to 2.5 cm using a pair of lenses, then focussed to a line in the cell using a cylindrical lens ($f = 8$ cm). The diameter of the input beam in the first stage is about 200-300 micron and about 2-3 mm in the second stage. The pump beam is slightly defocussed in the second stage to accommodate this beam size. The third stage is 10 cm long and is pumped in a longitudinal geometry. Here the pump

Figure I.1

Design for a three-stage dye amplifier pumped by the second harmonic of a Nd:YAG laser:

DVP	Direct vision prism
SF	Spatial filter
SA	Saturable absorber
BS	Beamsplitter (100% R at 532 nm, 100% T at 600 nm)
KDP	Frequency doubling crystal
F	Filters to absorb 1064 nm

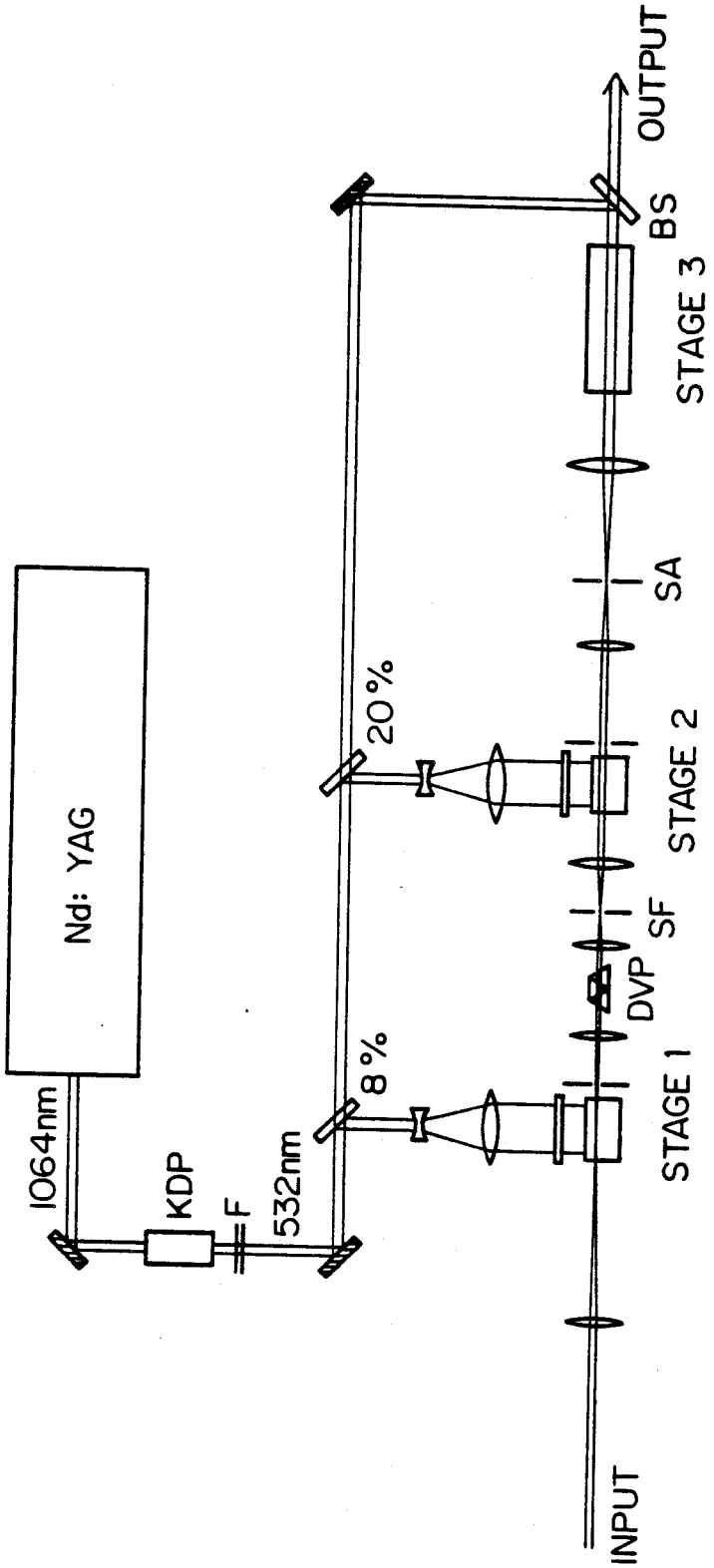
Nd: YAG
1064nm
KDP
F
532nm
8%
20%
DVP
SF
SA
BS
INPUT
OUTPUT
STAGE 1
STAGE 2
STAGE 3

beam is unfocussed and the dye laser beam is expanded to match its diameter ($\simeq$ 6 mm). The pump source was the frequency doubled output of a Q-switched Nd:YAG laser (Quanta Ray DCR1). The pulse energy at 532 nm is $\sim$60-70 mJ. The fraction of this energy directed into the first stage is $\sim$8%, into the second stage $\sim$20%, and into the final stage $\sim$70%.

The second most important design consideration is the suppression of amplified spontaneous emission (ASE). In an inverted gain medium, photons emitted by spontaneous emission can cause stimulated emission and be amplified, which must be avoided in an amplifier since it steals gain from the input pulse to be amplified. In many ways the ASE is analogous to noise in an electronic amplifier [3]. The extent of ASE depends on geometrical considerations of the excited gain volume. By using a long, thin excited volume, the solid angle which is available for ASE is minimized [4]; thus the choice of the 2.5 cm and 10 cm gain regions in the current design. Obviously another consideration is that the spontaneous emission from one stage be well isolated from the next. There are two approaches that can be applied here. One approach utilizes the better directionality of the laser beam compared with the spontaneous emission. Because the laser beam can be focussed to a smaller spot size than the diffuse spontaneous emission, a pinhole placed in the focal plane of a lens will act as a "noise filter" [3]. This is used between the first and second stages; a direct vision prism first spatially disperses the spectrally-broad ASE to enhance the contrast in relative angular divergence of the "signal" and "noise." A spatial filter, consisting of a lens and 50μ pinhole is used after the prism. The ratio of ASE to

signal can be reduced by a factor between 100 and 1000 with this arrangement. A second approach is to use a saturable absorber between stages. Because the signal beam has a higher intensity than the ASE, the signal suffers less absorption loss in the saturable absorber. By adjusting the concentration of a saturable absorber such as malachite green, it should be possible to absorb all the ASE with little loss to the signal. This method should work best when the signal is very intense, and so is used between the second and third stages in this design.

Obviously the arrival of the picosecond input pulses at each amplifier stage must coincide with the presence of a pump pulse. The pump pulses obtained from the Nd:YAG laser are about 8 nsec in duration, which facilitates the synchronization somewhat; that is, synchronization to within a few nanoseconds is required, which should be readily possible with electronic circuitry. However, because the Nd:YAG laser operates at a much lower repetition rate (10 Hz) than the mode-locked CW dye laser (82 MHz), not every pulse can be amplified; in this system only one pulse in every 8.2 million can be amplified. The synchronization scheme is shown in Figure I.2. The Nd:YAG laser has three modes of operation: internal control, external control, and mixed control. The latter mode was used here; the flashlamp circuit in the laser was allowed to run under internal control, but the triggering of the Q-switch was externally controlled. A timing pulse synchronized with the lamp firing was delayed by a few hundred microseconds before it triggered an external pulse generator, which produced a 15 ns wide gating pulse for a linear gate circuit (ORTEC LG 101). The signal from a photodiode monitoring a fraction of

Figure I.2

Schematic of the system used to achieve synchronization of the dye laser input pulse train and the Q-switched pulses from the Nd:YAG laser. See text for details.

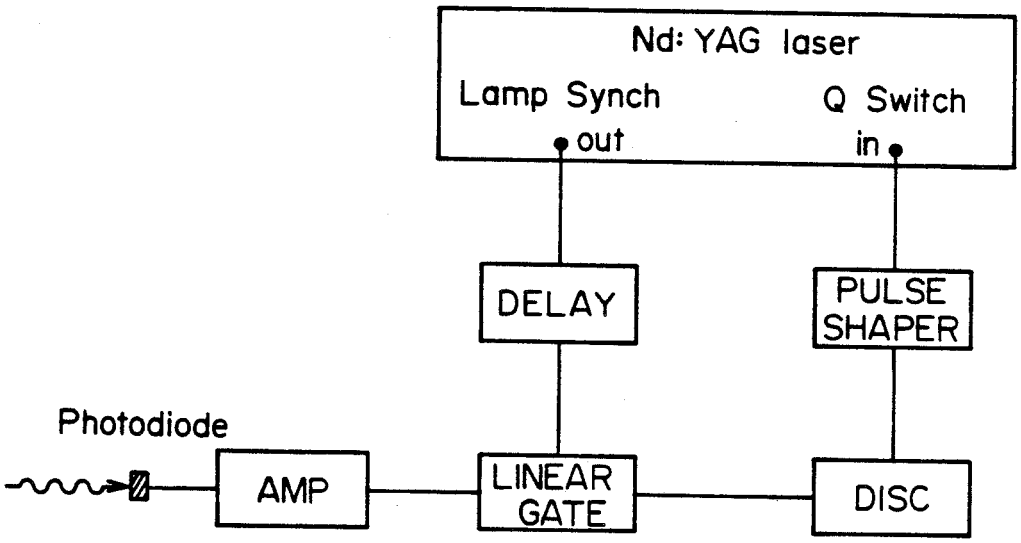
Nd: YAG laser
Lamp Synch
out
Q Switch
in
DELAY
PULSE
SHAPER
Photodiode
AMP
LINEAR
GATE
DISC

the dye laser output was input to the linear gate. Because the gate width was 15 ns, only one electrical pulse in the pulse train was transmitted through the gate to the output. This pulse triggered a discriminator (ORTEC 436), whose output was converted into a pulse suitable for triggering the Q-switch under external control. The total delay between the lamp pulse and the Q-switch firing was about 700 μsec, and was adjustable over a range of 60 nsec in 1 nsec steps to synchronize exactly the peak of the pump pulse and the dye laser pulse. Note that the pulse selected by the gate circuit is not the same one that is amplified--it is a pulse much later in the train that is amplified. However, the selected pulse is synchronized with all the subsequent pulses in the train and hence can be used to synchronize the Q-switch firing. The total timing jitter of the entire system was measured to be ±2 nsec, which was mainly due to an inherent jitter in the pulse formation in the Nd:YAG laser. The jitter in the electronic system was less than 1 nsec. The synchronizing system in Figure I.2 was found to work very well.

At the time of writing the first stage of the dye amplifier has been set up and tested. The gain was about a factor of 50 using rhodamine 6G as the gain medium; however, much higher gain should be possible using a different dye, such as kiton red. Ippen et al. [5] have recently reported on a three-stage dye amplifier very similar to the design shown here in Figure I.1. These authors report total gain of 10^4 to 10^5 for 120 mJ of pump energy. Since the pump energy available from the Nd:YAG laser used in the present design is ≃ 65 mJ; a somewhat smaller gain is expected here.

Appendix I - References

1. L. Allen, J. H. Eberly, Optical Resonance and Two-Level Atoms, John Wiley & Sons, New York, 1975.

2. R. R. Alfano, S. L. Shapiro, Chem. Phys. Lett. 3, 407 (1971).

3. H. Kogelnik, A. Yariv, Proc. IEEE 52, 165 (1964).

4. M. H. Gassman, H. Weber, Opto-Elec. 3, 177 (1971).

5. E. P. Ippen, C. V. Shank, J. M. Wiesenfeld, A. Migus, Phil. Trans. R. Soc. London A298, 225 (1980).

Appendix II

Nonlinear Least-Squares Curve Fitting

II.1 Introduction

An important component of the time-resolved spectroscopy experiments described in this thesis was the analysis of the experimental data. The data were most often in the form of an intensity or transmission change (the dependent variable) versus time (the independent variable). What must be extracted from these data are estimates of certain quantities such as excited state lifetimes, or pulse-widths, or critical transfer distances, or even torsional rigidities. A common approach can be used in all the cases encountered in this work. The quantities of interest are considered to be variable parameters which are to be estimated by adjusting their values so as to obtain the best representation of the data by the appropriate model (from which the parameters arise). One method for adjusting the parameters to obtain the best fit is called the least-squares method [1]. In all the cases of relevance to this work, the model involved a nonlinear function of the parameters. For example, in Chapter 2 the autocorrelation data are fit by the Pike-Hercher model with parameters such as the pulse width Δt_p, coherence time Δt_c, and ratio R. The first two of these, Δt_p and Δt_c, appear in the model as squared exponents of exponentials, clearly a nonlinear function. The ratio appears as a linear parameter. Thus, in general, the method of nonlinear least-squares [1,2] had to be applied to fit the experimental data obtained in this work.

II.2 The Least-Squares Problem

The model to be fitted to the experimental data is specified in general as,

$$E(y) = f(x_1, x_2, \cdots, x_m; \beta_1, \beta_2, \cdots, \beta_k) \qquad \text{(II.1a)}$$

$$= f(\underset{\sim}{x}, \underset{\sim}{\beta}) \qquad \text{(II.1b)}$$

where y is the dependent variable, E(y) is the expected value of y according to the model, $\underset{\sim}{x} = x_1, \cdots, x_m$ are independent variables, and $\underset{\sim}{\beta} = \beta_1, \cdots, \beta_k$ are a set of k parameters.

The set of n data points are represented as

$$(Y_i, X_{1i}, X_{2i}, \cdots, X_{mi}) \quad , \qquad i = 1,2,\cdots,n \qquad \text{(II.2)}$$

where Y_i, $X_{1i}, \cdots$ etc. are the values of y and $x_1, \cdots$ etc. at the i^{th} data point. Each value of the dependent variable y has an uncertainty σ_i (standard deviation = σ_i, variance = σ_i^2, weight = $1/\sigma_i^2$).

A "goodness-of-fit" criterion, called the reduced chi-squared value, is introduced. It is defined as

$$\chi_r^2 = (n-k)^{-1} \sum_{i=1}^{n} \frac{1}{\sigma_i^2} [Y_i - \hat{Y}_i]^2 \qquad \text{(II.3)}$$

where $\hat{Y}_i$ is the predicted value of the dependent variable at the i^{th} data point. The problem of least-squares is to compute those estimates of the parameters $\underset{\sim}{\beta}$ which will minimize χ_r^2. The reason for the name "least squares" is now obvious, since the method seeks to minimize the weighted sum of the squared residuals in Eq. (II.3).

II.3 The Gauss-Newton Method

One method for nonlinear least-squares curve fitting, due to Gauss and Newton, is to expand the model f in a first order Taylor series in the parameters. The nonlinear problem is thus approximated by a linear least-squares problem for which the solution is already known [1]. The expansion will be most accurate in the region of parameter space close to the location of the true minimum of χ_r^2. With this limitation, the expansion is written through the linear terms only, as follows:

$$\left\langle Y(\underset{\sim}{x}_i, \underset{\sim}{b}+\underset{\sim}{\delta}_t)\right\rangle = f(\underset{\sim}{x}_i,\underset{\sim}{b}) + \sum_{j=1}^{k} \left(\frac{\partial f}{\partial b_j}\right) (\delta_t)_j \qquad \text{(II.4)}$$

or in matrix notation,

$$\langle Y \rangle = \underset{\sim}{f}_o + P\,\underset{\sim}{\delta}_t \qquad \text{(II.5)}$$

The vector $\underset{\sim}{b}$ is the approximation to the true parameter vector $\underset{\sim}{\beta}$ within this linearized model; the converged value of $\underset{\sim}{b}$ is the least-squares best estimate of $\underset{\sim}{\beta}$. The vector $\underset{\sim}{\delta}_t$ is a set of small parameter corrections; the subscript "t" denotes that these corrections are calculated from the Taylor series expansion. The $\langle\,\rangle$ brackets denote predictions made within the linearized model. The n x k matrix P is given by,

$$P = (\partial f_i/\partial b_j) \quad , \qquad i = 1,2,\cdots,n;\ j = 1,2,\cdots,k \qquad \text{(II.6)}$$

The value of χ_r^2 in this linearized model is

$$\left\langle \chi_r^2 \right\rangle = (n-k)^{-1} \sum_{i=1}^{n} \frac{1}{\sigma_i^2}\left[Y_i - \left\langle Y_i \right\rangle\right]^2 \qquad \text{(II.7)}$$

The aim is to find the values of the parameter corrections $\underset{\sim}{\delta}_t$ which minimize $\langle \chi_r^2 \rangle$. Since $\underset{\sim}{\delta}_t$ appears linearly in Eq. (II.4), it can be found by the usual linear least-squares procedure of setting $\partial \langle \chi_r^2 \rangle / \partial \delta_j = 0$ for all j [1]. The solution to this problem is equivalent [1] to solving the following equation in matrix notation:

$$A \, \underset{\sim}{\delta}_t = \underset{\sim}{B} \tag{II.8}$$

where $$A = P^T P$$

and $$B = \left(\frac{1}{\sigma_i^2} \sum_{i=1}^{n} (Y_i - f_i) \cdot \partial f_i / \partial b_j\right), \; j = 1,2,\cdots,k$$

To implement this method, one starts with an initial guess for the parameters $\underset{\sim}{b}^{(o)}$. The vector $\underset{\sim}{B}$ and the k x k symmetric matrix A are then evaluated according to Eqs. (II.7) and (II.8). The parameter corrections $\underset{\sim}{\delta}_t^{(o)}$ are found by solving Eq. (II.6) by matrix methods:

$$\underset{\sim}{\delta}_t = A^{-1} \, \underset{\sim}{B} \tag{II.9}$$

where A^{-1} is the inverse of matrix A, and can be found numerically using the Gauss–Jordan method [1]. The new estimate of the parameter vector is $b^{(1)} = b^{(o)} + \underset{\sim}{\delta}_t^{(o)}$, which is then used to calculate a new parameter correction $\underset{\sim}{\delta}_t^{(1)}$. This process is continued until the decrease in the chi-squared value from one iteration to the next is less than a predetermined (small) tolerance. The converged set of parameters is then the best estimate of the true parameters $\underset{\sim}{\beta}$.

II.4 The Gradient Method

Another method for nonlinear least-squares simply traverses parameter space by following the direction of steepest-descent of the function χ_r^2. This direction is equal to the negative of the gradient of χ_r^2. Thus,

$$\underset{\sim}{\delta}_g = -(\partial\chi_r^2/\partial b_1,\ \partial\chi_r^2/\partial b_2, \cdots,\ \partial\chi_r^2/\partial b_k)^T \qquad \text{(II.10)}$$

where the subscript "g" denotes that the parameter corrections are evaluated by the gradient method. Typically, the parameter corrections calculated above are scaled by some small step size, and an iterative procedure is employed to locate the true minimum by computing the new search directions at each iteration according to (II.10). There is a trade-off between having a small enough step size to accurately locate the minimum and a size large enough to ensure rapid convergence [1].

II.5 The Marquardt Algorithm

Marquardt [2] has compared the two approaches described above, and has developed a more efficient method which incorporates the best features of each. Marquardt [2] noted that the correction vectors $\underset{\sim}{\delta}_t$ and $\underset{\sim}{\delta}_g$ are often almost 90° apart, a consequence of the severe elongation of the χ_r^2 surfaces in parameter space. Any improved method seeks to interpolate between $\underset{\sim}{\delta}_t$ and $\underset{\sim}{\delta}_g$. Marquardt showed [2] that the effect of adding a small positive increment λ to the diagonal elements of the A matrix has the desired effect, the size of λ controlling the interpolation between the two extremes. Thus, instead of solving Eq. (II.8), one has the equation

$$(A + \lambda I)\underset{\sim}{\delta} = \underset{\sim}{B} \qquad \text{(II.11)}$$

where I is the identity matrix. When λ is small, $\underset{\sim}{\delta} \simeq \underset{\sim}{\delta}_t$, and the Taylor series solution is retrieved. When λ is large, the diagonal elements of the matrix dominate, and Eq. (II.11) can be approximated by

$$B_j \simeq \lambda \delta_j A_{jj}$$

which yields a correction in the same direction as the gradient, but scaled by A_{jj} and reduced by λ . In a typical application of Eq. (II.11) one expects that relatively large values of λ would be used initially to rapidly find the general location of the minimum, then small λ values would be used, corresponding to the Taylor series expansion which is very accurate in this region. Marquardt has developed an optimal strategy, which is now known as the "Marquardt algorithm." The algorithm may be summarized as [1,2]:

1. Compute $\chi_r^2(\underset{\sim}{b})$, where $\underset{\sim}{b}$ are the initial parameter estimates.
2. Start initially with $\lambda = .001$.
3. Compute $\underset{\sim}{\delta}$ (according to Eq. (II.11)) and $\chi_r^2(\underset{\sim}{b} + \underset{\sim}{\delta})$ for this choice of λ.
4. If $\chi_r^2(\underset{\sim}{b} + \underset{\sim}{\delta}) > \chi_r^2(\underset{\sim}{b})$, increase λ by a factor of 10 and repeat step (3).
5. If $\chi_r^2(\underset{\sim}{b} + \underset{\sim}{\delta}) < \chi_r^2(\underset{\sim}{b})$, decrease λ by a factor of 10, consider $\underset{\sim}{b}' = \underset{\sim}{b} + \underset{\sim}{\delta}$ to be the new starting point, and return to step (3), substituting $\underset{\sim}{b}'$ for $\underset{\sim}{b}$.

At each iteration it may be necessary to recompute the parameter increments a number of times to optimize λ according to this algorithm. However, the A and B matrices need only be accumulated once per iteration,

and it is this operation which requires the most computation time. The advantage of the Marquardt algorithm is that each iteration is much more effective than either the Gauss-Newton or the gradient method.

Marquardt [2] noted another point which is helpful in implementing this method. It has been found that it is useful to scale the matrices before solving Eq. (II.11) to improve the numerical aspects of least-squares computing [2]. The A and B matrices are scaled as follows:

$$A^* = \frac{A_{jj'}}{\sqrt{A_{jj}}\sqrt{A_{j'j'}}} \tag{II.12}$$

$$B^* = (B_j / \sqrt{A_{jj}}) \tag{II.13}$$

Instead of solving (II.11), one now solves the following equation:

$$(A^* + \lambda I)\,\underset{\sim}{\delta}^* = \underset{\sim}{B}^* \tag{II.14}$$

The true parameter corrections are then,

$$\delta_j = \delta_j^* / \sqrt{A_{jj}} \tag{II.15}$$

It was this method that was used in practice.

II.6 Error Determination

The least-squares method also enables an estimate of the uncertainty in each of the optimized parameters. The relationship is surprisingly simple [1]; the variance of the j^{th} parameter is equal to the j^{th} diagonal element of the inverse A matrix.

$$\sigma^2_{b_j} = (A^{-1})_{jj} \qquad \text{(II.16)}$$

It can be shown [1] that incrementing b_j by an amount $\Delta b_j = \sigma^2_{b_j}$, and optimizing the remaining parameters will increase χ^2_r by exactly 1.

Confidence intervals for each parameter are related to the variances in (II.16) by a numerical factor that depends upon the number of variable parameters. For example, for 5 variable parameters, the 95% confidence intervals are equal to the variance multiplied by 3.33. The 95% confidence intervals were used as error ranges in this work, rather than the variances.

II.7 Application of Curve-Fitting Methods

The typical procedure used for analyzing data with these nonlinear least-squares curve fitting methods is now described. All computations were performed on a PDP 11/23 computer. For each data-fitting application encountered in this work, a separate program was written which contained the following units:

MAIN — The main program; reads the data file from disk, establishes the initial parameter values, and selects the output listing device. All subroutines are called from MAIN.

Subroutines:

FDERIV — Computes the residual $(Y_i - f_i)$, the derivatives $\partial f_i/\partial b_j$, and the weight $w_i = 1/\sigma_i^2$ at each data point i. The derivatives are evaluated from analytical expressions appropriate to each model.

NLLSMV — Performs nonlinear least-squares adjustment according to the Marquardt algorithm; accumulates the A* and B* matrices, optimizes the λ value, computes the parameter corrections $\underset{\sim}{\delta}$, and the χ^2_r value of each iteration. Determines when convergence has been reached.

MATINV — Numerically inverts the A* matrix.

OUTPUT — Outputs the parameters $\underset{\sim}{b}$, the λ value, and χ^2_r at each iteration. Also outputs the parameter correlation matrix after the final iteration.

NOTATE — Prints a summary of the final parameter values, their 95% confidence intervals, and the final value of χ^2_r.

TKPLOT — Plots the data and best-fit function on a Tektronix TN1706 digital plotter.

TKRESD — Plots the weighted residuals, $R_i = 1/\sigma_i^2 \, [Y_i - f_i]$.

TKAUTO — Calculates and plots the autocorrelation function of the residuals [3],

$$A(\tau) = \sum_{i=1}^{n} R(i)\, R(\tau+i) / \sum_{i=1}^{n} R(i)^2$$

The subroutines NLLSMV, MATINV, OUTPUT, TKAUTO, and library routines (TKLIBR) associated with TKPLOT were generously supplied by Dr. R. J. Robbins.

Appendix II - References

1. P. R. Bevington, Data Reduction and Error Analysis for the Physical Sciences, McGraw-Hill, New York, 1969.

2. D. W. Marquardt, J. Soc. Ind. Appl. Math. 11, 431 (1963).

3. A. Grinvald, I. Z. Steinberg, Anal. Biochem. 59, 583 (1974).